

2012

# Sequence Specific Interactions Between DNA and Single-Walled Carbon Nanotubes

Daniel Roxbury  
*Lehigh University*

Follow this and additional works at: <http://preserve.lehigh.edu/etd>

---

## Recommended Citation

Roxbury, Daniel, "Sequence Specific Interactions Between DNA and Single-Walled Carbon Nanotubes" (2012). *Theses and Dissertations*. Paper 1310.

This Dissertation is brought to you for free and open access by Lehigh Preserve. It has been accepted for inclusion in Theses and Dissertations by an authorized administrator of Lehigh Preserve. For more information, please contact [preserve@lehigh.edu](mailto:preserve@lehigh.edu).

# Sequence Dependent Interactions Between DNA and Single-Walled Carbon Nanotubes

by

Daniel Roxbury

Presented to the Graduate and Research Committee  
of Lehigh University  
in Candidacy of the Degree of  
Doctor of Philosophy

in

Chemical Engineering

Lehigh University

May 2012

# Certificate of Approval

Approved and recommended for acceptance as a dissertation in partial fulfillment of the requirements for the degree of Doctor of Philosophy.

---

Date

---

Prof. Anand Jagota,  
Dissertation Advisor

---

Accepted Date

Committee Members:

---

Prof. Jeetain Mittal

---

Prof. Hugo Caram

---

Prof. Slava V. Rotkin

---

Prof. Dimitri Vezenov

# Acknowledgements

I would first like to thank my parents, Jeff and Susan, to whom I dedicate this thesis. For as long as I can remember, they have encouraged me to pursue whatever it was that made me happy. Through grade school, high school, undergraduate and graduate studies, they could see the determination that I possessed and would always reassure me that one day I would see all of my dreams come true. I will never forget what they have done for me, and appreciate everything more than words can describe. I would also like to thank my sister, Julie, for putting up with me over the years. Even though we've had our disagreements, I feel that living together the past 5 years has brought us closer and that we will appreciate this further on down the road. Next I would like to thank my girlfriend, Victoria. Thank you for standing by me down the most testing stretch of my life thus far. You will always be my best friend and I will always love you.

Thank you to my thesis advisor, Professor Anand Jagota. Your seemingly endless insight and patience has transformed me from the naive undergraduate to the accomplished independent researcher that I am today. It has not always been easy, but you have never given up faith in me. Thanks to you, I feel undeniably more motivated, as an individual, as I now continue my research career. For that, I am greatly appreciative of all that you have invested in me.

Thank you to all the members of my dissertation committee: Professor Hugo Caram, Professor Jeetain Mittal, Professor Slava V. Rotkin, and Professor Dimitri

Vezenov. Thank you for all the advice you have given me over the years. It is with these helpful comments and guidance that I have been able to ‘think outside of the box’ and mature as an independent thinker. A special thanks to Professor Mittal for all of the assistance you have given me for my theoretical work. You have been a great co-advisor to me, and I wish you the best as you continue your early career at Lehigh. Thank you Dr. Ming Zheng, Dr. Xiaomin Tu, and Dr. Constantine Khripin at NIST in Gaithersburg, MD. Without many useful discussions and collaborations with you, much of the research presented in this thesis would not have been possible. Additionally, thank you Dr. Debabrata Mukhopadhyay, Dr. Santanu Bhattacharya, and Xun Gong at the Mayo Clinic in Rochester, MN. From our collaborative efforts, I have learned many useful biomedical techniques and principles that normally I would never have had the chance to experience.

Finally, thank you to all of my lab mates that I have worked with at Lehigh University: Dr. Suresh Manohar, Dr. Shilpi Vajpayee, Ying Bai, Nichole Nadermann, Sara Iliafar, Walter Jokiel, Bryan Postelnek, David Marchand, and Akshaya Shankar. It has been my pleasure to work with you the last 5 years of my life. I wish you all the best in your future research careers.

Thank you!

Daniel Roxbury

May 2012

# Table of Contents

<b>Acknowledgements .....</b>	<b>iii</b>
<b>List of Figures.....</b>	<b>vii</b>
<b>List of Tables .....</b>	<b>xiii</b>
<b>Abstract.....</b>	<b>1</b>
<b>Chapter 1: Introduction .....</b>	<b>3</b>
1.1. The Single-Walled Carbon Nanotube .....	4
1.2. Novel Material and Biomedical Applications of SWCNTs.....	5
1.3. Deoxyribonucleic Acid .....	8
1.4. DNA-SWCNT Hybrids.....	10
1.5. Thesis Outline .....	12
1.6. References.....	15
<b>Chapter 2: Recognition Ability of DNA for Carbon Nanotubes Correlates With Their Binding Affinity .....</b>	<b>18</b>
2.1. Introduction.....	19
2.2. Experimental Methods.....	22
2.3. DNA-Surfactant Exchange on the Carbon Nanotube .....	26
2.4. Analysis of Surfactant Exchange Kinetics.....	45
2.5. Fluorescence Measurements on (6,5) Recognition Sequences .....	64
2.6. Conclusions.....	66
2.7. Acknowledgements.....	67
2.8. References.....	68
2.9. Appendix.....	70
<b>Chapter 3: Molecular Simulation of DNA <math>\beta</math>-Sheet and <math>\beta</math>-Barrel Structures on Graphite and Single-Walled Carbon Nanotubes .....</b>	<b>90</b>
3.1. Introduction.....	91
3.2. Molecular Simulation Methodology .....	94
3.3. Ordered $\beta$ -Sheet and $\beta$ -Barrel Structures.....	95
3.4. (GT) <sub>4</sub> Sheets on Graphite.....	101
3.5. (GT) <sub>30</sub> $\beta$ -Barrels on SWCNTs .....	114
3.6. Conclusions.....	123
3.7. Acknowledgements.....	124

3.8.	References.....	125
3.9.	Appendix.....	127
<b>Chapter 4: Sequence Specific Self-Stitching Motif of Short Single-Stranded DNA on a Single-Walled Carbon Nanotube.....</b>		<b>131</b>
4.1.	Introduction.....	132
4.2.	Methodologies.....	134
4.3.	Results and Discussion .....	136
4.4.	Conclusions.....	155
4.5.	Acknowledgements.....	156
4.6.	References.....	157
4.7.	Appendix.....	159
<b>Chapter 5: Molecular-Basis of Single-Walled Carbon Nanotube Recognition by Single-Stranded DNA .....</b>		<b>165</b>
5.1.	Introduction.....	166
5.2.	Methodologies.....	169
5.3.	Results and Discussion .....	174
5.4.	Conclusions.....	182
5.5.	Acknowledgements.....	183
5.6.	References.....	184
5.7.	Appendix.....	186
<b>Chapter 6: DNA Conjugated SWCNTs Enter Endothelial Cells via Rac1 Mediated Macropinocytosis .....</b>		<b>202</b>
6.1.	Introduction.....	203
6.2.	Experimental Methods.....	206
6.3.	Cytotoxicity of DNA-SWCNT on HUVEC Cells .....	209
6.4.	Cellular Internalization Confirmed by Electron Microscopy .....	213
6.5.	Uptake Inhibition Studies .....	214
6.6.	Conclusions.....	219
6.7.	Acknowledgements.....	220
6.8.	References.....	221
6.9.	Appendix.....	223
<b>Chapter 7: Conclusions .....</b>		<b>226</b>
7.1.	Experimental Determination of DNA-SWCNT Binding Strengths .....	227
7.2.	Molecular Simulation of Various DNA-SWCNT Structures .....	227
7.3.	Cellular Interactions with DNA-SWCNT Hybrids.....	228
7.4.	Future Work.....	228
<b>CV Daniel Roxbury.....</b>		<b>231</b>

# List of Figures

<b>Figure 1.1</b>	Molecular representation of a (6,5)-SWCNT and depiction of how the nanotube was constructed. ....	5
<b>Figure 1.2</b>	An illustrated route to bio-functionalized SWCNTs. ....	8
<b>Figure 1.3</b>	Molecular representation of ssDNA showing all four DNA bases in single and double-stranded fashion.....	9
<b>Figure 1.4</b>	AFM image and molecular representation showing the helical nature of DNA on a SWCNT.....	11
<b>Figure 2.1</b>	Optical adsorption spectra from (TAT) <sub>4</sub> -wrapped SWCNTs illustrating differences among SEC fractions.....	23
<b>Figure 2.2</b>	AFM image of (TAT) <sub>4</sub> -SWCNTs deposited onto a silicon wafer. ....	23
<b>Figure 2.3</b>	Samples of (GT) <sub>15</sub> -SWCNTs sonicated in the presence of SDS and SDBS surfactant.....	27
<b>Figure 2.4</b>	Raw data from surfactant-induced exchange experiments of (GT) <sub>15</sub> -SWCNT hybrids.....	30
<b>Figure 2.5</b>	Effect of free DNA concentration on the surfactant exchange of (TAT) <sub>4</sub> -SWCNT hybrids. ....	32
<b>Figure 2.6</b>	Determination of surfactant CMC and evaluation of possible interactions between DNA and SDBS. ....	34
<b>Figure 2.7</b>	Fitting of data obtained from (TAT) <sub>4</sub> -SWCNT surfactant exchange .....	37
<b>Figure 2.8</b>	Schematic illustration of the process SDBS surfactant exchange. The reaction occurs in two distinct stages. ....	37
<b>Figure 2.9</b>	Effect of free DNA concentration on the equilibrium fraction of defect-free DNA-SWCNTs for (TAT) <sub>4</sub> T. ....	38
<b>Figure 2.10</b>	Effect of reduced concentration of SDBS on the rate of surfactant exchange for (TAT) <sub>4</sub> -SWCNTs.....	38
<b>Figure 2.11</b>	Quantified effect of SDBS concentration on stage I and stage II processes. ....	39
<b>Figure 2.12</b>	Effect of SWCNT length on stage II kinetics of surfactant exchange.....	44



<b>Figure 2.13</b>	Stage I data for all of the examined DNA-SWCNT hybrids. ....	48
<b>Figure 2.14</b>	Arrhenius plot for Stage I kinetics. ....	49
<b>Figure 2.15</b>	Stage II data for all of the examined DNA-SWCNT hybrids.....	51
<b>Figure 2.16</b>	Eyring plot for (TAT) <sub>4</sub> -SWCNT hybrids.....	55
<b>Figure 2.17</b>	Plot illustrating the relationship between activation enthalpy and activation entropy for all of the examined hybrids. ....	58
<b>Figure 2.18</b>	Proposed molecular model to explain differences among closely related DNA sequence SWCNT hybrids. ....	60
<b>Figure 2.19</b>	Effect of urea on the surfactant exchange reaction for (TAT) <sub>4</sub> -SWCNT hybrids. ....	62
<b>Figure 2.20</b>	Comparison between surfactant exchange on SEC versus non-SEC samples for (TAT) <sub>4</sub> and (TAT) <sub>4</sub> T. ....	64
<b>Figure 2.21</b>	Two-dimensional photoluminescence maps illustrating differences in SWCNT dispersion efficiencies among (TAT) <sub>4</sub> and closely related sequences. ....	66
<b>Figure 2.22</b>	Schematic of the competitive adsorption model between two molecules of differing size adsorbing to the same substrate.....	76
<b>Figure 2.23</b>	Pictorial representation of equilibrium equations from the competitive adsorption model.....	76
<b>Figure 2.24</b>	Reaction coordinate energy diagram for a standard bimolecular reaction.....	81
<b>Figure 2.25</b>	Molecular representation of one strand of HexCoil-Ala polypeptide on a (6,5)-SWCNT.....	86
<b>Figure 2.26</b>	Two-dimensional photoluminescence map for Comocat SWCNT sample dispersed with HexCoil-Ala peptide.....	87
<b>Figure 2.27</b>	Absorbance data from attempted surfactant exchange on the peptide-SWCNT hybrid. ....	87
<b>Figure 2.28</b>	Binary dispersing efficiency of SDBS and either peptide, (GT) <sub>30</sub> , or (TAT) <sub>4</sub> T. ....	89

<b>Figure 3.1</b>	Molecular representation for the construction of a novel DNA $\beta$ -barrel.....	96
<b>Figure 3.2</b>	Schematic of the four DNA bases shown with hydrogen bond donors and acceptors.....	98
<b>Figure 3.3</b>	DNA dimer configurations with and without a graphite substrate. Application of DNA tiling units in the construction of DNA $\beta$ -sheet structures.....	99
<b>Figure 3.4</b>	Simulated structures of DNA $\beta$ -sheets constructed from strands of $(GT)_4$ .....	108
<b>Figure 3.5</b>	Base centroid positions for simulated DNA $\beta$ -sheets.....	110
<b>Figure 3.6</b>	Cumulative distribution function for Thymine and Guanine DNA bases from their mean location.....	112
<b>Figure 3.7</b>	Fraction of hydrogen bonds as a function of simulated time for $\beta$ -sheet structures.....	114
<b>Figure 3.8</b>	Seven configurations of $(GT)_{30}$ -(6,5)-SWCNT $\beta$ -barrel hybrids before and after 6 ns of simulation.....	117
<b>Figure 3.9</b>	Simulated data showing that removal of the SWCNT collapses the DNA secondary structure.....	118
<b>Figure 3.10</b>	Simulation of $(GT)_{30}$ -(6,5)-SWCNT $\beta$ -barrel illustrating the formation of a hydrogen bonded G-quartet structure.....	119
<b>Figure 3.11</b>	Progression of inter-strand hydrogen bonds for selected $(GT)_{30}$ -(6,5)-SWCNT $\beta$ -barrel structures as a function of simulation time.....	120
<b>Figure 3.12</b>	Chiral angle versus diameter for simulated $(GT)_{30}$ -(6,5)-SWCNT $\beta$ -barrel hybrids.....	122
<b>Figure 4.1</b>	Starting structures for simulated configurations of $(TAT)_4$ on a (6,5)-SWCNT.....	136
<b>Figure 4.2</b>	Probability distribution functions (PDFs) for angle $\theta$ , between SWCNT normal and base normal.....	138
<b>Figure 4.3</b>	Phosphorus and base-centroid distances from SWCNT centers as functions of simulated time.....	139

<b>Figure 4.4</b>	Snapshot of (TAT) <sub>4</sub> -(6,5)-SWCNT showing the emergence of base-alternating motif. ....	141
<b>Figure 4.5</b>	Dominant clusters of simulated structures when considering DNA backbone atoms constrained to an RMSD cutoff of 0.45 nm. ....	142
<b>Figure 4.6</b>	Percentage of structures in a right-handed configuration versus unclear as determined by DNA sequence. ....	144
<b>Figure 4.7</b>	Snapshots from a continuous trajectory show the transition from a left-handed helix to a right-handed helix occurs within the first 30 ns of simulation.....	145
<b>Figure 4.8</b>	Helical handedness for (TAT) <sub>4</sub> -(6,5)-SWCNT configuration as determined by local helical angles.....	145
<b>Figure 4.9</b>	Available stitching configurations for a 12 base DNA strand simulated on a (6,5)-SWCNT.....	148
<b>Figure 4.10</b>	Geometric model for ssDNA on a SWCNT. ....	150
<b>Figure 4.11</b>	Simple model illustrating the electrostatic contribution associated with bending a line of charges. ....	152
<b>Figure 4.12</b>	Snapshot of (TAT) <sub>4</sub> -(6,5)-SWCNT illustrating how a base can flip sides of the backbone to accommodate a particular type of stitch.....	154
<b>Figure 4.13</b>	Two-dimension PMF plots for radius of gyration versus DNA end-to-end distance of all simulated configurations. ....	160
<b>Figure 4.14</b>	Two-dimension PMF plots for radius of gyration versus the number of DNA-DNA hydrogen bonds.....	161
<b>Figure 4.15</b>	Two-dimension PMF plots for radius of gyration versus the number of DNA-water hydrogen bonds. ....	162
<b>Figure 4.16</b>	Snapshots of the sequence (TAT) <sub>4</sub> on the (6,5)-SWCNT at 587 K. ....	163
<b>Figure 4.17</b>	Populations by stitching configuration found for (TAT) <sub>4</sub> simulated on (6,5) and (9,1)-SWCNTs.....	164
<b>Figure 5.1</b>	Starting structures for configurations of multiple strands of DNA simulated on a single SWCNT.....	170
<b>Figure 5.2</b>	Procedure for finding appropriate RMSD cutoffs for backbone clustering.....	172

<b>Figure 5.3</b>	Clustering of the simulated structures according to the backbone positions of a single DNA strand. ....	175
<b>Figure 5.4</b>	Clustering of the simulated structures according to the backbone positions of all three DNA strands. Mean smallest distance maps show how the simulated structures compare to idealized forms.....	177
<b>Figure 5.5</b>	End-to-end distribution plots for DNA strands on the various DNA-SWCNT simulated configurations. ....	180
<b>Figure 5.6</b>	Dispersing efficiency of (TAT) <sub>4</sub> versus (T) <sub>12</sub> as shown in two-dimensional photoluminescence maps. ....	182
<b>Figure 5.7</b>	Histogram of RMSD distance from the dominant cluster in the three strand (TAT) <sub>4</sub> -(6,5)-SWCNT simulated configuration.....	187
<b>Figure 5.8</b>	Backbone dihedral distributions for (TAT) <sub>4</sub> -(6,5)-SWCNT and (T) <sub>12</sub> -(6,5)-SWCNT configurations. ....	188
<b>Figure 5.9</b>	Clustering analysis performed on the (CCG) <sub>2</sub> CC-(8,7)-SWCNT three strand configuration. ....	190
<b>Figure 5.10</b>	Clustering analysis performed on the (CCG) <sub>2</sub> CC-(6,5)-SWCNT three strand configuration. ....	190
<b>Figure 5.11</b>	Hydrogen bonding trends for (TAT) <sub>4</sub> on (6,5)-SWCNT as a function of number of DNA strands.....	192
<b>Figure 5.12</b>	Hydrogen bonding trends for (CCG) <sub>2</sub> CC on (8,7)-SWCNT as a function of number of DNA strands.....	193
<b>Figure 5.13</b>	Solvent accessible area to the SWCNT surface for configuration of (TAT) <sub>4</sub> and (CCG) <sub>2</sub> CC-SWCNTs.....	194
<b>Figure 5.14</b>	REMD simulation of HexCoil-Ala peptide on a (6,5)-SWCNT.....	196
<b>Figure 5.15</b>	Top two clusters from REMD simulation of two strands of..... HexCoil-Ala peptide on (6,5)-SWCNT	197
<b>Figure 5.16</b>	Additional two-dimensional photoluminescence maps for (TAT) <sub>4</sub> and (T) <sub>12</sub> dispersion efficiency experiments. ....	199
<b>Figure 5.17</b>	Quantitative data derived from the photoluminescence maps. ....	200

<b>Figure 5.18</b>	Effect of size-exclusion chromatography on the fluorescence of SWCNT sample. ....	201
<b>Figure 6.1</b>	MTT assay for cytotoxicity of purified, length-sorted DNA-SWCNT hybrids.....	212
<b>Figure 6.2</b>	TEM images of SWCNTs localized inside of HUVEC cells. ....	214
<b>Figure 6.3</b>	Cells are incubated with 5'-FAM modified DNA to show that DNA does not enter the cells unless it is conjugated to SWCNTs. ....	215
<b>Figure 6.4</b>	Confocal fluorescence micrographs show the effect of certain uptake inhibition drugs on SWCNT internalization. NIR spectroscopy corroborates the findings.....	218
<b>Figure 6.5</b>	Confocal fluorescence micrographs of cells after treatment with Rac1-T17DN show negligible uptake of SWCNT. ....	219
<b>Figure 6.6</b>	Monitoring the amount of DNA-SWCNT hybrids internalized by HUVEC cells as a function of incubation time.....	224
<b>Figure 6.7</b>	Effect of cellular media on solutions of DNA-SWCNT hybrids.....	225

# List of Tables

<b>Table 2.1</b>	Free energies, enthalpies, and entropies of DNA-SWCNT defect formation .....	49
<b>Table 2.2</b>	Activation free energies, enthalpies, and entropies for DNA displacement by SDBS from the SWCNT surface .....	57
<b>Table 3.1</b>	DNA tiling unit parameters.....	101
<b>Table 3.2</b>	DNA $\beta$ -barrel parameters.....	104
<b>Table 3.3</b>	SWCNT intrinsic properties .....	105
<b>Table 3.4</b>	Fraction of hydrogen bonds remaining for simulated $\beta$ -barrels.....	121
<b>Table 3.5</b>	Constraining potential parameters for simulated $\beta$ -barrels.....	121
<b>Table 3.6</b>	Physical DNA dimer hydrogen bond models .....	127
<b>Table 6.1</b>	Pharmacological inhibitors and methods .....	209

## **Abstract**

It is known that single-stranded DNA adopts a helical wrap around a single-walled carbon nanotube (SWCNT), forming a water-dispersible hybrid molecule. The ability to sort mixtures of SWCNTs based on chirality (electronic species) has recently been demonstrated using special short DNA sequences that recognize certain matching SWCNTs of specific chirality. This thesis investigates the intricacies of DNA-SWCNT sequence-specific interactions through both experimental and molecular simulation studies. The DNA-SWCNT binding strengths were experimentally quantified by studying the kinetics of DNA replacement by a surfactant on the surface of particular SWCNTs. Recognition ability was found to correlate strongly with measured binding strength, e.g. DNA sequence  $(TAT)_4$  was found to bind 20 times stronger to the (6,5)-SWCNT than sequence  $(TAT)_4T$ .

Next, using replica exchange molecular dynamics (REMD) simulations, equilibrium structures formed by (a) single-strands and (b) multiple-strands of 12-mer oligonucleotides adsorbed on various SWCNTs were explored. A number of structural motifs were discovered in which the DNA strand wraps around the SWCNT and ‘stitches’ to itself via hydrogen bonding. Great variability among equilibrium structures was observed and shown to be directly influenced by DNA sequence and SWCNT type. For example, the (6,5)-SWCNT DNA recognition sequence,  $(TAT)_4$ , was found to wrap in a tight single-stranded right-handed helical conformation. In contrast, DNA sequence  $T_{12}$  forms a  $\beta$ -barrel left-handed structure on the same SWCNT. These are the first

theoretical indications that DNA-based SWCNT selectivity can arise on a molecular level.

In a biomedical collaboration with the Mayo Clinic, pathways for DNA-SWCNT internalization into healthy human endothelial cells were explored. Through absorbance spectroscopy, TEM imaging, and confocal fluorescence microscopy, we showed that intracellular concentrations of SWCNTs far exceeded those of the incubation solution, which suggested an energy-dependent pathway. Additionally, by means of pharmacological inhibition and vector-induced gene knockout studies, the DNA-SWCNTs were shown to enter the cells via Rac1-mediated macropinocytosis.



# **Chapter 1**

## **Introduction**

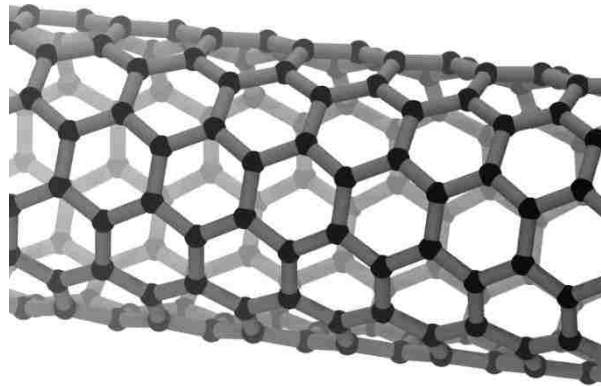
*Over the past decade, the extraordinary potential of functionalized single-walled carbon nanotubes (SWCNTs) has been extensively studied by the scientific community. From chemical sensing to electronics to medical devices, novel applications continue to push the advancing front in nano-materials research. For biological applications, hybrids of SWCNTs and bio-polymers, such as DNA or peptides, are crucial and enable their non-destructive internalization into living organisms. Additionally, the hybrids can function as advanced biomolecule sensing and delivery devices. Toxicology studies, at both the cellular and whole-organism level, thus help to facilitate the widespread adoption of SWCNTs in biomedical practices. In materials applications, hybrids of certain sequences of single-stranded DNA (ssDNA) and SWCNTs were shown to be of utmost importance for their intrinsic ability to chirality-sort SWCNTs. The highly selective sorting ability of the aforementioned DNA sequences, termed 'recognition sequences', suggests formation of novel secondary structures on the SWCNT. To aid in the design of DNA recognition sequences and ultimately control a release of cargo upon reaching a target destination, a molecular basis of DNA-SWCNT structure is sought. Through collaborative experimental and theoretical efforts, this thesis explores the sequence-specific interactions of DNA-SWCNT hybrid structures.*

## 1.1 The Single-Walled Carbon Nanotube

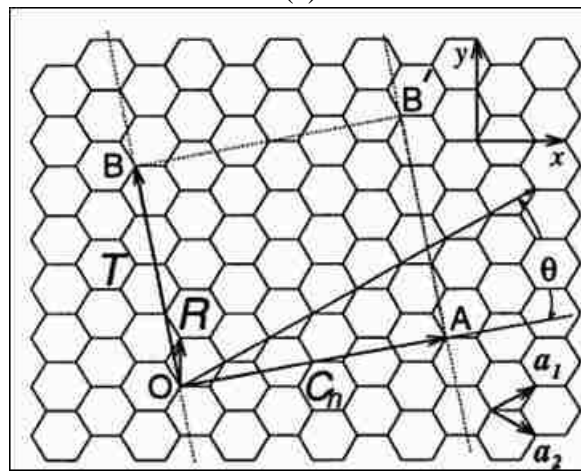
Nano-scale materials have recently attracted much attention for their exotic chemical and physical behavior. The single-walled carbon nanotube (SWCNT) is no exception. Having been discovered in 1993, with credit to both Iijima et al. and Bethune et al.,<sup>1-2</sup> the SWCNT can be approximated as a one-dimensional form of aromatic carbon imagined by rolling a hexagonal graphene sheet into a seamless cylinder (Figure 1.1a). For classification purposes, SWCNT diameters are determined by the direction and multiplicity of two primary unit vectors ( $\mathbf{a}_1$  and  $\mathbf{a}_2$  in Figure 1.1b). The ‘chiral vector’,  $\mathbf{OA}$ , whose length is found as  $\mathbf{C}_h = n\mathbf{a}_1 + m\mathbf{a}_2$ , becomes the circumference of the particular SWCNT. The characteristic indices,  $(n,m)$ , become the SWCNT’s chirality, and are commonly used to identify it as such. Perpendicular to  $\mathbf{C}_h$ , the vector  $\mathbf{T}$  points in the axial direction of the SWCNT.

Characterizing the chirality of a SWCNT serves a dual purpose as it determines not only the diameter but also the electronic nature of the SWCNT. Using the chiral indices, if  $n - m$  is a multiple of three, the particular SWCNT is semi-metallic, i.e. semiconducting with a negligible energy gap between valence and conducting bands, else it is semiconducting.<sup>3</sup> In the case of very small diameter SWCNTs, this relationship is not valid as a (5,0)-SWCNT is metallic in nature. The dependence of bandgap on SWCNT structure has been well-studied with the conclusion that the bandgap energy increases as SWCNT diameter decreases. For a (6,5)-SWCNT in vacuum, the bandgap energy is approximately 1.25 eV. The bandgap is marginally affected (up to 2% change in bandgap energy) by the SWCNT’s surrounding environment.<sup>4-5</sup> The bane and the promise of SWCNTs lie in the fact that numerous chiralities, and thus species with

differing electronic structure, are fabricated in their production. It is then imperative to be able to sort them.



(a)



(b)

**Figure 1.1.** (a) A molecular representation of a semi-conducting (6,5)-SWCNT. The hexagonal lattice of aromatic carbon is rolled into a seamless cylinder. (b) For classification purposes, SWCNTs chiral vectors are composed of multiples of unit vectors  $\mathbf{a}_1$  and  $\mathbf{a}_2$  with length 0.249 nm.<sup>6</sup> This particular chiral vector, shown by  $C_n = OA$ , is (4,2).

## 1.2 Novel Material and Biomedical Applications of SWCNTs

With continued research, it is thought that carbon nanotubes will be a household name for many reasons. Single or multi-walled carbon nanotubes have been used in molecular electronics devices such as field emitting transistors (FETs) since they are able to carry very large current densities (greater than  $10^{13}$  A/m<sup>2</sup>).<sup>7-8</sup> Novel methods to create

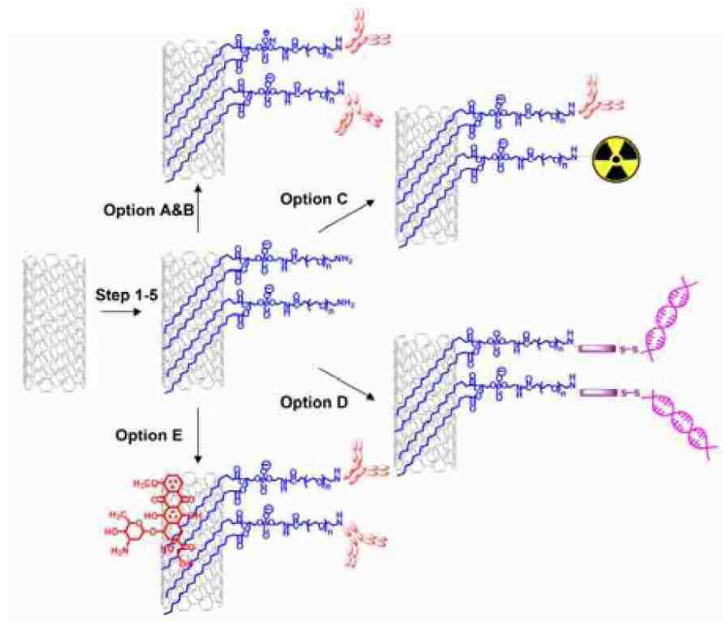
high-throughput and efficient FET devices have been reported.<sup>9-10</sup> For research in alternative energies, the possibility of the use of SWCNTs for hydrogen storage has been explored.<sup>11-12</sup> Additionally, theoretically ideal *p-n* junctions have been created with SWCNTs to obtain photoconversion efficiencies greater than 5% for use in photovoltaic cells.<sup>13</sup> As enhanced structural tools, SWCNTs can be attached to atomic force microscopy (AFM) tips and used in tapping mode to probe nano-structured surfaces.<sup>14</sup> By this method, SWCNT functionalized AFM tips have been used as nano-injectors to deliver cargo across cellular membranes.<sup>15</sup> Additionally, carbon nanotubes have been utilized for their extraordinary tensile strengths in polymer composite materials.<sup>16</sup>

By virtue of their unique, quasi one-dimensional nature in which all of the atoms are exposed to the local environment, SWCNTs possess intrinsic optical properties ideal for use in biological detection and imaging. Hybrid formation with biomolecules greatly improves the biocompatibility of such SWCNTs.<sup>17-19</sup> It is also known that short length SWCNTs (less than 1 $\mu$ m) exhibit low cytotoxicity.<sup>20-22</sup> Recently, much effort has been given to the prospect of biofunctionalized SWCNT hybrids as optical tags for *in vitro* and *in vivo* molecular imaging using Raman scattering,<sup>23-24</sup> photoacoustic response,<sup>25</sup> and near-infrared (NIR) fluorescence.<sup>26-27</sup> SWCNTs have been used as NIR fluorescent beacons to tag live cells on gold surfaces.<sup>28</sup> The SWCNTs generally exhibit band-gap fluorescence in the region of 800-1400 nm, an ideal section of spectrum transparent to live tissue.<sup>4, 26</sup> Furthermore, SWCNTs exhibit zero photobleaching under continued excitation.<sup>29</sup>

Hybrids of biopolymers and SWCNTs have also been used extensively in the detection of certain biochemical species.<sup>30-31</sup> Using modulations in fluorescence from

individual SWCNTs, single molecule detection of  $H_2O_2$  has been demonstrated.<sup>32</sup> Peptide-functionalized SWCNTs have been used to detect chemical compounds through modulations of the peptide secondary structure.<sup>33</sup>

In nanomedicine applications such as drug and gene delivery, SWCNTs are an ideal loadable vector. Work by Hongjie Dai et al. at Stanford University has shown that many biological molecules can be non-covalently attached to SWCNTs such that the optical integrity of the nanotube is not disrupted.<sup>34</sup> First, SWCNTs are aqueously solubilized with a PEG-ylated phospholipid molecule (PL-PEG). To the PL-PEG, biological molecules such as siRNA,<sup>19, 35</sup> peptides,<sup>36</sup> and antibodies<sup>37</sup> can easily be covalently conjugated (shown in Figure 1.2). Additionally, hydrophobic molecules, such as the chemotherapy drug doxorubicin, can be adsorbed directly to the surface of the SWCNT without the need for a PL-PEG intermediary. Hybrids can be created in combinations such that covalently attached antibodies direct the targeted delivery of drugs to cells displaying a certain antigen.

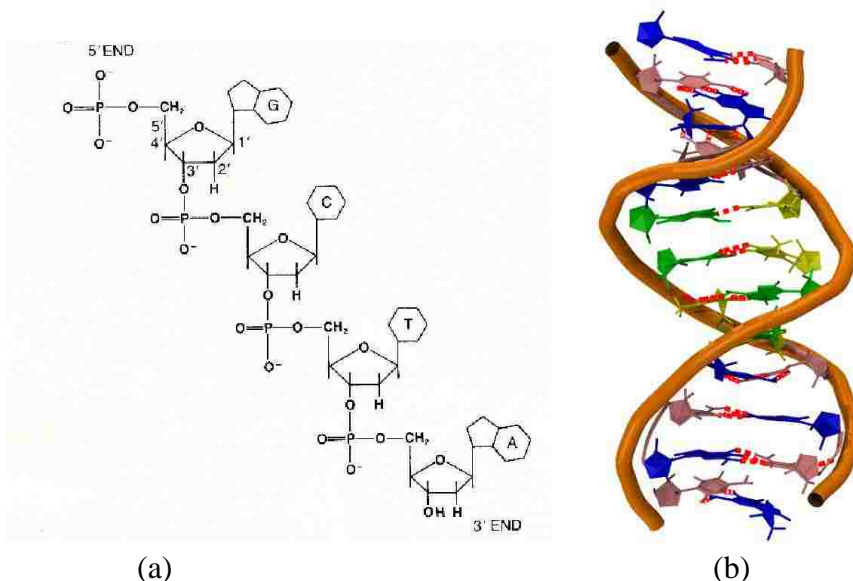


**Figure 1.2.** An illustration from Dai et al. showing route to SWCNT functionalization via PEG-ylated phospholipid intermediaries.<sup>34</sup> The SWCNTs can be non-covalently functionalized with (Option A&B) antibodies, (Option C) antibodies/radiotracers, (Option D) siRNA, and (Option E) antibodies/chemotherapy drugs.

### 1.3 Deoxyribonucleic Acid

Deoxyribonucleic acid (DNA), one of the most fundamental and ubiquitous of biological molecules, has been thoroughly studied since the discovery of its structure in 1953.<sup>38</sup> DNA is a biological polymer (biopolymer) comprised of four types of monomer nucleotides. Single strands of DNA, ssDNA, can be synthetically fabricated at high yield and purity in lengths up to 100 nucleotides. A nucleotide itself is composed of a negatively charged phosphate group and sugar ring, known as the backbone, and one of four nitrogenous aromatic bases (Figure 1.3a). In DNA, the bases are adenine, guanine, thymine, and cytosine, (abbreviated A, G, T, and C, respectively). Thymine and cytosine contain the benzene derivative pyrimidine, which has nitrogen substituted for carbon at positions one and three of the six-member ring. Adenine and guanine are known as

purines, possessing a pyrimidine ring fused with a five-member imidazole ring. For this reason, A and G are significantly larger in size than T and C. This will be of importance for theoretical implications, since all four bases cannot be modeled as occupying the same volume (or SWCNT surface area). Within a single nucleotide there exist hydrophilic (phosphate group) and hydrophobic regions (aromatic base). Therefore, DNA is an amphiphilic molecule and thus has associated surface acting properties. In particular, it allows DNA to solubilize hydrophobic particles in aqueous media.



**Figure 1.3.** (a) Schematic representation of ssDNA.<sup>39</sup> (b) Molecular representation of dsDNA. The orange represents the phosphate-sugar backbone while bases A, G, T, and C are represented in green, blue, yellow, and pink, respectively. The red dashed lines between bases are hydrogen bonds.

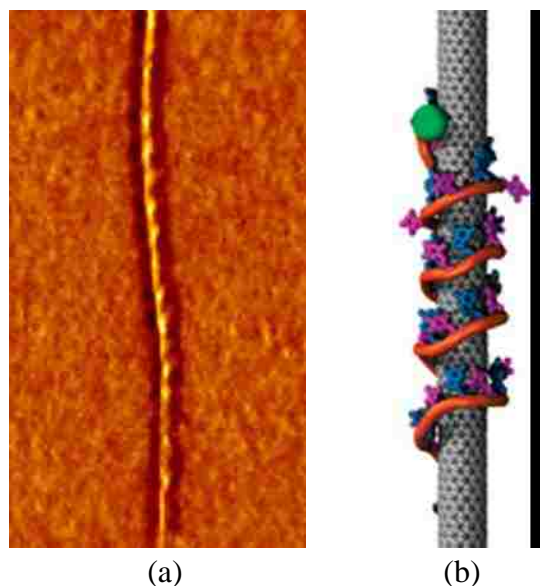
Like most biopolymers, DNA exhibits a high degree of hydrogen bonding. In its naturally occurring double-stranded (dsDNA) form, B-DNA, bases hydrogen-bond to those adjacent on the complementary strand via Watson-Crick base pairing (Figure 1.3b). In particular, A is complementary to T and G to C. The A-T pair has two hydrogen bonds while G-C has three. This thesis will show that hydrogen bonding is highly

significant in enforcing secondary structure even when strands are adsorbed onto hydrophobic surfaces such as graphene or SWCNTs. Furthermore, non-Watson-Crick hydrogen bonding pairs are also possible, such as A-A or G-T, and can additionally serve to stabilize emergent secondary structures.

## 1.4 DNA-SWCNT Hybrids

As mentioned previously, as-fabricated SWCNTs contain a variety of chiralities, each with characteristic electronic properties. Several recent attempts have been made to control the chirality of SWCNTs in the production phase.<sup>40-42</sup> Alternatively, much effort has been put forth to separating mixtures of SWCNTs, post-production. In these methods, SWCNTs are first singly-dispersed in aqueous solvent using amphiphilic molecules such as surfactants,<sup>43-45</sup> proteins,<sup>46-47</sup> or ssDNA.<sup>48-49</sup> In the case of ssDNA, solubilization is particularly effective. The DNA bases have been shown to stack non-covalently on the surface of the SWCNT through overlapping  $\pi$ -orbitals. Since the phosphate on the backbone carries a negative charge, the hybridized molecule (DNA-SWCNT) is rendered water soluble. Atomic force microscopy images and preliminary molecular dynamics (MD) computer simulations have suggested a helical nature of DNA while adsorbed onto the SWCNT (Figure 1.4).<sup>49-50</sup> The negative charge that each hybrid molecule carries also repels it from other hybrids. These singly-dispersed DNA-SWCNTs can now be manipulated with much greater ease.





**Figure 1.4.** (a) AFM image, from Zheng et al., depicting the helical nature of  $(GT)_{30}$  ssDNA on a single SWCNT.<sup>49</sup> Molecular dynamics simulation, from Johnson et al., of the DNA sequence  $(GT)_{20}$  on an  $(11,0)$ -SWCNT.<sup>50</sup> Again, a helical configuration of DNA on the SWCNT is indicated.

Solutions of dispersed SWCNTs have been sorted according to length,<sup>51</sup> diameter,<sup>52</sup> and most recently, chirality, by density gradient ultracentrifugation<sup>53-54</sup> and ion exchange chromatography (IEX).<sup>55</sup> A research group, led by Ming Zheng at NIST, has empirically identified a set of short ssDNA oligomers (10-20 mers) which, upon IEX processing, will select and enrich to high purity one particular chirality of SWCNT. For instance, the DNA sequence  $(TAT)_4$ , i.e. 5'-TATTATTATTAT-3', will enrich the  $(6,5)$ -SWCNT to 90% purity from a mixture of multiple chirality SWCNTs.

Upon initiation of the thesis work, it was originally observed that certain sequences, such as  $(GT)_{30}$ , enabled the selective enrichment of certain small diameter SWCNTs.<sup>56</sup> It was originally hypothesized that modulation of linear charge density, arising from structural variations among the hybrids, enable IEX to accomplish SWCNT chirality separation.<sup>56-57</sup> At the time, many of the proposed hybrid structures were largely hypothetical or based on indirect evidence. The important work on DNA recognition

sequences for SWCNTs published by Tu et al. had offered new secondary structures, known as  $\beta$ -barrels, for DNA bound to SWCNTs.<sup>55</sup> The specificity of the identified DNA recognition sequences suggests that SWCNTs preferentially select certain DNA sequences based on a lock-and-key type mechanism. Hydrogen bonding is again hypothesized to play a critical role in the DNA-SWCNT specificity. Unfortunately, to date, direct imaging of DNA-SWCNT hybrids remains unable to explain the sequence-dependent nature of DNA-SWCNT interactions.

It is with these preliminary findings and proposed structures that motivation for the presented research arises. In this thesis, experimental and theoretical studies have been performed to answer the following critical questions to more fully understand the nature of DNA-SWCNT hybrids:

1. What novel structures of DNA arise when it is confined to the surface of a SWCNT?
2. How does the SWCNT-adsorbed structure of a recognition DNA sequence differ from that of an *ordinary* DNA sequence?
3. What is the basis of this difference and how can it be quantified?
4. What are the biomedical implications associated with recognition DNA-SWCNT hybrids?

## **1.5 Thesis Outline**

The studies presented in this thesis attempt to answer the questions posed previously regarding sequence-specific interactions between DNA and SWCNTs. Experimentally, binding strengths of recognition DNA and related sequences to

SWCNTs were quantified to illustrate the large variations among hybrid structures. Computational simulations were then performed to probe the sequence-specific structures at the molecular level. Finally, work has been performed to investigate interactions between living cells and recognition DNA-SWCNT hybrids. Below is an outline of the presented material:

- Chapter 2 presents a surfactant based displacement method to measure and quantify differences in binding strengths between various DNA sequences on a particular type of SWCNT. In particular, we found that the binding strengths of DNA *recognition sequences* to the (6,5)-SWCNT were extraordinarily strong as compared to close relatives.
- Chapter 3 explores idealized novel DNA structures when bound to carbon nanomaterials (graphene and SWCNTs). A library of DNA dimer tiles was identified in an attempt to build two-dimensional ordered DNA structures. Using DNA sequences composed entirely of (GT) repeats several theorized  $\beta$ -sheet and  $\beta$ -barrel structures were simulated on graphene and SWCNTs, respectively. From short simulations, we surmised that chirality and diameter matching between  $\beta$ -barrel and SWCNT are crucial for hybrid stability.
- Chapter 4 recognizes the need for equilibrium MD simulations of ssDNA-SWCNT hybrids. For this purpose we employed the replica exchange MD (REMD) technique; simulations of single-strands of DNA on a SWCNT have shown that equilibrium hybrid structures depend significantly upon DNA sequence and composition. A dominant self-stitched motif was observed where DNA makes a complete wrap

- around the SWCNT and hydrogen bonds (stitches) to itself. A competition between entropy and hydrogen bonding was shown to govern the equilibrium structures.
- Chapter 5 investigates how and whether the presence of multiple ssDNA strands interacting on a single SWCNT results in ordered structures. Again using REMD simulation, DNA motifs were shown to depend strongly on the DNA sequence as well as SWCNT chirality. Most surprisingly, helicity of the DNA while adsorbed to the SWCNT was shown to change orientation (right-handed to left-handed) merely by introducing small changes in the DNA sequence.
  - Chapter 6 demonstrates the DNA-SWCNT's ability to be internalized into healthy human endothelial cells. For purposes of targeted delivery and imaging, it is important to know the exact mechanism of cellular uptake. It is shown, by both a pharmacological knockout study and gene therapy, that pristine hybrids are internalized by means of a Rac1-mediated macropinocytosis mechanism.
  - Chapter 7 concludes this thesis with the major findings on the sequence-dependent structure of DNA-SWCNT hybrids and presents ideas for future work.

## 1.6 References

- (1) Iijima, S.; Ichihashi, T., *Nature* **1993**, *363* (6430), 603-605.
- (2) Bethune, D. S.; Klang, C. H.; de Vries, M. S.; Gorman, G.; Savoy, R.; Vazquez, J.; Beyers, R., *Nature* **1993**, *363* (6430), 605-607.
- (3) Saito, R.; Dresselhaus, G.; Dresselhaus, M. S., Imperial College Press: London, 1999.
- (4) Bachilo, S. M.; Strano, M. S.; Kittrell, C.; Hauge, R. H.; Smalley, R. E.; Weisman, R. B., *Science* **2002**, *298*, 2361-2366.
- (5) Choi, J. H.; Strano, M. S., *Applied Physics Letters* **2007**, *90*, 223114.
- (6) Slavcheva, G. Optical Activity of a Carbon Nanotube. <http://www.gaby-slavcheva.co.uk/contact-us/optical-activity-of-a-carbon-nanotube>.
- (7) Javey, A., Carbon Nanotube Field-Effect Transistors  
Carbon Nanotube Electronics. Kong, J.; Javey, A., Eds. Springer US: 2009; pp 63-86.
- (8) Martel, R.; Schmidt, T.; Shea, H. R.; Hertel, T.; Avouris, P., *Applied Physics Letters* **1998**, *73* (17), 2447-2449.
- (9) Nougaret, L.; Happy, H.; Dambrine, G.; Derycke, V.; Bourgoin, J. P.; Green, A. A.; Hersam, M. C., *Applied Physics Letters* **2009**, *94* (24), 243505-3.
- (10) Aikawa, S.; Xiang, R.; Einarsson, E.; Chiashi, S.; Shiomi, J.; Nishikawa, E.; Maruyama, S., *Nano Research* **2011**, *4* (6), 580-588.
- (11) Liu, C.; Fan, Y. Y.; Liu, M.; Cong, H. T.; Cheng, H. M.; Dresselhaus, M. S., *Science* **1999**, *286* (5442), 1127-1129.
- (12) Cheng, H.-M.; Yang, Q.-H.; Liu, C., *Carbon* **2001**, *39* (10), 1447-1454.
- (13) Lee, J. U., *Applied Physics Letters* **2005**, *87* (7), 073101-3.
- (14) Wilson, N. R.; Macpherson, J. V., *Nat Nano* **2009**, *4* (8), 483-491.
- (15) Chen, X.; Kis, A.; Zettl, A.; Bertozzi, C. R., *Proceedings of the National Academy of Sciences* **2007**, *104* (20), 8218-8222.
- (16) Sementsov, Y.; Prikhod'ko, G.; Kartel, M.; Tsebrenko, M.; Aleksyeyeva, T.; Ulyanchychi, N., Carbon Nanotubes Filled Composite Materials  
Carbon Nanomaterials in Clean Energy Hydrogen Systems - II. Zaginaichenko, S. Y.; Schur, D. V.; Skorokhod, V. V.; Veziroglu, A.; İbrahimoglu, B., Eds. Springer Netherlands: 2011; Vol. 2, pp 183-195.
- (17) Liu, Z.; Cai, W.; He, L.; Nakayama, N.; Chem, K.; Sun, X.; Chen, X.; Dai, H., *Nature Nanotechnology* **2007**, *2*, 47-52.
- (18) Liu, Z.; Davis, C.; Cai, W.; He, L.; Chen, X.; Dai, H., *PNAS* **2008**, *105* (5), 1410-1415.
- (19) Liu, Z.; Winters, M.; Holodniy, M.; Dai, H., *Angew. Chem.* **2007**, *119*, 2069-2073.
- (20) Kostarelos, K., *Nature Biotechnology* **2008**, *26*, 774-776.
- (21) Poland, C. A.; Duffin, R.; Kinloch, I.; Maynard, A.; Wallace, W. A. H.; Seaton, A.; Stone, V.; Brown, S.; MacNee, W.; Donaldson, K., *Nature Nanotechnology* **2008**, *3*, 423-428.
- (22) Warheit, D. B.; Laurence, B. R.; Reed, K. L.; Roach, D. H.; Reynolds, G. A. M.; Webb, T. R., *Toxicology Sciences* **2003**, *77* (1), 117-125.
- (23) Liu, Z.; Li, X.; Tabakman, S. M.; Jiang, K.; Fan, S.; Dai, H., *J. Am. Chem. Soc.* **2008**, *130* (41), 13540-13541.

- (24) Zavaleta, C.; de la Zerda, A.; Liu, Z.; Keren, S.; Cheng, Z.; Schipper, M.; Chen, X.; Dai, H.; Gambhir, S. S., *Nano Letters* **2008**, *8* (9), 2800-2805.
- (25) Zerda, A.; Zavaleta, C.; Keren, S.; Vaithilingam, S.; Bodapati, S.; Liu, Z.; Levi, J.; Smith, B. R.; Ma, T. J.; Oralkan, O.; Cheng, Z.; Chen, X.; Dai, H.; Khuri-Yakub, B. T.; Gambhir, S. S., *Nature Nanotechnology* **2008**, *3*, 557-562.
- (26) Welsher, K.; Liu, Z.; Darancioglu, D.; Dai, H., *Nano Letters* **2008**, *8* (2), 586-590.
- (27) Jin, H.; Heller, D. A.; Strano, M. S., *Nano Letters* **2008**, *8* (6), 1577-1585.
- (28) Hong, G.; Tabakman, S. M.; Welsher, K.; Chen, Z.; Robinson, J. T.; Wang, H.; Zhang, B.; Dai, H., *Angewandte Chemie International Edition* **2011**, *50* (20), 4644-4648.
- (29) Cherukuri, P.; Bachilo, S. M.; Litovsky, S. H.; Weisman, R. B., *Journal of the American Chemical Society* **2004**, *126* (48), 15638-15639.
- (30) Boghossian, A. A.; Zhang, J.; Barone, P. W.; Reuel, N. F.; Kim, J.-H.; Heller, D. A.; Ahn, J.-H.; Hilmer, A. J.; Rwei, A.; Arkalgud, J. R.; Zhang, C. T.; Strano, M. S., *ChemSusChem* **2011**, *4* (7), 848-863.
- (31) Kim, J.-H.; Patra, C. R.; Arkalgud, J. R.; Boghossian, A. A.; Zhang, J.; Han, J.-H.; Reuel, N. F.; Ahn, J.-H.; Mukhopadhyay, D.; Strano, M. S., *ACS Nano* **2011**, *5* (10), 7848-7857.
- (32) Jin, H.; Heller, D. A.; Kalbacova, M.; Kim, J.-H.; Zhang, J.; Boghossian, A. A.; Maheshri, N.; Strano, M. S., *Nat Nano* **2010**, *5* (4), 302-309.
- (33) Heller, D. A.; Pratt, G. W.; Zhang, J.; Nair, N.; Hansborough, A. J.; Boghossian, A. A.; Reuel, N. F.; Barone, P. W.; Strano, M. S., *Proceedings of the National Academy of Sciences* **2011**, *108* (21), 8544-8549.
- (34) Liu, Z.; Tabakman, S. M.; Chen, Z.; Dai, H., *Nat. Protocols* **2009**, *4* (9), 1372-1381.
- (35) Kam, N. W. S.; Liu, Z.; Dai, H., *J. Am. Chem. Soc.* **2005**, *127*, 12492-12493.
- (36) Kam, N. W. S.; Liu, Z.; Dai, H., *J. Am. Chem. Soc.* **2004**, *126*, 6850-6851.
- (37) Chen, Z.; Tabakman, S. M.; Goodwin, A. P.; Kattah, M. G.; Darancioglu, D.; Wang, X.; Zhang, G.; Li, G.; Liu, Z.; Utz, P. J.; Jiang, K.; Fan, S.; Dai, H., *Nature Biotechnology* **2008**, *26* (11), 1285-1292.
- (38) Watson, J. D.; Crick, F. H., *Nature* **1953**, *171*, 737.
- (39) Saenger, W., Springer-Verlag: New York, 1984.
- (40) Picher, M.; Anglaret, E.; Arenal, R.; Jourdain, V., *ACS Nano* **2011**, *5* (3), 2118-2125.
- (41) Koziol, K. K. K.; Ducati, C.; Windle, A. H., *Chemistry of Materials* **2010**, *22* (17), 4904-4911.
- (42) Zhu, Z.; Jiang, H.; Susi, T.; Nasibulin, A. G.; Kauppinen, E. I., *Journal of the American Chemical Society* **2010**, *133* (5), 1224-1227.
- (43) Islam, M. F.; Rojas, E.; Bergey, D. M.; Johnson, A. T.; Yodh, A. G., *Nano Lett.* **2003**, *3* (2), 269-273.
- (44) Matarredona, O.; Rhoads, H.; Li, Z.; Harwell, J. H.; Balzano, L.; Resasco, D. E., *J. Phys. Chem. B* **2003**, *107*, 13357-13367.
- (45) Moore, V. C.; Strano, M. S.; Haroz, E. H.; Hauge, R. H.; Smalley, R. E., *Nano Lett.* **2003**, *3* (10), 1379-1382.
- (46) Dieckmann, G. R.; Dalton, A. B.; Johnson, P. A.; Razal, J.; Chen, J.; Giordano, G. M.; Munoz, E.; Musselman, I. H.; Baughman, R. H.; Draper, R. K., *J. Am. Chem. Soc.* **2003**, *125*, 1770-1777.

- (47) Grigoryan, G.; Kim, Y. H.; Acharya, R.; Axelrod, K.; Jain, R. M.; Willis, L.; Drndic, M.; Kikkawa, J. M.; DeGrado, W. F., *Science* **2011**, *332* (6033), 1071-1076.
- (48) Zheng, M.; Jagota, A.; Semke, E. D.; Diner, B. A.; Mclean, S. R. L.; Richardson, R. E.; Tassi, N. G., *Nature Materials* **2003**, *2*, 338-343.
- (49) Zheng, M.; Jagota, A.; Strano, M. S.; Santos, A. P.; Barone, P.; Chou, S. G.; Diner, B. A.; Dresselhaus, M. S.; Mclean, S. R. L.; Onoa, G. B.; Samsonidze, G. G.; Semke, E. D.; Usrey, M.; Walls, D. J., *Science* **2003**, *302* (5650), 1545-1548.
- (50) Johnson, R. R.; Johnson, A. T. C.; Klein, M. L., *Nano Letters* **2008**, *8* (1), 69-75.
- (51) Huang, X.; Mclean, S. R. L.; Zheng, M., *Analytical Chemistry* **2005**, *77* (19), 6225-6228.
- (52) Arnold, M. S.; Green, A. A.; Hulvat, J. F.; Stupp, S. I.; Hersam, M. C., *Nat Nano* **2006**, *1* (1), 60-65.
- (53) Posseckardt, J.; Battie, Y.; Fleurier, R.; Lauret, J.-S.; Loiseau, A.; Jost, O.; Mertig, M., *physica status solidi (b)* **2010**, *247* (11-12), 2687-2690.
- (54) Zhang, Y.; Zheng, L., *Nanoscale* **2010**, *2* (10), 1919-1929.
- (55) Tu, X.; Manohar, S.; Jagota, A.; Zheng, M., *Nature* **2009**, *460* (7252), 250-253.
- (56) Zheng, M.; Semke, E. D., *J. Am. Chem. Soc.* **2007**, *129* (19), 6084-6085.
- (57) Khripin, C. Y.; Manohar, S.; Zheng, M.; Jagota, A., *Journal of Physical Chemistry C* **2009**, *113* (31), 13616-13621.

## Chapter 2

### **Recognition Ability of DNA for Carbon Nanotubes Correlates With Their Binding Affinity\***

*The ability to sort mixtures of carbon nanotubes (SWCNTs) based on chirality has recently been demonstrated using special short DNA sequences that recognize certain matching SWCNTs of specific chirality. In this work we report on a study of the relationship between recognition sequences and the strength of their binding to the recognized SWCNT. We have chosen the (6,5) SWCNT and its corresponding DNA recognition sequences for investigation in this study. Binding strength is quantified by studying the kinetics of DNA replacement by a surfactant, which is monitored by following shifts in the absorption spectrum. We find that recognition ability correlates strongly with binding strength so measured; addition or subtraction of just one base from the recognition sequence can enhance the kinetics of DNA displacement some twenty-fold. The surfactant displaces DNA in two-steps, a rapid first stage lasting less than a few seconds, followed by progressive removal lasting tens of minutes. Kinetics of the second stage are analyzed to extract activation energies. Fluorescence studies support*

---

\* Portions of this chapter have been published in Langmuir:

D Roxbury, X Tu, M Zheng, A Jagota. "Recognition Ability of DNA for Carbon Nanotubes Correlates with Their Binding Affinity" *Langmuir* **27**, 8282 (2011)



*the finding that the DNA sequence that recognizes the (6,5)-SWCNT forms a more stable hybrid than its close relatives.*

## **2.1 Introduction**

Many novel applications for single-walled carbon nanotubes (SWCNTs) have been developed based on their unusual physical and electrical properties.<sup>1-4</sup> However, as-produced, SWCNTs comprise a variety of chiralities and are clumped together due to their high aspect ratios.<sup>5,6</sup> Solution-based processing has been successful for effective dispersion of individual SWCNTs. Several amphiphilic molecules, such as surfactants,<sup>7-9</sup> peptides,<sup>10</sup> and lipids,<sup>11,12</sup> have been shown to adsorb non-covalently on the hydrophobic SWCNT sidewall, effectively solubilizing the resultant hybrid molecule in aqueous medium.

Single-stranded DNA (ssDNA), having both a hydrophilic backbone and hydrophobic bases, was demonstrated as having SWCNT dispersing capabilities<sup>13</sup> allowing subsequent sorting by diameter and length.<sup>14,15</sup> Atomic force microscopy suggests a helically wrapped structure.<sup>15</sup> More recently it has been shown that a sequence-specific motif exists whereby particular short ssDNA sequences recognize specific chirality SWCNTs, permitting their separation from a mixture.<sup>16</sup> These recognition sequence hybrids, which show high selectivity towards their respective chirality SWCNT, suggest a highly ordered ssDNA secondary-structure proposed to be stabilized by base-SWCNT adsorption as well as by inter-base hydrogen bonding.<sup>16-18</sup>

To understand the nature of ssDNA-SWCNT interactions, it is useful first to consider arrangements formed by individual DNA bases on planar graphite. Overlapping

$\pi$ -orbitals are known to cause aromatic bases to stack on aromatic substrates.<sup>19,20</sup> Base adsorption at the graphite-water interface results in the formation of a self-assembled monolayer<sup>21-23</sup> and the strength of adsorption was found to be in the following order, (G>A>T>C).<sup>21</sup> Numerous studies have been performed, through AFM and STM imaging,<sup>23-26</sup> with monolayer adsorbed DNA bases showing the emergence of a two-dimensional crystalline structure thought to be stabilized by inter-base cyclic hydrogen bonds.<sup>24,27,28</sup> Supramolecular structures created at solid-liquid interfaces, composed of guanine, adenine, and mixtures of adenine/thymine and guanine/cytosine have also been investigated.<sup>23-25,27,29-31</sup> Single base adsorption on a SWCNT, modeled computationally through thermodynamic integration,<sup>32,33</sup> was found to be in agreement with base-graphite binding strength order.

Little is known about how or if DNA bases form ordered structures when the bases are linked to form ssDNA, or when the surface on which they adsorb is a cylindrical carbon nanotube. Binding strengths for homopolymeric DNA on graphite, investigated through molecular dynamics (MD) simulation peeling,<sup>34</sup> suggest the same trend, (G>A>T>C), as measured for individual bases. Contrary to this, experimental values for peeling homopolymer DNA from graphite go as (T>A>C).<sup>35</sup> DNA-SWCNT hybrids composed of DNA strands less than ten bases were shown to thermally dissociate in yet another trend, (G>C>A>T).<sup>36</sup> Also in this study, binding free energies of entire ssDNA strands to SWCNTs were argued to increase monotonically with increasing sequence length.

The evidence of DNA-SWCNT recognition sequences suggests formation of a highly ordered oligomeric ssDNA arrangement on the SWCNT. DNA  $\beta$ -barrel structures

have been proposed as such an ordered form of ssDNA in which backbone and bases are both arranged helically on an imaginary cylinder.<sup>16,17</sup> The interior of the structure is hollow and permits the insertion of a SWCNT of a specific diameter. The barrels are generally composed of two or more strands of ssDNA wrapped helically and stabilized by inter-strand hydrogen bonding between bases. This conformation allows for all of the DNA bases to be adsorbed on the SWCNT sidewall as well as for base-to-base hydrogen-bonding.<sup>37,38</sup>

In this study, we report the results of experiments to probe the binding strength of DNA strands to a specific SWCNT (6,5). (It was chosen for its natural abundance in the CoMoCAT sample, which significantly reduces the sample preparation burden.) We do so by studying the kinetics of competitive binding for the surface of the SWCNT between a small surfactant molecule, sodium dodecylbenzene sulfonate (SDBS), which has a high affinity for adsorbing on the SWCNT sidewall,<sup>39</sup> and the pre-wrapped DNA. When present in sufficient concentration in the solution, SDBS displaces DNA from the SWCNT at a characteristic temperature-dependent rate. The exchange process from DNA-covered to SDBS-covered SWCNTs can conveniently be followed by characteristic shifts in optical absorbance, a solvatochromic effect.<sup>40</sup> Transition state theory<sup>41</sup> can be used quantitatively to extract activation energies, allowing quantitative comparison among sequences for binding to a given SWCNT species. We expect that some of the general findings about the relative binding strengths of DNA sequences will apply to other DNA-SWCNT combinations, which will be studied in future work.

In addition to hybrid dissociation, correlation with SWCNT dispersion efficiencies was monitored through photoluminescence measurements for various DNA

sequences. Furthermore, a surfactant-exchange method was employed to strip DNA off the SWCNT to prevent any wrapping effects on fluorescence intensities.

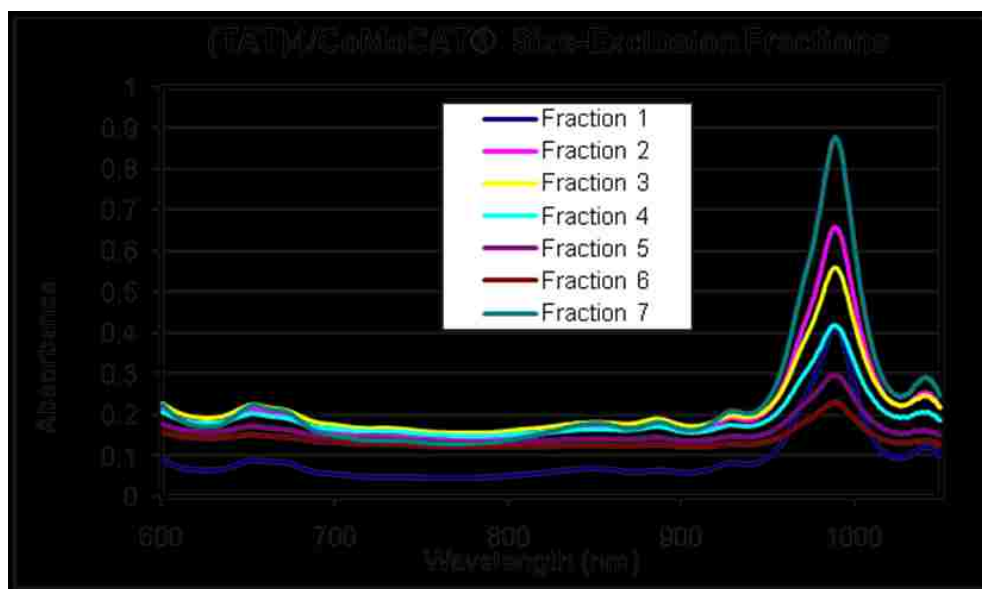
## 2.2 Experimental Methods

Raw (6,5)-rich (>80%) CoMoCAT carbon nanotubes, obtained from *South West NanoTechnologies (SWeNT)*, and single-stranded DNA, obtained from *Integrated DNA Technologies (IDT)*, in a 1 mg : 1 mg weight ratio, were sonicated using a *Branson* probe ultrasonicator for 90 minutes at 8 W output power in 4 mL of 2xSSC buffer. All chemicals other than SWCNT and DNA were purchased from *Sigma-Aldrich*. The resultant dispersion was centrifuged (*Eppendorf* micro-centrifuge) for 90 minutes at 13k RPM to precipitate any undispersed SWCNTs. The extracted supernatant was then fed through size exclusion columns (2000 Å, 1000 Å and 300 Å pore size, *Sepax Technologies*) via HPLC (*AKTA UPC-10 GE*) and fractionated to further remove excess DNA and sort SWCNTs according to length<sup>14</sup>. Since CoMoCAT SWCNTs are rich in the (6,5) chirality, a relative estimate of hybrid concentration can be determined from the intensity of the E<sub>11</sub> transition for (6,5) at 990 nm, (Figure 2.1). Estimates of absolute concentration of SWCNT in solution have been made by using an extinction coefficient at the 990 nm wavelength, however, this has recently been found to underestimate concentrations in short SWCNT length fractions while overestimating concentrations in longer SWCNT fractions.\* We acknowledge this discrepancy and have taken precautions

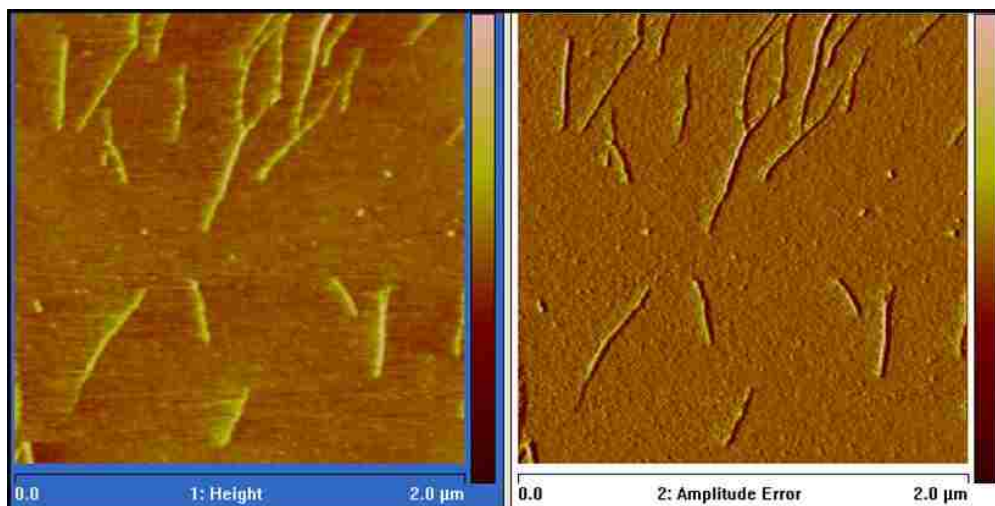
---

\* Summarized from: C Khripin, X Tu, M Zheng. “Measuring the Concentration of Colloidal Single-Walled Carbon Nanotubes: Effect of Nanotube Length” (in preparation).

to use a narrow range of SWCNT lengths throughout the experimental study in efforts to avoid absolute concentration effects.



**Figure 2.1.** Optical absorption spectra from 600-1050 nm of  $(\text{TAT})_4$ -wrapped SWCNTs showing differences among size-exclusion fractions. Free DNA as well as other impurities are removed from the samples in the process of size-exclusion chromatography.



**Figure 2.2.** Atomic force microscopy image showing  $(\text{TAT})_4$ -SWCNTs deposited on a SAM-coated silicon wafer. Singly-dispersed SWCNTs (found here in the lower left-hand of the image) have lengths in the range of 250-350 nm.\* The color bar for height and amplitude error images are given as minimum and maximum values of 0 – 10 nm and -10 – 10 mV, respectively.

\* This image has been graciously provided by Ms. Sara Iliafar of Lehigh University.

The length of SWCNTs used for the majority of the experiments was an SEC fraction of SWCNT length range 250-350 nm, verified by atomic force microscopy (AFM) imaging (*Veeco Nanoscope*), (Figure 2.2). It turns out that that the kinetics of surfactant exchange depend strongly on length so that the ability to sort them by length is important. The fractions were then exchanged to a 10 mM 7.1 pH phosphate buffer through microcentrifuge filtration (100 kDa cut-off *Microcon*). (This buffer exchange is required because SDBS is ineffective at the higher salt concentration needed for SEC separation.) Relative concentrations of (6,5) SWCNTs in solution were verified by optical absorbance at the  $E_{11}$  transition, 990 nm, and fractions were diluted as such so that  $Abs_{990} = 1.0 \pm 0.01$  across samples. A stock solution of 0.2 wt % sodium dodecylbenzene sulfonate (SDBS) was made in the same 10 mM phosphate buffer solution. A volume of 100  $\mu$ L was preheated in a quartz micro-cuvette to the desired temperature in a constant temperature peltier device (held constant at various temperatures, 20°-80°C) and mixed (by pipette mixing) with equal volume of DNA-SWCNT fraction to obtain effective SDBS concentration of 0.1 wt% (below experimentally determined critical micelle concentrations (CMC) value of 0.223). It is important to maintain a surfactant concentration below CMC since in this regime surface tension still dramatically depends upon surfactant concentration. Moreover, the order of the reaction is known to be influenced by the state of the surfactant (e.g. free or in micelles). Therefore, we have controlled the experiments such that surfactant is purely in its free state. Because the mass of the cuvette far exceeds that of the injected sample, equilibration of temperature after injection of DNA-SWCNT is estimated to take less than five seconds. Upon

mixing, surfactant exchange was monitored through a time-dependent changing optical absorbance signal (*Varian Cary 50 UV/Vis/NIR Spectrophotometer*). The time between mixing and the start of the absorbance scan was less than three seconds.

Surface tensions and CMC's of various SDBS/buffer/DNA solutions were estimated by means of a drop counting method. Using a 0.5 mL syringe with circular tip opening of radius 0.25 mm, the number of drops was counted in various SDBS, Sodium deoxycholate (SDC), and DNA concentrations ranging from 0 – 3 wt% in a 10 mM phosphate buffer solution. The number of drops would increase as surface tension of solution decreased to a plateau value (for the case of SDBS, its CMC)<sup>42</sup>. Note that while this method cannot be used in this form to estimate surface tension, it does yield information on the CMC.

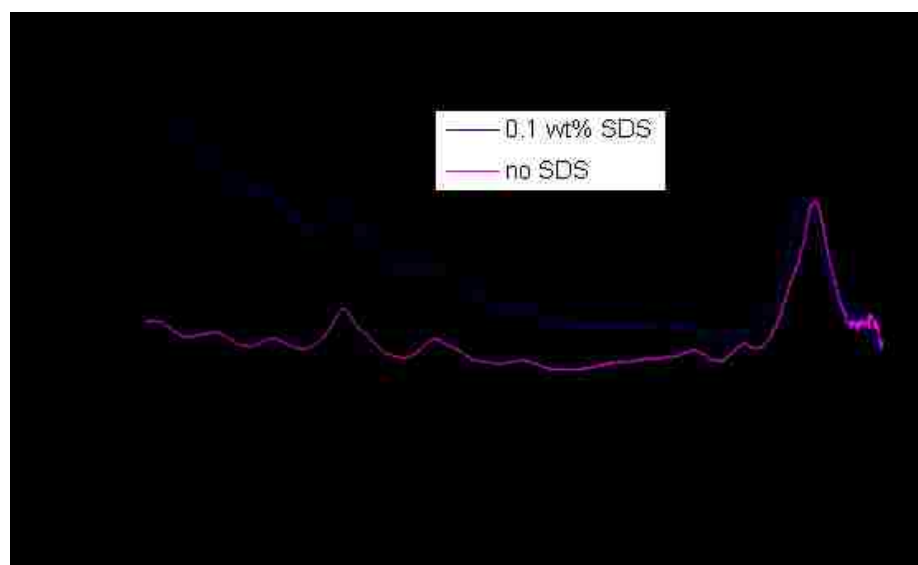
*HiPCO* SWCNTs (*Rice University*) were dispersed with ssDNA in the same manner as previously described, but in 0.1 M NaCl solution. Without the use of size-exclusion, supernatant was diluted 20x before fluorescence measurements using a *Horiba Jobin Yvon Nanolog-3* spectrofluorometer with a liquid nitrogen-cooled InGaAs detector. The sample was measured in a 10 mm square quartz cuvette. The light source is a 450W Xenon lamp. Both the excitation and emission wavelength were scanned in 10 nm increments with an 8 nm slit. Additionally, both the lamp and the detector possess intrinsic spectral efficiencies that need to be corrected for. Therefore, in the emission spectra, two correction factors were incorporated. SDC was added to the diluted sample to make final concentration of 1 wt % to replace the DNA coating with surfactant. Fluorescence intensities were measured and correlated with the dispersion efficiency of the DNA sequences.

### 2.3 DNA-Surfactant Exchange on the Carbon Nanotube

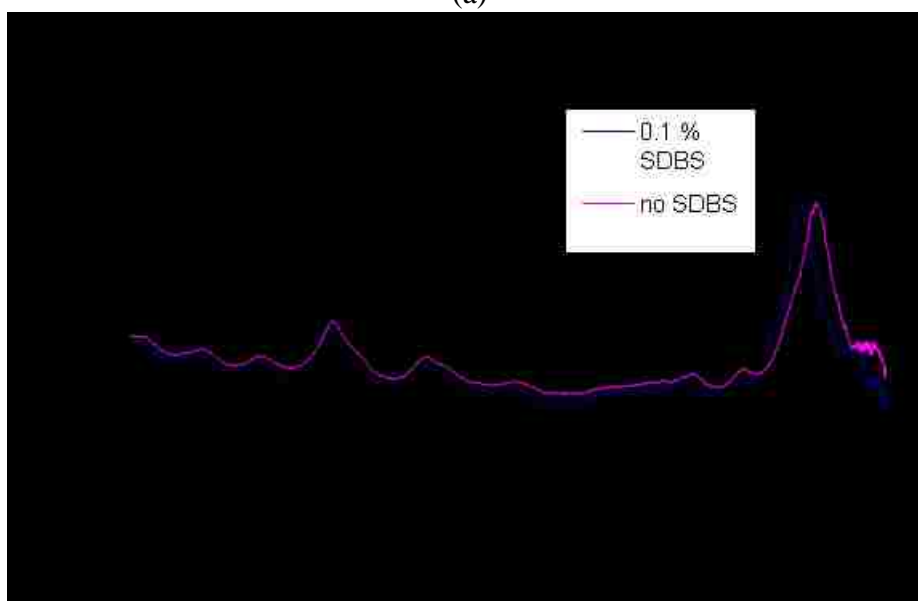
Optical absorption spectra from clean singly-dispersed SWCNTs show prominent peaks due to the semi-conducting band gap of nanotubes.<sup>7,9</sup> The positions of these peaks are strongly dependent on the environment of the SWCNTs.<sup>43</sup> For example, replacing DNA by surfactant causes a solvatochromic shift ascribed to be due to a change in effective dielectric constant<sup>40</sup>. In this study, we use this fact to monitor a temperature-dependent, kinetically controlled exchange of the surface coverage of a (6,5) chirality SWCNT from ssDNA to surfactant, SDBS. For this particular SWCNT, the  $E_{11}$  transitions when covered by DNA or by SDBS are at 990 nm and 978 nm, respectively. By using the surfactant as a common reference, and by analyzing the kinetics of its exchange for DNA on the surface of the SWCNT, our aim is to determine certain characteristics of the relative binding strengths for ssDNA on SWCNTs.

In a preliminary trial, we found that on sonication of (GT)<sub>15</sub>-CoMoCAT SWCNTs in the presence of excess sodium dodecyl sulfate (SDS), the  $E_{11}$  transition of the (6,5) SWCNT was shifted from ~990 to ~982 nm, presumably due to a conversion between DNA-covered and sodium dodecylsulfate (SDS)-covered nanotubes. However, the effects of intense sonication caused significant baseline absorbance drift that proved detrimental for accurate measurements of peak intensities, (Figure 2.3a). An alternative to long sonication times was sought. A different surfactant, SDBS, known to have a higher affinity for the SWCNT sidewall, was considered. Sonication time was also reduced in an effort to eliminate the baseline drift. SDBS was found to shift  $E_{11}$  transitions to ~978 nm, (Figure 2.3b).





(a)



(b)

**Figure 2.3.** (a)  $(GT)_{15}$ -SWCNT hybrids under 30 minutes intense sonication in the presence of 0.1 wt% SDS. Note the large change in absorbance intensity in the left part of the spectrum. This is caused primarily by metal impurities ablated from the tip of the sonication probe. (b) The same experiment is repeated, instead with SDBS for 5 minutes of sonication. Much less baseline drift is observed.

It was found that by increasing the temperature of the solution, DNA-surfactant exchange could be sped up dramatically. Figure 2.4a shows a typical temperature-induced exchange with varying concentrations of SDBS. In each case, a solution of

DNA-SWCNT hybrids was incubated with a known amount of SDBS for 10 minutes. A final absorption spectrum was taken in the region of the  $E_{11}$  peak for (6,5) SWCNTs so that its shift due to change of its local environment could be monitored. The data show a progressively increasing shift in the absorbance peak with increasing SDBS concentration with two limiting cases representing the limits where SWCNTs are coated purely by DNA (990 nm) or purely by SDBS (978 nm).

### 2.3.1 Replacement of DNA by SDBS can be monitored by absorption spectroscopy.

Absorption data shown in Figure 2.4 could be interpreted in two ways: as a SWCNT population going from the limit of DNA-covered to SDBS-covered through a sequence of intermediate states, or as a mixture of the two limiting states that each keeps its identity. In support of the latter of the two scenarios, imagine that the spectral curves given in figure 2.4a represent a combination of two species (DNA-covered and SDBS-covered SWCNTs) rather than a series of intermediate species. We use a standard Lorentzian lineshape

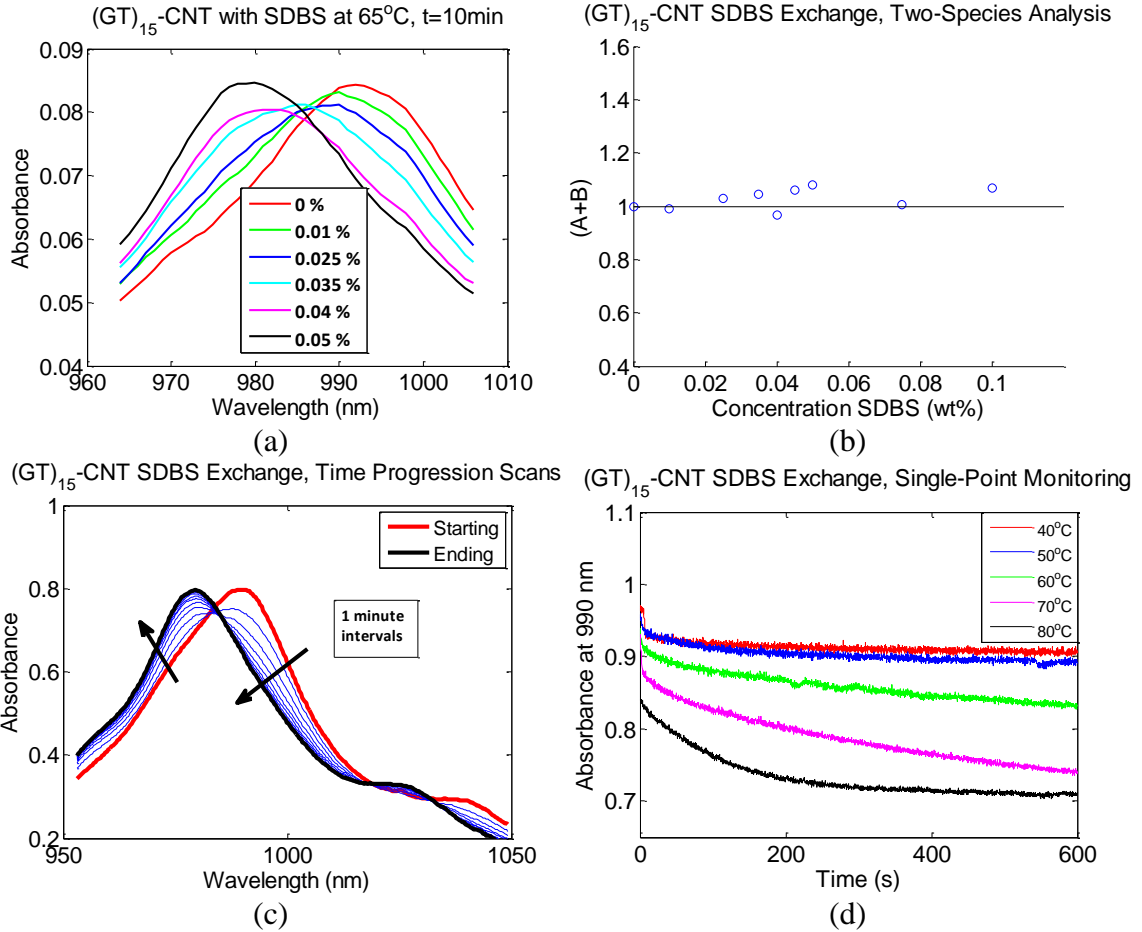
$$\Phi = \frac{a}{(b - x_o)^2 + a^2} \quad (2.1)$$

to fit the absorbance line shape in the pure DNA-covered and SDBS-covered SWCNT limits. We then fit intermediate absorbance data by a linear combination of the two limiting functions,

$$\Phi_{combined} = A \left[ \frac{a_1}{(b_1 - x_o)^2 + a_1^2} \right] + B \left[ \frac{a_2}{(b_2 - x_o)^2 + a_2^2} \right] + c' \quad (2.2)$$

thus representing the intermediate state as a combination of the two limiting states. Then a test of the hypothesis that intermediate compositions are linear combinations of the limiting ones is that 'A' and 'B should add to 1. Figure 2.4b shows that this is indeed the case. (Regarding  $A+B$  as a random variable, we find that the 95% confidence interval for the mean to be [0.998, 1.057], i.e., we can accept the hypothesis that  $A+B=1$  with this confidence level.)

Another way to conduct this type of experiment is to fix the SDBS concentration at a relatively high level, e.g. 0.1 wt%. Time evolution absorbance scans then show a progressive shift, presumably correlated again with an exchange of adsorbed chemical species. Figure 2.4c shows an example of this process with absorbance scans in the wavelength range 950-1050 nm at time intervals of 1 minute. The absorbance at any position along the 950-1050 wavelength interval can be monitored as a function of time.



**Figure 2.4.** (a) Absorption spectra of  $(GT)_{15}/SWCNT$  hybrids after incubation for 10 minutes in various SDBS concentrations. We observe a systematic shift in the (6,5) E11 peak position. (b) Test that intermediate stages of the reaction can be represented by a linear combination of the pure limiting species (DNA or SDBS coated SWCNTs), equation (2).  $(A+B)$  should equal unity to be consistent with this hypothesis, where ‘A’ and ‘B’ are the pre-factors from the fitted data. (c) Absorption spectra of  $(GT)_{15}/SWCNT$  hybrids incubated in 0.1 wt% SDBS at a constant temperature of 70°C, showing a time-dependent shift in concentrations of DNA-covered and SDBS-covered SWCNTs. (d) Raw data for temperature-dependent kinetics measured by decay of the 990 nm absorption peak for  $(GT)_{15}/SWCNT$  hybrids. Data show a two-step mechanism with a quick initial change followed by a more gradual decrease. Note that data collection has stopped after 600s, even though completion of the reaction has not yet been reached (clearly evident in 40C, 50C, and 60C samples).

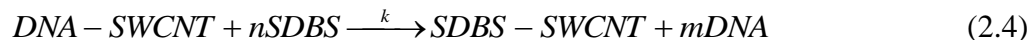
Notice in figures 2.4a and 2.4c the presence of a wavelength at which absorbance does not change as the DNA is exchanged for the SDBS. This further supports the hypothesis that absorbance in the intermediate stages when DNA/SWCNTs have been partially replaced by SDBS/SWCNTs is well-represented as a linear mixture of pure SDBS and DNA coated spectra over a wide range of time and SDBS concentration. Specifically, this “pivot point” corresponds to the value of  $x_o$  (the wavelength) at which the absorbance of the two pure species is the same. Clearly, the absorbance at this wavelength would remain unchanged if intermediate compositions were linear combinations of the pure species. It can be found by taking the derivative of Equation 2.2 (where  $B = 1 - A$ ) with respect to  $A$ ; in Figure 2.4c, the pivot point can be seen at ~982 nm.

$$\frac{d\Phi}{dA} = \frac{a_1}{(b_1 - x_o)^2 + a_1^2} - \frac{a_2}{(b_2 - x_o)^2 + a_2^2} = 0 \quad (2.3)$$

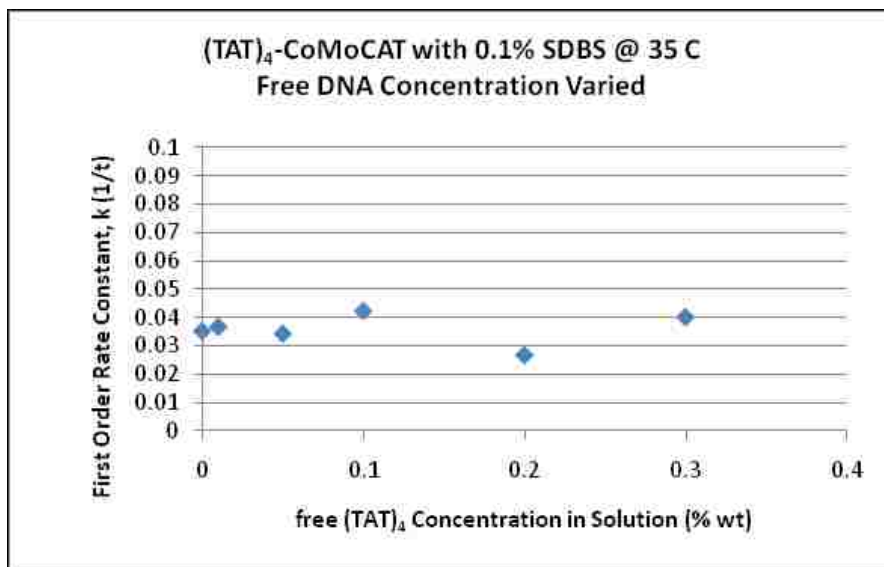
Because  $(A+B)$  in equation 2 sum to unity, the reaction can be followed by tracking the evolution of absorbance at a convenient wavelength, say at 990 nm,  $Abs_{990}$ , as shown in Figure 2.4d. Provisionally, we adopt the hypothesis that any given SWCNT is either covered entirely by DNA or entirely by SDBS. The effect of SWCNT length on kinetics of surfactant exchange, presented later, are consistent with this hypothesis; it would also explain why the absorption spectra are very well represented as a mixture of two pure species.

### **2.3.2 The DNA/surfactant exchange is a kinetically limited reaction.**

Under the conditions reported in this paper, we find that the replacement of DNA by SDBS can be written as the reaction



which proceeds to the right at a rate,  $k(T)$ , independent of free DNA concentration. To confirm this, we measured the kinetics as SDBS was kept at a relatively high concentration and the concentration of free DNA in solution was varied. Rough estimates suggest a 7:1 weight ratio of SDBS is needed to completely coat the SWCNT surface;<sup>44</sup> all of the presented exchange experiments were kept at a 100:1 SDBS:SWCNT weight ratio (0.1 wt%). We found that the concentration of free DNA, at concentrations up to 0.3 wt%, did not affect the rate at which SDBS displaced DNA on the SWCNT, thus leading to the interpretation that if there is enough SDBS to coat the SWCNTs, full exchange will take place, (Figure 2.5). A second important conclusion is that the process is kinetic, not an equilibrium adsorption process.

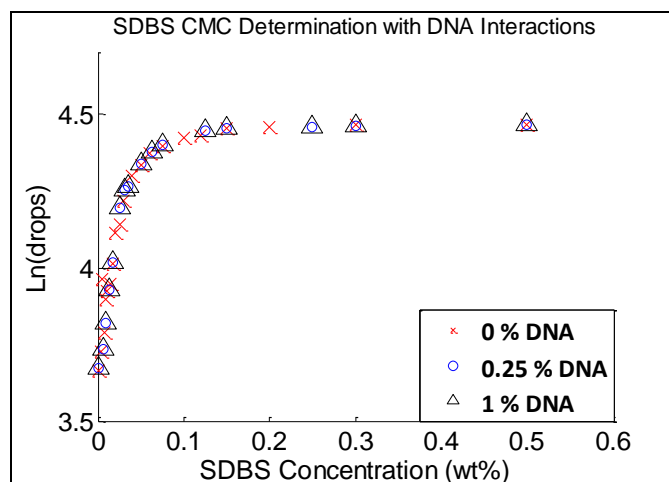


**Figure 2.5.** Keeping SDBS concentration in excess, concentration of free DNA, (TAT)<sub>4</sub>, is varied. We find that the first-order rate constant ( $k$ ) is insensitive to the concentration of free DNA.

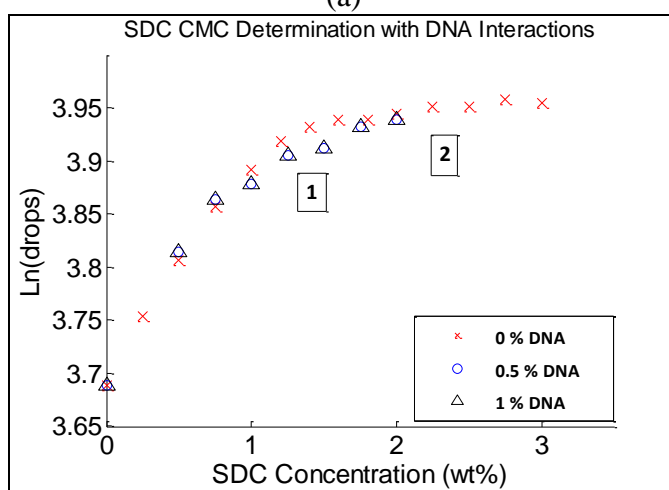
### **2.3.3 Interaction between DNA and SDBS in solution can be neglected.**

In order to show that SDBS is not forming complex and kinetic-altering structures with single-stranded DNA, surface tension measurements were performed. A simple drop counting method using a syringe was employed to estimate surface tension<sup>42</sup>. For a fixed volume and tip area, the number of drops will increase as the surface tension of the solution decreases. For surfactants, the number of drops will reach a plateau value at a critical micelle concentration (CMC). This serves as the threshold beyond which any additional added surfactant forms micelles and does not affect the surface tension of the solution. In figure 2.6a, the number of drops is plotted as a function of SDBS concentration for three different concentrations of free DNA. The overlapping data suggests that at these surfactant and DNA concentrations, interactions between the two are negligible. The CMC value can be estimated for the given experimental conditions as the concentration at which the curve attains a constant value, ~0.15 wt% SDBS. We conclude that (a) interaction between DNA and SDBS can be neglected, which helps to simplify the surfactant exchange process into a quasi-first order chemical reaction, and (b) we can find surfactant concentrations below CMC where it exchanges for the DNA in a reasonable time duration.

In a similar fashion, solutions containing varying amounts of SDC and DNA were tested for any interactions affecting surface tension. It was found that there was significant interaction between 1 – 2 wt% SDC which may be important when trying to extract kinetic information from SDC-exchange experiments, Figure 2.6b. For this study, however, we have only focused on extracting information from SDBS-exchange.



(a)



(b)

**Figure 2.6.** (a) Determination of surfactant CMC and evaluation of possible interactions with free DNA for SDBS. SDBS appears not to have any significant interaction with free ssDNA over the range of concentrations examined. (b) The same procedure is repeated for the surfactant, SDC. Between markers ‘1’ and ‘2’ there seem to be interactions causing deviation from the 0 % DNA curve.

### 2.3.4 The DNA/surfactant exchange occurs in two stages.

Figure 2.4d shows typical data on the time-dependent decay in absorbance at 990 nm for  $(GT)_{15}/\text{SWCNT}$  hybrids incubated in 0.1 % SDBS at different temperatures. We notice a rapid initial drop in absorbance, lasting no more than 3 seconds (all of the solutions started at an absorbance of  $1 \pm 0.01$ ). We show later that this initial drop varies strongly and systematically by DNA sequence type and temperature. We also would like



to acknowledge that the initial drop may arise due to effects outside the realm of this SWCNT reaction. For instance, if DNA-SWCNT hybrids adsorb to the plastic pipette used to mix the solutions or the quartz cuvette, then the concentration would be artificially reduced. For the sake of simplicity, we have chosen to neglect any effects to this nature.

There is a second process that proceeds at a slower pace, with a characteristic exponential decay, (Figure 2.7). To analyze these experimental data quantitatively, we introduce a two-step sequential mechanism for the interaction of SDBS with the DNA-SWCNT hybrid. A working hypothesis for the physical basis of a two-step process is sketched in Figure 2.8.

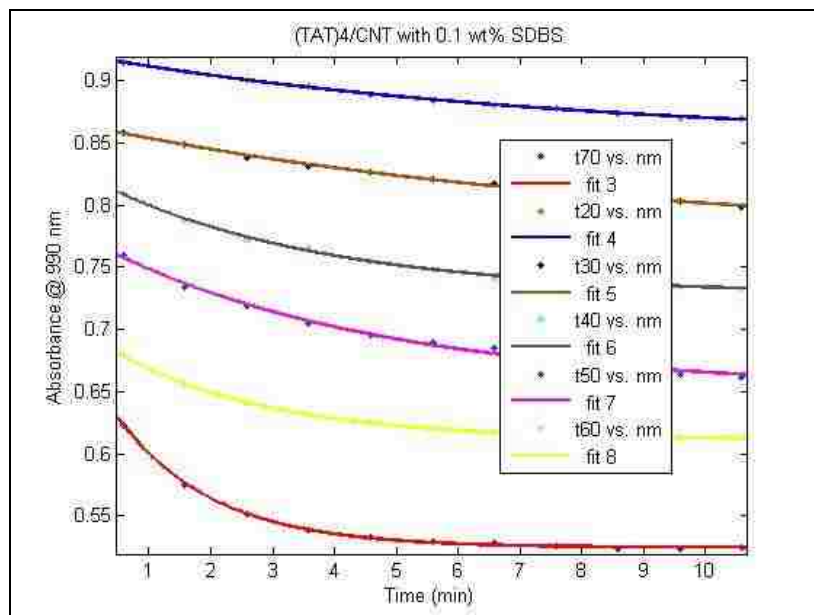
Data presented in Section 2.3.1 and the length effect reported in Section 2.3.5 both suggest that the dispersion consists of SWCNTs each coated entirely either by DNA or by SDBS. This, in turn, suggests that DNA removal is a rapid process and the rate-limiting step is the formation of a defect in the coating. We propose that some fraction of the population of DNA-SWCNT have at least one defect; others are defect-free. Stage 1, then, corresponds to the rapid removal of DNA from those that initially have at least one defect. Stage 2 corresponds to the thermally activated formation of defects in the initially defect-free DNA-SWCNT rods. The initial drop in absorbance was found to be independent of free DNA concentration in solution, leading to the interpretation that defects are due to local disorder in the DNA strand arrangement, rather than due to entire DNA strands coming off the SWCNT, (Figure 2.9).

As a measure of the extent of the reaction, we monitor,  $Abs_{990}$  and represent it by the additive combination

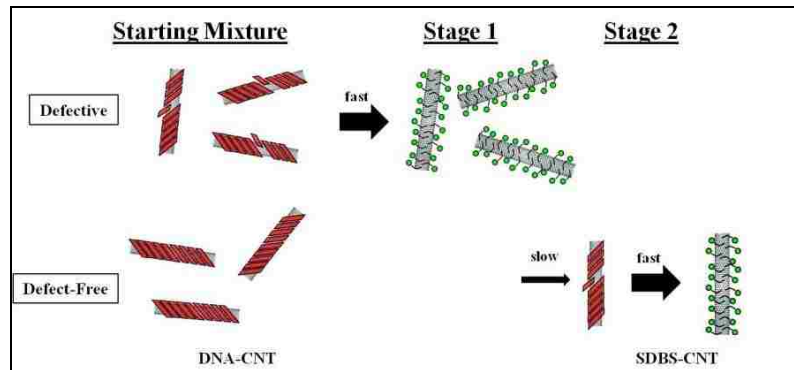
$$Abs_{990} = A_o \left( a_1 + a_2 e^{-t/\tau_2} \right) \quad (2.5)$$

where  $A_o$  is the initial absorbance of the dispersion, which we maintain as unity. Stage 1 occurs immediately on addition of the DNA-SWCNT dispersion to the pre-heated SDBS solution. Stage 2 begins with an absorbance of  $Abs_{990}=A_o(a_1+a_2)$ , and asymptotically approaches  $Abs_{990}=A_o a_1$ , where  $0 \leq a_1, a_2 \leq 1$ , and  $(a_1 + a_2) \leq 1$ . The decay of absorbance in the second step follows well the exponential decay assumed in Equation 2.5. This suggests that our reaction (Equation 2.4) is operating as a first-order or pseudo-first order reaction, where rate depends on [DNA-SWCNT] and [SDBS] is kept in excess. Because the timescales of the two stages are drastically different, we propose to analyze each step of the mechanism separately.

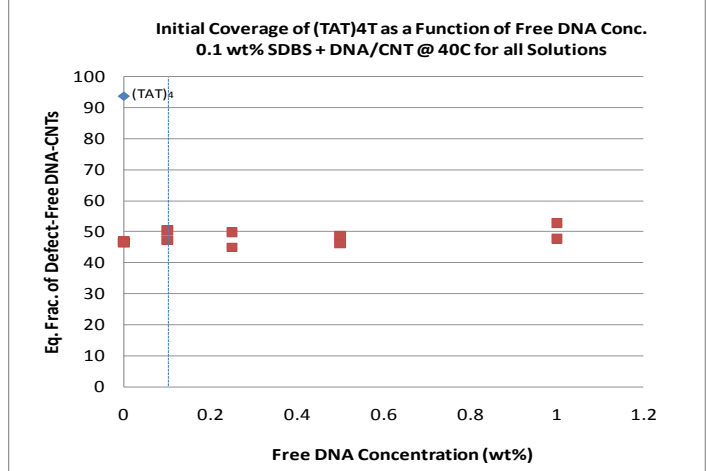
To confirm that the reaction is operating under sufficient excess of SDBS when it is at a concentration of 0.1%, we compare in Figure 2.10 the kinetics of stage 2 under this condition with another experiment with concentration lowered below the 7:1 weight ratio with SWCNTs expected to be insufficient for full coverage of all SWCNTs. For a concentration of SDBS sufficiently high to be in excess, a full shift in  $E_{11}$  peak position can be seen. At the lowered concentration, attenuation of the 990 nm peak halts by the end of 10 minutes because SDBS falls below the reported 7:1 weight ratio and is no longer in excess.



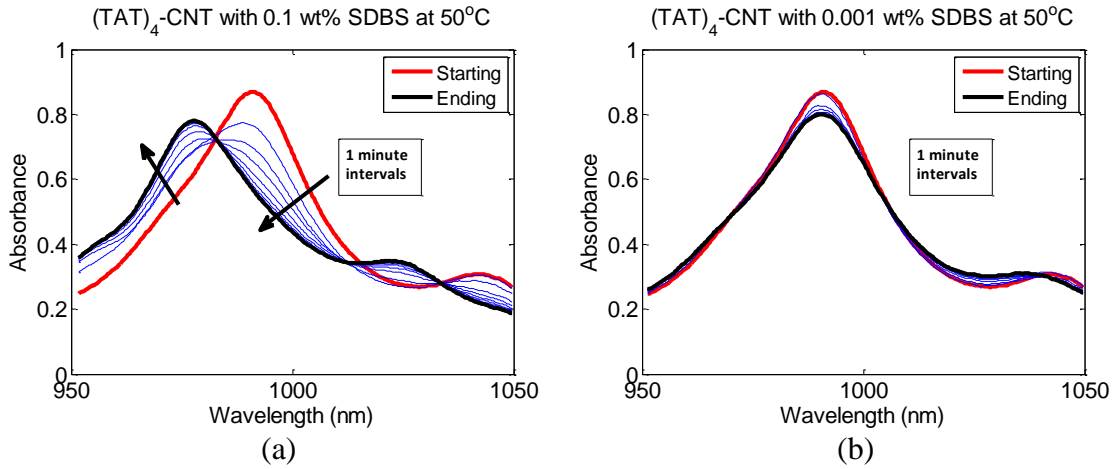
**Figure 2.7:** Data from representative  $(TAT)_4$ -SWCNT surfactant-exchange experiment along with fits using equation 2.5 that yield the rate constant. Legend labels “t20 – t70” refer to the temperature in degrees Celsius. Note that not only do the characteristic exponential rates of decay increase with increasing temperature, but also the y-axis intercepts decrease, suggesting an initial drop in absorbance that increases with increasing temperature.



**Figure 2.8.** Schematic drawing illustrating the process of exchanging DNA for SDBS on the surface of SWCNTs. A two-step mechanism is proposed, consistent with observed data. As a working hypothesis we propose that in Stage 1, SDBS rapidly adsorbs onto SWCNTs with defects in the DNA coating. The DNA is quickly displaced from the SWCNT. In Stage 2, the subsequent removal of DNA from (initially) defect-free SWCNTs is limited by the rate of formation of new defects.



**Figure 2.9.** Equilibrium fraction of defect-free DNA-SWCNTs for (TAT)<sub>4</sub>T showing little change as a function of free DNA concentration.



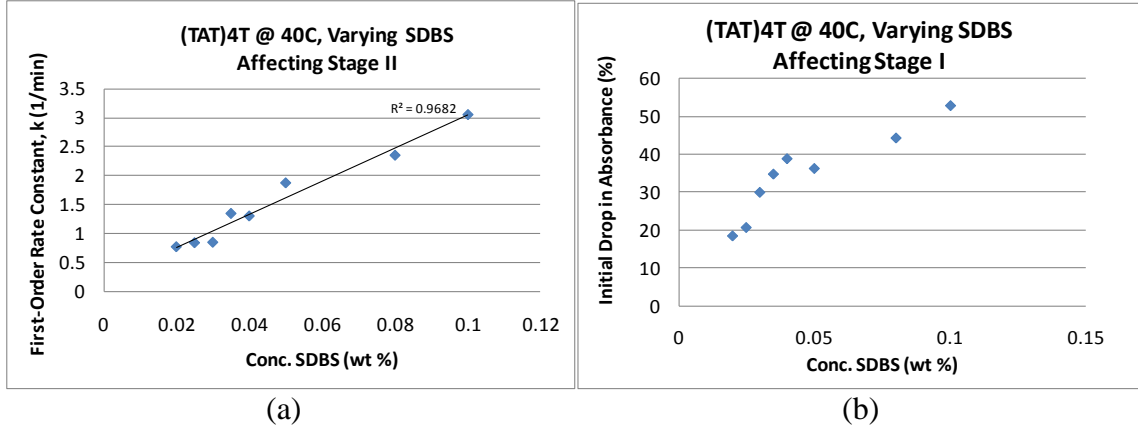
**Figure 2.10.** (TAT)<sub>4</sub>/SWCNT hybrids under incubation with (a) 0.1 wt% and (b) 0.01 wt% SDBS at 50°C. The higher concentration of SDBS results in full coverage of SWCNTs and a complete shift is seen. At the lower concentration, the transformation of DNA-SWCNT into SDBS-SWCNT halts as SDBS is depleted.

We have also found that reaction rate increases linearly with SDBS concentration (Figure 2.11a) so that the rate of reaction (Equation 2.4) can be written as

$$\frac{d[\text{DNA} - \text{SWCNT}]}{dt} = -k'[\text{DNA} - \text{SWCNT}][\text{SDBS}] \quad (2.6)$$

When SDBS is in sufficient excess, as is the case for experiments reported in the remainder of this manuscript, it can fully coat all of the SWCNTs without significant loss of concentration in the bulk. Then, [SDBS] is absorbed into the rate constant and, if

[SDBS] is held fixed, [DNA-SWCNT] decays exponentially in time, as observed experimentally. The fact that the rate of reaction is linear in [SDBS] implies that the stoichiometric ratio between a DNA-SWCNT rod and SDBS is 1-1, suggesting that the activated state limiting reaction rate consists of a single SDBS molecule invading a defect in the DNA coating on the SWCNT.



**Figure 2.11.** (a) Influence of SDBS concentration on the rate of DNA removal in stage 2. (b) The initial drop in absorbance at 990 nm upon introduction of SDBS also depends largely on concentration of SDBS.

It is useful to see whether the discussion presented above is consistent with the irreversible, 2-stage reaction drawn in Figure 2.8. Let us represent Figure 2.8 by the simplified irreversible reaction,  $A \rightarrow B \rightarrow C$ . We note that SDBS is present in excess and participates in the reactions.

Taking [SDBS] to be in excess, simple kinetics of stage 2 can be written as follows.

$$\begin{aligned}
 -\frac{dA}{dt} &= k_1[A] \\
 -\frac{dB}{dt} &= -k_1[A] + k_2[B] \\
 -\frac{dC}{dt} &= -k_2[B]
 \end{aligned}
 \tag{2.7}$$

Since the reactions are irreversible, if initially the concentration of A is  $A_o$ , its concentration follows first-order kinetics,

$$[A] = [A]_o e^{-k_1 t} \quad (2.8)$$

Substituting (2.8) into the expression for B.

$$\frac{d[B]}{dt} + k_2[B] = k_1[A]_o e^{-k_1 t} \quad (2.9)$$

This differential equation follows a standard form with solution,

$$\begin{aligned} \frac{dy}{dx} + yf(x) &= g(x) \\ e^{\int f(x)dx} y &= \int e^{\int f(x)dx} g(x)dx + c \end{aligned} \quad (2.10)$$

This gives a final expression for B, after giving the initial condition of  $[B]_o=0$ .

$$[B] = \frac{k_1}{k_2 - k_1} (e^{-k_1 t} - e^{-k_2 t}) [A]_o \quad (2.11)$$

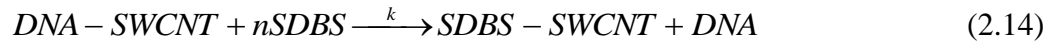
Since, at all times  $[A] + [B] + [C] = [A]_o$ ,

$$[C] = \left( 1 + \frac{k_1 e^{-k_2 t} - k_2 e^{-k_1 t}}{k_2 - k_1} \right) [A]_o \quad (2.12)$$

Figure 2.7 for stage 2 shows a single exponential. Our data show that  $k_2 \gg k_1$ , that is, defect nucleation ( $A \rightarrow B$ ) is much slower than SDBS displacing DNA ( $B \rightarrow C$ ). This implies  $k_1 \exp(-k_2 t) \ll k_2 \exp(-k_1 t)$ , and  $k_2 - k_1 \cong k_2$ . The observed rate of formation of C is then,

$$[C] = (1 - e^{-k_1 t}) [A]_o = 1 - [A] \quad (2.13)$$

Where  $[A]_o$  is the concentration of DNA-SWCNT at the start of stage 2. In particular, the parameters of the second, fast, step do not matter. In fact, stage 2, ( $A \rightarrow B$ ), which is governed by defect nucleation rate, involves SDBS



Since [SDBS] is in excess, we can write this as pseudo-first order ( $A \rightarrow B$ ) ([SDBS] does not change substantially over the course of the reaction).

$$\frac{d[DNA - SWCNT]}{dt} = -k[SDBS]^n [DNA - SWCNT] = -k_1 [DNA - SWCNT] \quad (2.15)$$

$$k_1 = k[SDBS]^n$$

Therefore,  $k_1$  is expected to depend on [SDBS]. Figure 2.11 shows that this dependence is linear, suggesting  $n=1$ .

### **2.3.5 Rate of reaction increases with SWCNT length, suggesting that DNA removal on a single SWCNT is limited by nucleation of a defect.**

Consider a series of samples each with the same total length of SWCNT but with different average lengths of SWCNT fragments (Figure 2.12a). Experimentally, fixed total length of SWCNT corresponds to a fixed starting absorbance, as we maintain in our experiments. Different average length of individual SWCNTs can be selected by choosing different SEC fragments.

We imagine that in stage 2 substitution of DNA by SDBS will generally first require a nucleation step, perhaps a defect in the DNA coating large enough to admit adsorption of some SDBS, followed by progressive growth of this region as SDBS molecules replace DNA. For ease, think of a nucleation site as a chink in the DNA armor where SDBS molecules could potentially invade. The overall observed rate of removal will be limited by the slower of the two processes. Two limiting cases would be (a)

nucleation rate  $\gg$  growth rate, or (b) nucleation rate  $\ll$  growth rate. Furthermore, we can imagine two limiting cases for nucleation sites: heterogeneously only at SWCNT ends, or homogeneously throughout the length of SWCNT. Together, these give us four limiting possibilities:

**1. Nucleation rate  $\gg$  growth rate with nucleation only at SWCNT ends.** DNA removal begins simultaneously at all SWCNT ends. The rate of the reaction (Equation 2.6) will be proportional to the number of fragments,  $L/l$ , i.e., meaning that kinetics would be more rapid for samples with shorter SWCNTs, in inverse proportion to their length.

**2. Nucleation rate  $\ll$  growth rate with nucleation only at SWCNT ends.** DNA removal rate is governed by nucleation of defects at SWCNT ends. The number of nucleation events is proportional to  $L/l$  and the rate goes as  $L/l \times l$ , and thus is independent of SWCNT length.

**3. Nucleation rate  $\gg$  growth rate with homogeneous nucleation sites along SWCNT length.** In this case, defects nucleate rapidly and DNA is removed at characteristic rate. Neither process depends in SWCNT length so the kinetics would be expected to be independent of SWCNT length.

**4. Nucleation rate  $\ll$  growth rate with homogeneous nucleation sites along SWCNT length.** The nucleation rate is proportional to the total length of SWCNT in the sample,  $L$ . However, since growth is rapid, each nucleation event results in conversion of one SWCNT. The rate of DNA removal is then proportional to the rate of nucleation (independent of SWCNT length) times the length of each SWCNT,  $l$ . Since  $L$  is held constant, rate of removal is linear in SWCNT length.



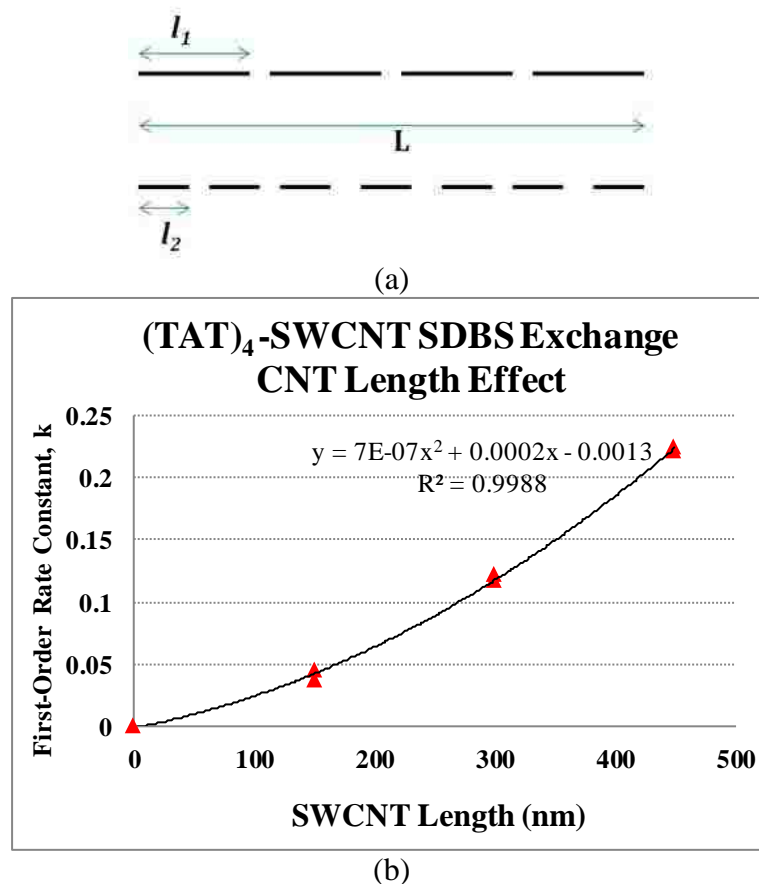
Figure 2.12b shows that the kinetics, as measured by the first order rate constant, depend strongly on SWCNT length, increasing approximately linearly with it, consistent with the fourth hypothesis just cited. That is, DNA removal appears to be limited by homogeneous nucleation of defects on the SWCNT sidewall followed by rapid substitution of DNA by SDBS. Note that this hypothesis then also explains why (a) intermediate states in stage 2 are represented well as a mixture of pure SDBS and DNA coated SWCNTs, (b) kinetics depend linearly on SDBS concentration. It also suggests that a starting DNA-SWCNT dispersion is comprised of some with and others without a pre-existing defect. Those with a defect are converted rapidly in stage 1 to SDBS-coated SWCNTs; the remaining are converted in stage 2 at a rate limited by nucleation of new defects.

This means that the rate of conversion of DNA-SWCNT to SDBS/SWCNT (in units of length of SWCNT) is

$$\frac{d[\text{DNA} - \text{SWCNT}]}{dt} = -\frac{dN}{dt}l \quad (2.16)$$

where  $\frac{dN}{dt}$  is the rate of defect nucleation. The nucleation rate, in turn, depends on concentration of SDBS, remaining length of DNA coated SWCNTs ( $[\text{DNA-SWCNT}]$ ) and a reference frequency,  $\nu$ , per unit SWCNT length per SDBS concentration:

$$\frac{dN}{dt} = \nu[\text{DNA} - \text{SWCNT}][\text{SDBS}] \quad (2.17)$$



**Figure 2.12.** (a) Schematic drawing depicting two cases, each with the total SWCNT length,  $L$ , but with different average individual SWCNT length,  $l_1$  and  $l_2$ . (b) Stage 2 kinetics for  $(TAT)_4$  at  $30^\circ\text{C}$  as a function of average SWCNT length ( $l$ ). A second-order polynomial has been fit to the data (passing through the origin) which shows good agreement.

The reference frequency contains a Boltzmann factor in the free energy of an activation free energy, which will be introduced in the following section. Combining Equations 2.15, 2.16, and 2.17, we get

$$\frac{d[\text{DNA} - \text{SWCNT}]}{dt} = -\nu \cdot l[\text{DNA} - \text{SWCNT}][\text{SDBS}] = -k[\text{DNA} - \text{SWCNT}] \quad (2.18)$$

The first equality, is identical in form to the experimentally observed form, equation 2.6, and additionally reveals the linear dependence of rate of reaction on

SWCNT length. The second equality is obtained if [SDBS] is maintained at a constant excess value as we do for the remainder of the manuscript (0.1% by wt) and SWCNT length is also held fixed (250-350 nm SEC fraction, for the remainder of this manuscript), unless otherwise noted.

From this, we can support two hypotheses distinguishing stage 1 and stage 2. These are that the first stage arises from defects (nucleation sites) in the structure that the SDBS attacks immediately. Stage 2, then, is the thermally activated stage in which new defects have to be created.

## **2.4 Analysis of Surfactant Exchange Kinetics**

We begin by examining the first stage of the kinetics of surfactant exchange. Because the first stage occurs rapidly, we can extract only a single measure from this part of the experiment – the total decrease in adsorption before the second stage of the DNA removal process commences. We follow by analyzing the kinetics of the second stage in greater detail. Specifically, we use Eyring kinetics to extract activation enthalpies for different sequences. In the subsequent sections, we examine the results of fluorescence studies.

### **2.4.1 Stage 1: Probing the Initial Coverage of DNA on the SWCNT.**

In this study, we have chosen to examine three families of DNA sequences. The first comprises the 30-mers:  $(TAT)_{10}$ ,  $(GT)_{15}$ ,  $(TATT)_7TA..$  The second and third are based on sequences that recognize (6,5) SWCNTs:  $(TAT)_4$  and  $(CGT)_3C$  (as shown by Tu et al.<sup>16</sup>). Among the recognition sequences, families were made by subtracting or adding

one to two bases. For example, surfactant-exchange was performed on (TAT)<sub>3</sub>T, (TAT)<sub>3</sub>TA, (TAT)<sub>4</sub>, (TAT)<sub>4</sub>T, and (TAT)<sub>4</sub>TA.

To characterize the quick first stage, initial concentrations of the DNA-covered SWCNTs were adjusted so that the absorbance of the E<sub>11</sub> peak at 990 nm was  $1 \pm 0.01$ . Instead of scanning the entire wavelength range, we followed the decay of absorbance at 990 nm at short time intervals (e.g., Figure 2.4d). To determine the extent to which DNA-SWCNTs are converted at the end of stage 1, we extrapolated the second-stage kinetics to zero time. Figure 2.13 shows these intercept values for a variety of sequences as a function of temperature. We notice a strong, non-monotonic, dependence on sequence length and an increase of stage 1 DNA-SWCNT conversion with increasing temperature.

As argued in Section 2.3.4, we interpret stage 1 as quick removal of DNA from the subpopulation of DNA-SWCNT that already has at least one nucleated defect on it. Because we are extracting the data at zero time, this measurement can be interpreted as the equilibrium fraction of DNA-SWCNTs without a defect,  $f_{nd}$ . In terms of the measured absorbance, it is estimated as (see equation 5).

$$f_{nd} = \frac{a_2}{1 - a_1} \quad (2.19)$$

The fraction of DNA-SWCNTs with at least one defect is  $f_d = 1 - f_{nd}$ . For example, in an experiment the second stage kinetics for (TAT)<sub>4</sub>T had a zero-time intercept value of 0.84. The intensity of the 990 nm peak starts at 1.01 (fully DNA-covered,  $A_o$ ) and ends at 0.71 (fully SDBS-covered). Therefore,  $a_1 + a_2 = 0.84/1.01$ ,  $a_1 = 0.71/1.01$ , and the equilibrium

fraction of defect-free DNA-SWCNTs is  $f_{nd} = \frac{a_2}{1 - a_1} = \frac{0.84 - 0.71}{1 - 0.71} = 0.43$

Figure 2.13a plots the fraction of defect-free DNA-SWCNTs for a variety of sequences as a function of temperature. Figure 2.13c shows a more direct comparison between sequences at a given temperature of 40°C. Within a family, we find significant, non-monotonic, differences with sequence length. For example, both (TAT)<sub>4</sub>T and (TAT)<sub>3</sub>TA, have significantly smaller fractions of defect-free DNA-SWCNT than the recognition sequence (TAT)<sub>4</sub>. Similarly, both (CGT)<sub>3</sub> and (CGT)<sub>3</sub>CG have significantly smaller fractions of defect-free DNA-SWCNT than the recognition sequence (CGT)<sub>3</sub>C. Let us interpret the fraction of defect-free DNA-SWCNT to result from the equilibrium

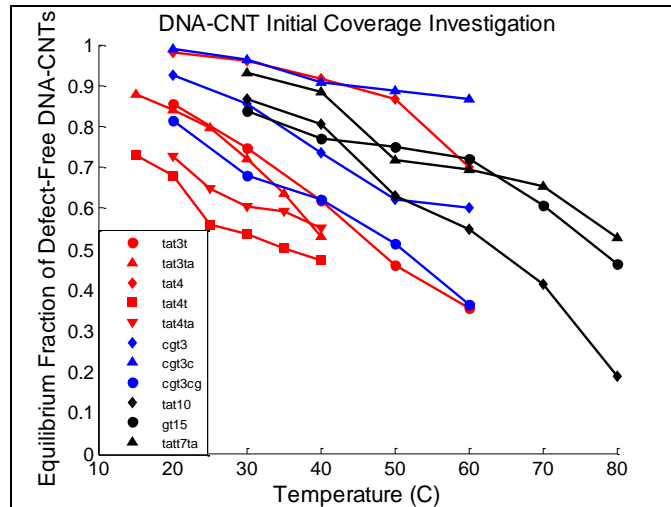
$$[DNA - SWCNT]_{defect-free} \overset{K_{eq}}{\rightleftharpoons} [DNA - SWCNT]_{defective} \quad (2.20)$$

(Note that this is at fixed [SDBS]. Figure 2.11b shows that the equilibrium depends on [SDBS].) Then, we can associate an equilibrium constant and free energy of defect formation,  $\Delta G(T)$ , as

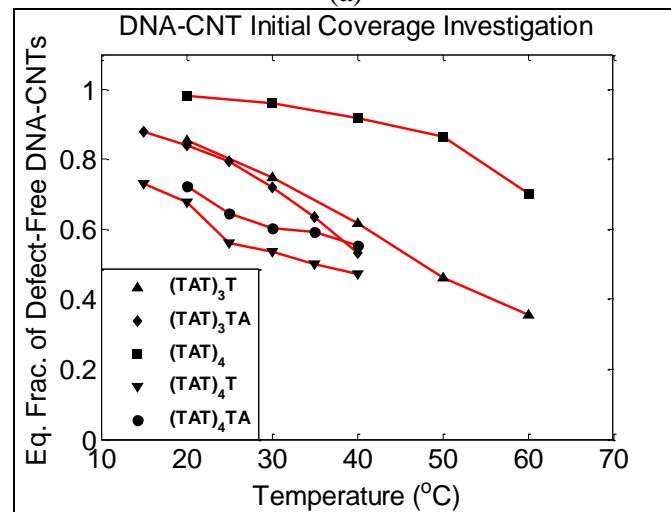
$$K_{eq} = \frac{[DNA - SWCNT]_{defective}}{[DNA - SWCNT]_{defect-free}} = e^{\frac{-\Delta G}{k_B T}} = e^{\frac{-\Delta H}{k_B T}} e^{\frac{\Delta S}{k_B}} \quad (2.21)$$

$$\ln(K_{eq}) = \frac{-\Delta G}{k_B T} = -\frac{\Delta H}{k_B T} + \frac{\Delta S}{k_B} \quad (2.22)$$

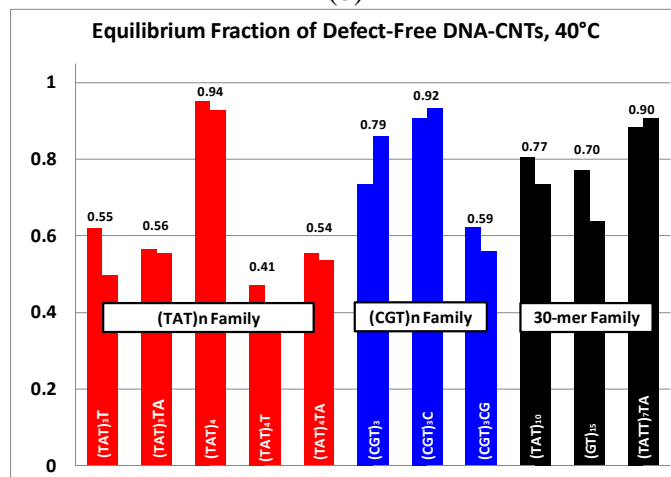
These quantities are found from a linear Arrhenius plot of  $\ln(K_{eq})$  vs.  $1/T$ , (Figure 2.14), and are reported in Table 2.1.



(a)



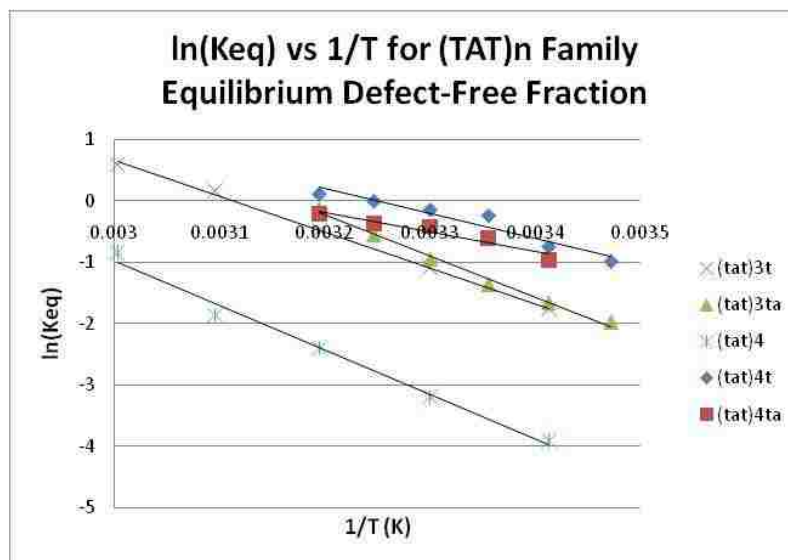
(b)



(c)

**Figure 2.13.** Fraction of defect-free DNA-SWCNT for (a) all examined sequences and (b) the (TAT)<sub>4</sub> family as a function of temperature. Significant non-monotonic differences are observed between sequences of the same family. (c) Comparison of

defect-free DNA-SWCNT fractions at 40°C. Two runs were performed on each sequence with the average value reported above columns. The two noticeable outliers, (TAT)<sub>4</sub> and (CGT)<sub>3</sub>C, are the recognition sequences for the (6,5) SWCNT.



**Figure 2.14.** Data from Stage 1 experimentally determined fractions of defect-free DNA-SWCNTs. Plot shows a strong linear dependence between  $\ln(K_{eq})$  and  $1/T$  from which thermodynamic values of entropy, enthalpy, and free energy differences can be calculated.

**Table 2.1.** Free energies, enthalpies and entropies (along with confidence intervals, CI, of the fit) of defect formation extracted from fraction of DNA-SWCNT converted to SDBS-SWCNT at the end of stage 1.

Sequence	$\Delta H/k_B T$ (300K) with 95% CI	$\Delta S/k_B$ with 95% CI	$\Delta G/k_B T$ ( 300K) with 95% CI
(TAT) <sub>3</sub> T	$19.4 \pm 0.02$	$18.1 \pm 0.02$	$1.3 \pm 0.02$
(TAT) <sub>3</sub> TA	$22.2 \pm 0.10$	$21.1 \pm 0.09$	$1.1 \pm 0.1$
(TAT) <sub>4</sub>	$24.2 \pm 0.14$	$20.8 \pm 0.12$	$3.4 \pm 0.14$
(TAT) <sub>4</sub> T	$13.6 \pm 0.49$	$13.2 \pm 0.48$	$0.4 \pm 0.49$
(TAT) <sub>4</sub> TA	$10.8 \pm 0.43$	$10.2 \pm 0.41$	$0.6 \pm 0.43$
(CGT) <sub>3</sub>	$18.0 \pm 0.39$	$16.0 \pm 0.35$	$2.0 \pm 0.39$
(CGT) <sub>3</sub> C	$22.1 \pm 1.31$	$18.5 \pm 1.09$	$3.7 \pm 1.31$
(CGT) <sub>3</sub> CG	$15.5 \pm 0.16$	$14.5 \pm 0.15$	$1.1 \pm 0.16$
(GT) <sub>15</sub>	$11.6 \pm 0.50$	$9.6 \pm 0.42$	$1.8 \pm 0.5$
(TATT) <sub>7</sub> TA	$17.3 \pm 0.61$	$14.7 \pm 0.51$	$2.6 \pm 0.61$
(TAT) <sub>10</sub>	$22.6 \pm 0.35$	$20.4 \pm 0.31$	$2.3 \pm 0.35$

Note again the differences among sequences of the same family ((TAT)<sub>4</sub> vs. (TAT)<sub>4</sub>T) and between sequences of the same length ((GT)<sub>15</sub> vs. (TAT)<sub>10</sub>). At 300K, free energy of defect formation in the recognition sequences, (TAT)<sub>4</sub> and (CGT)<sub>3</sub>C, is some 2  $k_B T$  greater than for sequences that differ by only one base. This is consistent with our previous suggestion that recognition sequences have a more ordered structure as compared to related non-recognition sequences.<sup>16</sup> While we have not conducted a similar sequence-length comparison for the longer 30-mers, it is interesting to note that differences between sequences are somewhat attenuated compared to the shorter sequences. That is, it is not the absolute strength of binding but rather the difference between binding strength among related sequences and for related SWCNTs (not studied here) that is responsible for the discriminating recognition shown by certain sequences. Note also the significantly larger magnitude of binding enthalpies compared to binding free energy. We ask the reader to keep these numbers in mind; magnitudes of these values will be discussed in the following section as both stage 1 and stage 2 relate to DNA-SWCNT binding strengths.

#### **2.4.2 Stage 2: Analysis of DNA-displacement kinetics.**

To analyze the second step of the interaction between SDBS and DNA-SWCNT, we consider the reaction corresponding to the irreversible displacement of DNA by SDBS, Equation 2.4, and the corresponding rate Equations 2.6 and 2.18. That is,

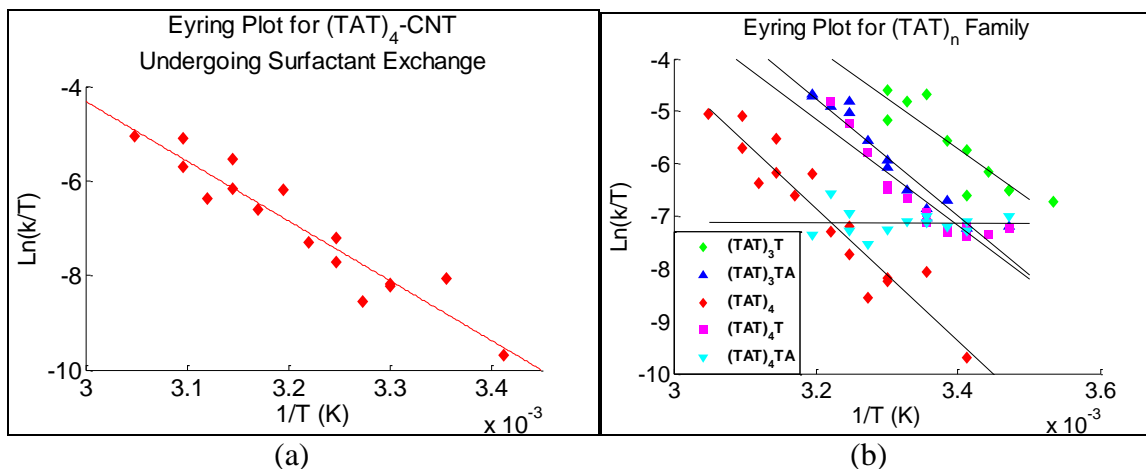
$$\frac{[DNA - SWCNT]}{[DNA - SWCNT]_o} = e^{-kt} \quad (2.23)$$

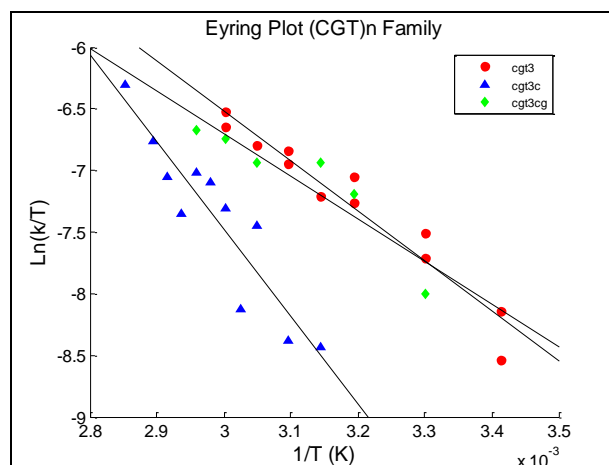


Interpreting the rate constant using Eyring's activated rate theory,<sup>41</sup> allows one to relate it to activation enthalpy and entropy as

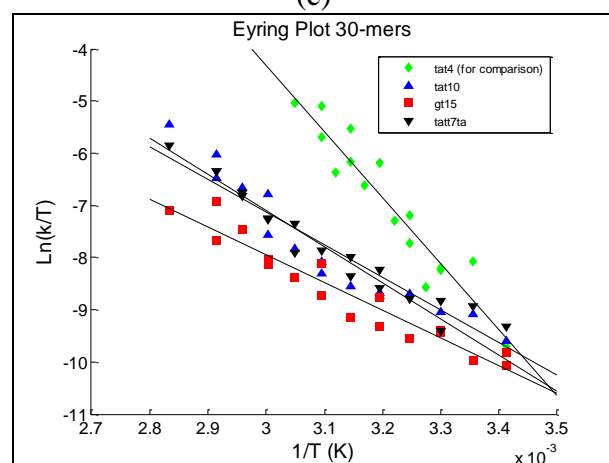
$$\ln\left(\frac{k}{T}\right) = \ln(\alpha) - \frac{\Delta H^\ddagger}{k_B T} + \frac{\Delta S^\ddagger}{k_B} \quad (2.24)$$

where  $\alpha$  is proportional to a rate, length of SWCNTs and [SDBS], as discussed in Section 2.3.5. For the present purposes, this remains a constant quantity. The rate constant,  $k$ , is extracted by fitting the kinetics of change in absorbance at different temperatures using Equation 2.23. The activation enthalpy,  $-\Delta H^\ddagger$ , can be determined from the slope of  $\ln(k/T)$  vs.  $1/T$ . In principle one could also obtain absolute activation entropy,  $\Delta S^\ddagger$ , from the intercept except that the attempt rate pre-factor contains many unknown (albeit constant) factors. However, if we make the (we feel, reasonable) assumption that the pre-factor is the same for different DNA strands, then we can estimate differences in activation entropy between different compositions. An example of such a plot is shown for  $(TAT)_4$ /SWCNT in figure 2.15a. Figure 2.15b compares measurements within the  $(TAT)_n$  family, while (c) and (d) show Eyring plots for  $(CGT)_n$  and 30-mer families, respectively.

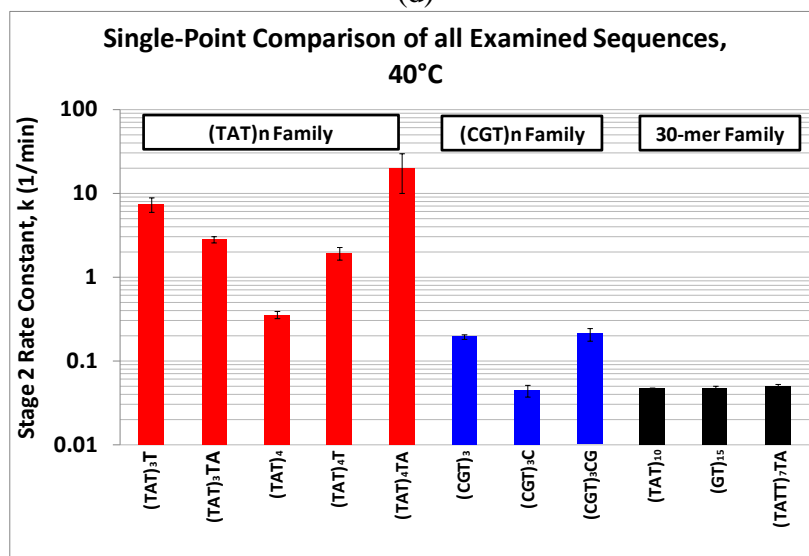




(c)



(d)



(e)

**Figure 2.15.** (a) Eyring plot of rate constant,  $\ln(k/T)$ , vs.  $1/T$  enables the extraction of activation enthalpy and relative entropy of second stage kinetics. Rate constants were calculated from the decay in absorbance at 990 nm, representing the DNA-covered/(6-5)-SWCNT  $E_{11}$  transition. Eyring plots for the (b)  $(TAT)_n$ , (c)  $(CGT)_n$ , and (d) 30-mer

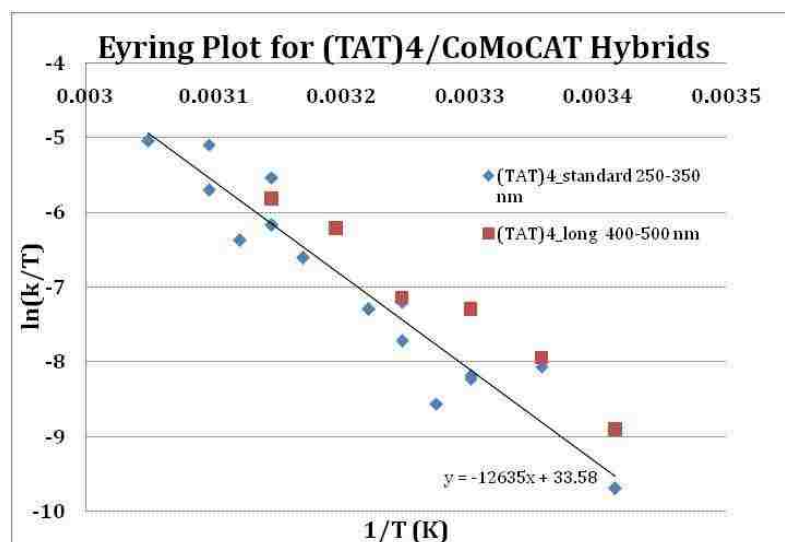
family of sequences (e) A single-point comparison (at 40°C) is shown, with standard error, demonstrating that DNA recognition sequences are stable compared to their compositional cousins.

Within the (TAT)<sub>n</sub> family of sequences it is apparent that there is a strong and non-monotonic dependence of stage 2 reaction rate on sequence, mirroring the results of stage 1. Figure 2.15e plots the rate constant at a fixed temperature (40°C). The (6,5) recognition sequence, (TAT)<sub>4</sub>, is removed at a rate about 20 times slower than either (TAT)<sub>4</sub>T or (TAT)<sub>3</sub>TA, both of which differ from it by only one base in length. Similarly, in the (CGT)<sub>n</sub> family, the recognition sequence, (CGT)<sub>3</sub>C, is removed at a much slower rate than either of its compositional neighbors, (CGT)<sub>3</sub>CG or (CGT)<sub>3</sub>. Along with the results of stage 2, this finding shows a strong relationship between recognition and binding strength. All sequences in the (TAT)<sub>n</sub> family have similar slope on this plot (reflecting similar transition enthalpy) except the sequence (TAT)<sub>4</sub>TA, which presented a behavior very unlike the other (TAT)<sub>n</sub> sequences. The near lack of temperature dependence suggests a very small activation barrier, where the rate of reaction is governed almost entirely by the pre-exponential factor.

Note that the 30-mers are removed at a rate significantly slower than the shorter DNA sequences, slower even than the special recognition sequences. As noted earlier, this suggests that the discriminative ability of the shorter sequences comes not so much from their absolute binding strength but from their differential binding. We have shown earlier that, for a given DNA sequence, kinetics increase linearly with SWCNT length, which we interpreted as a defect nucleation-limited mechanism. If, additionally, we imagine that defects are likely to nucleate near ends of DNA strands, we surmise the number of nucleation sites and hence the nucleation rate is inversely proportional to the

DNA length. If somehow there is an effective ligating effect between short strands on the SWCNT, then the number of nucleation sites can be greatly reduced, e.g.  $(TAT)_4$  vs.  $(TAT)_4T$ , and a short strand of DNA can behave more like that of longer sequence.

During the course of the experiment, surfactant exchange had been performed on SWCNTs of well-controlled length. Through SEC purification, samples were made at relatively high concentration with a controlled SWCNT length of 250-350 nm, which was confirmed experimentally by AFM imaging. This length range contained the highest concentration by weight of SWCNTs and thus was used for nearly all the experiments. To understand the effect of SWCNT length, surfactant exchange was performed on SEC fractions with different SWCNT lengths. In the case of  $(TAT)_4$ , three different fractions were examined, designated 'fraction 1, 3, and 5'. These contained SWCNTs of length 100-200, 250-350, and 400-500 nm, respectively. When performing surfactant exchange on these samples under the same experimental conditions, it was found that the longer SWCNTs undergo DNA removal at a faster rate than the shorter ones. In fact, from the three samples examined, there appeared to be a linear trend between length of SWCNT and rate of DNA removal (Figure 2.12b). Furthermore, a temperature-dependent study was performed on the longer SWCNT fraction (Figure 2.16) and we found that there indeed was a systematic increase in rate for each temperature set point examined. The ratio of rate constant for the longer SWCNTs to shorter ones turned out to be  $1.59 \pm 0.44$ , allowing us to state with confidence that longer SWCNTs proceed faster than shorter ones. Note that this ratio is similar to the ratio of mean lengths.



**Figure 2.16.** Temperature-dependent comparison study between fractions 1 and 3 of (TAT)<sub>4</sub> SEC sample, longer SWCNT lengths showing faster kinetics of DNA removal.

Activation enthalpies and entropy differences, presumably representing the amount of energy required to elevate a particular “activation unit” from an adsorbed to a transition state (TS), were extracted from the fitted data and are summarized in Table 2.2. Also shown are activation free energy differences using (TAT)<sub>4</sub> as a reference. It is interesting to note that these differences are comparable to those found by analysis of stage 1 data, supporting our hypothesis that stage 1 represents an equilibrium concentration of defective DNA-SWCNT and that stage 2 represents the kinetics of nucleation of defects in initially defect-free DNA-SWCNTs. Although at this point the identity of the TS unit is unknown, we can assume the TS of the reaction is the point at which one or a few DNA bases, are just slightly lifted, before SDBS or even water can get into the created space to solvate them. Activation energies can be compared to experimentally documented DNA base free energies in an attempt to pinpoint the TS unit. Additionally, the conformational entropy loss for changing the conformation of single-stranded DNA from a random coil to an outstretched chain can be estimated at 1

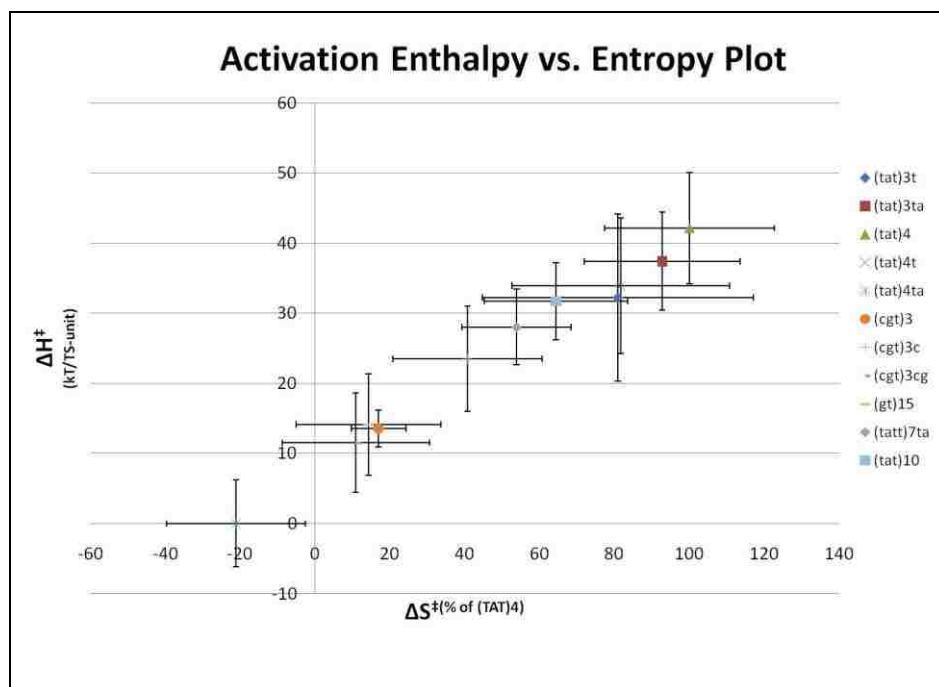
$k_B T / \text{Kuhn-length}$ .<sup>19,45</sup> For ssDNA in a 10 mM ionic solution, Kuhn length is roughly 5 nm, corresponding to 7-8 nucleotides.<sup>19,46</sup> Since the TS unit is likely comprised of only a few DNA bases, conformational activation entropies will all be far less than  $1 k_B T$ .

Extracted enthalpic values range from  $\sim 10\text{-}40 k_B T$ . The lower end of this range matches well measured free energy of DNA base-graphite binding found through single molecule peeling experiments  $\sim 8\text{-}11 k_B T / \text{base}$ <sup>35</sup> suggesting that the transition state unit in these cases could involve a single base. The larger numbers could imply that a greater number of bases are desorbed at the transition state, or that additional interactions, such as hydrogen bonding between DNA bases are involved.<sup>16,17</sup> In vacuum, a hydrogen bond between two DNA bases can be as much as  $\sim 10.9 k_B T / \text{bond}$ , but is only  $\sim 3.4 k_B T / \text{bond}$  in a fully solvated state.<sup>47,48</sup> Because only half of the base is solvated when adsorbed onto graphite or a SWCNT, the actual energy of a hydrogen bond will be somewhere in between these two values. Since the observed TS activation energies appear to be closer to that of a single base than full strand adsorption energies, we propose a TS unit composed of 1-2 bases with the possible breaking of hydrogen bonds being the distinguishing property.

**Table 2.2.** Activation enthalpy with entropy and free energy differences (with respect to (TAT)<sub>4</sub>) for tested sequences obtained from Eyring plot linear fits.

sequence	$\Delta H^\ddagger/k_B T$ (300K) with 95% CI	$\Delta(\Delta S^\ddagger/k_B)$ (Subtracted from (TAT) <sub>4</sub> ) with 95% CI	$\Delta(\Delta G^\ddagger)/k_B T$ (300K, Subtracted from (TAT) <sub>4</sub> )
(tat)3t	$32.2 \pm 11.9$	$6.4 \pm 12.1$	3.4
(tat)3ta	$37.4 \pm 7.0$	$2.4 \pm 7.6$	2.3
(tat)4	$42.1 \pm 7.9$	---	---
(tat)4t	$33.9 \pm 9.7$	$6.2 \pm 9.7$	2.0
(tat)4ta	$0 \pm 6.2$	$40.7 \pm 7.6$	1.4
(cgt)3	$13.6 \pm 2.6$	$27.9 \pm 2.4$	0.7
(cgt)3c	$23.5 \pm 7.5$	$19.9 \pm 6.7$	-1.3
(cgt)3cg	$11.5 \pm 7.1$	$29.9 \pm 6.6$	0.7
(gt)15	$17.7 \pm 7.2$	$25.6 \pm 6.5$	-1.2
(tatt)7.5	$20.8 \pm 5.4$	$22.0 \pm 4.9$	-0.7
(tat)10	$23.1 \pm 5.5$	$19.9 \pm 6.4$	-0.9

From Table 2.2, values of activation enthalpies and entropies can be compared on one plot in an enthalpy-entropy compensation diagram. Figure 2.17 illustrates that most sequences lie within one standard deviation away from a line passing through the origin in activation energy space. We propose the larger the distance away from the origin, the greater amount of stability that particular DNA/SWCNT hybrid possesses.



**Figure 2.17.** Activation enthalpy vs. entropy compensation plot for all examined DNA/SWCNT hybrids.

Based on molecular simulations, we have previously proposed a novel ordered DNA  $\beta$ -barrel structure stabilized by non-Watson-Crick hydrogen-bonding between bases on adjacent DNA strands.<sup>18</sup> An example germane to the (TAT)<sub>n</sub> family is the possible formation of AT-quartets which are bound together by 6 hydrogen bonds.<sup>24</sup> A transition state requiring removal of one or two of the bases would require breaking 6 hydrogen bonds, and activation enthalpies would approach those found in a structure such as (TAT)<sub>4</sub>. The presence or lack of such h-bonding at the ends of strands might account for the strong sequence-specificity (Figure 2.18). The activated state then likely consists of partial removal of 1-2 bases, which involves an increase in free energy because initially there will not be enough space for water or SDBS to insert itself. SDBS, consisting of a benzene ring attached to a hydrocarbon tail, can be crudely estimated to be the same size as, if not slightly bigger than, one ‘mer’ of DNA, consistent with the assumption that the

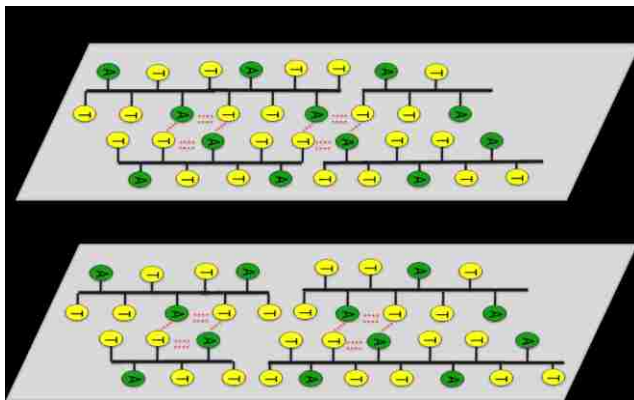


TS unit consists of 1-2 DNA bases. For the sake of argument, let us assume that the transition state is the same for all sequences (one to two bases slightly lifted up) and that differences in activation free energy arises from the nature of the structure of the DNA-SWCNT that needs to be disrupted. For example, if the DNA molecules are adsorbed as random coils interacting only by steric exclusion of each other, we expect the main contribution to the activation enthalpy to come from base-stacking interactions. On the other hand, if the DNA strands are interacting with each other via hydrogen bonds, then their disruption will contribute to the activation energy.

Why might there be differences between sequences, both by composition (e.g. (GT)<sub>30</sub> vs (TAT)<sub>10</sub>) and, by length within a sequence family (e.g., (TAT)<sub>4</sub> vs (TAT)<sub>4</sub>T)? Again, we propose that the activated state likely does not distinguish strongly between sequence composition and length. Therefore, we seek for the difference in the nature of the DNA adsorbed state. To explain compositional differences of thermodynamic values in strands of the same length, examine the difference between (GT)<sub>15</sub> and (TATT)<sub>7</sub>TA. Generally, purine bases, because of their two aromatic rings, have a higher affinity for adsorbing on a hydrophobic surface.<sup>48</sup> Purely by this comparison, (GT)<sub>15</sub> should have a higher affinity, and thus slower removal kinetics, than sequences such as (TATT)<sub>7</sub>TA and (TAT)<sub>10</sub>. This is indeed not the case as the  $\Delta H^\ddagger$  value for (GT)<sub>15</sub> is within error of the other 30-mer sequences tested. We propose hydrogen bonding will then account for the differences seen. A sequence like (GT)<sub>15</sub> is able to form G-quartets on the surface of a SWCNT,<sup>18</sup> while (TATT)<sub>7</sub>TA may form AT-quartets. The ability and frequency of quartet formation, bringing added stabilizing hydrogen bonds, is one hypothesis to explain the disparities.

Recall Table 2.1, which contains free energy differences between defective and defect-free states of DNA-SWCNTs. These magnitudes of the values are comparable to activation free energy differences measured for stage 2, which suggests that the TS unit (Table 2.2) is related to the unit reported in Table 2.1.

In regards to differences seen in the short recognition DNA sequences, we propose an extended hydrogen bonding scheme connecting multiple strands of DNA together on the SWCNT surface, (Figure 2.18). Shown as parallel strands on an unrolled SWCNT, consecutive strands may be able to ligate together to form DNA strands with effective lengths much larger than an individual strand. Hydrogen bonds, and even AT-quartet formation<sup>24</sup> are proposed to play a vital role in DNA-SWCNT hybrid stability. Additionally, sequences which can hydrogen bond to a further extent should have a lower starting free energy.

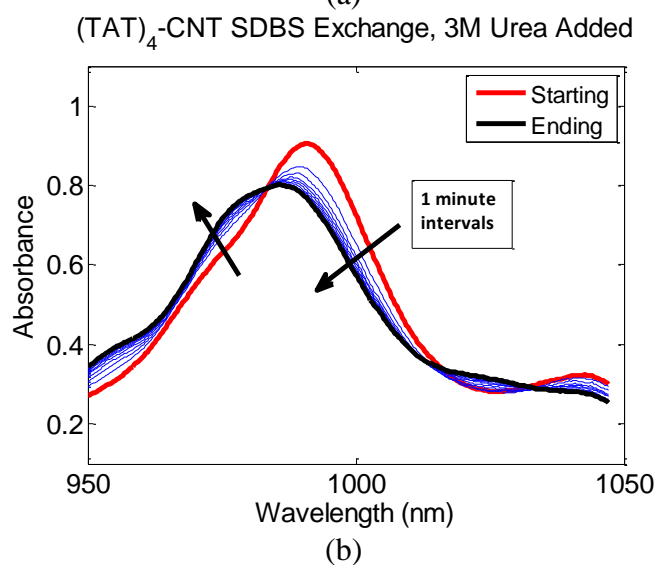
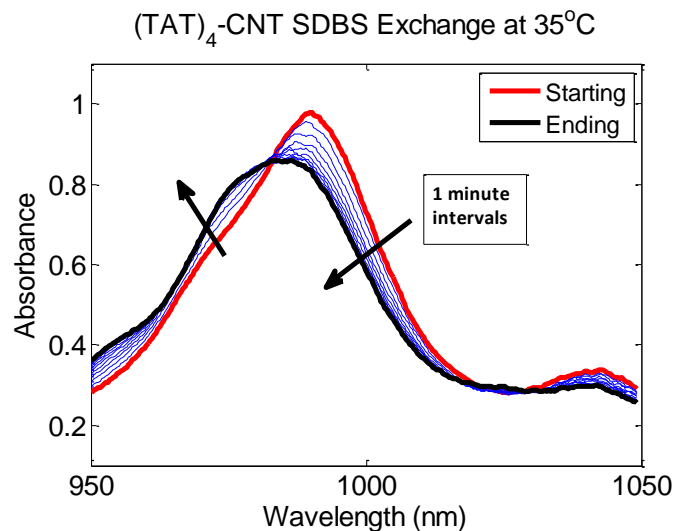


**Figure 2.18.** Proposed model to explain differences between  $(TAT)_4$  and its relatives. Stability may increase for sequences with the ability to ligate ends of adjoining strands through hydrogen bonds and AT-quartet formation.

#### 2.4.2.1 Effect of Urea on DNA-SDBS Exchange.

One hypothesis to explain the differences in the observed rate constants among sequences of a given length is the existence of extended inter-strand hydrogen bonding.

If a particular sequence contains DNA bases that are able to hydrogen bond to a neighboring strand, hybrid stability should be greatly increased. A simple way to test this hypothesis is to introduce an agent that interferes with hydrogen bond acceptors and donors in nucleic acids. Urea has been used extensively in the past, at concentrations in the range 1-12 M, to disrupt hydrogen bonding in the double-stranded DNA molecule. In figure 2.19a and b, (TAT)<sub>4</sub>-SWCNT hybrids are subjected to 0.1 % SDCBS at 35°C with and without urea at a concentration of 3M for 10 minutes incubation. Notice the qualitatively faster 990 nm peak decay in the solution containing urea, suggesting that the breaking of DNA base hydrogen bonds decreases the overall stability of the hybrid. Moreover, equilibrium fraction of defect-free SWCNTs (Stage I) decreased from 0.97 to 0.89. Likewise, the reaction rate (Stage 2) increased from 0.2 to 0.6, a factor of three times faster.

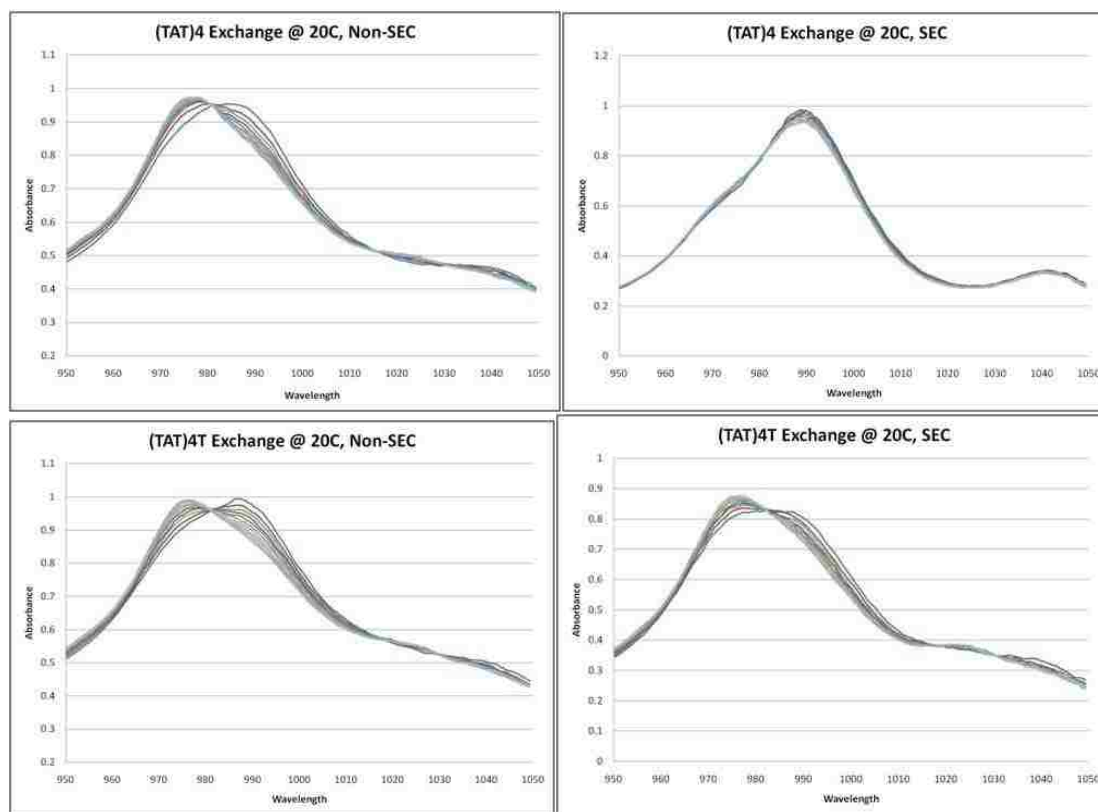


**Figure 2.19.** (TAT)<sub>4</sub>-SWCNT hybrids, at a concentration equal to that used in section 3, were incubated with 0.1 wt% SDBS at 35°C without (a) and with (b) 3 M Urea for 10 minutes.

#### 2.4.2.2 SEC vs. non-SEC Samples.

All the data presented so far are on samples subjected to size-exclusion chromatography using an HPLC instrument (see section 2.2). In view of the strong length-dependence of kinetics, this process is critically important. It also removes any impurities and free DNA in the sample. However, because ion-exchange (IEX) separations have often been conducted using samples that were not subjected to SEC

separation and purification, it is pertinent to ask how the SEC process modifies the dispersion. We have observed that recovery of the SWCNT sample can strongly depend on DNA length, e.g. longer DNA strands have higher recovery in the resulting SEC fractions. As a control experiment, we performed surfactant exchange on as-prepared samples prior to purification and length-sorting by SEC. We find that these samples demonstrate quite different kinetics than their SEC counterparts. The (TAT)<sub>4</sub> non-SEC sample converted to SDBS-SWCNT an order of magnitude faster than its SEC version. Furthermore, (TAT)<sub>4</sub>T non-SEC conversion was a bit slower than that of the respective SEC sample, and even slightly slower than the non-SEC recognition sequence (TAT)<sub>4</sub>, (Figure 2.20). These results suggest that SEC sorting, critical for our experiments, modifies the population in DNA-SWCNT dispersions. SEC samples are of controlled length, while non-SEC samples contain a broad range of lengths (100 - 500+ nm). The relatively low recovery after SEC suggests that this process removes a great number of poorly wrapped DNA-SWCNT (greater than 90% of the hybrids) leaving only the 'best' in the resulting fractions. This experiment further highlights the importance of careful sample preparation, i.e., the use of SEC in this instance, to obtain well-controlled starting samples.



**Figure 2.20.** Surfactant exchange studies for non-SEC (left) and SEC (right) samples using (TAT)<sub>4</sub> (top) and (TAT)<sub>4</sub>T (bottom) sequences. In SEC samples, (TAT)<sub>4</sub> is the stronger binding of the two sequences, while the trend is reversed in non-SEC samples.

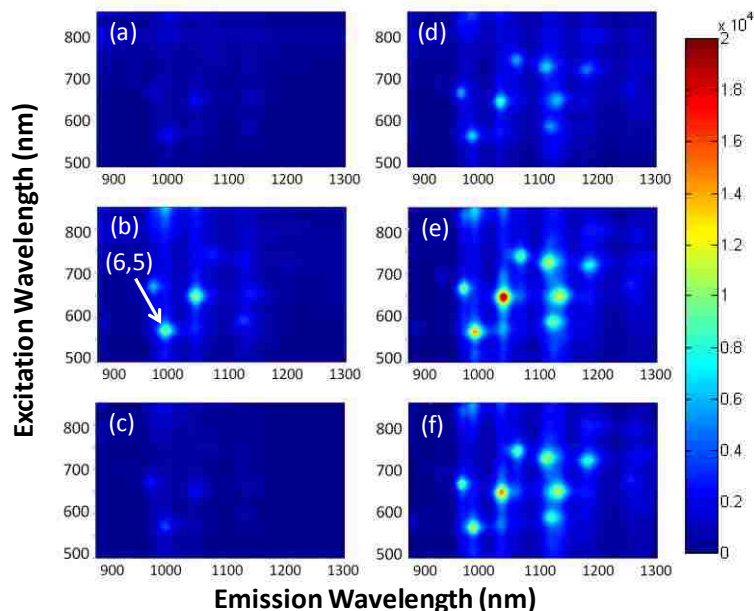
## 2.5 Fluorescence Measurements on (6,5) Recognition Sequences\*

In a parallel study, fluorescence spectroscopy was used to demonstrate the superior dispersing capability of the (6,5) recognition sequence, (TAT)<sub>4</sub>. Three sequences, (TAT)<sub>3</sub>TA, (TAT)<sub>4</sub>, and (TAT)<sub>4</sub>T, each differing from the others by only one DNA base, were used to disperse *HiPCo* tubes followed by fluorescence spectroscopic analysis. *HiPCo* tubes contain nanotube species of a broader range of diameters than CoMoCAT, which helps better to demonstrate the selectivity of the recognition sequences. A 2D fluorescence map can simultaneously provide spectral information for

---

\* This work has been performed by Xiaomin Tu and Ming Zheng at the National Institute of Standards and Technology

each semiconducting species in a sample, allowing the investigation of individual chirality nanotubes as well as the quality of the dispersion as a whole. From the fluorescence maps (Figure 2.21b), we find that nanotubes wrapped by (TAT)<sub>4</sub> are the brightest among the three samples (Figure 2.21a-c). There are multiple factors that could contribute to the brighter fluorescence for (TAT)<sub>4</sub>. Besides the concentration of the nanotubes, the fluorescence of carbon nanotubes is extremely sensitive to the environment, and different DNA sequences may adopt varied structures to influence the fluorescence intensity. To eliminate the effect of DNA-wrapping on the fluorescence signals, DNA was replaced on the SWCNT surface by addition of SDC to provide an equivalent environment for all nanotubes. SDC can effectively replace DNA on the nanotube surface and enhance the fluorescence of carbon nanotubes. After the addition of SDC (figure 2.21d-e), the overall fluorescence intensities increased for all three samples. However, nanotubes in the sample initially dispersed by (TAT)<sub>4</sub> were still the brightest, indicative of the highest concentration of nanotubes present in the sample. Thus, it is reasonable to conclude that higher nanotube fluorescence signals in (TAT)<sub>4</sub> is resulted from the better dispersion efficiency of the recognition sequence. It is possible that a stable structure of (TAT)<sub>4</sub> on the nanotube surface (e.g., Fig. 2.18) allows a greater quantity of tubes to be dispersed. Dispersion efficiency is an important parameter in determining DNA sequences that support separation. Good dispersion efficiency is critical for effective separation. The fluorescence results complement the kinetic data on (TAT)<sub>4</sub>, demonstrating its unique properties that enable the nanotube purification.



**Figure 2.21.** 2D photoluminescence map on (a,d)  $(TAT)_3TA$ ; (b,e)  $(TAT)_4$ ; (c,f)  $(TAT)_4T$ –dispersed HiPco nanotubes. Sample (a-c) are in DNA, and (d-f) are measured in 1 wt% SDC.

## 2.6 Conclusions

In this study, we have investigated the DNA sequence-specific binding strength and selectivity for the (6,5) carbon nanotube. Using previously reported recognition DNA strands, a surfactant-exchange method was employed to explore quantitatively differences among closely related sequences. Among certain families of short DNA strands, e.g.  $(TAT)_3TA$ ,  $(TAT)_4$ , and  $(TAT)_4T$ , the correlation between DNA-SWCNT binding strength and DNA length was non-monotonic. The (6,5) recognition sequence  $(TAT)_4$  was observed to bind  $\sim 20$  times stronger than either  $(TAT)_3TA$  or  $(TAT)_4T$ , suggesting the formation of a stable secondary structure in the recognition sequence. Furthermore, a two-stage process was observed in which a certain fraction of DNA-SWCNTs, presumably with existing defects in their DNA coverage, were immediately exchanged with SDBS, followed by a slower process, presumably proceeding at a rate



limited by time-dependent defect nucleation. Recognition sequences were found to have the lowest concentration of initially defective DNA-SWCNTs as well as the lowest rate constants for subsequent kinetics of conversion. These data, coupled with 2D photoluminescence studies, shed light on the superior SWCNT dispersing capabilities of recognition DNA sequences. Other techniques, such as capillary electrophoresis (CE) or direct imaging of individual tubes, may prove just as beneficial in determining DNA-SWCNT binding strengths and could be the subject of future research. In this study we have focused on a single SWCNT chirality, (6,5). A natural follow-up study would be to examine the differential binding ability of a given DNA sequence on different SWCNT chiralities. It will also be interesting to attempt direct monitoring of DNA dissociation from SWCNTs as this will confirm or dispute many of the hypotheses formulated.

## **2.7 Acknowledgement**

This work, shown explicitly in Section 2.5, was performed with the collaboration of Xiaomin Tu at NIST in Gaithersburg, MD. I would also like to thank the assistance of Anand Jagota and Ming Zheng for serving as mentors in this work. Finally, I acknowledge Bryan Postelnek of Lehigh University for his assistance in the surfactant exchange data collection and analysis. This work was funded by the National Science Foundation through grants CMS-0609050 and CMMI-1014960.

## 2.8 References

- (1) Ajayan, P. M., *Chem. Rev.* 1999, 99, 1787-1800.
- (2) Baughman, R. H.; Zakhidov, A. A.; de Heer, W. A., *Science* 2002, 297, 787-792.
- (3) Jorio, A.; Dresselhaus, G.; Dresselhaus, M. S., Springer: 2008.
- (4) Saito, R.; Dresselhaus, G.; Dresselhaus, M. S., Imperial College Press: London, 1999.
- (5) Bahr, J. L.; Mikkelsen, E. T.; Bronikowski, M. J.; Smalley, R. E.; Tour, J. M., *Chem. Commun.* 2001, 193-194.
- (6) Furtado, C. A.; Kim, U. J.; Gutierrez, H. R.; Pan, L.; Dickey, E. C.; Eklund, P. C., *J. Am. Chem. Soc.* 2004, 126, 6095-6105.
- (7) Bachilo, S. M.; Strano, M. S.; Kittrell, C.; Hauge, R. H.; Smalley, R. E.; Weisman, R. B., *Science* 2002, 298, 2361-2366.
- (8) Moore, V. C.; Strano, M. S.; Haroz, E. H.; Hauge, R. H.; Smalley, R. E., *Nano Lett.* 2003, 3 (10), 1379-1382.
- (9) O'Connell, M. J.; Bachilo, S. M.; Huffman, C. B.; Moore, V. C.; Strano, M. S.; Haroz, E. H.; Rialon, K. L.; Boul, P. J.; Noon, W. H.; Kittrell, C.; Ma, J.; Hauge, R. H.; Weisman, R. B.; Smalley, R. E., *Science* 2002, 297, 593-596.
- (10) Dieckmann, G. R.; Dalton, A. B.; Johnson, P. A.; Razal, J.; Chen, J.; Giordano, G. M.; Munoz, E.; Musselman, I. H.; Baughman, R. H.; Draper, R. K., *J. Am. Chem. Soc.* 2003, 125, 1770-1777.
- (11) Kam, N. W. S.; Liu, Z.; Dai, H., *J. Am. Chem. Soc.* 2005, 127, 12492-12493.
- (12) Kam, N. W. S.; O'Connell, M. J.; Wisdom, J. A.; Dai, H., *Proc. Natl. Acad. Sci.* 2005, 102, 11600-11605.
- (13) Zheng, M.; Jagota, A.; Semke, E. D.; Diner, B. A.; Mclean, S. R. L.; Richardson, R. E.; Tassi, N. G., *Nature Materials* 2003, 2, 338-343.
- (14) Huang, X.; Mclean, S. R. L.; Zheng, M., *Analytical Chemistry* 2005, 77 (19), 6225-6228.
- (15) Zheng, M.; Jagota, A.; Strano, M. S.; Santos, A. P.; Barone, P.; Chou, S. G.; Diner, B. A.; Dresselhaus, M. S.; Mclean, S. R. L.; Onoa, G. B.; Samsonidze, G. G.; Semke, E. D.; Usrey, M.; Walls, D. J., *Science* 2003, 302 (5650), 1545-1548.
- (16) Tu, X. M.; Manohar, S.; Jagota, A.; Zheng, M., *Nature* 2009, 460 (7252), 250-253.
- (17) Khripin, C. Y.; Manohar, S.; Zheng, M.; Jagota, A., *Journal of Physical Chemistry C* 2009, 113 (31), 13616-13621.
- (18) Roxbury, D.; Manohar, S.; Jagota, A., *J. Phys. Chem. C* 2010, 114 (31), 13267-13276.
- (19) Manohar, S.; Tang, T.; Jagota, A., *Journal of Physical Chemistry C* 2007, 111 (48), 17835-17845.
- (20) McCarthy, B.; Coleman, J. N.; Czerw, R.; Dalton, A. B.; Panhuis, M. I. H.; Maiti, A.; Drury, A.; Bernier, P.; Nagy, J. B.; Lahr, B.; Byrne, H. J.; Carroll, D. L.; Blau, W. J., *Journal of Physical Chemistry B* 2002, 106 (9), 2210-2216.
- (21) Sowerby, S. J.; Cohn, C. A.; Heckl, W. M.; Holm, N. G., *Proceedings of the National Academy of Sciences of the United States of America* 2001, 98 (3), 820-822.
- (22) Sowerby, S. J.; Edelwirth, M.; Heckl, W. M., *Journal of Physical Chemistry B* 1998, 102 (30), 5914-5922.

- (23) Tao, N. J.; Shi, Z., *Journal of Physical Chemistry* 1994, 98 (5), 1464-1471.
- (24) Mamdouh, W.; Dong, M. D.; Xu, S. L.; Rauls, E.; Besenbacher, F., *Journal of the American Chemical Society* 2006, 128 (40), 13305-13311.
- (25) Mamdouh, W.; Kelly, R. E. A.; Dong, M. D.; Kantorovich, L. N.; Besenbacher, F., *Journal of the American Chemical Society* 2008, 130 (2), 695-702.
- (26) Sowerby, S. J.; Edelwirth, M.; Reiter, M.; Heckl, W. M., *Langmuir* 1998, 14 (18), 5195-5202.
- (27) Edelwirth, M.; Freund, J.; Sowerby, S. J.; Heckl, W. M., *Surface Science* 1998, 417 (2-3), 201-209.
- (28) Sowerby, S. J.; Stockwell, P. A.; Heckl, W. M.; Petersen, G. B., *Origins of Life and Evolution of the Biosphere* 2000, 30 (1), 81-99.
- (29) Gu, J. D.; Leszczynski, J., *Journal of Physical Chemistry A* 2000, 104 (31), 7353-7358.
- (30) Otero, R.; Schock, M.; Molina, L. M.; Laegsgaard, E.; Stensgaard, I.; Hammer, B.; Besenbacher, F., *Angewandte Chemie-International Edition* 2005, 44 (15), 2270-2275.
- (31) Xu, S. L.; Dong, M. D.; Rauls, E.; Otero, R.; Linderoth, T. R.; Besenbacher, F., *Nano Letters* 2006, 6 (7), 1434-1438.
- (32) Johnson, A. T.; Johnson, C.; Klein, M. L., *Small* 2010, 6 (1), 31-34.
- (33) Manohar, S.; Mantz, A. R.; Bancroft, K. E.; Hui, C. Y.; Jagota, A.; Vezenov, D. V., *Nano Lett.* 2008, 8 (12), 4365-4372.
- (34) Shi, X.; Kong, Y.; Zhao, Y.; Gao, H., *Acta Mechanica Sinica* 2005, 21 (3), 249-256.
- (35) Manohar, S. DNA-SWCNT Interactions. Lehigh, Bethlehem, 2010.
- (36) Albertorio, F.; Hughes, M. E.; Golovchenko, J. A.; Branton, D., *Nanotechnology* 2009, 20.
- (37) Cathcart, H.; Nicolosi, V.; Hughes, J. M.; Blau, W. J.; Kelly, J. M.; Quinn, S. J.; Coleman, J. N., *J. Am. Chem. Soc.* 2008, 130, 12734-12744.
- (38) Coleman, J. N., *Adv. Func. Mater.* 2009, 19, 3680-3695.
- (39) Islam, M. F.; Rojas, E.; Bergey, D. M.; Johnson, A. T.; Yodh, A. G., *Nano Lett.* 2003, 3 (2), 269-273.
- (40) Choi, J. H.; Strano, M. S., *Applied Physics Letters* 2007, 90, 223114.
- (41) Eyring, H., *Chem. Rev.* 1935, 3, 107-115.
- (42) Chao, C.Y.; Carvajal, D.; Szleifer, I.; Shull, K.R., *Langmuir* 2008, 24, 2472-2478.
- (43) Chou, S. G.; Ribeiro, H. B.; Barros, E. B.; Santos, A. P.; Nezich, D.; Samsonidze, G. G.; Fantini, C.; Pimenta, M. A.; Jorio, A.; Filho, F. P.; Dresselhaus, G.; Dresselhaus, M. S.; Saito, R.; Zheng, M.; Onoa, G. B.; Semke, E. D.; Swan, A. K.; Unlu, M. S.; Goldberg, B. B., *Chem. Phys. Lett.* 2004, 397, 296-301.
- (44) Matarredona, O.; Rhoads, H.; Li, Z.; Harwell, J. H.; Balzano, L.; Resasco, D. E., *J. Phys. Chem. B* 2003, 107, 13357-13367.
- (45) Bustamante, C.; Bryant, Z.; Smith, S. B., *Nature* 2003, 421, 423-427.
- (46) Tinland, B.; Pluen, A.; Sturm, J.; Weill, G., *Macromolecules* 1997, 30 (19), 5763-5765.
- (47) Stofer, E.; Chipot, C.; Lavery, R., *J. Am. Chem. Soc.* 1999, 121, 9503-9508.
- (48) Saenger, W., Springer-Verlag: New York, 1984.
- (49) Grigoryan, G., Kim, Y.H., Acharya, R., Axelrod, K., Jain, R.M., Willis, L., Drndic, M., Kikkawa, J.M., DeGrado, W.F., *Science* 2010, 332, 6033, 1071.

## 2.9 Appendix

### 2.9.1 Preliminary Models for Competitive Adsorption of Surfactant and DNA on a SWCNT

Upon initial observation of the surfactant-induced displacement reaction, it was thought that the process was governed by an equilibrium adsorption isotherm model. Competitive adsorption models were investigated and an attempt was made to fit the experimental data. In the first derivation, a statistical mechanics approach is developed to model two-components of the same size which compete for surface sites on a particular substrate. In the second derivation, a chemical reaction approach is taken to model the competitive adsorption between two molecules of differing sizes to a substrate.

#### Statistical Mechanics Adsorption Model

To begin, let  $p \rightarrow$  SDS,  $q \rightarrow$  DNA, and  $s \rightarrow$  SWCNT. Therefore, there are  $N_s$  total sites on the SWCNT surface,  $n_{ps}$  SDS molecules, and  $n_{qs}$  DNA molecules. The number of allowable configurations is then given by:

$$W_s = \frac{N_s!}{n_{ps}!n_{qs}!(N_s - n_{ps} - n_{qs})!} \quad (2.25)$$

with the partition function:

$$Z = \exp\left(-\frac{n_{ps}\Delta\mu_p - n_{qs}\Delta\mu_q}{k_B T}\right) \cdot W_s \quad (2.26)$$

The Gibbs free energy of the surface is:

$$\begin{aligned} G_s &= -k_B T \ln Z \\ G_s &= n_{ps}\Delta\mu_p + n_{qs}\Delta\mu_q - k_B T \ln W_s \end{aligned} \quad (2.27)$$

Where,

$$\ln W_s = \ln N_s! - \ln n_{ps}! - \ln n_{qs}! - \ln(N_s - n_{ps} - n_{qs})! \quad (2.28)$$

Applying Stirling's Approximation:

$$\ln N! \approx N \ln N - N \quad (2.29)$$

Then,

$$\begin{aligned} \ln W_s &\approx N_s \ln N_s - N_s - n_{ps} \ln n_{ps} + n_{ps} - n_{qs} \ln n_{qs} + n_{qs} \\ &\quad - (N_s - n_{ps} - n_{qs}) \ln (N_s - n_{ps} - n_{qs}) + (N_s - n_{ps} - n_{qs}) \\ &= -N_s \ln \frac{N_s - n_{ps} - n_{qs}}{N_s} - n_{ps} \ln \frac{n_{ps}}{N_s - n_{ps} - n_{qs}} - n_{qs} \ln \frac{n_{qs}}{N_s - n_{ps} - n_{qs}} \end{aligned} \quad (2.30)$$

$$\ln W_s = -(N_s - n_{ps} - n_{qs}) \ln \left( \frac{N_s - n_{ps} - n_{qs}}{N_s} \right) - n_{ps} \ln \frac{n_{ps}}{N_s} - n_{qs} \ln \frac{n_{qs}}{N_s}$$

Solving for free energy:

$$\begin{aligned} G_s &= n_{ps} \Delta \mu_p^{\blacksquare} + n_{qs} \Delta \mu_q^{\blacksquare} + k_B T (N_s - n_{ps} - n_{qs}) \ln \left( \frac{N_s - n_{ps} - n_{qs}}{N_s} \right) \\ &\quad + k_B T n_{ps} \ln \frac{n_{ps}}{N_s} + k_B T n_{qs} \ln \frac{n_{qs}}{N_s} \end{aligned} \quad (2.31)$$

The chemical potential for p on the surface is given by:

$$\begin{aligned} \frac{\partial G_s}{\partial n_{ps}} &= \Delta \mu_p^{\blacksquare} - k_B T \ln \frac{N_s - n_{ps} - n_{qs}}{N_s} + k_B T \left( \frac{N_s - n_{ps} - n_{qs}}{N_s - n_{ps} - n_{qs}} \right) N_s \frac{-1}{N_s} \\ &\quad + k_B T \ln \frac{n_{ps}}{N_s} + k_B T \frac{n_{ps}}{n_{ps}} \frac{N_s}{N_s} \end{aligned} \quad (2.32)$$

$$\mu_{ps}^{\blacksquare} = \Delta \mu_p^{\blacksquare} + k_B T \left( \ln \frac{n_{ps}}{N_s} - \ln \frac{N_s - n_{ps} - n_{qs}}{N_s} \right)$$

similarly for q:

$$\mu_{qs}^{\blacksquare} = \Delta \mu_q^{\blacksquare} + k_B T \left( \ln \frac{n_{qs}}{N_s} - \ln \frac{N_s - n_{ps} - n_{qs}}{N_s} \right) \quad (2.33)$$

The previous derivations are for the adsorbed phase (on the SWCNT). The same procedure must be repeated for the bulk phase (aqueous medium). Similar expressions for allowable configurations and partition function are given by:

$$W_B = \frac{N_B!}{n_{pB}!n_{qB}!(N_B - n_{pB} - n_{qB})!} \quad (2.34)$$

$$Z_B = \exp\left(-\frac{n_{pB}\Delta\mu_p^\circ - n_{qB}\Delta\mu_q^\circ}{k_B T}\right) \cdot W_B \quad (2.35)$$

The Gibbs free energy in the bulk is given by:

$$G_s = -k_B T \ln Z_B$$

$$G_s = k_B T \left[ n_{pB} \ln \frac{n_{pB}}{N_B} + n_{qB} \ln \frac{n_{qB}}{N_B} + (N_B - n_{pB} - n_{qB}) \ln \frac{(N_B - n_{pB} - n_{qB})}{N_B} \right] \quad (2.36)$$

Additionally, the chemical potential of p in bulk:

$$\mu_{pB} = \frac{\partial G_B}{\partial n_{pB}} = k_B T \ln \frac{n_{pB}}{N_B} + k_B T \frac{n_{pB}}{n_{pB}} \frac{N_B}{N_B} - k_B T \ln \frac{N_B - n_{pB} - n_{qB}}{N_B} - k_B T \frac{N_B - n_{pB} - n_{qB}}{N_B - n_{pB} - n_{qB}} \frac{N_B}{N_B}$$

$$\mu_{pB} = k_B T \left( \ln \frac{n_{pB}}{N_B} - \ln \frac{N_B - n_{pB} - n_{qB}}{N_B} \right) \quad (2.37)$$

Similarly, the chemical potential of q in bulk:

$$\mu_{qB} = k_B T \left( \ln \frac{n_{qB}}{N_B} - \ln \frac{N_B - n_{pB} - n_{qB}}{N_B} \right) \quad (2.38)$$

Making appropriate chemical potentials equal at equilibrium:

$$\mu_{ps} = \mu_{pB}$$

$$\mu_{qs} = \mu_{qB}$$

$$\begin{aligned} \mu_p^\blacksquare + k_B T \ln \frac{n_{ps}}{N_s - n_{ps} - n_{qs}} &= k_B T \ln \frac{n_{pB}}{N_B - n_{pB} - n_{qB}} \approx k_B T \ln \frac{n_{pB}}{N_B} \\ \mu_q^\blacksquare + k_B T \ln \frac{n_{qs}}{N_s - n_{ps} - n_{qs}} &= k_B T \ln \frac{n_{qB}}{N_B} \end{aligned} \quad (2.39)$$

It is then assumed that  $N_b \gg n_{pB}, n_{qB}$ . Now, simplifying and rearranging:

$$\begin{aligned} \frac{n_{ps}}{N_s - n_{ps} - n_{qs}} &= \frac{n_{pB}}{N_B} \exp\left(-\frac{\Delta\mu_p^\blacksquare}{k_B T}\right) \\ \frac{n_{ps}/N_s}{1 - \frac{n_{ps}}{N_s} - \frac{n_{qs}}{N_s}} &= \frac{n_{pB}}{N_B} \exp\left(-\frac{\Delta\mu_p^\blacksquare}{k_B T}\right) \end{aligned} \quad (2.40)$$

A few variables are now redefined:

$$\begin{aligned} \frac{n_{ps}}{N_s} &= \frac{c_{ps}}{c_s^*} \\ \frac{n_{qs}}{N_s} &= \frac{c_{qs}}{c_s^*} \\ \frac{n_{pB}}{N_B} &= \frac{c_{pB}}{c_B^*} \\ \frac{n_{qB}}{N_B} &= \frac{c_{qB}}{c_B^*} \end{aligned} \quad (2.41)$$

The redefined variables are then plugged into the adsorption equations:

$$\begin{aligned} \frac{\frac{c_{ps}}{c_s^*}}{1 - \frac{c_{ps}}{c_s^*} - \frac{c_{qs}}{c_s^*}} &= \frac{c_{pB}}{c_B^*} \exp\left(-\frac{\Delta\mu_p^\blacksquare}{k_B T}\right) \\ \frac{c_{ps}}{c_s^*} \left(1 + \frac{c_{pB}}{c_B^*} \exp\left(-\frac{\Delta\mu_p^\blacksquare}{k_B T}\right)\right) + \frac{c_{qs}}{c_s^*} \frac{c_{pB}}{c_B^*} \exp\left(-\frac{\Delta\mu_p^\blacksquare}{k_B T}\right) &= \frac{c_{pB}}{c_B^*} \exp\left(-\frac{\Delta\mu_p^\blacksquare}{k_B T}\right) \end{aligned} \quad (2.42)$$

Similarly for q:

$$\frac{c_{qs}}{c_s^*} \left( 1 + \frac{c_{pB}}{c_B^*} \exp\left(-\frac{\Delta\mu_q}{k_B T}\right) \right) + \frac{c_{ps}}{c_s^*} \frac{c_{pB}}{c_B^*} \exp\left(-\frac{\Delta\mu_q}{k_B T}\right) = \frac{c_{pB}}{c_B^*} \exp\left(-\frac{\Delta\mu_q}{k_B T}\right) \quad (2.43)$$

To solve the coupled equations, x and y are defined as such:

$$\frac{c_{ps}}{c_s^*} = x, \quad \frac{c_{qs}}{c_s^*} = y \quad (2.44)$$

which results in the following simple equations:

$$\begin{aligned} xA + yB &= B \\ xD + yC &= D \end{aligned} \quad (2.45)$$

Upon Solving:

$$\begin{aligned} y &= \frac{D}{1+B+D} \\ x &= \frac{B}{1+B+D} \end{aligned} \quad (2.46)$$

Where,

$$\begin{aligned} B &= \frac{c_{pB}}{c_B^*} \exp\left(\frac{-\Delta\mu_p}{k_B T}\right) \\ D &= \frac{c_{qB}}{c_B^*} \exp\left(\frac{-\Delta\mu_q}{k_B T}\right) \end{aligned} \quad (2.47)$$

Therefore, we arrive at the following expressions, in accordance with published derivations,<sup>1</sup>

---

<sup>1</sup> Berry, R. S.; Rice, S. A.; Ross, J., Second ed.; Oxford University Press: New York, 2000.

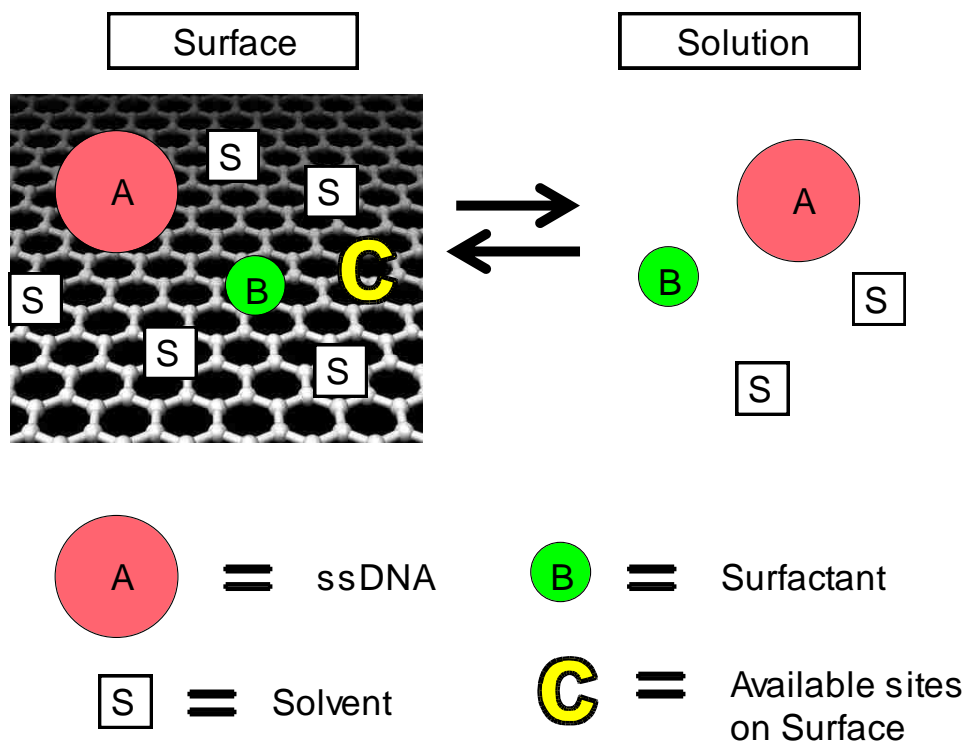


$$\frac{c_{ps}}{c_s^*} = \frac{\frac{c_{pB}}{c_B^*} \exp\left(-\frac{\Delta\mu_p}{k_B T}\right)}{1 + \frac{c_{pB}}{c_B^*} \exp\left(-\frac{\Delta\mu_p}{k_B T}\right) + \frac{c_{qB}}{c_B^*} \exp\left(-\frac{\Delta\mu_q}{k_B T}\right)} \quad (2.48)$$

$$\frac{c_{qs}}{c_s^*} = \frac{\frac{c_{qB}}{c_B^*} \exp\left(-\frac{\Delta\mu_q}{k_B T}\right)}{1 + \frac{c_{pB}}{c_B^*} \exp\left(-\frac{\Delta\mu_p}{k_B T}\right) + \frac{c_{qB}}{c_B^*} \exp\left(-\frac{\Delta\mu_q}{k_B T}\right)}$$

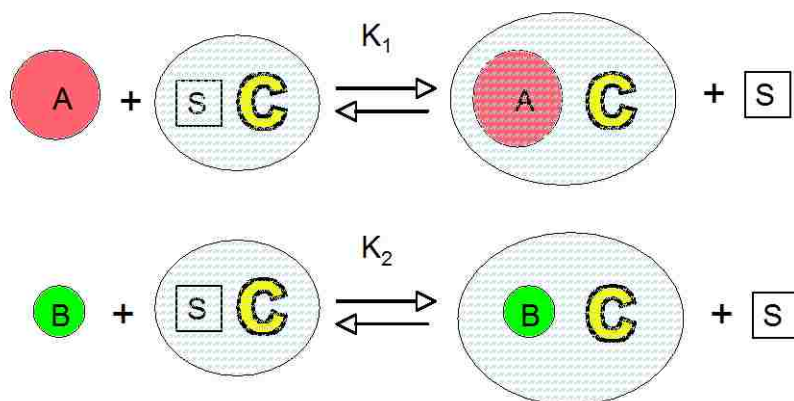
### **Chemical Reaction Adsorption Model**

In the following derivation, two molecules of differing size (A and B) are able to adsorb onto available sites (C) on an unrolled SWCNT (graphene sheet). Also present are solvent molecules (S). It is assumed that there is a reversible reaction between a surface-adsorbed state and a bulk solution state. Figure 2.22 is a schematic of the adsorption model.



**Figure 2.22.** Schematic showing the competitive adsorption between DNA (A) and surfactant (B) to find available surface sites (C) on an unrolled SWCNT. There is an equilibrium between surface-adsorbed and bulk solution states.

In this model, there are two parallel reversible reactions. This is again shown schematically in Figure 2.23.



**Figure 2.23.** Chemical equations for described competitive adsorption model.

These two equations have equilibrium constants as follows:

$$\begin{aligned}
 K_1 &= \frac{[AC][S]}{[A][C]} \\
 K_2 &= \frac{[BC][S]}{[B][C]}
 \end{aligned}
 \tag{2.49}$$

The following terms are then redefined:

$$\begin{aligned}
 [AC] &\rightarrow C_A^s \\
 [BC] &\rightarrow C_B^s \\
 [A] &\rightarrow C_A^b \\
 [B] &\rightarrow C_B^b \\
 [S] &\rightarrow C_s^* \\
 [C] &\rightarrow C_s^* - rC_A^s - C_B^s
 \end{aligned}
 \tag{2.50}$$

where the subscripts 'b' and 's' denote bulk and surface, respectively. The number of available sites on the surface is equal to the total number of sites on the surface ( $C_s^*$ ) minus the number of A molecules on the surface times the A:B size ratio, 'r', minus the number of B molecules on the surface. Upon plugging this in,  $K_1$  and  $K_2$  are rewritten as:

$$\begin{aligned}
 K_1 &= \exp\left(-\frac{\Delta\mu_A}{k_B T}\right) = \frac{C_A^s C_b^*}{C_A^b (C_s^* - rC_A^s - C_B^s)} \\
 K_2 &= \exp\left(-\frac{\Delta\mu_B}{k_B T}\right) = \frac{C_B^s C_b^*}{C_B^b (C_s^* - rC_A^s - C_B^s)}
 \end{aligned}
 \tag{2.51}$$

It is now desirable to solve for the fractional surface coverage of A and B represented by the ratios ( $C_A^s/C_s^*$ ) and ( $C_B^s/C_s^*$ ), respectively. After some manipulation, we have:

$$\frac{C_A^b}{C_b^*} \exp\left(-\frac{\Delta\mu_A}{k_B T}\right) = \frac{C_A^s / C_s^*}{1 - r \frac{C_A^s}{C_s^*} - \frac{C_B^s}{C_s^*}}$$

$$\frac{C_A^b}{C_b^*} \exp\left(-\frac{\Delta\mu_A}{k_B T}\right) - r \frac{C_A^s}{C_s^*} \frac{C_A^b}{C_b^*} \exp\left(-\frac{\Delta\mu_A}{k_B T}\right) - \frac{C_B^s}{C_s^*} \frac{C_A^b}{C_b^*} \exp\left(-\frac{\Delta\mu_A}{k_B T}\right) = \frac{C_A^s}{C_s^*} \quad (2.52)$$

$$\frac{C_A^s}{C_s^*} \left(1 + r \frac{C_A^b}{C_b^*} \exp\left(-\frac{\Delta\mu_A}{k_B T}\right)\right) + \frac{C_B^s}{C_s^*} \frac{C_A^b}{C_b^*} \exp\left(-\frac{\Delta\mu_A}{k_B T}\right) = \frac{C_A^b}{C_b^*} \exp\left(-\frac{\Delta\mu_A}{k_B T}\right)$$

Similarly,

$$\frac{C_B^s}{C_s^*} \left(1 + \frac{C_B^b}{C_b^*} \exp\left(-\frac{\Delta\mu_B}{k_B T}\right)\right) + r \frac{C_A^s}{C_s^*} \frac{C_B^b}{C_b^*} \exp\left(-\frac{\Delta\mu_B}{k_B T}\right) = \frac{C_B^b}{C_b^*} \exp\left(-\frac{\Delta\mu_B}{k_B T}\right) \quad (2.53)$$

To solve the coupled equations, the following variables are redefined:

$$\frac{C_A^s}{C_s^*} = x$$

$$\frac{C_B^s}{C_s^*} = y$$

$$\frac{C_A^b}{C_b^*} \exp\left(-\frac{\Delta\mu_A}{k_B T}\right) = A$$

$$\frac{C_B^b}{C_b^*} \exp\left(-\frac{\Delta\mu_B}{k_B T}\right) = B \quad (2.54)$$

Therefore, the resulting equations follow the form:

$$x(1 + rA) + yA = A$$

$$xrB + y(1 + B) = B \quad (2.55)$$

Finally, the competitive adsorption isotherm equations are written as follows:

$$\frac{C_A^s}{C_s^*} = \frac{\frac{C_A^b}{C_b^*} \exp\left(-\frac{\Delta\mu_A}{k_B T}\right)}{1 + r \frac{C_A^b}{C_b^*} \exp\left(-\frac{\Delta\mu_A}{k_B T}\right) + \frac{C_B^b}{C_b^*} \exp\left(-\frac{\Delta\mu_B}{k_B T}\right)} \quad (2.56)$$

$$\frac{C_B^s}{C_s^*} = \frac{\frac{C_B^b}{C_b^*} \exp\left(-\frac{\Delta\mu_B}{k_B T}\right)}{1 + r \frac{C_A^b}{C_b^*} \exp\left(-\frac{\Delta\mu_A}{k_B T}\right) + \frac{C_B^b}{C_b^*} \exp\left(-\frac{\Delta\mu_B}{k_B T}\right)}$$

With these final equations, it is observed that the surface concentration of A depends on the bulk concentrations of both A and B, and their respective chemical potentials. However, it was found experimentally that surfactant coverage on the SWCNTs did not depend upon how much DNA was present in the bulk (see figure 2.5). Additionally, the previous equilibrium model makes the incorrect assumption that a single strand of DNA must be completely desorbed before surfactant is able to adsorb. In reality, the polymeric nature of DNA will enable surfactant to begin adsorbing to the surface as soon as the first nucleotide of DNA desorbs. In effect, a single strand of DNA can be partially desorbed from the surface. This led to the realization that the observed process is not in equilibrium, but rather is kinetic. Because of this, Eyring kinetics were used to interpret the experimental data quantitatively; the equilibrium adsorption models are presented here in the Appendix for completeness.

## 2.9.2 Reaction Kinetics, Transition State Theory, and a Derivation of the Eyring Equation

Transition state theory, the quantitative data analysis method used in section 2.4.2, is employed to interpret the observed surfactant-induced displacement reaction. Here, a brief derivation of the Eyring equation is presented using transition state theory.<sup>41</sup>

Consider the bimolecular reaction where  $A$  and  $B$  are the reactants, and  $C$  is the product.



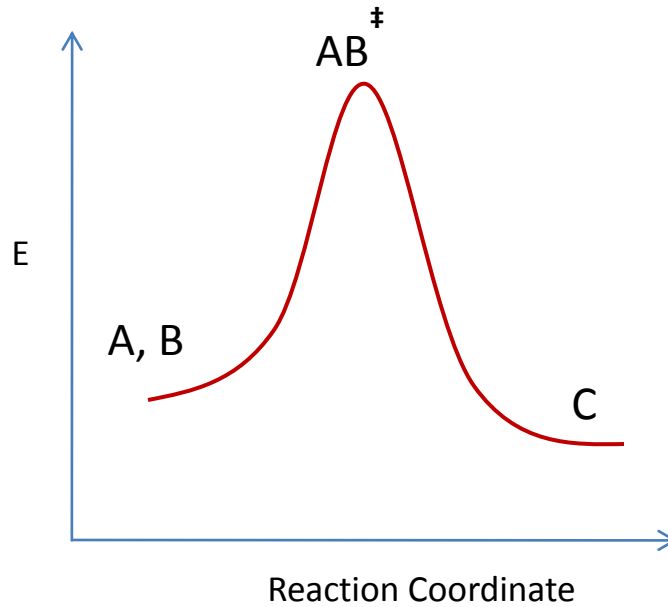
If this were treated as an elementary reaction, then the rate of production of  $C$  should depend on the concentrations of  $A$  and  $B$ .

$$\frac{d[C]}{dt} = k[A][B] \quad (2.58)$$

Transition state theory assumes that there is an instantaneous intermediary step in which a transition complex,  $AB^\ddagger$ , is formed.



A schematic drawing is shown in Figure 2.24 representing the energy associated with the reaction. The height of the barrier governs the overall rate of the reaction. Therefore, the formation of the  $AB$  complex from reactants  $A$  and  $B$  is the rate determining step.



**Figure 2.24.** Reaction coordinate energy diagram for a standard bimolecular reaction.

From equation 2.59, the rate of change in the concentration of AB complex can be found:

$$\frac{d[AB^\ddagger]}{dt} = k_1[A][B] - k_{-1}[AB^\ddagger] - k_2[AB^\ddagger] \quad (2.60)$$

Futhermore, it is assumed that the reactants and the transition state are in a quasi-equilibrium:

$$k_1[A][B] = k_{-1}[AB^\ddagger] \quad (2.61)$$

Therefore, the rate equation simplifies to,

$$\frac{d[AB^\ddagger]}{dt} = -k_2[AB^\ddagger] = -\frac{d[C]}{dt} \quad (2.62)$$

i.e., where the last equality in (2.62) follows from the recognition that  $\frac{d[AB^\ddagger]}{dt}$  equals the rate of production of C. The reaction rate  $k_2$  in this equation is often called the ‘universal constant for a transition state’ and is found by a statistical mechanics derivation of activated complex partition functions, in which the vibrational mode is the dominant

mode. For ideal bimolecular systems, the value of  $k_2$  is found to be approximately  $k_B T/h$  ( $\sim 6 \cdot 10^{12}$  at room temperature). This can be thought of as an attempt frequency that is intrinsic to the system at hand. In the main text of this chapter, the attempt frequency is an unknown parameter for the DNA-SWCNT + SDBS system of reactants. For this reason, in Table 2.2, differences between activation free energy barriers (i.e.  $\Delta(\Delta G^\ddagger)$ ) have been reported relative to the sequence (TAT)<sub>4</sub> rather than finding the absolute activation free energy for each sequence.

For the equilibrium reaction between the reactants  $A, B$  and the activated complex  $AB^\ddagger$ , the equilibrium rate constant can be written:

$$\frac{[AB^\ddagger]}{[A][B]} = \frac{k_1}{k_{-1}} = K^\ddagger \quad (2.63)$$

$$[AB^\ddagger] = K^\ddagger [A][B] \quad (2.64)$$

From here, the  $[AB^\ddagger]$  from equation 2.64 can be inserted into equation 2.62

$$-\frac{d[AB^\ddagger]}{dt} = \frac{k_B T}{h} K^\ddagger [A][B] \quad (2.65)$$

Therefore, the overall rate constant,  $k$ , can be given for the entire reaction:

$$k = \frac{k_B T}{h} K^\ddagger \quad (2.66)$$

Using thermodynamic relationships, activation enthalpy, entropy, and free energies can be found:

$$\Delta G^\ddagger = -R \cdot T \cdot \ln(K^\ddagger) \quad (2.67)$$

$$\Delta G^\ddagger = \Delta H^\ddagger - T\Delta S^\ddagger \quad (2.68)$$

Combining,



$$\ln(K^\ddagger) = -\frac{\Delta H^\ddagger}{RT} + \frac{\Delta S^\ddagger}{R} \quad (2.69)$$

The Eyring equation is then found by substituting equation 2.69 into equation 2.66.

Finally, after some algebraic manipulations, the following equations are found:

$$k = \frac{k_B T}{h} e^{-\frac{\Delta H^\ddagger}{RT}} e^{\frac{\Delta S^\ddagger}{R}} \quad (2.70)$$

$$\ln(k) = \ln\left(\frac{k_B T}{h}\right) - \frac{\Delta H^\ddagger}{RT} + \frac{\Delta S^\ddagger}{R} \quad (2.71)$$

$$\ln\left(\frac{k}{T}\right) = \ln\left(\frac{k_B}{h}\right) - \frac{\Delta H^\ddagger}{RT} + \frac{\Delta S^\ddagger}{R} \quad (2.72)$$

### 2.9.3 Surfactant Exchange on Peptide-Dispersed SWCNTs

In addition to ssDNA and surfactants, certain specially designed polypeptide sequences have been shown to aqueously disperse SWCNTs.<sup>10,49</sup> In particular, Grigoryan *et al.* have identified a 30-amino acid long peptide known as ‘HexCoil-Ala’ (AEAESALEYAQQALEKAQLALQAARQALKA) which enhances the dispersion of small diameter SWCNTs such as (6,5) and (8,3).<sup>49</sup> In Figure 2.25, a molecular representation is shown for one strand of polypeptide on a (6,5)-SWCNT. In the schematic, the peptide remains adsorbed to the surface of the SWCNT due to hydrophobic interactions between the hydrophobic peptide residues (shown in white) and the aromatic SWCNT carbon atoms. In experimental conditions, HexCoil-Ala assumes its name by forming six member tube-like aggregates which possess a hollow interior. The aggregates are capable of forming around SWCNTs of a particular diameter to form very stable hybrid complexes. Their strength will be examined by the following method.

For the work presented in the following section, 50 g of uncleaved HexCoil-Ala peptide sample was generously gifted to us by Dr. William DeGrado from his laboratory at the University of Pennsylvania. To synthesize, the peptides were grown on amine groups of porous microparticles with extremely high surface area. This particular peptide was grown on a “rink amide resin.” Before the peptide could be used in SWCNT conjugation, they first had to be cleaved from the resin and then purified using reverse-phase HPLC.<sup>2</sup>

To perform the cleavage, the peptide-rink resin sample was placed in a flask and 20% by volume piperidine in dimethylformamide (DMF) was added until the sample was just covered. The mixture was allowed to react for 30 minutes to remove N-terminal protection groups. The solution was then transferred to a sintered glass funnel and a vacuum was applied. There, it was washed 3 times with DMF and then 3 more with dichloromethane (DCM). Next, the vacuum dried sample was placed in a solution of 20% by volume trifluoroacetic acid (TFA) in DCM, also containing 3% by volume 1,3-dimethoxybenzene. The mixture stood for 15 minutes and then was washed with DCM. Finally, the filtrates were combined and 10 times its volume was added in cold ether. The mixture was kept at 4°C overnight to precipitate the uncleaved peptide sample.

To perform the HPLC purification of the now-cleaved peptide sample, reverse-phase chromatography was used with a “C4” HPLC column. Two buffers were made: (A) 0.1% TFA in H<sub>2</sub>O and (B) 0.1% TFA, 90% acetonitrile in H<sub>2</sub>O. The column was then equilibrated with one column volume (CV) of buffer A. The flow rate was chosen such that the back pressure remains below 1500 psi. In general, this equates to 10

---

<sup>2</sup> Based on the procedure found in Stathopoulos, P.; Papas, S.; Tsikaris, V. *J. Pept. Sci.* **2006**, *12*, 227-32.

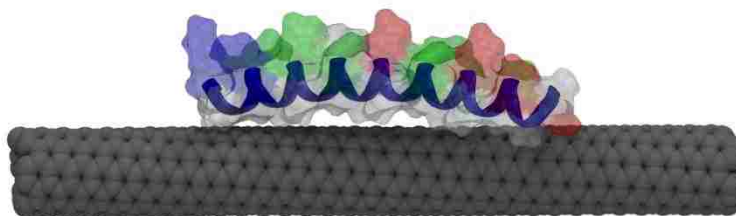
mL/min. Five mg of the cleaved peptide sample, dissolved in 1 mL of buffer A, was then loaded into the column. Buffer B was then introduced to the column in a linearly increasing gradient, i.e. 1 %/minute. The eluent sample can then be monitored by UV spectroscopy at either 215 or 280 nm. The 215 nm peak was found to be a much more sensitive peak to monitor. When the amount of buffer B was between 60 and 80%, the majority of the sample eluted from the column, seen as the large peak in the elution profile. It is important to be able to retrieve as much as possible of this sample in a fraction collector device attached to the HPLC instrument.

To test the purity of the peptide sample, MALDI mass spectroscopy was performed. Here, the HPLC purified and dried sample was spotted onto a MALDI plate with 30  $\mu$ L of 88% by weight formic acid. Upon drying, the plate was inserted into the MALDI instrument where laser evaporation of the sample was converted to a highly precise molecular weight. For the HexCoil-Ala, the MALDI instrument determined the molecular weight to be 3182.5 g/mol. The theoretical molecular weight was determined to be 3185.5 g/mol. Therefore, the sample was determined to be greater than 95% purity.

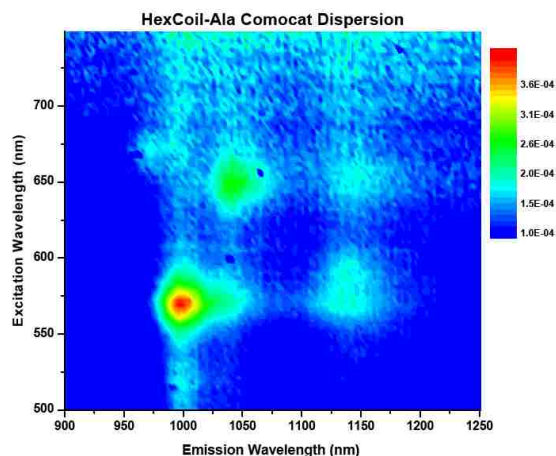
A dispersion was created using HPLC purified HexCoil-Ala sample. In a 10:1 ratio of peptide:Comocat-SWCNT, hybrids were created in the same fashion as DNA-SWCNT synthesis (90 minutes of tip sonication at 8 Watts followed by 90 minutes of centrifugation at 16,000 xg). Following this, a two-dimensional photoluminescence map was constructed to determine relative levels of dispersed SWCNTs by chirality. In Figure 2.26, it is seen that (6,5)-SWCNTs are well dispersed with photoluminescence signatures at (ex. 569 nm, em. 993 nm), which is slightly shifted compared to DNA dispersed sample (ex. 574 nm, em. 990 nm). The reason may be attributed to differences

in the amount of solvent shielding that the SWCNT experiences. It is interesting that the HexCoil-Ala peptide shows dispersion selectivity for (6,5)-SWCNTs, even more so than the (6,5) DNA recognition sequence, (TAT)<sub>4</sub>.

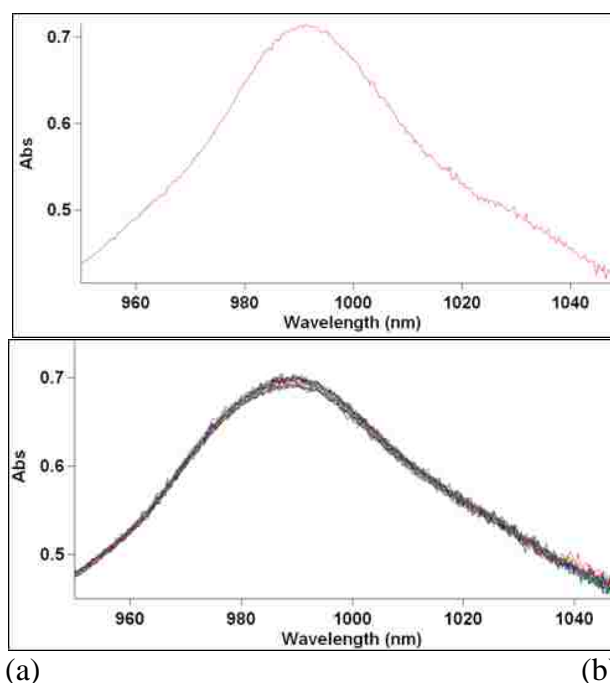
In a similar method to that presented in this chapter for finding DNA-SWCNT binding strengths, surfactant induced displacement was attempted to find the peptide-SWCNT binding strength. Figure 2.27a shows the initial NIR absorbance scan showing a single, well-dispersed (6,5)-SWCNT rich sample which peaks at 993 nm. Following the same protocol as the DNA-SWCNT experiment, SDBS is introduced to the peptide-SWCNT sample at 0.1 weight % and 60°C. Almost instantaneously, a shoulder emerges at 978 nm, reminiscent of SDBS-covered SWCNTs. However, after 30 minutes of incubation, there is negligible change in the intensity/shape of the 993 nm peak (Figure 2.27b). To explain this, one may hypothesize that in the starting sample of peptide-SWCNT, there are hybrids with incompletely formed HexCoil aggregates. These are immediately displaced from the surface of the SWCNT and transferred to SDBS (seen as the shoulder at the 978 nm position). The other population in the starting sample, i.e. the hybrids with a completely formed HexCoil covering, is *immune* to the SDBS molecules since they have a much higher activation energy for displacement.



**Figure 2.25.** Molecular representation of one strand of HexCoil-Ala polypeptide on a (6,5)-SWCNT. The polypeptide remains adsorbed to the SWCNT surface due to specifically designed hydrophobic interactions.



**Figure 2.26.** Two-dimensional photoluminescence map for Comocat SWCNT sample dispersed with HexCoil-Ala polypeptide. The dominant peak (red) represents the (6,5)-SWCNT, with excitation 569 nm and emission 993 nm.



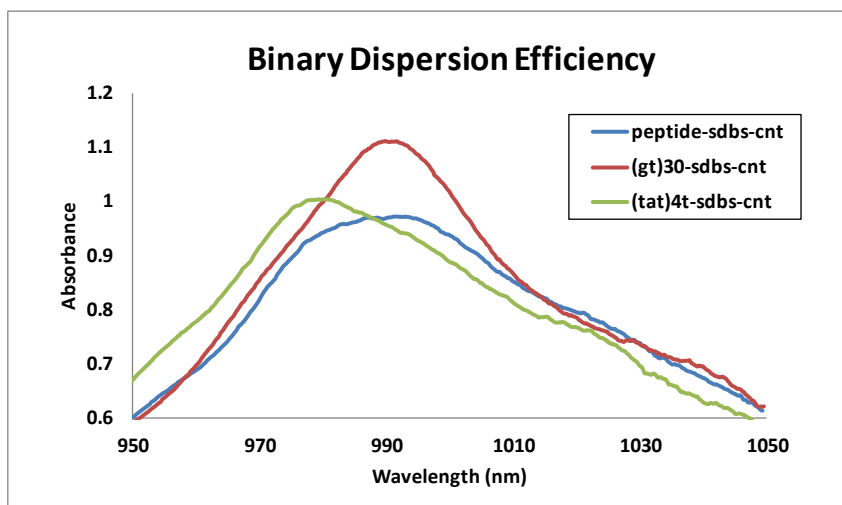
**Figure 2.27.** (a) Initial absorbance scan for HexCoil-Ala-dispersed SWCNTs. A dominant peak is seen at 993 nm corresponding to the (6,5)-SWCNT. (b) When introduced to a solution of 0.1 wt% SDBS at 60°C, there is an immediate shoulder formation at 978 nm. However, after 30 minutes of incubation at this elevated temperature, there is negligible change in the 993 nm peak.

## 2.9.4 Binary Dispersions

In all of the previous work, surfactant was added to the samples to induce exchange after the initial dispersion of SWCNTs was performed. To probe the fact that SDBS, DNA, and peptide interactions may be different under sonication conditions (in which local temperatures and pressures can reach 5000 Kelvin and 1000 atm, respectively),<sup>3</sup> an experiment was performed in which SWCNTs were dispersed in solutions with more than one dispersant. In essence, SWCNTs were dispersed with SDBS and either DNA (two kinds: (GT)<sub>30</sub> or (TAT)<sub>4</sub>T) or HexCoil-Ala polypeptide. For consistency, dispersions were made such that dispersant1:dispersant2:SWCNT remained 10:10:1, by weight, across all samples. In Figure 2.28, absorbance scans indicate that the (GT)<sub>30</sub>-SDBS sample contained the most DNA-dispersed SWCNTs (evident from the ratio of the 990:978 nm peaks). The peptide-SDBS sample contained both species (peptide-SWCNT at 993 nm and SDBS-SWCNT at 978 nm). Finally, the (TAT)<sub>4</sub>T-SDBS sample contained primarily SDBS-SWCNTs with evidence of a few DNA-SWCNTs from the slight shoulder found at 990 nm. In future studies, this may be a good assay to qualitatively rank the binding strengths of certain molecules to SWCNTs.

---

<sup>3</sup> Suslick, K. S.; Hammerton, D. A.; Cline, R. E., Sonochemical hot spot. *Journal of the American Chemical Society* **1986**, *108* (18), 5641-5642.



**Figure 2.28.** Absorbance scan of Comocat SWCNT sample dispersed with equal quantities of two dispersants: SDBS and HexCoil-Ala peptide, (GT)<sub>30</sub>, or (TAT)<sub>4</sub>T DNA.

## **Chapter 3**

### **Molecular Simulation of DNA $\beta$ -Sheet and $\beta$ -Barrel Structures on Graphite and Single-Walled Carbon Nanotubes\***

*It has recently been discovered that certain short DNA sequences recognize specific single-walled carbon nanotubes (SWCNTs), allowing a mixture to be sorted into individual types. A novel  $\beta$ -Sheet and  $\beta$ -Barrel secondary DNA motif has been proposed as the structural basis for this recognition. In this study, using molecular simulation we investigate a class of DNA structures that can be formed by inter-strand hydrogen bonding, their stability in planar and barrel form, and whether they can form the basis for SWCNT recognition. We show how a library of DNA  $\beta$ -Barrel structures can be built from base-dimer tiling units. Various combinations of the  $(GT)_n$  family of sequences have been studied in greater detail, both as adsorbed in planar form to graphite and as wrapped helically on a SWCNT surface. We find that G-quartet formation brings stability to the  $\beta$ -Sheet, while diameter and chirality matching between the proposed DNA  $\beta$ -barrel and core SWCNT stabilizes an ordered hybrid structure.*

---

\* Portions of this chapter have been published in the Journal of Physical Chemistry C

D Roxbury, S Manohar, A Jagota. "Molecular Simulation of DNA  $\beta$ -Sheet and  $\beta$ -Barrel Structures on Graphite and Single-Walled Carbon Nanotubes" *J. Phys. Chem. C* **114**, 31, 13267 (2010)



### 3.1 Introduction

It is well-known that the secondary structure of biopolymers such as proteins and nucleic acids is a principal determinant of their function via interactions with other biopolymers. The DNA double-helices (B-DNA, A-DNA, Z-DNA, S-DNA)<sup>1-7</sup> and proteins with  $\alpha$ -helix,  $\beta$ -sheet and  $\beta$ -barrel<sup>8-9</sup> motifs are well known examples. As in these examples, secondary structure is usually stabilized by non-covalent interactions. When biopolymers encounter material surfaces, especially those of nanomaterials, they can adopt novel, sometimes ordered, conformations.

Our interest is in the interactions between DNA and carbon nanotubes. Single-stranded DNA (ssDNA) and single-walled carbon nanotubes (SWCNT) form a stable hybrid that renders the latter water-dispersable<sup>10</sup> and has enabled successful separation by length and diameter.<sup>10-12</sup> It has recently been shown that certain short ssDNA sequences recognize specific SWCNTs, thus allowing their separation from a mixture by ion exchange chromatography.<sup>13</sup> High selectivity strongly suggests that an ordered structure is formed by the recognition sequence around a particular SWCNT. Novel  $\beta$ -sheet and  $\beta$ -barrel secondary structures for DNA stabilized both by hydrogen bonding and by base stacking onto the substrate have been proposed as the structural basis for recognition.<sup>13-14</sup> Furthermore, well-defined charge densities for (GT)<sub>30</sub>-SWCNT hybrids<sup>14</sup> measured using capillary electrophoresis also suggest a well-ordered DNA structure. In this manuscript, using molecular simulations, we explore the structure and stability of these novel DNA motifs.

In order to build models for ordered structures based on oligomeric DNA adsorption, it is useful to consider first structures formed by DNA bases themselves.

Several studies have been conducted to understand the adsorption of DNA bases onto solid surfaces that has relevance to our study.<sup>15</sup> The adsorption isotherms for different bases at the graphite-water interface show that stronger adsorption occurs in the order,<sup>16</sup> (G>A>T>C) due to their tendency to form self-assembled monolayers.<sup>16-18</sup> The aromatic ring structures of DNA bases are known to stack on an aromatic surface due to overlapping  $\pi$ -orbitals<sup>19-20</sup> and often the bases are laterally stabilized by base-base dimer formation<sup>21-23</sup> through inter-base cyclic hydrogen bonding which is further stabilized by  $\pi$ -bond cooperativity. All the dimers considered in this work have a *minimum of two hydrogen bonds*.<sup>24-25</sup> Homobase dimers in a *centrosymmetric* configuration are favored because the purines and pyrimidines have large dipole moments which are cancelled in an *antiparallel* configuration.<sup>23-24</sup> Centrosymmetric dimers can pack into a flat sheet stabilized by hydrogen bonding interactions between adjacent dimers. Several high resolution AFM and STM images of bases adsorbed onto a substrate reveal the above picture.<sup>18, 22, 26-27</sup> Apart from dimers, guanine, adenine and mixtures of adenine/thymine, guanine/uracil or guanine/cytosine are known to form supramolecular structures at the liquid/solid interface.<sup>18, 21-22, 26, 28-30</sup> Guanine-rich telomeric DNA in human chromosomes is of significant interest because of the recombination- and degradation-protection that G-quartet structures confer.<sup>31-33</sup>

What ordered structures can surface-adsorbed ssDNA molecules form? To our knowledge, ordered structures based on oligomeric ssDNA molecules on flat (e.g., graphite) and curved (e.g. SWCNT) surfaces have not been studied previously. (It is known that ssDNA strands with length much greater than their Kuhn length generally adsorb onto a flat surface as random coils.) The existence of some ordered structures is

highly plausible given the evidence of SWCNT recognition by certain short strands of ssDNA and the demonstrated propensity of bases to organize into 2D structures. Indeed, one may view the class of ordered ssDNA structures as a subset of those permitted by association of free bases with the additional constraints that arise because bases are covalently attached via a sugar-phosphate backbone. In general, both ssDNA and dsDNA adsorb onto hydrophobic substrates,<sup>34-36</sup> ssDNA adsorbing stronger than dsDNA.<sup>37</sup> We propose that ssDNA molecules readily adsorb to hydrophobic surfaces, such as graphite and SWCNT, to form hybrids through  $\pi$ -stacking interactions between the DNA base and the surface and inter-base hydrogen bonding, while the negatively charged phosphate backbone is exposed to water.

Molecular simulations of a *single* short ssDNA strand on a SWCNT showed disordered structures with nonhelical loop structure representing the global free energy minimum<sup>38-39</sup> suggesting the necessity of multiple short strands to form an ordered structure. The main contributors to the free energy of the DNA/SWCNT hybrid were shown to be a competition between adhesive interactions between DNA and SWCNT and electrostatic repulsion between charges on the DNA backbone.<sup>19</sup> Interestingly, the predominant feature in the minimum free-energy conformations of (GT)<sub>7</sub> is one in which *DNA bases alternate* on either side of the backbone, which minimizes steric hindrance.<sup>38</sup> We now shift our focus to the assumption that multiple strands are interacting on graphite and/or nanotube surfaces. From previously stated evidence, we assume that bases on antiparallel strands have the propensity to form hydrogen-bonded dimers. We show that with these constraints the DNA strands can form an ordered inter-strand hydrogen bonded 2D sheet structure on a flat substrate like graphite which can then be folded in

several ways into 3D-barrel structures with discrete diameters. A plausible mechanism for the recognition of SWCNTs by ssDNA is then the matching of their diameters and chirality. The ordered structures we propose, sheets and barrels, are analogous to secondary structures of proteins,  $\beta$ -sheets and  $\beta$ -barrels, respectively. We begin by describing the procedure for constructing the ordered structures on graphite and SWCNTs. For a particular DNA sequence,  $(GT)_n$ , using molecular dynamics (MD) simulations with explicit water molecules, we study the stability of ordered  $\beta$ -sheet structures on graphite and the factors governing stability. In order to examine our hypothesis that recognition comes from matching the a DNA barrel and SWCNT, we perform MD simulations of several DNA  $\beta$ -barrel structures around a (6,5) SWCNT.

### 3.2 Molecular Simulation Methodology

All structures were first created in *Materials Studio*® workplace<sup>40</sup> and converted into formats suitable for other programs. Strands of two-dimensional  $(GT)_n$  sheets were formed anti-parallel to each other and minimized in vacuum at zero Kelvin on a 2D hexagonal sheet of  $sp^2$  hybridized carbon using the *CHarMM* (v. 35) force-field and program.<sup>41</sup> (The atoms in the sheet were constrained against motion by a spring of strength  $13.9 \text{ Nm}^{-1}$ .) For  $\beta$ -sheet simulations, a water box was created around the entire structure with a sufficient number of  $\text{Na}^+$  ions added to balance the charge created by the negatively charged phosphates on the DNA backbone. The structures were then heated and equilibrated over a period of 20 ps each using the *NAMD* (v. 2.7b2) molecular modeling package.<sup>42</sup> For  $\beta$ -barrel simulations, the aromatic carbon sheet was first removed and the remaining DNA sheet was folded around a circumferential axis into a

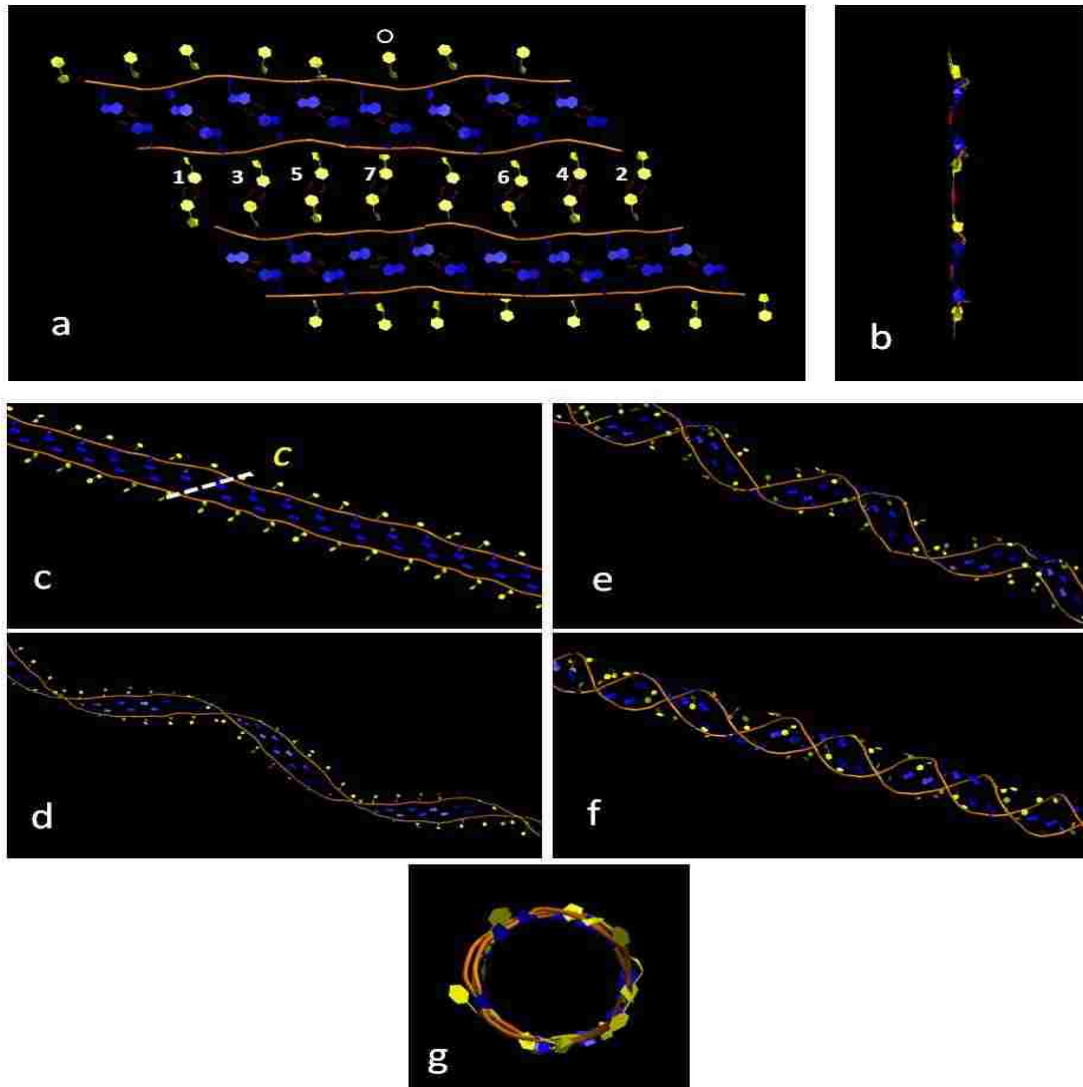
3D barrel structure. A (6,5) chirality carbon nanotube was inserted into the DNA barrel and the full structure was minimized in *CHarMM* (again constraining the SWCNT atoms). A waterbox (40 x 40 x 300 Å) was created to envelop the hybrid structure, and charge-neutralizing Na<sup>+</sup> counterions were added. Heating and equilibration similar to those described above were applied to the  $\beta$ -barrel using the *NAMD* molecular modeling program. All configurations were then ready for dynamic simulation (graphite and SWCNT carbon atoms remained constrained). Each configuration has been run for at least 6 ns with a timestep of 1 fs and a data recording interval of 10 ps.

### 3.3 Ordered $\beta$ -Sheet and $\beta$ -Barrel Structures

#### 3.3.1 Construction of $\beta$ -Sheets and $\beta$ -Barrels

This section introduces the new class of ordered DNA structures,  $\beta$ -sheets and  $\beta$ -barrels. A step-by-step procedure, using the (GT)<sub>n</sub> sequence as an illustration, is presented that explains the construction of the periodic, hydrogen-bonded sheet and barrel structures. As mentioned in the Introduction, single adsorbed short ssDNA chains on a substrate maximize stacking and minimize steric hindrance by adopting conformations in which bases alternate from one side to the other of the DNA backbone<sup>38</sup>. We have found that two such strands placed adjacent and anti-parallel to each other on a surface can form inter-strand hydrogen bonded 2D sheets.<sup>13-14</sup> This hydrogen bonded structure can be extended to form a periodic 2D sheet structure on graphite as illustrated in Figure 3.1a. It shows anti-parallel (GT)<sub>n</sub> strands arranged so that inter-strand Guanines can form hydrogen bonds. This ordered structure can be extended indefinitely in either planar direction. Following a particular roll-up vector,  $\mathbf{c}$ , one can

create a DNA  $\beta$ -barrel structure by hydrogen bonding inter-strand Thymines (Figure 3.1b, c). It is clear that only certain, discretized, values of  $c$  are allowed, which means that the resulting barrels will have distinct diameters and helical pitches (Figure 3.1f, g).



**Figure 3.1.** (a) Four  $(GT)_8$  strands in a sheet configuration shown with GG and TT inter-strand hydrogen bonding. Guanine bases are shown in blue and Thymine in yellow. Connecting via hydrogen bonds the Thymine labeled 'O' to Thymines labeled '1'-'7' gives seven distinct rollup vectors. (b) Side view of  $(GT)_8$  sheets. (c) An extended  $(GT)_n$  ribbon showing one specific rollup vector (white dashed line). Roll-up progression shown, (d) and (e), resulting in final DNA  $\beta$ -barrel structure, (f) and (g).

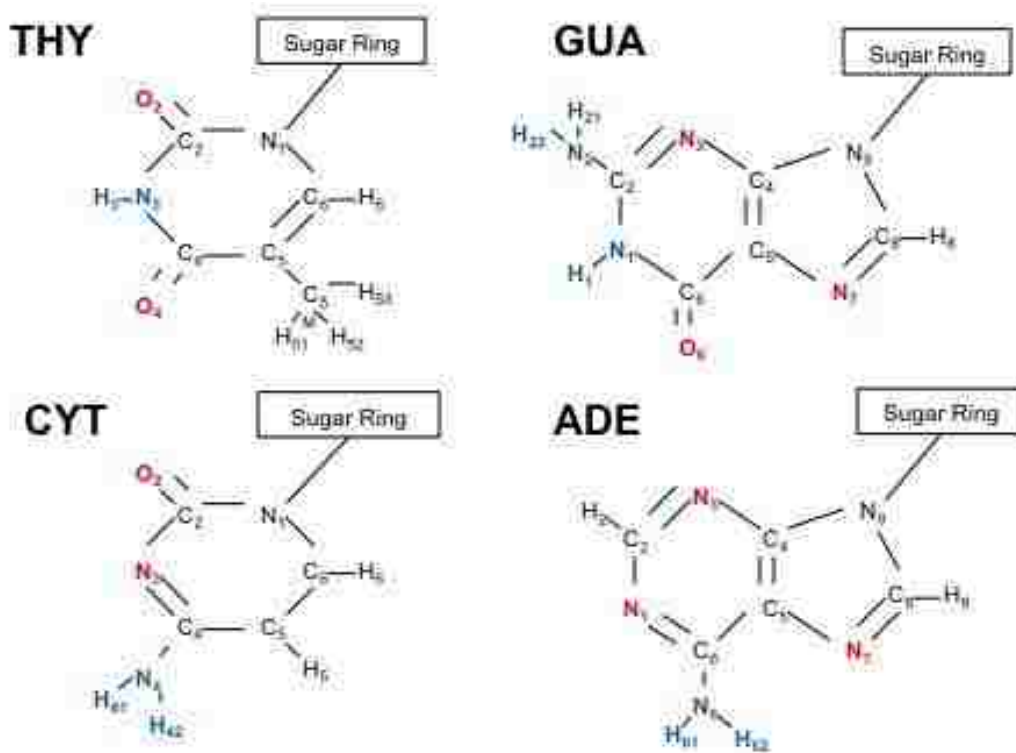
### 3.3.2 Tiling Units

The example described in the previous section shows how antiparallel ssDNA sheets can be hydrogen-bonded into an extended sheet and then rolled into a barrel. In order to examine systematically the variety of ways in which such structures can be constructed, we adopt as tiling units elements of the set of hydrogen-bonded base dimers, each attached covalently to a sugar-phosphate backbone. Figure 3.2 shows the four bases, (Gua, Ade, Thy and Cyt), with possible hydrogen bond donor/acceptor pairs. These four bases can be combined into 28 possible hydrogen-bonding dimers with at least two hydrogen bonds each.<sup>24</sup> Because we are interested in extended periodic structures, we impose the additional constraint that the backbones be parallel or anti-parallel to each other and in the same plane as the bases. In this work, we consider structures in which the base alternates to the left and right of the backbone, although structures that violate this condition can also be constructed using the tiling units. Examining all possible dimers, the following picture emerges.

- Only non-Watson-Crick base pairing is possible; Watson-Crick base pairing is inconsistent with parallel backbones.
- Neighboring strands must be antiparallel.
- Along a given strand, the O4' atoms in the sugar rings alternately point up and down as the base alternates from one side to the other.
- The glycosyl sugar-base linkage on the same strand should all be in either syn or anti\* configuration.

---

\* 'Syn' vs. 'anti' configurations designate one of two ranges of torsion angle that the sugar-base glycosyl linkage can assume. We follow the same reference for nomenclature of atoms in the DNA structure



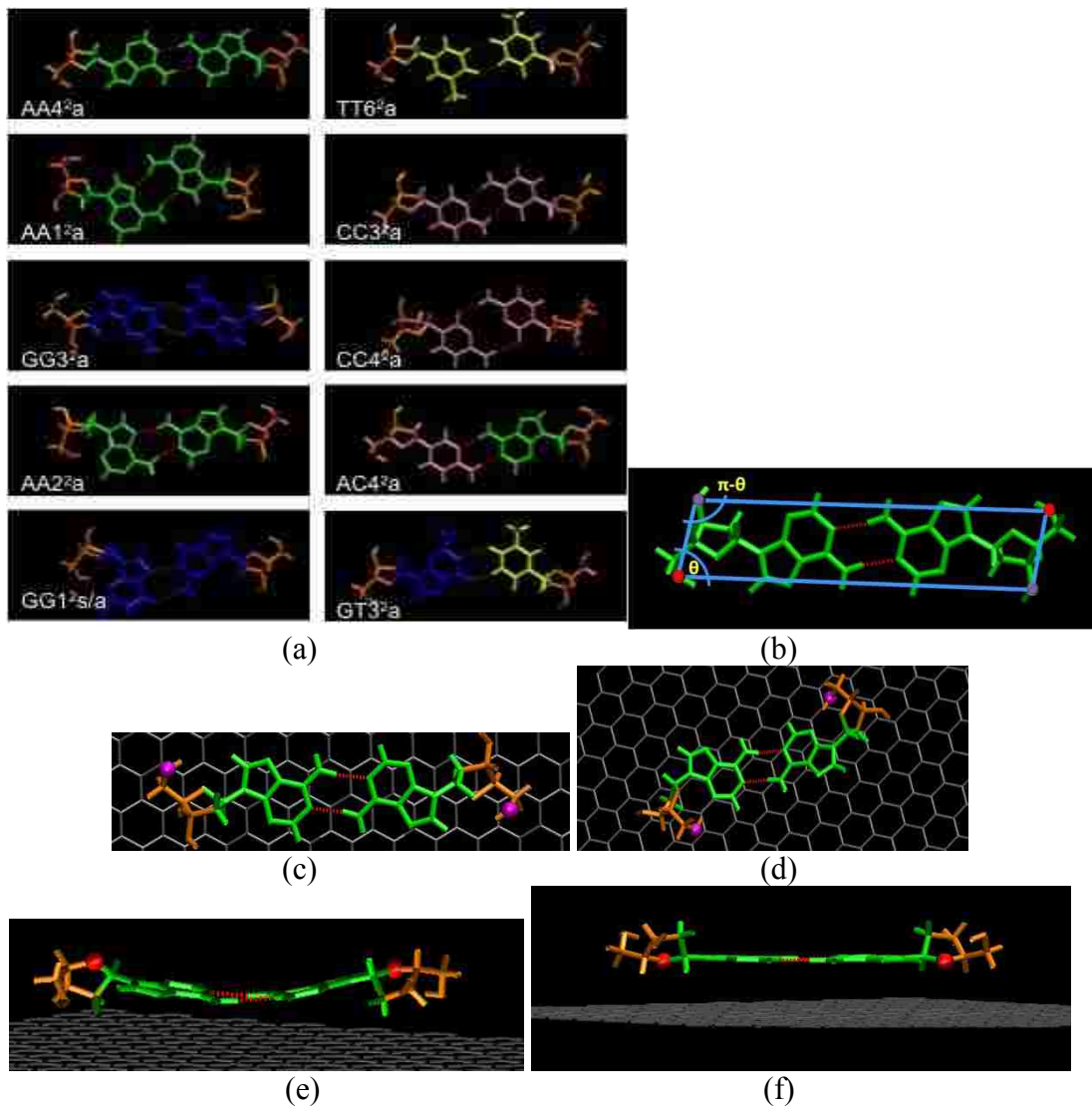
Donor pairs shown in blue. Acceptors shown in red.

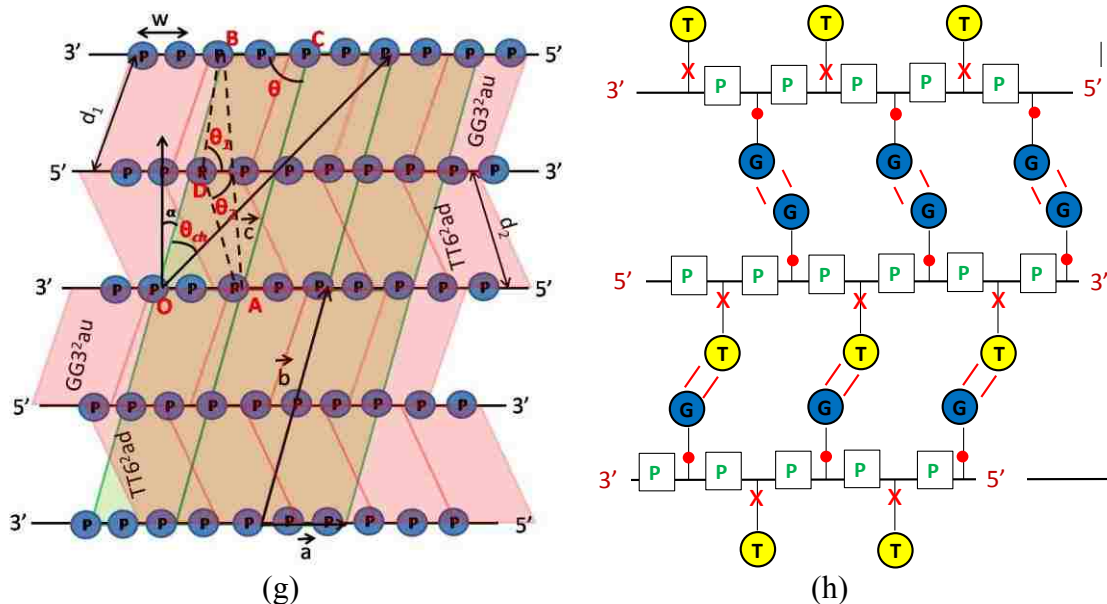
**Figure 3.2.** DNA Bases (Guanine, Thymine, Adenine, Cytosine) showing hydrogen bonding donor pairs and acceptors.

With these constraints, only 10 of the 28 hydrogen-bonding possibilities survive (Figure 3.3a). The nomenclature is based on that of Saenger's planar nucleic acid dimers,<sup>24</sup> e.g., GT3<sup>2</sup>au refers to a dimer with hydrogen bonding between Guanine and Thymine, with '3' based on the third documented GT configuration, the superscript '2' referring to two hydrogen bonds, and 'a' to the 'anti' orientation of the glycosyl torsion. A rotation of the backbones with respect to the base by 180° about the glycosyl bond results in a new allowed configuration, doubling the number of configurations to 20 (Figure 3.3c vs. 3.3d). Further possibilities can emerge if one considers the placement of the O4' oxygen with respect to the plane on which the strand adsorbs (Figure 3.3e vs



3.3f). However, whether or not new overall configurations emerge depends on the composition, which will be apparent as we develop the example of  $(GT)_n$ . Table 3.1 displays parameter values for the 40 aforementioned tiling units. Notice that there are significant differences in the distance between adjacent strands but that the angle  $\theta$  does not vary much between dimers.





**Figure 3.3.** (a) Ten possible inter-base hydrogen bonding dimer configurations are allowed with given constraints. (b) Each dimer is represented as a parallelogram tiling unit and characterized by the distance between the O3' (purple) to O5' (red) atoms and an angle,  $\theta$ . (c,d) O3' atoms (purple) in syn configuration, 's', versus anti, 'a'. (e,f) O4' atoms (red) away from graphite, 'u', versus away, 'u'. (g)  $(GT)_4$  sheets on graphite employing  $GG3^2au$  and  $TT6^2ad$  tiling units. In this case the final 'd' refers to O4' pointing 'down' towards the substrate and 'u' refers to it pointing 'up', away from the substrate. (h) An example of  $(GT)_n$  sheet structure with three tiling units (upon repeating)  $GG3^2ad$ ,  $TT6^2au$  and  $GT^2au$  showing that numerous sheet structures are possible even for a simple sequence like  $(GT)_n$ .

**Table 3.1:** Average parameters for the ten DNA dimer tiling units shown in Fig. 3a, in ‘anti-down’ configuration, minimized on graphite in vacuum.

Tiling Unit	Avg $\theta$	Avg O3’-O5’ distance (Å)	Tiling Unit	Avg $\theta$	Avg O3’-O5’ distance (Å)
AA4 <sup>2</sup> su	84.2	16.1	TT6 <sup>2</sup> su	78.5	14.7
AA4 <sup>2</sup> sd	85.2	16.1	TT6 <sup>2</sup> sd	81.6	14.3
AA4 <sup>2</sup> ad	85.4	18.9	TT6 <sup>2</sup> ad	80.8	16.3
AA4 <sup>2</sup> au	84.7	18.6	TT6 <sup>2</sup> au	81.3	16.0
AA1 <sup>2</sup> su	81.0	15.8	CC3 <sup>2</sup> su	80.4	13.7
AA4 <sup>2</sup> sd	79.6	15.4	CC3 <sup>2</sup> sd	83.1	13.4
AA4 <sup>2</sup> ad	81.3	15.8	CC3 <sup>2</sup> ad	85.6	15.9
AA4 <sup>2</sup> au	82.3	15.9	CC3 <sup>2</sup> au	85.0	15.4
GG3 <sup>2</sup> su	86.5	15.9	CC4 <sup>2</sup> su		
GG3 <sup>2</sup> sd	84.0	15.6	CC4 <sup>2</sup> sd		
GG3 <sup>2</sup> ad	87.1	18.6	CC4 <sup>2</sup> ad		
GG3 <sup>2</sup> au	86.0	18.6	CC4 <sup>2</sup> au		
AA2 <sup>2</sup> su	81.9	16.2	AC4 <sup>2</sup> su	85.4	15.0
AA2 <sup>2</sup> sd	83.0	15.8	AC4 <sup>2</sup> sd	87.0	14.7
AA2 <sup>2</sup> ad	82.6	17.0	AC4 <sup>2</sup> ad	86.5	17.3
AA2 <sup>2</sup> au	82.4	16.9	AC4 <sup>2</sup> au	85.8	17.4
GG1 <sup>2</sup> su	82.4	14.3	GT3 <sup>2</sup> su	81.8	15.0
GG1 <sup>2</sup> sd	83.3	14.4	GT3 <sup>2</sup> sd	83.2	14.7
GG1 <sup>2</sup> ad	83.5	16.0	GT3 <sup>2</sup> ad	83.0	17.3
GG1 <sup>2</sup> au	80.7	16.2	GT3 <sup>2</sup> au	83.4	17.0

\*Note that the CC4<sup>2</sup> value is not reported as this configuration minimizes to CC3<sup>2</sup> on graphite.

### 3.4 (GT)<sub>4</sub> Sheets on Graphite\*

#### 3.4.1 Creating DNA $\beta$ -Sheets

Using the 40 allowed tiling units, one can create many sheet structures. We regard this as providing a set of starting structures that can be studied using molecular

---

\* The work in this section was performed by Dr. Suresh Manohar at Lehigh University.

simulation. We find that the order implied by tiling with dimers can evolve into more complex structures, e.g., by the formation of G-quartets, A-quartets and AT-quartets.<sup>21-22,</sup>

<sup>43</sup> These increase the number of hydrogen bonds and are known to be stable structures.<sup>29</sup>

In this study we focus attention on the sequence  $(GT)_n$ , which is one of a small set of special SWCNT-recognizing sequences. Using molecular dynamics (MD) simulations we have studied the equilibrium structure and stability of a few sheet and barrel structures formed by this sequence. It is a daunting task to study all the sheet structures through MD and hence a coarse grain model or procedure will probably be needed to predict stable sheet structures similar to the algorithms that can predict the protein  $\beta$ -sheets.<sup>8-9</sup>

Figure 3.3g shows one type of sheet structure that can be made using  $(GT)_n$  strands. The dimension of the tiling unit is specified by two vectors and the angle between them. From the dimensions of tiling units, one can calculate the dimension of the sheet unit cell given by vectors,  $\mathbf{a}$  and  $\mathbf{b}$ , with magnitudes  $a$  and  $b$ , and the angle between them. Here we present the derivation for sheet structures created using a variety of tiling possibilities.

A sheet is formed by  $GG3^2au/TT6^2ad$  tiling units shown by pink shaded regions in Figure 3.3g. Dimensions of the  $GG3^2au$  tiling unit are  $d_1 = 18.6 \text{ \AA}$ ,  $w = 6.1 \text{ \AA}$  and  $\theta_1 = 86.0^\circ$ . Dimensions of the  $TT6^2ad$  tiling unit are  $d_2 = 16.6 \text{ \AA}$ ,  $w = 6.1 \text{ \AA}$  and  $\theta_2 = 80.9^\circ$ . The region OACB represents a unit cell of the sheet with unit cell vectors  $\mathbf{a}$  and  $\mathbf{b}$  making angle  $\theta$  between them. The unit cell parameters can be determined from the tiling unit dimensions as shown below.

$$AB = \sqrt{d_1^2 + d_2^2 - 2d_1d_2 \cos(\theta_1 + \theta_2)} = 35 \text{ Angstroms} \quad (3.1)$$

$$\text{angle}DAB = \sin^{-1}\left(\frac{d_1 \sin(\theta_1 + \theta_2)}{AB}\right) = 6.9138^\circ \quad (3.2)$$

$$\text{angle}OAB = DAB + \theta_2 = 87.7898^\circ \quad (3.3)$$

$$a = OA = 2w = 12.2 \text{ Angstroms} \quad (3.4)$$

$$b = OB = \sqrt{OA^2 + AB^2 - 2 \cdot OA \cdot AB \cdot \cos(OAB)} = 36.6 \text{ Angstroms} \quad (3.5)$$

$$\theta = \sin^{-1}\left(\frac{AB \cdot \sin(OAB)}{OB}\right) = 72.7^\circ \quad (3.6)$$

Vector  $c$  joining two identical points on the lattice is the rolling vector.  $c$  can be written as a linear combination of unit cell vectors  $a$  and  $b$  as

$$c = pa + qb \quad (3.7)$$

where  $p$  and  $q$  can take integral values. The barrel thus formed is named the  $(p,q)$

DNA barrel. The angle,  $\theta_{ch}$ , is between  $c$  and  $OB$ . The magnitude of  $c$  corresponds to the circumference of the barrel which when divided by  $\pi$  gives the diameter of the barrel.

$$c = \sqrt{(pa)^2 + (qb)^2 - 2(pa)(qb)\cos(\pi - \theta)} = \sqrt{(pa)^2 + (qb)^2 + 2(pa)(qb)\cos(\theta)} \quad (3.8)$$

$$d_{\text{barrel}} = \frac{c}{\pi} \quad (3.9)$$

Subtracting twice the distance between the base and the nanotube surface ( $d_v$ , approximately  $3.5 \text{ \AA}$ ) from the barrel diameter gives the matching tube diameter,  $d_{\text{tube}}$ .

$$d_{\text{tube}} = d_{\text{barrel}} - 2d_v \quad (3.10)$$

The angle can be calculated as

$$\theta_{ch} = \sin^{-1}\left(\frac{pa \cdot \sin(\pi - \theta)}{c}\right) = \sin^{-1}\left(\frac{pa \cdot \sin(\theta)}{c}\right) \quad (3.11)$$

A line drawn normal to the vector  $c$ , will then be along the axial direction of the constructed  $\beta$ -barrel. The axial unit cell for SWCNTs is known to be a function of the chiral indices,  $(n,m)$ . For the  $(6,5)$ -SWCNT, this is  $41.1 \text{ \AA}$ . In the case of DNA  $\beta$ -

barrels, which are generally composed of several DNA tiling units, each with their intrinsic angle,  $\theta$ , it is highly unlikely that the axial unit cells for idealized rigid  $\beta$ -barrels will match those of SWCNTs. Moreover, a least common denominator approach must be used to find the unit cell for the DNA-SWCNT composite structure. In general, this will far exceed the length of the SWCNT. For this reason, matching of axial unit cells between DNA  $\beta$ -barrels and SWCNTs has been neglected.

Table 3.2 below shows the discrete set of DNA tube core diameters, and the corresponding chiral angle of the barrel.

**Table 3.2:** Intrinsic values of DNA  $\beta$ -barrel diameter and angle,  $\theta_{ch}$ , for  $(GT)_{30}$  structures.

$\mathbf{p}$ (across)		<b>-6</b>	<b>-5</b>	<b>-4</b>	<b>-3</b>	<b>-2</b>	<b>-1</b>	<b>0</b>	<b>1</b>	<b>2</b>	<b>3</b>	<b>4</b>
$\mathbf{q}$ (down)												
<b>1</b>	$\mathbf{d}_{\text{tube}}(\text{\AA})$	15.8	12.5	9.4	6.8	4.9	4.1	4.7	6.3	8.8	11.8	15.0
	$\theta_{\text{ch}}$	78.0°	72.4°	64.6°	53.6°	38.4°	19.5°	0°	16.2°	28.0°	36.4°	42.4°
<b>2</b>	$\mathbf{d}_{\text{tube}}(\text{\AA})$	20.7	18.5	16.9	15.8	15.3	15.5	16.3	17.7	19.7	22.0	24.6
	$\theta_{\text{ch}}$	53.7°	46.6°	38.5°	29.3°	19.5°	-9.5°	0°	8.6°	16.2°	22.6°	28.0°

A similar table can be constructed for SWCNTs of differing chirality.<sup>44</sup> Diameter and chiral angle can be found according to the equations below, and these are reported for a few semi-conducting SWCNTs in Table 3.3.

$$\text{diameter} = 2.49 \frac{\sqrt{m^2 + n^2 + mn}}{\pi} \quad (3.12)$$

$$\cos(\theta) = \frac{2n + m}{2\sqrt{m^2 + n^2 + mn}} \quad (3.13)$$

**Table 3.3:** Carbon nanotube intrinsic properties.

SWCNT Chirality	Diameter (Å)	Chiral Angle, $\theta$ (degrees)
(5,4)	6.19	58.55
(6,4)	6.91	23.41
(9,1)	7.56	5.21
(6,5)	7.56	26.99
(8,3)	7.81	15.29
(7,5)	8.27	24.50
(8,4)	8.39	19.11
(10,2)	8.83	8.95
(9,4)	9.14	17.48
(8,6)	9.64	25.28

### 3.4.2 Detailed study of (GT)<sub>4</sub> sheet structures

For (GT)<sub>n</sub> strands, there are four ways in which bases, G and T, can form hydrogen bonds that comply with the conditions imposed for an ordered structure. Accounting for the syn/anti conformations and up/down orientation of the oxygen atom in the sugar ring, there are 16 possible tiling units (4 GG3<sup>2</sup>, 4 GG1<sup>2</sup>, 4 TT6<sup>2</sup> and 4 GT3<sup>2</sup>). The 16 tiling units on a backbone can combine in several ways to form different ordered sheet structures which can be divided into two broad categories: sheets with homo-base pairing (HM sheets) and sheets with hetero-base pairing (HT sheets). The HM sheets have GG dimers on one side of the backbone and TT dimers on the other side giving rise to 32 sheet structures (4 GG3<sup>2</sup> × 4 TT6<sup>2</sup> and 4 GG1<sup>2</sup> × 4 TT6<sup>2</sup>). The constraint on the backbone (adjacent oxygen atoms point up and down; all bases on the same strand are in anti or syn configuration) reduces the number of HM sheets by a factor of four, i.e., to 8 HM sheets. Similarly, for the case of HT sheets with GT base pairing on either side of the backbone, the initial number of sheets, 16 (4 GT3<sup>2</sup> × 4 GT3<sup>2</sup>), is reduced to 4 sheets. This number is further reduced to 2 because the sheet formed from GT3<sup>2</sup>au on the one side and GT3<sup>2</sup>ad on the other side is identical to sheet formed from GT3<sup>2</sup>ad on the one

side and GT3<sup>2</sup>au on the other side. Hence, a total of 10 sheet structures can be formed by the (GT)<sub>n</sub> sequence.

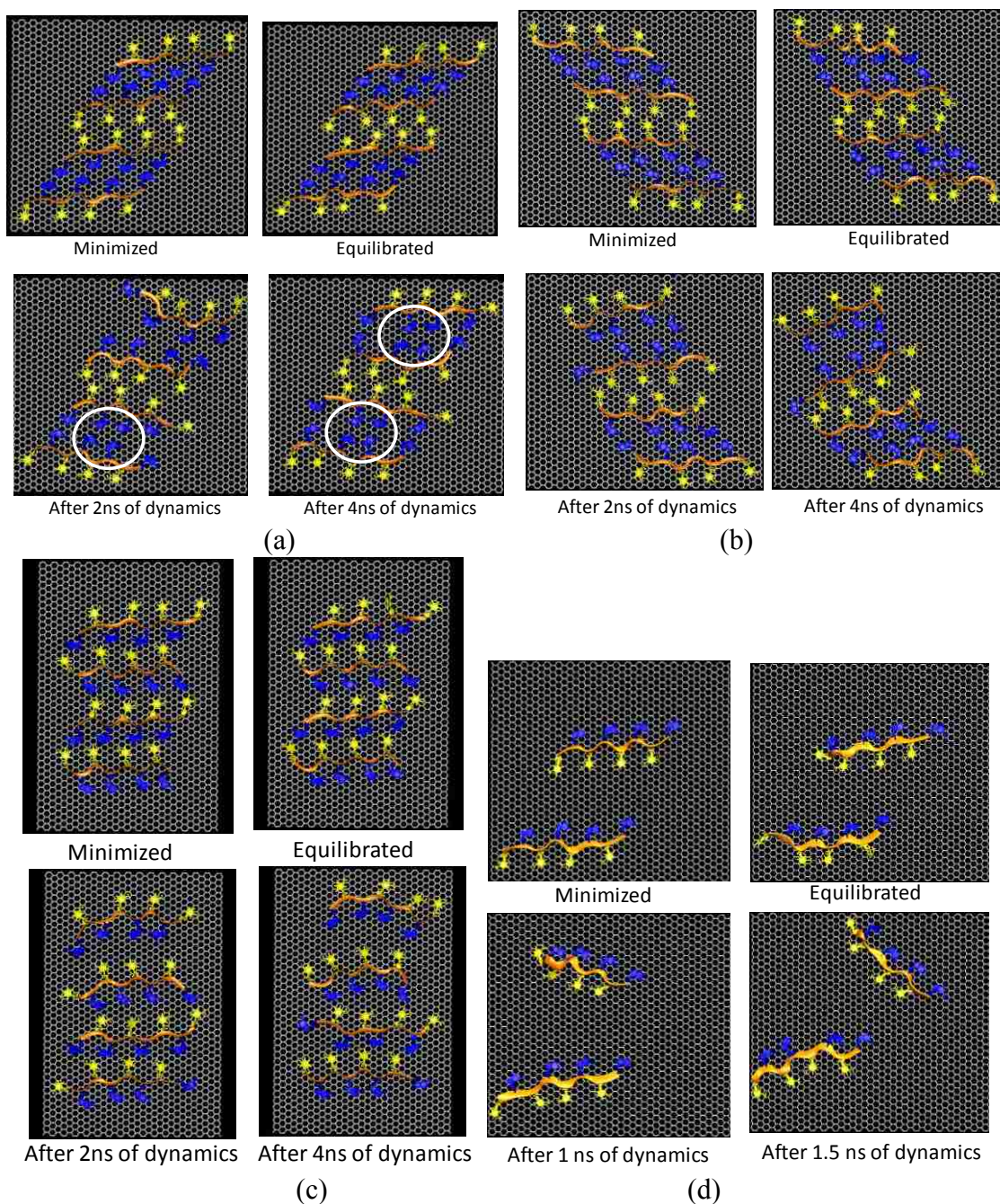
We further focus our attention on a few out of these 10 structures that are expected to be preferred, based on previous knowledge of base-sugar orientation and base adsorption onto surfaces. Ordered structures formed by nucleotides on graphite show that centrosymmetric hydrogen bonded dimers are preferred in homo-base pairing.<sup>21</sup> This implies that the GG1<sup>2</sup> dimer, being non-centrosymmetric, is less preferred and therefore the 4 sheets with GG1<sup>2</sup> dimer have not been studied. Further, in pyrimidines, the anti conformation is dominant while in purines, both anti and syn conformations are equally preferred.<sup>24</sup> We restrict our study to sheets with all bases in anti conformations. This leaves us with three sheet structures formed from (1) GG3<sup>2</sup>au and TT6<sup>2</sup>ad (sheet 1), (2) GG3<sup>2</sup>ad and TT6<sup>2</sup>au (sheet 2), and (3) GT3<sup>2</sup>ad and GT3<sup>2</sup>au (sheet 3) tiling units. Apart from the MD simulations of these three sheets, we conducted two control simulations – (i) sheet constructed from GG3<sup>2</sup>au and TT6<sup>2</sup>ad tiling units in the absence of graphite, and (ii) sheet made from GG3<sup>2</sup>au and TT6<sup>2</sup>ad tiling units with alternate strands removed. The control simulations were carried out to understand the stabilizing role of graphite and hydrogen bonding in ordered structures.

### 3.4.3 MD results for (GT)<sub>4</sub> sheets

Figure 3.4 shows the MD results for sheets 1, 2, and 3. The result for sheet 2 was similar to sheet 1 indicating that the orientation of oxygen atoms O4' in the sugar ring does not have a major influence on the sheet structure. The reason may be that there is an equal number of bases with O4' pointing toward and away from graphite in both cases.



Note that the starting minimized (Figure 3.4a) and the equilibrated sheet structures did not have G-quartets. Structures obtained after 2 ns and 4 ns show the formation of G-quartets which give extra-stability to this sheet structure. At 2 ns, the top two strands look disordered with a few hydrogen bonds broken but at 4 ns they find their hydrogen bonding partners, forming a G-quartet. (G-quartets are customarily stabilized further by a positive ion, say  $\text{Na}^+$ . However we did not have excess ions in our simulation.) Sheet 3 reveals a different picture. Many bases have broken their hydrogen bonds and the sheet appears to be disordered (Figure 3.4c). The formation of a G-quartet seems to be an important feature stabilizing the ordered sheet structure. Therefore, from among the three sheets, those with  $\text{GG3}^2\text{au}/\text{TT6}^2\text{ad}$  and  $\text{GG3}^2\text{ad}/\text{TT6}^2\text{au}$  tiling units are more stable than the sheets with  $\text{GT3}^2\text{au}/\text{GT3}^2\text{ad}$  tiling units.

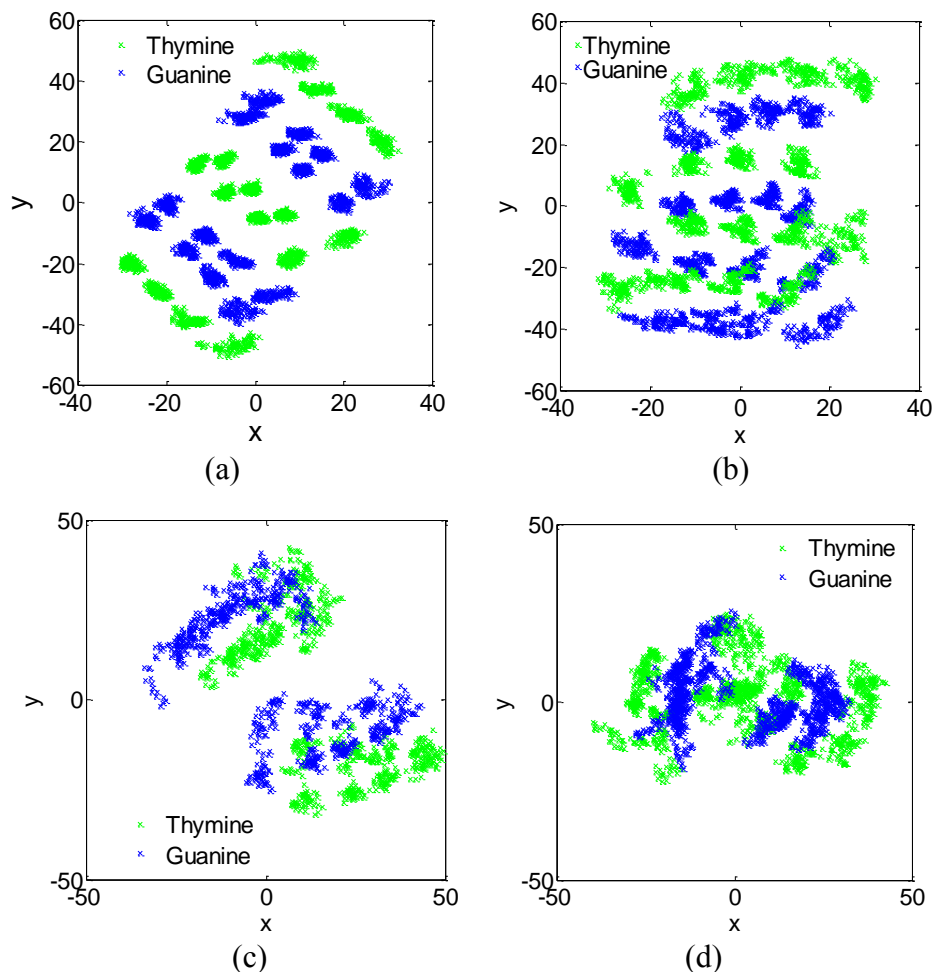


**Figure 3.4.** Molecular dynamics results for the  $(GT)_4$  sheet structure formed from (a)  $GG3^2_{au}$  and  $TT6^2_{ad}$  tiling units (sheet 1), (b)  $GG3^2_{ad}$  and  $TT6^2_{au}$  tiling units (sheet 2), (c)  $GT3^2_{au}$  and  $GT3^2_{ad}$  tiling units (sheet 3) and (d)  $GG3^2_{au}$  and  $TT6^2_{ad}$  tiling units (sheet 1) lacking alternate hydrogen bonding strands. G-quartets are highlighted by white ovals.

### 3.4.4 Analysis of Results

In this section, we analyze the stability of the ordered sheet structure formed by the (GT)<sub>4</sub> sequence. A parameter that describes order is the conformational space accessible to the bases of DNA that increases with the entropy of the bases. We expect that an ordered structure will have lower entropy and therefore its components will be confined to a smaller region. In order to obtain the accessible space for bases in the presence and absence of graphite or hydrogen bonding partners, we track the locations of their centroids during dynamics simulations in a plane parallel to the graphite substrate. Figures 3.5a,b show the base centroid positions for sheets 1 and 3 obtained between 4 and 5 ns of dynamics, and for two control simulations, respectively. It is evident from visual inspection of Figure 3.5a, the structure with GG/TT tiling units, that the bases remain quite confined to a small area. In comparison, the structure with GT tiling units, Figure 3.5b, has considerably larger fluctuations. This comparison more quantitatively supports the observation that the formation of G-quartets, by increasing the number of hydrogen bonding possibilities, provides considerable additional stability to the structure. This role of inter-strand hydrogen bonding is confirmed by the observation (Figure 3.5c) that, if alternate strands are removed from the simulations, therefore removing stabilization by inter-strand hydrogen bonds, the fluctuations of the remaining bases increases significantly (Figure 3.5c). Finally, if we retain all the ssDNA strands but remove the graphite layer, we find that the structure quickly loses its order (Figure 3.5d). Therefore, we conclude that both a substrate on which to adsorb strongly, and hydrogen bonding between strands, are required to stabilize  $\beta$ -sheet structures. Within the possibilities permitted by arrangements of the dimers introduced in the previous section, certain

structures achieve considerably greater stability by forming additional hydrogen bonding possibilities, e.g., by arranging neighboring Guanines into a quartet.



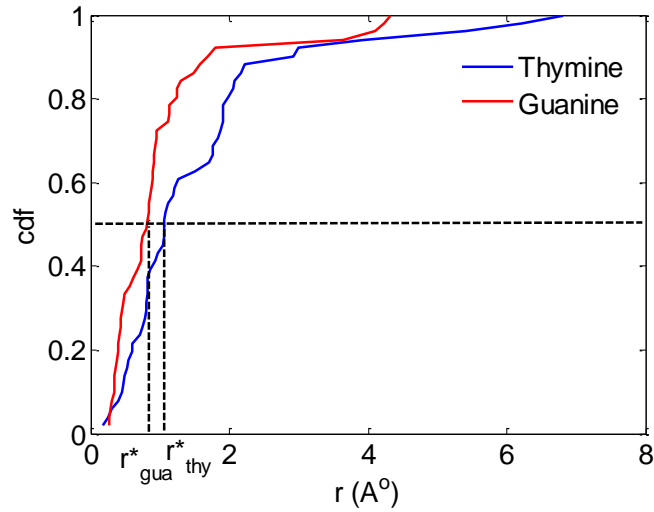
**Figure 3.5.** Base centroid positions for the  $(GT)_4$  sheet structures between 4 ns and 5 ns of dynamics: (a) sheet 1 with  $GG3^2au$  and  $TT6^2ad$  tiling units (b) sheet 3 with  $GT3^2au$  and  $GT3^2ad$  tiling units. (c) sheet 1 lacking alternate hydrogen bonding strands between 0.5 ns and 1.5 ns (d) sheet 1 lacking graphite surface between 0.5 ns and 1.25 ns.

To quantify accessible area for the bases, we analyze the distribution of base locations. We define two parameters corresponding to the freedom of the bases or the accessible space for bases, namely constraining radius,  $r^*$  and strength of constraining potential,  $k^*$ . The parameters are determined from the centroid locations of a base obtained within a 500 ps dynamics interval. Two factors that can give an incorrect

estimate of the constraining parameters are the overall drift and rotation of the sheet structure. We subtract the centroid of the sheet structure from the base centroid to remove the drift of the sheet and choose a relatively small time interval of 500 ps to reduce the error due to the rotation of the sheet. We assume that in 500 ps the base centroid should be able to access most of the available space. Over a time period of 500 ps, we calculate the cumulative distribution function (cdf) of the base centroid location as a function of the radial distance from its mean (Figure 3.6). The radial distance at which cdf is equal to 0.5 defines the constraining radius,  $r^*$  and the corresponding constraining effective spring constant,  $k^*$  is given as

$$k^* = \frac{2k_B T}{r^{*2}} \quad (3.14)$$

where  $k_B$  is the Boltzmann constant and  $T$  is the room temperature. We find  $r^*$  and  $k^*$  in time intervals of 500 ps each for dynamics results obtained between 2 ns and 6 ns, i.e.,  $r^*_1$  and  $k^*_1$  obtained between 2 ns and 2.5 ns,  $r^*_2$  and  $k^*_2$  obtained between 2.1 ns and 2.6 ns, ... and  $r^*_N$  and  $k^*_N$  obtained between 5.5 ns and 6 ns. We obtain the average values for  $r^*$  and  $k^*$  for each base in the sheet. Further averaging the values on the basis of type of base, thymine and guanine, we obtain the  $r^*$  and  $k^*$  values for thymine and guanine.

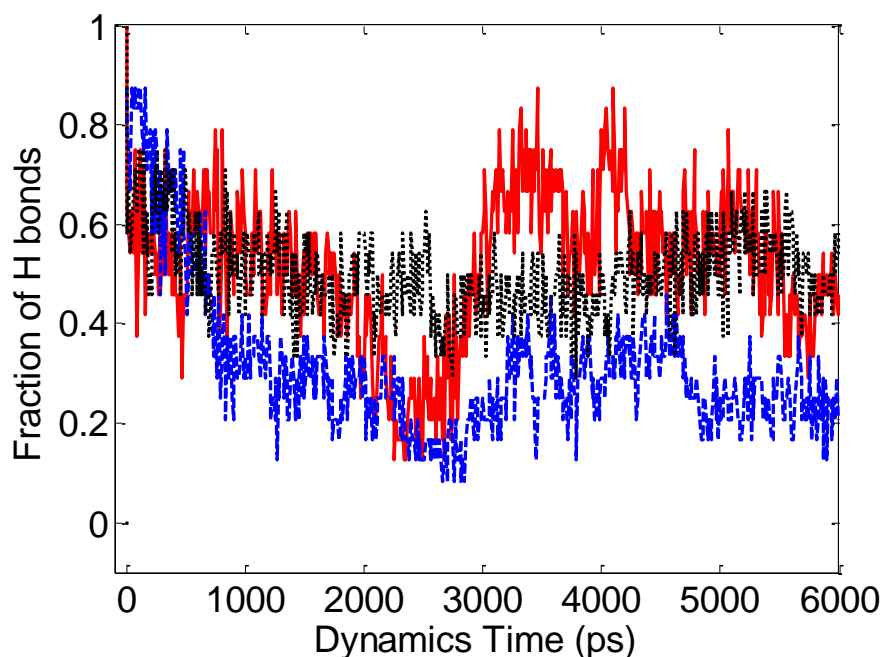


**Figure 3.6.** Cumulative distribution function (cdf) as a function of radial distance of bases from their mean location. The radial distance at which cdf equals 0.5 gives the constraining radius  $r^*$  and corresponding constraining spring  $k^*$ .

Large  $r^*$  or low  $k^*$  means more flexibility for bases leading to disorder in sheet structure and vice versa. ( $r^*_{thy}$  Å,  $k^*_{thy}$  Nm<sup>-1</sup>,  $r^*_{gua}$  Å,  $k^*_{gua}$  Nm<sup>-1</sup>) values for the three sheet structures with GG3<sup>2</sup>au/TT6<sup>2</sup>ad, GG3<sup>2</sup>ad/TT6<sup>2</sup>au and GT3<sup>2</sup>ad/GT3<sup>2</sup>au tiling units are (3.8±0.24, 0.13±0.02, 3.6±0.21, 0.11±0.01), (4.1±0.25, 0.09±0.01, 3.5±0.19, 0.11±0.01) and (4.12±0.25, 0.08±0.01, 3.7±0.19, 0.09±0.01), respectively (mean ± standard error). We find that, irrespective of how the tiling units are arranged to form sheet structures, the bases are constrained almost equally by the interactions predominantly arising between adjacent strands. Averaging the parameter values for thymine and guanine bases in all the sheet structures, we have ( $r^*_{thy}$  Å,  $k^*_{thy}$  Nm<sup>-1</sup>,  $r^*_{gua}$  Å,  $k^*_{gua}$  Nm<sup>-1</sup>) = (4±0.25, 0.1±0.01, 3.6±0.19, 0.11±0.01) which show quite similar constraining potentials for the bases, thymine and guanine. For the case of sheet 1 with GG3<sup>2</sup>au/TT6<sup>2</sup>ad tiling units lacking hydrogen bonding strands, these values are (6.4±0.23, 0.02±0.002, 7.2±0.37, 0.02±0.002). Large  $r^*$  and low  $k^*$  in the absence of

hydrogen bonding shows that hydrogen bonds are necessary to maintain order in the sheet structures.

As a second measure of relative stability of the sheet structure, we track the number of hydrogen bonds. The criteria for the existence of a hydrogen bond (A-H...B) between the donor pair (A-H) and the acceptor (B) are that the distance between H and B should be less than 3.5 Å and the angle AHB should be between 140° and 180°. Sheets 1 and 2, with GG3<sup>2</sup>au/TT6<sup>2</sup>ad and GG3<sup>2</sup>ad/TT6<sup>2</sup>au tiling units, respectively, have a significantly greater number of hydrogen bonds compared to sheet 3 with GT3<sup>2</sup>au/GT3<sup>2</sup>ad tiling units (Figure 3.7). This confirms our reasoning that the sheets 1 and 2 with favorable centrosymmetric hydrogen bonding and G-quartet configuration are more stable than sheet 3. From the study of ordered structures on planar graphite we therefore conclude that: (i) confinement to a plane by strong adsorption and inter-strand hydrogen bonding are both needed to stabilize ordered  $\beta$ -sheet structures, (ii) the centrosymmetric hydrogen bonding configuration is preferred, (iii) sheets formed by GG3<sup>2</sup>au/TT6<sup>2</sup>ad and GG3<sup>2</sup>ad/TT6<sup>2</sup>au tiling units are more stable than the sheets with GT3<sup>2</sup>au/GT3<sup>2</sup>ad tiling units, and (iv) G-quartet structures form spontaneously, contributing additionally to the stability of the ordered sheets.



**Figure 3.7.** Fraction of hydrogen bonds as a function of dynamics time for sheet 1 formed by GG3<sup>2</sup>ad/TT6<sup>2</sup>au tiling units (red solid line), sheet 2 formed by GG3<sup>2</sup>au/TT6<sup>2</sup>ad tiling units (black dotted line) and sheet 3 formed by GT3<sup>2</sup>au/GT3<sup>2</sup>ad tiling units (blue dashed line).

### 3.5 (GT)<sub>30</sub> $\beta$ -Barrels on SWCNTs

In this section we examine the hypothesis is that recognition of SWCNTs by  $\beta$ -barrels is based on matching diameter and chirality between the two by conducting MD simulations on a number of different  $\beta$ -barrels constructed from the same  $\beta$ -sheet, on a given, (6,5), SWCNT.

#### 3.5.1 Creating DNA $\beta$ -barrels

Starting with the 2D sheet structure, a barrel can be obtained by rolling the sheet in the direction of the roll-up vector,  $\mathbf{c}$ , and connecting two equivalent points on the periodic sheet, for example, two equivalent phosphorus atoms. The magnitude of the roll-



up vector becomes the circumference of the barrel. Discrete values for  $c$  imply discrete diameter barrels. Figure 3.1f shows one such barrel created by rolling in the direction shown in Figure 3.1c. The vector  $c$  can be written as a linear combination of unit cell parameters of the sheet,  $a$  and  $b$ , (Figure 3.3) as

$$c = pa + qb \quad (3.15)$$

where  $p$  and  $q$  are integers. The magnitude of the vector  $c$  is

$$c = \sqrt{(pa)^2 + (qb)^2 - 2pa \cdot qb \cdot \cos \theta} \quad (3.16)$$

Similar to the chirality of nanotubes, we can define the chirality of the barrels based on the roll-up direction and unit cell parameters. The angle between the roll-up vector  $c$  and the unit cell vector  $b$ ,  $\theta_{ch}$ , is given as

$$\theta_{ch} = \sin^{-1} \left( \frac{pa \cdot \sin(\pi - \theta)}{c} \right) = \sin^{-1} \left( \frac{pa \cdot \sin(\theta)}{c} \right) \quad (3.17)$$

to which we add angle,  $\alpha$ , to obtain the true chirality of the  $\beta$ -barrel (see Figure 3.3g). The diameter of the barrel,  $d_{barrel}$ , is found by dividing Equation (3.16) by  $\pi$  and the diameter of its available inner space is calculated by subtracting from it twice the vdW distance  $b_{vdw}$  between the base and the SWCNT ( $b_{vdw} \approx 3.5 \text{ \AA}$ ).

$$d_{tube} = d_{barrel} - 2b_{vdw} \quad (3.18)$$

### 3.5.2 Molecular Dynamics of (GT)<sub>30</sub> barrel structures

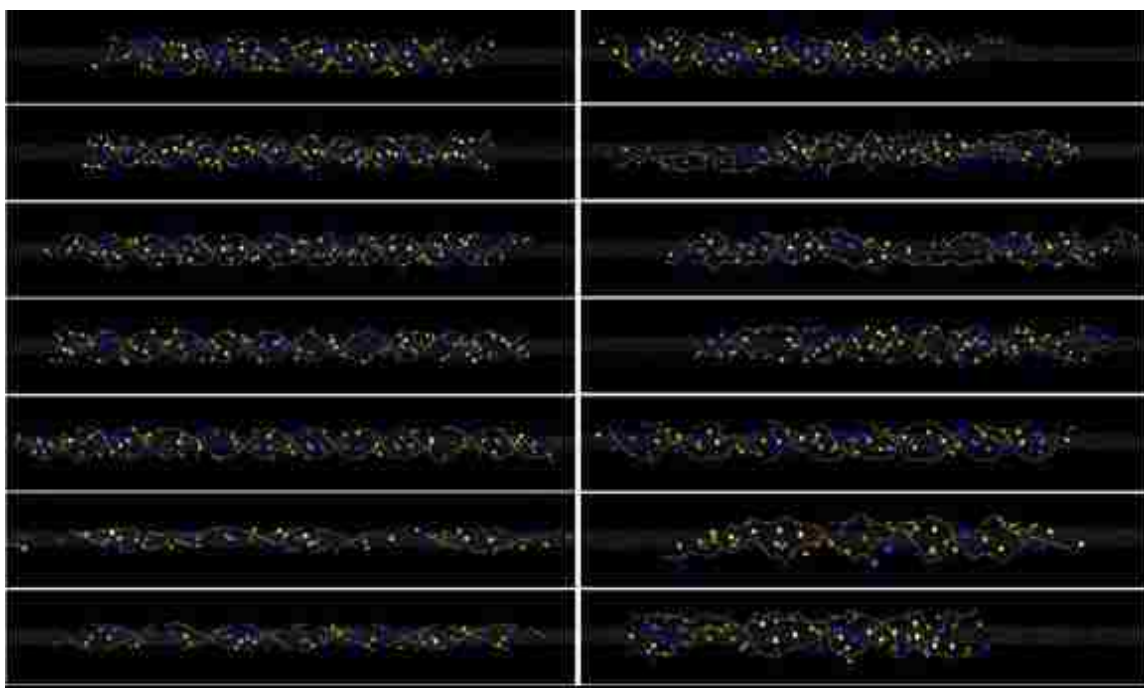
We carried out MD simulations with a number of  $\beta$ -barrel structures based on (GT)<sub>30</sub> sheets wrapped around a (6,5) SWCNT. Of the ten possible (GT)<sub>n</sub> sheets, we have chosen the GG-TT hydrogen-bonding scheme because of the greater stability it exhibited in MD simulations on graphite. In this study, we limit ourselves to the (6,5)

chirality nanotube because of its abundance in *SWeNT* CoMoCAT® nanotubes. We have examined seven different roll-up vectors (Figure 3.1a). Note that all of the rolling occurred “out of the page” so that the O4’ atoms in the Guanine sugar rings all pointed inward, or toward the SWCNT. Rolling “into the page” would form a second set of seven. For these seven barrels, we ask: Choosing one of the (GT)<sub>n</sub> sheets and a single type of SWCNT, what is the effect of choosing different roll-up vectors, each one of which yields a different radius and chirality? Specifically, do the molecular simulations support the notion that  $\beta$ -barrels that match the core SWCNT better are more ordered and stable?

### 3.5.3 Results for (GT)<sub>30</sub> $\beta$ -barrels

Figure 3.8 shows the seven structures at the beginning and after 6 ns of MD simulation. These seven are numbered sequentially 1 to 7, with decreasing  $\beta$ -barrel diameters. The largest diameter,  $d_{tube}$ , is 12.8 Angstroms while the smallest is 3.6 Angstroms, compared to 7.56 Angstroms for the core (6,5) SWCNT. Qualitatively, it can be seen that in all of the cases the DNA strands remain adsorbed onto the nanotube. Closer inspection shows that many of the T-T hydrogen bonds have broken, but in the more stable structures the G-G h-bonds largely remain intact. The tight-fitting case, with a starting barrel diameter of 3.6 Å, quickly becomes disordered. In order to create DNA/SWCNT hybrids with  $\beta$ -barrels smaller than the actual SWCNT diameter, carbon-carbon bond distances in the nanotubes were reduced, effectively reducing the SWCNT diameter. Once the SWCNT was able to be inserted into the  $\beta$ -barrel, the C-C bond distances were slowly increased and the structure was continuously minimized. The

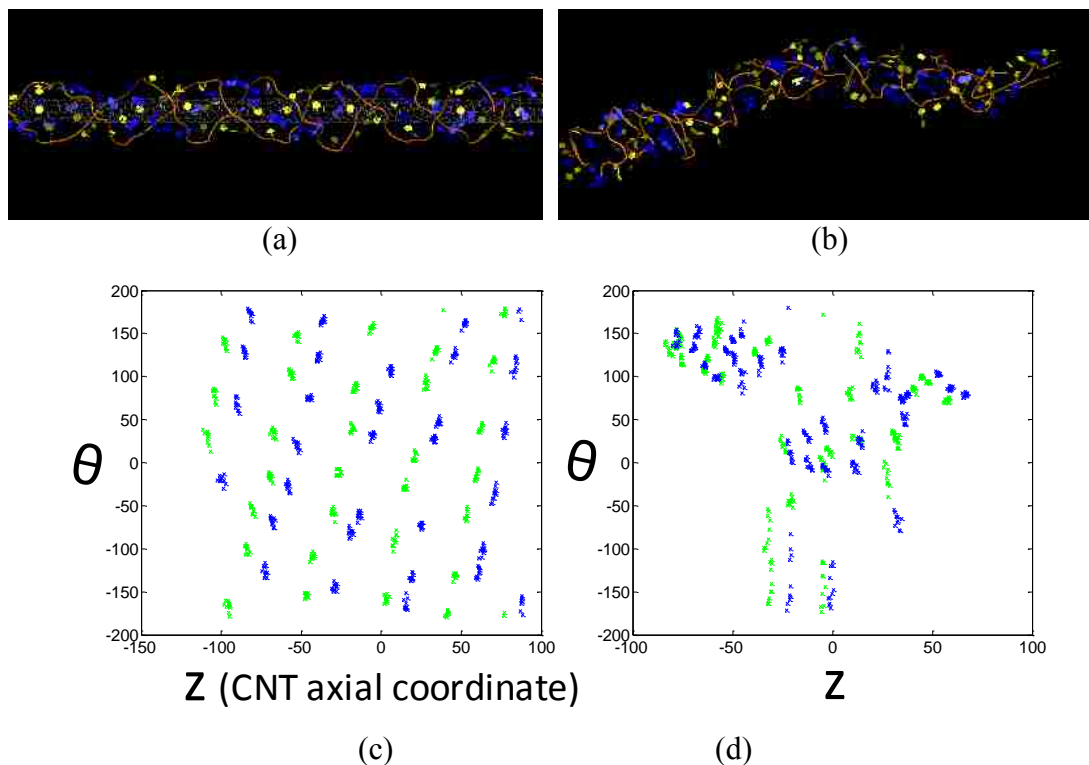
loose-fitting case, 12.8 Å in diameter, also loses order, although that is not so apparent from a visual inspection. The intermediate case shown in Figure 3.8, with barrel diameter of 7.7 Å, fits the SWCNT well and appears to maintain an ordered structure. We observed that when the  $\beta$ -barrel and SWCNT diameters are highly mismatched, the barrel responds to the imposed strain by deforming axially. In the process, inter-strand hydrogen bonds are broken. It is possible that, given sufficient simulation time, one configuration could transform into another by re-forming hydrogen bonds, effectively changing its rollup vector,  $c$ .



**Figure 3.8.** Seven configurations of DNA/SWCNT hybrid  $\beta$ -barrels before (left) and after (right) 6 ns dynamics simulation. Waterbox and  $\text{Na}^+$  counter-ions have been removed for ease of viewing.

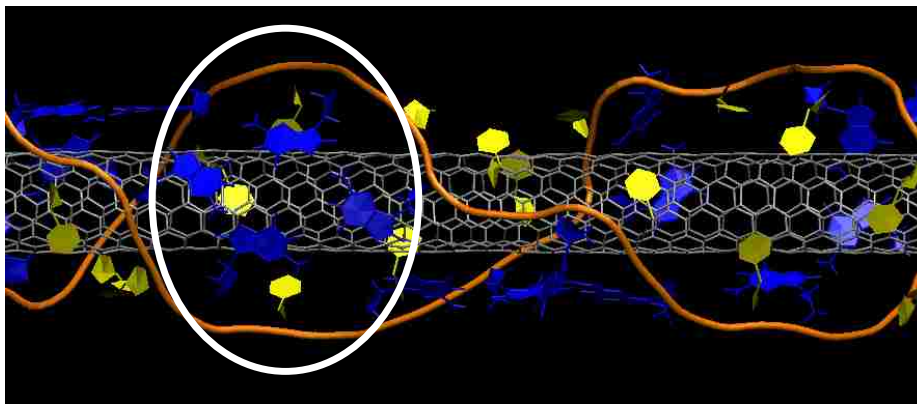
We conducted two control simulations to understand the stabilizing role of inter-strand hydrogen bonding and of the SWCNT core. Figures 3.9a and b show configuration 5 after 6 ns of dynamics simulation with and without a SWCNT core,

respectively. Figures 3.9c and d show base centroid positions for the structures at different times, reported as a function of the angle  $\theta$  around the circumference as one traverses down the axial length of the nanotube. From Figure 3.9b we observe that the barrel structure changes shape considerably and hence is no longer stable, absent the SWCNT core. Figure 3.9c clearly shows that with the stabilizing influence of the SWCNT core, base centroids remain in an ordered arrangement, which is lost when the SWCNT is removed, (Figure 3.9d). Similar to the case of sheets on graphite, we conducted a second control simulation in which one of the two (GT)<sub>30</sub> strands was removed. Again, we found that removal of inter-strand hydrogen bonds in this manner results in a large increase of disorder.



**Figure 3.9.** MD simulation of  $\beta$ -barrel structure, configuration 5, (a) with and (b) without a SWCNT core. Centroid positions for given for a 100 ps time frame (c) with and (d) without a SWCNT core.

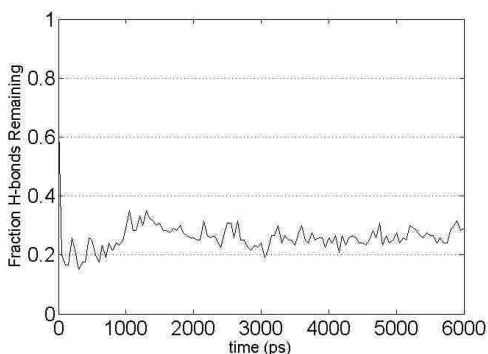
Like in the sheet structures, for the more stable configurations (e.g., numbers 4, 5) we observe the spontaneous formation of G-quartets. The flexibility of the backbone allows enough freedom so that this well-documented structure can emerge.<sup>43</sup> A particular instance is highlighted by the white oval in Figure 3.10 for configuration 5. Such quartet formation doubles the number of hydrogen bonds holding the barrel together by adding an extra four intra-strand hydrogen bonds per quartet. We suggest that the formation of such quartets is key to maintaining stability of the structures over long periods of time. The version of the barrel studied here consists of two helical grooves, one consisting of guanines and the other of thymines. Note that since the backbone deforms to accommodate the formation of the G-quartets in the guanine groove, Thymines in the neighboring groove are pulled away from each other, forcing their respective hydrogen bonds to break.



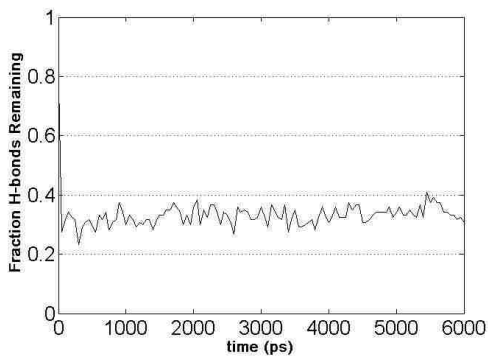
**Figure 3.10.** MD simulation showing development of the G-quartet structure on a nanotube, highlighted by the white oval.

For a more quantitative analysis of the MD simulations, we computed both the number of remaining hydrogen bonds (normalized by the starting value) and a constraining radius,  $r^*$ , as described in Section 3.4. Figure 11 shows a time progression plot of fraction of hydrogen bonds remaining versus time for configurations 4, 5, and 6.

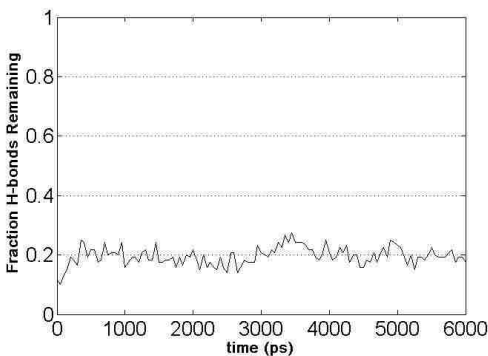
Note that all configurations start at 1 but initially drop off very rapidly as the  $\beta$ -barrels conform to the SWCNT substrate. Ultimately, they each reach a certain asymptotic value, which we have reported in Table 3.4. Table 3.5 provides constraining radius,  $r^*$ , and strength of constraining potential,  $k^*$  for various configurations studied.



(a)



(b)



(c)

**Figure 3.11.** Fraction of inter-strand hydrogen bonds present with respect to starting  $\beta$ -barrel configurations. Configurations 4, 5, and 6 shown. Note the rapid initial drop in h-bonds, followed by an asymptotic equilibrium number.

**Table 3.4.** Fraction of hydrogen bonds remaining at the end of 6 ns simulation, with standard error, for GG-TT  $\beta$ -barrel structures.

Configuration	Asymptotic	
	Fraction of H-bonds (after 6 ns)	(p,q)
1	0.286 ± 0.004	(4,1)
2	0.206 ± 0.006	(-3,1)
3	0.202 ± 0.003	(3,1)
4	0.265 ± 0.003	(-2,1)
5	0.353 ± 0.004	(2,1)
6	0.192 ± 0.003	(-1,1)
7	0.090 ± 0.012	(1,1)

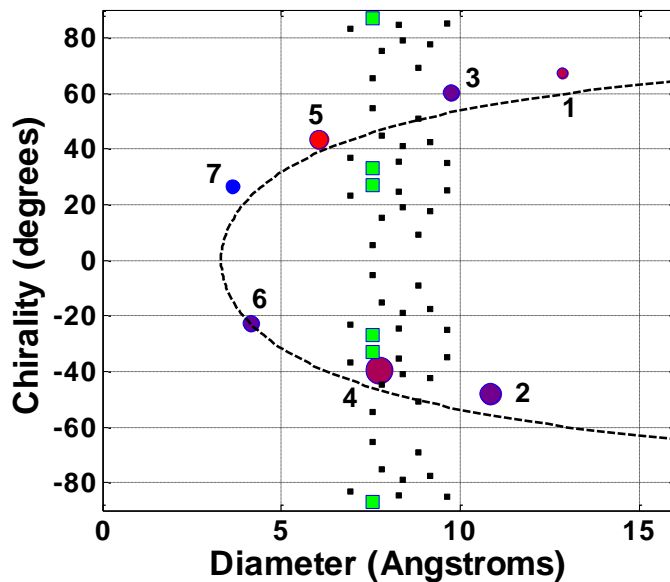
**Table 3.5.** Constraining potential parameters for (GT)<sub>30</sub>  $\beta$ -barrel simulations.

Configuratio n	$r^*_{gu}$ a	±	$r^*_{thy}$	±	$k^*_{gua}$	±	$k^*_{thy}$	±
1	5.1	0.08	5.1	0.09	0.070	3	0.071	3
2	3.7	0.13	3.5	0.12	0.091	5	0.097	4
3	4.1	0.10	4.0	0.09	0.069	3	0.069	3
4	3.2	0.09	3.3	0.10	0.11	5	0.10	5
5	3.9	0.10	3.8	0.09	0.070	3	0.074	3
6	4.1	0.15	3.6	0.12	0.067	4	0.085	4
7	4.6	0.14	4.4	0.12	0.055	3	0.059	3
<b>control</b>	21.3	0.34	21.5	0.30	0.002	4	0.0022	0

$r^*$  and  $k^*$  values reported in Å and nm<sup>-1</sup> with standard error, respectively. Control simulation is ‘configuration 3’ with one (GT)<sub>30</sub> strand removed to eliminate inter-strand hydrogen bonds.

To compare simulated the simulated values, a chart of SWCNT and  $\beta$ -barrel chirality vs. diameter is constructed. Figure 3.12 shows by small black squares a number of SWCNTs typically found in the CoMoCAT fabrication route. The larger green squares represent the (6,5) SWCNT, which is dominant in CoMoCAT and is the one studied here. Figure 3.12 also shows the seven barrel configurations as circles. The diameter of each circle is inversely proportional to  $r^*$ , i.e., larger circles represent more

confined and hence more stable DNA barrel structures. Each circle is colored on a gradient from blue to red, proportional to the number of H-bonds, i.e., structures represented by redder circles have a greater number of hydrogen bonds and are more stable. Therefore, an ordered DNA barrel structure is represented by a larger and redder circle. It is apparent from Figure 3.12 that there is a strong correlation between stability and order on the one hand, and the ‘distance’ from the (6,5) SWCNT on the other. In other words, the DNA barrels (4 and 5) that better match the (6,5) SWCNT diameter and chirality (closer to green squares) are more stable and ordered (larger and redder). The dashed line represents the locus of chirality and barrel diameter that would be achieved using average unit cell parameters and serves as a guide for the eye to observe the trend in discrete barrel diameters.



**Figure 3.12.** Chiral angle vs. diameter for GG-TT DNA  $\beta$ -barrels (circles) and CoMoCAT<sup>®</sup> SWCNTs, squares: (6,4), (9,1), (6,5), (8,3), (7,5), (8,4), (10,2), (9,4), and (8,6) SWCNT chiralities. The diameter of each circle is inversely proportional to  $r^*$ , i.e., larger circles represent more confined and hence more stable DNA barrel structures. Each circle is colored on a gradient from blue to red, proportional to the number of H-bonds, i.e., structures represented by redder circles have a greater number of hydrogen bonds and are more stable. Therefore, an ordered DNA barrel structure is represented by a larger and redder circle. Numeric values found in supporting information.



Several other facts are interesting. The allowed barrel diameters are in the correct range to match SWCNTs but are well-separated from each other, which allows discriminative 1-1 matching. The DNA barrels are quite flexible and the starting diameter and chirality can likely adjust somewhat. Consider the (9,1) SWCNT, which have the same diameter as (6,5) but different chirality. The results shown in Figure 3.9 suggest that both diameter and chirality matching play a role, thus providing a rationale for chirality-specific recognition.

The main findings of this section are (i) the SWCNT substrate, as well as inter-strand hydrogen bonding, are necessary to stabilize the DNA barrel structures; (ii) Recognition by DNA  $\beta$ -barrels of SWCNTs appears to require matching of both diameter and chirality; (iii) The formation of quartet structures contributes significant additional stabilizing influence.

### 3.6 Conclusions

Using molecular simulations, we have examined the proposed structural basis for the recently discovered ability of certain ssDNA sequences to recognize specific carbon nanotubes. Molecular dynamics simulations support the idea that stable ssDNA strands can form  $\beta$ -sheet and  $\beta$ -barrel structures when adsorbed onto a surface such as graphite or a carbon nanotube. We have identified a set of 20 base-dimer tiling units that can be used to form extended, ordered, DNA sheet structures. In this work, we have studied the (GT)<sub>n</sub> sequence in some detail. We find that, by the formation of G-quartets, sheets with

separate GG and TT tiling units are significantly more stable than those with GT tiling units.

Using the stable sheet form, we have simulated seven different DNA barrels around a (6,5) SWCNT core. We find that both the SWCNT core and inter-strand hydrogen bonds are needed for a stable and ordered DNA  $\beta$ -barrel. The results also show that better matching of diameter and chirality with the core SWCNT confers higher stability and order on the DNA  $\beta$ -barrels. This finding therefore supports the hypothesis that chirality-specific recognition of SWCNTs by DNA proceeds by matching of DNA  $\beta$ -barrel diameter and chirality with that of the core SWCNT. The proposed ordered DNA models provide the structural basis for SWCNT recognition in SWCNT purification via ion-exchange chromatography. They also predict the charge density and mass ratio of the DNA—SWCNT hybrid in good agreement with previous capillary electrophoresis measurements<sup>14</sup> without any additional fitting parameters.

### **3.7 Acknowledgment**

This work, especially in Section 3.4, was performed in collaboration with Suresh Manohar of Lehigh University. I would like to thank Anand Jagota for his mentoring activities. The work was supported by the National Science Foundation under Grant CMS-0609050. Additionally, we gratefully acknowledge many useful discussions with Ming Zheng and Xiaomin Tu of NIST.

### 3.8 References

- (1) Watson, J. D.; Crick, F. H., *Nature* **1953**, *171*, 737.
- (2) Vargason, J. M.; Henderson, K.; Ho, P. S., *Proceedings of the National Academy of Sciences of the United States of America* **2001**, *98* (13), 7265-7270.
- (3) Basham, B.; Schroth, G. P.; Ho, P. S., *Proceedings of the National Academy of Sciences of the United States of America* **1995**, *92* (14), 6464-6468.
- (4) Rich, A.; Zhang, S. G., *Nature Reviews Genetics* **2003**, *4* (7), 566-572.
- (5) Ha, S. C.; Lowenhaupt, K.; Rich, A.; Kim, Y. G.; Kim, K. K., *Nature* **2005**, *437* (7062), 1183-1186.
- (6) Barciszewski, J. F., B.; Clark, C., Springer: New York, 1999.
- (7) Ahsan, A.; Rudnick, J.; Bruinsma, R., *Biophysical Journal* **1998**, *74*, 132-137.
- (8) Cheng, J.; Randall, A. Z.; Sweredoski, M. J.; Baldi, P., *Nucleic Acids Research* **2005**, *33*, W72-W76.
- (9) Cheng, J. L.; Baldi, P., *Bioinformatics* **2005**, *21*, I75-I84.
- (10) Zheng, M.; Jagota, A.; Semke, E. D.; Diner, B. A.; Mclean, S. R. L.; Richardson, R. E.; Tassi, N. G., *Nature Materials* **2003**, *2*, 338-343.
- (11) Zheng, M.; Jagota, A.; Strano, M. S.; Santos, A. P.; Barone, P.; Chou, S. G.; Diner, B. A.; Dresselhaus, M. S.; Mclean, S. R. L.; Onoa, G. B.; Samsonidze, G. G.; Semke, E. D.; Usrey, M.; Walls, D. J., *Science* **2003**, *302* (5650), 1545-1548.
- (12) Huang, X.; Mclean, S. R. L.; Zheng, M., *Analytical Chemistry* **2005**, *77* (19), 6225-6228.
- (13) Tu, X. M.; Manohar, S.; Jagota, A.; Zheng, M., *Nature* **2009**, *460* (7252), 250-253.
- (14) Khripin, C. Y.; Manohar, S.; Zheng, M.; Jagota, A., *Journal of Physical Chemistry C* **2009**, *113* (31), 13616-13621.
- (15) Sowerby, S. J.; Holm, N. G.; Petersen, G. B., *Biosystems* **2001**, *61* (1), 69-78.
- (16) Sowerby, S. J.; Cohn, C. A.; Heckl, W. M.; Holm, N. G., *Proceedings of the National Academy of Sciences of the United States of America* **2001**, *98* (3), 820-822.
- (17) Sowerby, S. J.; Edelwirth, M.; Heckl, W. M., *Journal of Physical Chemistry B* **1998**, *102* (30), 5914-5922.
- (18) Tao, N. J.; Shi, Z., *Journal of Physical Chemistry* **1994**, *98* (5), 1464-1471.
- (19) Manohar, S.; Tang, T.; Jagota, A., *Journal of Physical Chemistry C* **2007**, *111* (48), 17835-17845.
- (20) McCarthy, B.; Coleman, J. N.; Czerw, R.; Dalton, A. B.; Panhuis, M. I. H.; Maiti, A.; Drury, A.; Bernier, P.; Nagy, J. B.; Lahr, B.; Byrne, H. J.; Carroll, D. L.; Blau, W. J., *Journal of Physical Chemistry B* **2002**, *106* (9), 2210-2216.
- (21) Edelwirth, M.; Freund, J.; Sowerby, S. J.; Heckl, W. M., *Surface Science* **1998**, *417* (2-3), 201-209.
- (22) Mamdouh, W.; Dong, M. D.; Xu, S. L.; Rauls, E.; Besenbacher, F., *Journal of the American Chemical Society* **2006**, *128* (40), 13305-13311.
- (23) Sowerby, S. J.; Stockwell, P. A.; Heckl, W. M.; Petersen, G. B., *Origins of Life and Evolution of the Biosphere* **2000**, *30* (1), 81-99.
- (24) Saenger, W., Principles of Nucleic Acid Structure. Cantor, C. R., Ed. Springer-Verlag: New York, 1984; pp 134-135.
- (25) Jeffrey, G. A.; Saenger, W., Springer-Verlag: 1991.




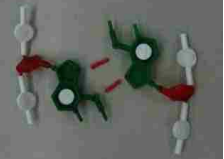
- (26) Mamdouh, W.; Kelly, R. E. A.; Dong, M. D.; Kantorovich, L. N.; Besenbacher, F., *Journal of the American Chemical Society* **2008**, *130* (2), 695-702.
- (27) Sowerby, S. J.; Edelwirth, M.; Reiter, M.; Heckl, W. M., *Langmuir* **1998**, *14* (18), 5195-5202.
- (28) Xu, S. L.; Dong, M. D.; Rauls, E.; Otero, R.; Linderoth, T. R.; Besenbacher, F., *Nano Letters* **2006**, *6* (7), 1434-1438.
- (29) Otero, R.; Schock, M.; Molina, L. M.; Laegsgaard, E.; Stensgaard, I.; Hammer, B.; Besenbacher, F., *Angewandte Chemie-International Edition* **2005**, *44* (15), 2270-2275.
- (30) Gu, J. D.; Leszczynski, J., *Journal of Physical Chemistry A* **2000**, *104* (31), 7353-7358.
- (31) Hackett, J. A.; Feldser, D. M.; Greider, C. W., *Cell* **2001**, *106* (3), 275-286.
- (32) Parkinson, G. N.; Lee, M. P. H.; Neidle, S., *Nature* **2002**, *417* (6891), 876-880.
- (33) Phillips, K.; Dauter, Z.; Murchie, A. I. H.; Lilley, D. M. J.; Luisi, B., *Journal of Molecular Biology* **1997**, *273* (1), 171-182.
- (34) Brett, A. M. O.; Chiorcea, A. M., *Langmuir* **2003**, *19*, 3830-3839.
- (35) Paquim, A. C.; Oretskaya, T. S.; Brett, A. M. O., *Biophysical Chemistry* **2006**, *121* (2), 131-141.
- (36) Paquim, A. C.; Oretskaya, T. S.; Brett, A. M. O., *Electrochimica Acta* **2006**, *51* (24), 5037-5045.
- (37) Cardenas, M.; Braem, A.; Nylander, T.; Lindman, B., *Langmuir* **2003**, *19*, 7712-7718.
- (38) Johnson, R. R.; Kohlmeyer, A.; Johnson, A. T. C.; Klein, M. L., *Nano Letters* **2009**, *9* (2), 537-541.
- (39) Martin, W.; Zhu, W.; Krilov, G., *Journal of Physical Chemistry B* **2008**, *112* (50), 16076-16089.
- (40) *Materials Studio (R)*, Accelrys Inc.: San Diego, CA.
- (41) *CHARMM v. 35b2*, Cambridge, MA.
- (42) Phillips, J. C.; Braun, R.; Wang, W.; Gumbart, J.; Tajkhorshid, E.; Villa, E.; Chipot, C.; Skeel, R. D.; Kale, L.; Schulten, K., *Journal of Computational Chemistry* **2005**, *26*, 1781-1802.
- (43) Davis, J. T., *Angewandte Chemie-International Edition* **2004**, *43* (6), 668-698.
- (44) Saito, R.; Dresselhaus, G.; Dresselhaus, M. S., Imperial College Press: London, 1999.

## 3.9 Appendix


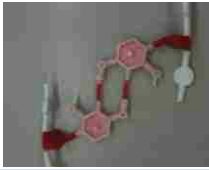



### 3.9.1 Systematic DNA Base Hydrogen Bond Study by Physical Manipulation

In his book, *Principles of Nucleic Acid Structure*, Saenger describes 28 possible conformations in which two bases on different DNA strands can hydrogen bond with at least two hydrogen bonds.<sup>24</sup> With the use of physical models, purchased from *TheDNAStore.com*, we have systematically examined the 28 conformations while applying the conditions that **1)** bases must be coplanar, **2)** neighboring strands must be antiparallel, **3)** along a given strand, the O4' atoms in the sugar rings alternately point up and down as the base alternates from one side to the other, and **4)** the glycosyl sugar-base linkage on the same strand should all be in either syn or anti configuration. Below in Table 3.6 are snapshots of the DNA models in the 28 conformations. If certain configurations are not possible, it is explicitly stated so. In summary, 18 of the 28 configurations have been eliminated due to steric hindrances either between DNA bases or adjacent strand backbones. The configurations remaining are: I, II, III, V, VII, XII, XIV, XV, XXVI, and XXVII.

**Table 3.6.** Hydrogen bonding in DNA base dimer arrangements

Configur- ation	Bases Involved	<i>Syn</i> -Image	<i>Anti</i> -Image	Comments
I	Ade-Ade			
II	Ade-Ade			

III	Gua-Gua			
IV	Gua-Gua		---	Prohibited by steric constraints
V	Ade-Ade			
VI	Gua-Gua		---	Prohibited by intersecting backbones
VII	Gua-Gua			
VIII	Ade-Gua	---		Prohibited by intersecting backbones
IX	Ade-Gua	---		Prohibited by intersecting backbones
X	Ade-Gua	---		Prohibited by intersecting backbones
XI	Ade-Gua	---		Prohibited by intersecting backbones
XII	Thy-Thy			

XIII	Ura-Ura	---	---	Not examining Uracil bases
XIV	Cyt-Cyt			
XV	Cyt-Cyt			
XVI	Ura-Ura	---	---	Not examining Uracil bases
XVII	Ura-Ura	---	---	Not examining Uracil bases
XVIII	Thy-Cyt		---	Prohibited by intersecting backbones
XIX	Gua-Cyt		---	Prohibited by intersecting backbones
XX	Ade-Thy	---		Prohibited by intersecting backbones
XXI	Ade-Ura	---	---	Not examining Uracil bases
XXII	Gua-Ura		---	Prohibited by intersecting backbones
XXIII	Ade-Thy			Prohibited by intersecting backbones
XXIV	Ade-Ura	---	---	Not examining Uracil bases

XXV	Ade-Cyt		---	Prohibited by intersecting backbones
XXVI	Ade-Cyt			
XXVII	Gua-Thy			
XXVIII	Gua-Ura	---	---	Not examining Uracil bases



## **Chapter 4**

### **Sequence Specific Self-Stitching Motif of Short Single-Stranded DNA on a Single-Walled Carbon Nanotube\***

*The DNA-single-walled carbon nanotube (SWCNT) hybrid molecule has attracted significant attention recently for its ability to disperse and sort SWCNTs according to their chirality. Key for utilizing their unique properties is an understanding of the structure of DNA adsorbed on the SWCNT surface, which we study here using molecular simulations. Using replica exchange molecular dynamics (REMD), we explore equilibrium structures formed by single strands of 12-mer oligonucleotides, of varying sequence, adsorbed on a (6,5)-SWCNT. We find a consistent motif in which the DNA strand forms a right-handed helical wrap around the SWCNT, stabilized by ‘stitches’ (hydrogen bonding between distant bases) to itself. Variability among equilibrium populations of DNA self-stitched structures was observed and shown to be directly influenced by DNA sequence and composition. Competition between conformational entropy and hydrogen bonding between bases is predicted to be responsible for the formation of random versus stitched configurations.*

---

\* Portions of this chapter have been published in the Journal of the American Chemical Society

D Roxbury, A Jagota, J Mittal. “Sequence Specific Self-Stitching Motif of Short Single-Stranded DNA on a Single-Walled Carbon Nanotube” *J. Am. Chem. Soc.* **133**, 34, 13545 (2011)

## 4.1 Introduction

Due to its natural amphiphilic behavior,<sup>1</sup> single-stranded DNA (ssDNA) has been shown, through experimental<sup>2-4</sup> and molecular simulation studies,<sup>5-6</sup> to wrap helically around the outside of single-walled carbon nanotubes (SWCNTs). Hydrophobic DNA bases non-covalently bind to the hydrophobic SWCNT surface through  $\pi$ - $\pi$  stacking, with base-dependent binding strengths,<sup>7</sup> while the charge-carrying phosphate-sugar backbone enables dispersion in aqueous medium.<sup>5, 8</sup> Novel applications of DNA-SWCNT hybrids have ranged from chemical detection<sup>9-10</sup> to the innate ability to solubilize and sort SWCNTs based on their chirality, length and diameter.<sup>2, 11</sup> Generally, longer DNA sequences (>30 mers) were shown to have higher thermal stability than shorter ones.<sup>12</sup> However, in recent work, Tu *et al.* have shown that highly sequence-specific short DNA oligomers (10-20 mers), deemed ‘recognition sequences’, can select certain types (chiralities) of SWCNTs from mixtures.<sup>13</sup> This recognition ability of ssDNA has been used to solve a long-standing recalcitrant problem of structure-based sorting of complex mixtures of SWCNTs.<sup>13-14</sup> By quantifying the binding strength through measurement of DNA displacement from the surface of SWCNTs by surfactant molecules, it has been shown experimentally that the addition or subtraction of one base from a recognition sequence strongly affects the relative DNA-SWCNT binding strength,<sup>15</sup> supporting the idea of highly sequence-specific binding. For example, it was found that sequence (TAT)<sub>4</sub>, (i.e. TATTATTATTAT) being the recognition sequence for the (6,5) chirality SWCNT, binds ~20 times stronger than either (TAT)<sub>4</sub>T or (TAT)<sub>3</sub>TA. Interestingly, while longer oligonucleotides (>30 mers) bind stronger than shorter ones (e.g., (TAT)<sub>10</sub>

binds an order of magnitude stronger than (TAT)<sub>4</sub>) they do not show the strong sequence-specificity that the shorter ones do.

Molecular simulation has played a significant role in understanding DNA-SWCNT hybrid structures. Previous studies by Johnson *et al.*, involving a single strand of long ssDNA (60-mer) simulated near an (11,0)-SWCNT, have shown that spontaneous wrapping occurs when the two species encounter each other.<sup>6</sup> More recently, Johnson *et al.* modeled the sequence (GT)<sub>7</sub> around an (11,0)-SWCNT employing replica exchange molecular dynamics (REMD),<sup>16-17</sup> in an effort to reduce the probability that structures remain trapped in local energy minima.<sup>18</sup> From their ~100 ns REMD simulation it was concluded that single strands of DNA can form a variety of structures on the surface of a SWCNT, with no clear preferred state. Furthermore, they have concluded that there is little sequence specificity and in particular no structure forms that would permit longer-range order (multiple strands). It is difficult to reconcile this proposal with the experimental finding of strong sequence-specific recognition. In a previous study, we examined ordered structures that surface-adsorbed oligonucleotides could assume.<sup>19</sup> In agreement with Johnson *et al.*,<sup>18</sup> we found that surface-adsorbed strands of ssDNA prefer a motif in which bases alternate from side to side on the backbone, minimizing crowding, and that hydrogen bonding between adsorbed bases on different strands could lead to the emergence of secondary structures. A number of base pair dimers (including non-Watson-Crick base pairs) were studied systematically, and used to construct DNA  $\beta$ -barrel structures, leading to the hypothesis that such hydrogen bonded structures might stabilize an ordered DNA arrangement as the basis for SWCNT recognition. Since only traditional MD simulations were performed for relatively short simulation times (10 ns),

no attempt was made to examine equilibrium structures. Here we present a study on the equilibrium sequence-specific structures arising from one strand binding to an SWCNT. The (6,5)-SWCNT, its recognition sequence, (TAT)<sub>4</sub>, and some related controls were chosen for simulation. The principal questions we wish to examine are, (a) What are the typical motifs in equilibrium? (b) How strongly does the prevalence and population of these motifs depend on DNA composition and sequence?

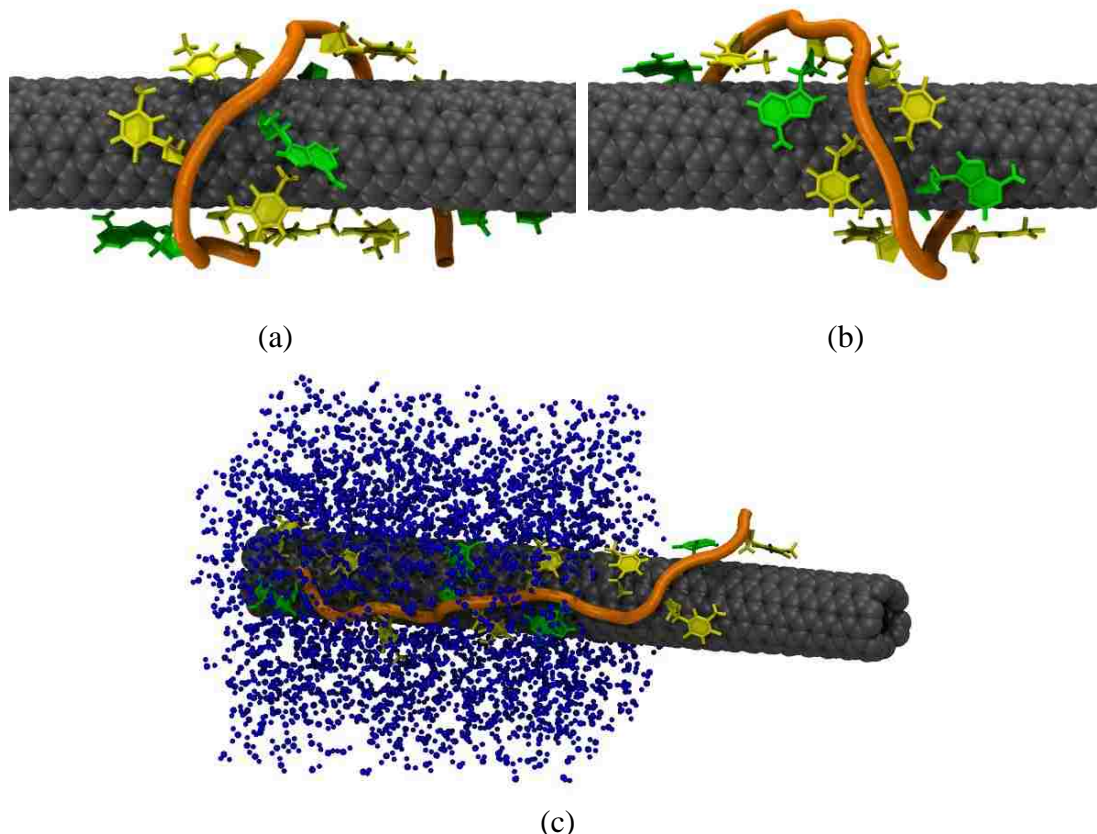
## 4.2 Methodologies

All-atom REMD simulations were performed to study the various structures that single strands of ssDNA can form when exposed to a pristine SWCNT surface. As mentioned previously, we chose the (6,5) chirality SWCNT and its hybrid with the (6,5) recognition DNA strand, (TAT)<sub>4</sub>, for study. As measures of comparison, several other related sequences were examined: A<sub>12</sub> and T<sub>12</sub>, and T<sub>4</sub>A<sub>4</sub>T<sub>4</sub>. The SWCNT used throughout the entire study was a periodic (6,5) chirality tube, 79.70Å in length and 7.46 Å in diameter, where end carbons were covalently bonded to adjacent image carbons. For SWCNT force field parameters, we have used standard CHARMM parameters for the sp<sup>2</sup> hybridized carbon atom. Previously it has been shown that the observed behavior with the CHARMM parameters is consistent with those of Amber-based parameters for SWCNT<sup>20</sup> as well as for oligonucleotides.<sup>21</sup> All structures were created in *Materials Studio*,<sup>22</sup> and visualized in *VMD*.<sup>23</sup>

To run the REMD simulations, the GROMACS 4.5.3 simulation package<sup>24-26</sup> was used with the CHARMM27 force field<sup>27-28</sup>. The DNA strands were initially placed in a *left-handed* helical configuration with all bases being adsorbed onto the SWCNT sidewall

in a backbone-alternating fashion. After a period of 50 ns, the majority of structures were found in the right-handed conformation, strongly suggesting that our results are independent of initial conditions and hence representative of equilibrium. Figure 4.1a and b shows the initial structure for (TAT)<sub>4</sub>-SWCNT, and that of a typical configuration after the initial equilibration period of 50 ns, respectively. The DNA-SWCNT hybrids were then solvated in a 79.7 x 34.6 x 34.6 Å water-box containing approximately 3,000 TIP3P model<sup>29</sup> water molecules and sodium counter-ions, placed randomly, to balance the negative phosphate charges (11 in total), with total system size ~10,000 atoms. Sodium ions were highly dynamic throughout the simulation and represent a concentration of 191.5 mM, not of unreasonable strength for a DNA buffer. A schematic is shown (Figure 4.1c) depicting the explicit water-box that is used in all simulations. Water molecules have not been displayed in any other figure throughout the paper for the sake of clarity. Structures were subjected to 100 ps heating (NVT) to get to 300 K. They were then ready for extended NVT REMD simulation using periodic boundary conditions in all directions with electrostatics calculated using the particle mesh Ewald method (PME).<sup>30</sup> Forty replicas were created for differing DNA sequences, starting in the same initial configuration, having temperatures ranging from 296 K to 587 K, with temperature intervals increasing as absolute temperature increased but chosen so that acceptance ratio remained around 20% with an exchange time of 2 ps. The forty replicas were then run for 200 ns, for a total computational time of 40 x 200 = 8000 ns. The last 150 ns of each configuration were considered production and used for analysis. The time step of the simulation was 2 fs. The trajectories were saved at every 10 ps, yielding a total of 15,000

snapshots for production analysis. For clustering, helicity, and stitching analysis, the room temperature (300 K) replica trajectory was used.



**Figure 4.1.** (a) (TAT)<sub>4</sub>-SWCNT hybrid started in a left-handed helical fashion with bases alternating on either side of the backbone. (b) After a given equilibration period, 50 ns, the majority of structures are found in a right-handed helical configuration (97% for (TAT)<sub>4</sub>). (c) Schematic showing the explicit water-box solvating the hybrids. (Water-box is half-removed in this picture, and fully removed in figures throughout the paper).

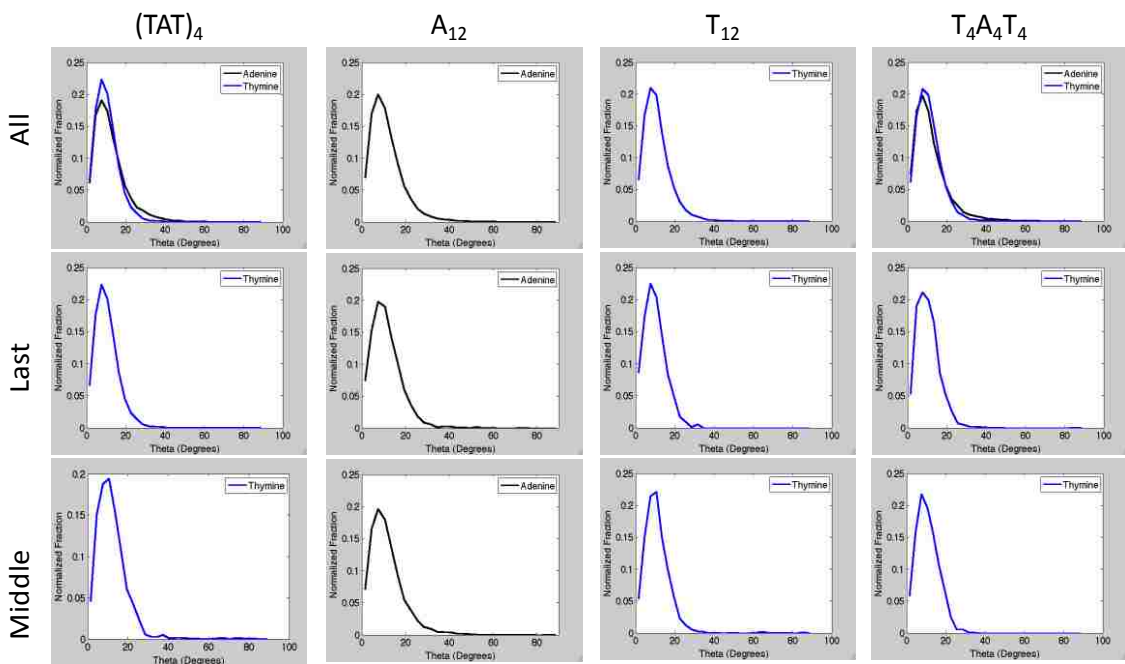
### 4.3 Results and Discussion

The aromatic nature of DNA bases (sharing of  $\pi$ -orbital electrons) gives rise to their intrinsic hydrophobic tendencies, including the ability to stack on hydrophobic surfaces<sup>1</sup>. Multiple reports have confirmed as much as  $10 k_B T/base$  stacking energies (in water) are experienced when DNA bases adsorb onto a flat hydrophobic surface, such as graphite.<sup>31</sup> Because there is at least one base per Kuhn length (a rigid segment of a

freely-jointed chain)<sup>32</sup> for oligonucleotides, they are strongly adsorbed and the entire chain is essentially constrained in the two dimensions of the surface. We have proposed that steric hindrance between adjacent DNA bases promotes conformations in which bases alternate on either side of the backbone. Additionally, bases in such conformations are readily available for hydrogen bonding with other bases.<sup>13-14, 19</sup> For 12-mer oligonucleotide chains it is easy to see that a relatively great amount of energy is required to remove a single chain from such a surface, suggesting that DNA remains bound and selectivity can arise from interactions between adsorbed bases. We therefore hypothesize that the majority of structures will follow the base-alternating motif and that bases will essentially remain stacked onto the SWCNT surface.

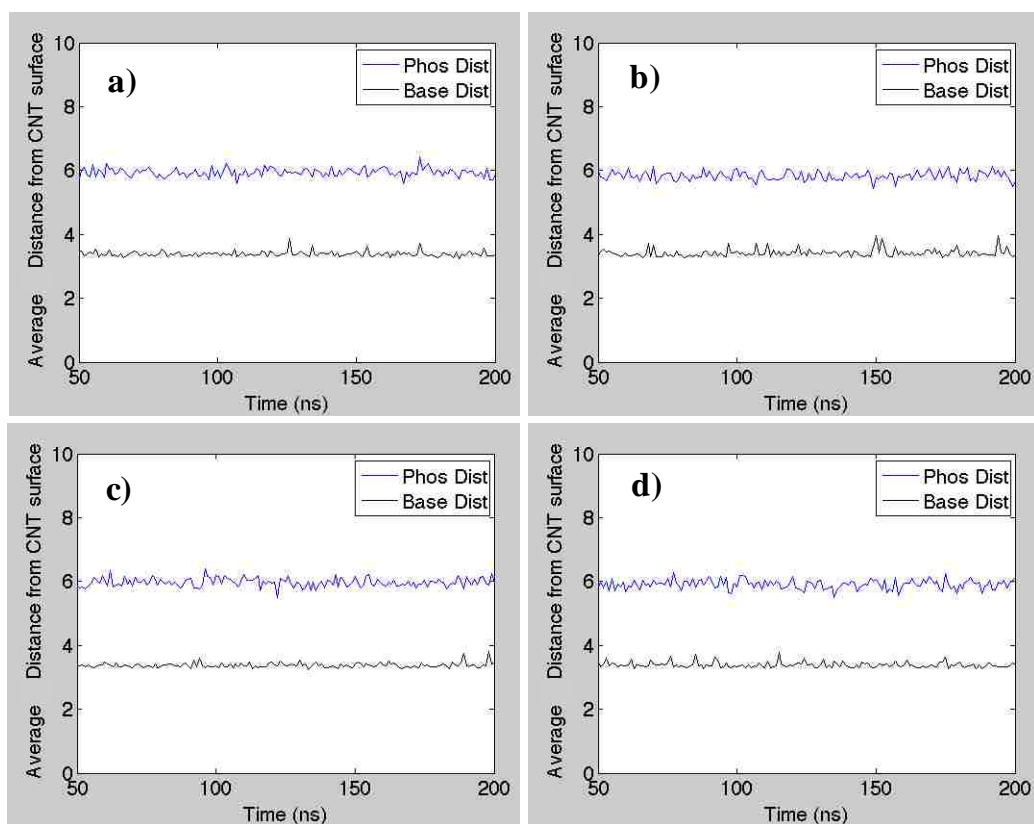
First we investigate the prevalence of the base-alternating motif and base-stacking probabilities for the single-strand (TAT)<sub>4</sub>-(6,5)-SWCNT hybrid and its close relatives, A<sub>12</sub>, T<sub>12</sub>, and T<sub>4</sub>A<sub>4</sub>T<sub>4</sub>. It is known that the aromatic nature of DNA bases causes them to adhere to aromatic surfaces through the overlapping of  $\pi$ -orbital electrons, known as  $\pi$ - $\pi$  stacking. An important characteristic of DNA-SWCNT hybrid structure is the degree to which bases stack on the SWCNT. For the data sampling duration (50-200 ns), the angle between the SWCNT normal and the base centroid normal,  $\theta$ , was monitored for all bases in all configurations. Figure 4.2 shows the probability distribution functions for all bases on the strand, the strand end bases, and the strand middle bases, *All*, *Last*, and *Middle*, respectively. Since there are 12 bases, there will be two end bases, and two middle bases, which will be averaged individually for analyzing. The bin size for plotting was 3° and the peak PDF location occurred at 7.5° (i.e., the third bin). It is apparent that, with the exception of rare non-zero probabilities, DNA bases prefer to stack on the SWCNT

surface at this particular temperature (300K). A quantitative measure of the fraction of bases stacked was obtained by defining all bases with normals within  $30^\circ$  of the SWCNT normal as stacked onto the SWCNT surface. On this basis, base stacking percentages were 98, 97, 98, and 98% for  $(TAT)_4$ ,  $A_{12}$ ,  $T_{12}$ , and  $T_4A_4T_4$ , respectively. To confirm that high temperatures allowed for bases to desorb and switch sides of the backbone at will, base stacking for  $(TAT)_4$  at the highest temperature, 587 K, was found to be 86%, roughly a 12% decrease.



**Figure 4.2.** Probability distribution functions (PDFs) for angle  $\theta$ , between SWCNT normal and base normal. DNA bases in all configurations exhibit the preference to stack on the SWCNT sidewall at an angle of  $7.5^\circ$ .



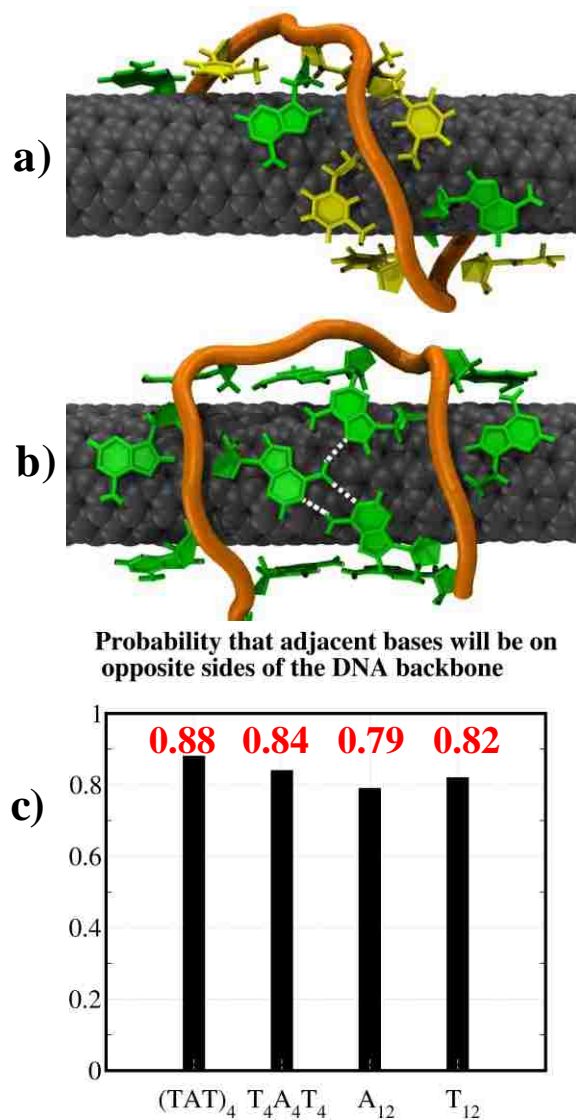


**Figure 4.3.** Phosphorus-SWCNT and Base-Centroid-SWCNT distances, averaged over all 12 nucleotides, as a function of time (ns) for (a)  $(TAT)_4$ , (b)  $A_{12}$ , (c)  $T_{12}$ , and (d)  $T_4A_4T_4$ .

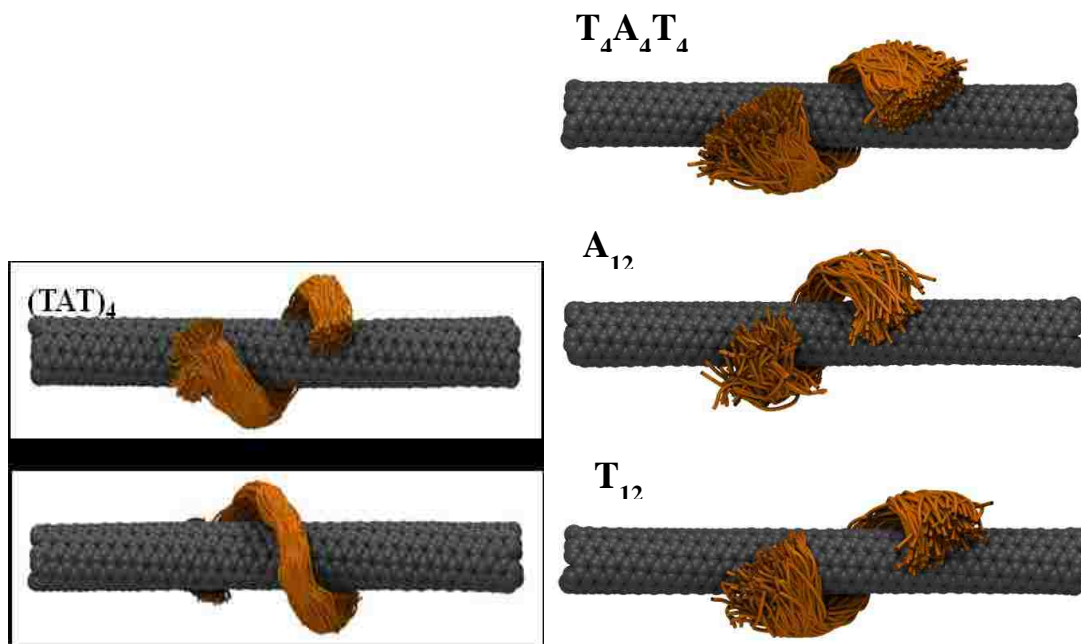
Collectively, we find that **98%** of all bases stack onto the SWCNT surface at 300K, establishing the expected strong base-SWCNT adsorption. Phosphorus and base-centroid distance from SWCNT surface was determined to be, on average,  $5.92 \pm 0.14 \text{ \AA}$  and  $3.65 \pm 0.09 \text{ \AA}$ , respectively. This did not vary substantially by DNA sequence, confirming the need for the phosphate to be hydrated and away from the SWCNT surface compared to the base, which stacks onto the SWCNT surface (Figure 4.3). Additionally, the probability that base  $i+1$  is on the opposite side of the backbone from base  $i$  was found. Figure 4.4 presents snapshots of  $(TAT)_4$  showing the base-backbone alternating motif, followed by associated probabilities for all of the DNA compositions examined.

Note that all strands started with alternating probability of '1'. As described later, deviation from this value of 1 leads to emergence of specialized structures.

To observe the underlying conformations associated with one strand REMD simulations, trajectories were grouped into clusters identified by predetermined criteria. In clustering analysis, groups of atoms are compared against others in the trajectory subject to a root mean squared cutoff distance (RMSD), at the same time removing rigid body rotations and translations. Thus, the clustering analysis reveals groups of similar conformations. In our analysis, only positions of the DNA backbone atoms were tracked (phosphate groups and sugar carbons), as this was deemed the most useful of clustering techniques. It was during clustering that we noticed the prevalence of the truly dominant structure. Figure 4.5 displays the most dominant cluster for (TAT)<sub>4</sub>, representing **94%** of structures, when clustering was performed based on a 0.45 nm backbone RMSD cutoff. Subjected to the same analysis, percentages of the largest clusters were 69, 90, and 84%, for T<sub>4</sub>A<sub>4</sub>T<sub>4</sub>, A<sub>12</sub>, and T<sub>12</sub>-SWCNT hybrids, respectively, also shown in Figure 4.5. The largest clusters all contain DNA in right-handed helical conformations. However, the helical angle, defined as the angle between DNA strand and SWCNT axis, can be noticeably different in a sequence-specific manner (e.g. A<sub>12</sub> has a distinctly larger helical angle (closer to 90°) than a sequence like T<sub>12</sub>). This can be directly related to the degree of DNA-base stitching, as shown later.



**Figure 4.4.** (a) A snapshot of a (TAT)<sub>4</sub> strand on (6,5) SWCNT displaying the base-alternating motif where consecutive bases are on opposite sides of the DNA backbone. Adenine (green) and thymine (yellow) bases participate in base-base hydrogen bonding (white dashed lines). (b) The *loop* structure found in A<sub>12</sub>, stabilized by hydrogen-bonds (white) between Adenine bases in the interior of the loop. (Water molecules have been removed for clarity). (c) Comparison of probabilities by DNA composition.



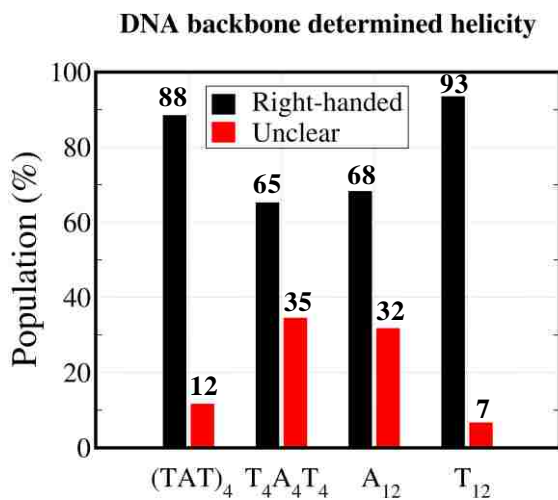
**Figure 4.5.** Clustered hybrids of  $(TAT)_4$ -SWCNTs after being subjected to a 0.45 nm RMSD cutoff of DNA backbone atoms after subtracting rigid body rotations and translations. The backbone atoms of the largest cluster, representing 94% of the trajectory, are shown viewed at strand ends (top-left), and rotated by  $180^\circ$  to show the middle of the strand (bottom-left). DNA-backbone clusters shown also for (top-right)  $T_4A_4T_4$ , (middle-right)  $A_{12}$ , and (bottom-right)  $T_{12}$ . Snapshots are overlaid DNA backbones of the largest cluster when subjected to a RMSD cutoff of 0.45 nm. Note the right-handed helicity of the clustered structures.

We note that all simulations were started with structures in a base-alternating, *left-handed* helical configuration. All of the examined oligonucleotides alter conformation significantly (including backbone and base placement) and most prefer a right-handed helical conformation about the SWCNT, (Figure 4.5). This strongly suggests that the initial configuration did not affect the observed results, which we can take to be representative of equilibrium behavior.

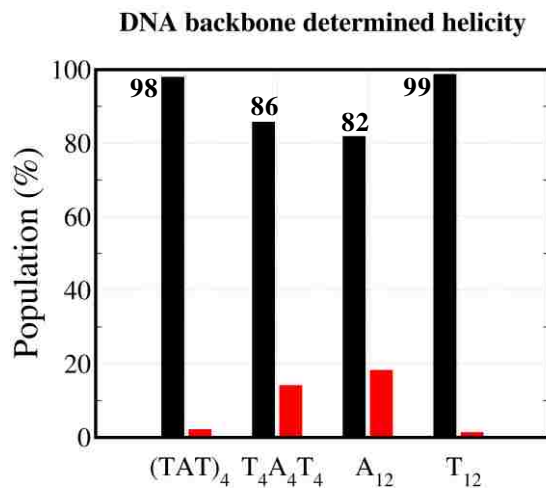
To quantify the DNA helical handedness, phosphorus atom positions were identified and monitored. Any given configuration has 11 phosphorus atoms, i.e. 10 adjacent phosphorus pairs. Local helical angles were determined for each phosphorus

pair (10 local helical angles per structure). While traversing the SWCNT axis (with increasing axial coordinate), phosphorus pairs determined to be locally right-handed were assigned a '1', else they were assigned a '0' for a locally left-handed helix. Because of the intrinsic DNA-backbone flexibility, a DNA strand with a visibly right-handed overall helical conformation may have a few local left-handed helical angles. Once this binary system was established, the following definition was adopted: If 8 out of 10 local helical angles were assigned '1', the structure was classified as right-handed and vice versa for left-handed. Furthermore, if a structure contained 5 consecutive local helical angles with the designation '1', without previous right-handed classification, it was also delineated as such. The same applies for left-handed if there were 5 in a row with designation '0'. Structures not designated either right or left-handed were termed 'unclear' and generally formed a *loop* structure (Figure 4.1b). In this way, it was confirmed that right-handed structures prevail in the equilibrium ensemble. Figure 4.6a shows the sequence-dependence of helical handedness. Note that  $T_4A_4T_4$  and  $A_{12}$  have distinctly lower percentages of structures in a right-handed helical formation. Surprisingly, across all sequences, the population of left-handed helical structures was negligible, and has been left out in Figure 4.6a. The relative trends were conserved (insensitive), independent of cutoff values, (Figure 4.6b). It was found that the initial left to right-handed helical transition occurred within the first 6-30 ns,. Interestingly, DNA passed through a  $90^\circ$  helical angle (oblong loop around SWCNT) rather than becoming outstretched (in the SWCNT axial direction) to accomplish the transformation, (Figure 7). To monitor the initial transient behavior from a starting left-handed helical structure, first left-handed, unclear, and right-handed structures were denoted as '-1', '0', and '1'. Figure 8 shows

window averaged data (averaging over 200 ps of snapshots), using the -1, 0, 1 notation scheme. By 30-50 ns, the initial transition from a left to right-handed helix has occurred, and thus the last 150 ns of production data usage can be justified.

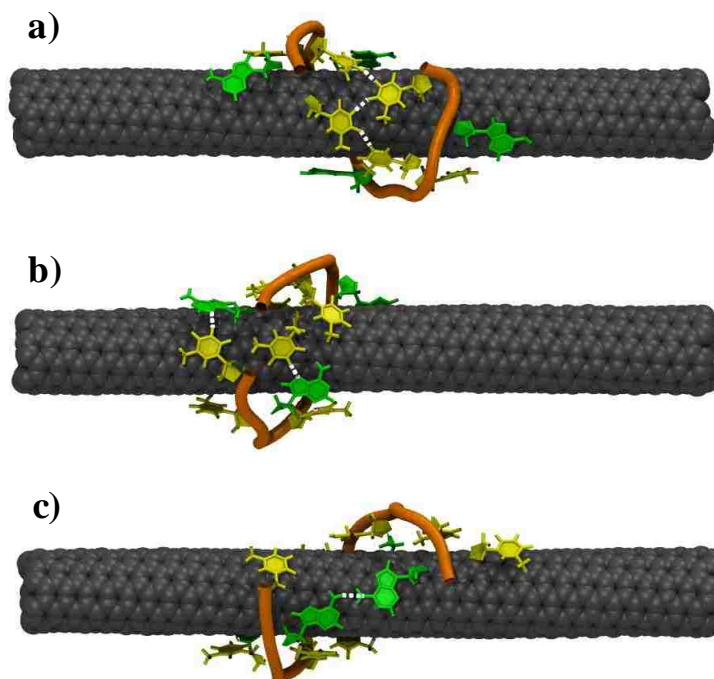


(a)

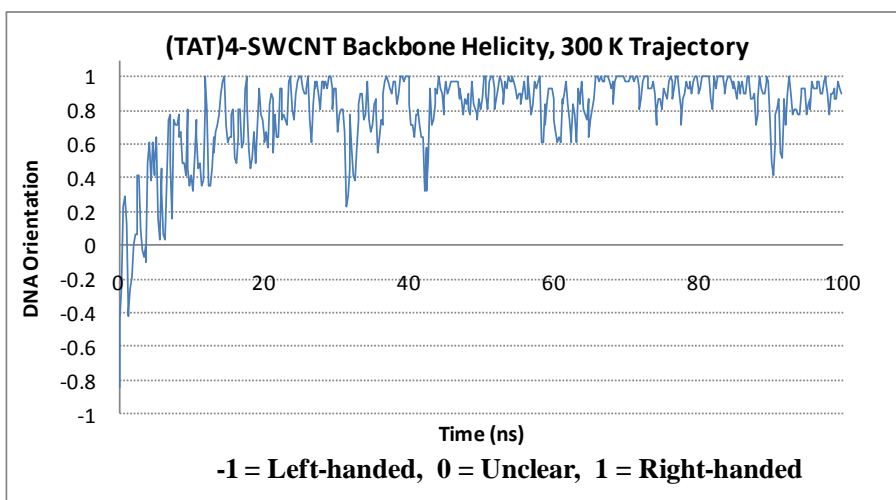


(b)

**Figure 4.6.** Sensitivity of results to our criterion for helical handedness. (a) Right-handedness defined as occurrence of eight locally right-handed helical angles (as in the main text), and (b) Right-handedness defined as occurrence of seven locally right-handed helical angles. Note that while the actual percentages change, the overall trend remains the same.



**Figure 4.7.** Snapshots taken from a continuous trajectory (i.e. a single replica that performs random walk in temperature-space). Starting in the left-handed helical configuration (a), the structure passes through a structure with a helical angle of  $90^\circ$  (b), before entering its preferred state of a right-handed helix (c). For this particular replica, the transition was approximately 6 ns of simulation time.



**Figure 4.8.** Initial transient behavior of the  $(TAT)_4$ -SWCNT hybrid. Using the same criteria for helical handedness as described in the main text, the designations ‘-1’ for left-handed, ‘0’ for unclear, and ‘1’ for right-handed were assigned. The average helicities were calculated for the 300 K trajectory using a window averaging frame of 200 ps. Between 30 and 50 ns, the replica appears to have fully completed the transition to a right-handed helix from an initially left-handed one.

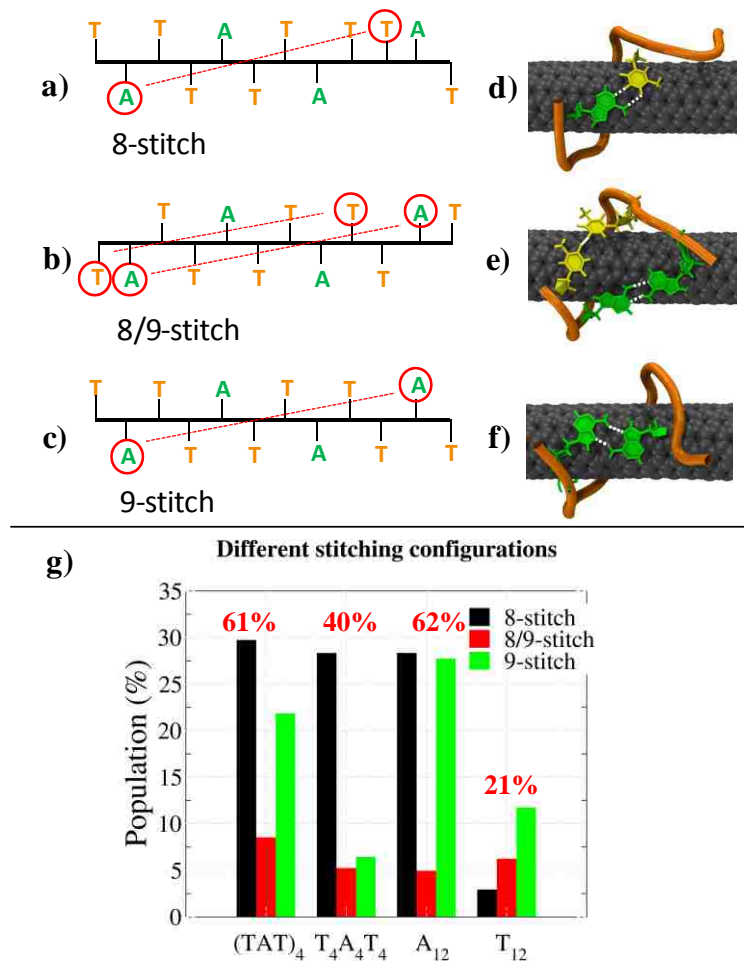
In a previous study of a different sequence/SWCNT combination ((GT)<sub>7</sub> on an (11,0)-SWCNT), Johnson *et al.*<sup>17</sup> found a loop-like dominant structure. Our finding of a dominant right-handed helical structure in the (TAT)<sub>4</sub>-(6,5) SWCNT hybrid highlights two new points. First, the backbone clustering analysis used in this work was found to be an effective tool to help reveal ordered structures. Secondly, our result indicates that the DNA/SWCNT hybrid system can have significant structural variation among DNA of varying sequence. Therefore, we can conclude that sequence-specificity, in addition to length, is crucial in determining equilibrium structure populations for these short oligomers.

It has been hypothesized that hydrogen bonding plays a critical role in stabilizing DNA-SWCNT structures. In support of this notion we found that the majority of structures contained at least one hydrogen bond, to *stitch* the ends of the DNA strands together. To quantify the presence of stitched structures, we define it to occur when a DNA strand makes a complete wrap around a SWCNT allowing distal bases to form at least one hydrogen bond. As shown in a later derivation, stitching itself results in a relatively large loss in DNA conformational entropy, only to be energetically compensated by the formation of a hydrogen bond or bonds. In Figure 4.9, using (TAT)<sub>4</sub> as the representative hybrid, we illustrate the three major types of stitches found in all DNA compositions studied. The ‘8-stitch’ refers to a hydrogen bond formed between one base, and another which is 8 nucleotides away (*i* and *i*+8). This particular stitch (Figure 4.9a) requires a base to switch to the opposite side of the backbone, as do all stitches that connect an even numbered separation of nucleotides. We presume that this configuration of three adjacent bases results in some increase in free energy due to



crowding, which is more than compensated for by the decrease in free energy due to hydrogen bond formation, resulting in a stable equilibrium structure. Also possible for 12-mers on (6,5)-SWCNTs are the ‘9-stitch’ and the ‘8/9-stitch’, consisting of both an 8-stitch and a 9-stitch. Figures 4.9a-c are only representative, i.e., there are a number of different conformations with 8 and 9-stitches. For the 8-stitch, A-T stitching is significantly preferred over T-T (60 vs. 39 %). In the case of the 9-stitch, A-A is highly favored over T-T (95 vs. 5 %). This highlights the importance of non-Watson-Crick base pairing in stabilizing surface-adsorbed DNA structures.

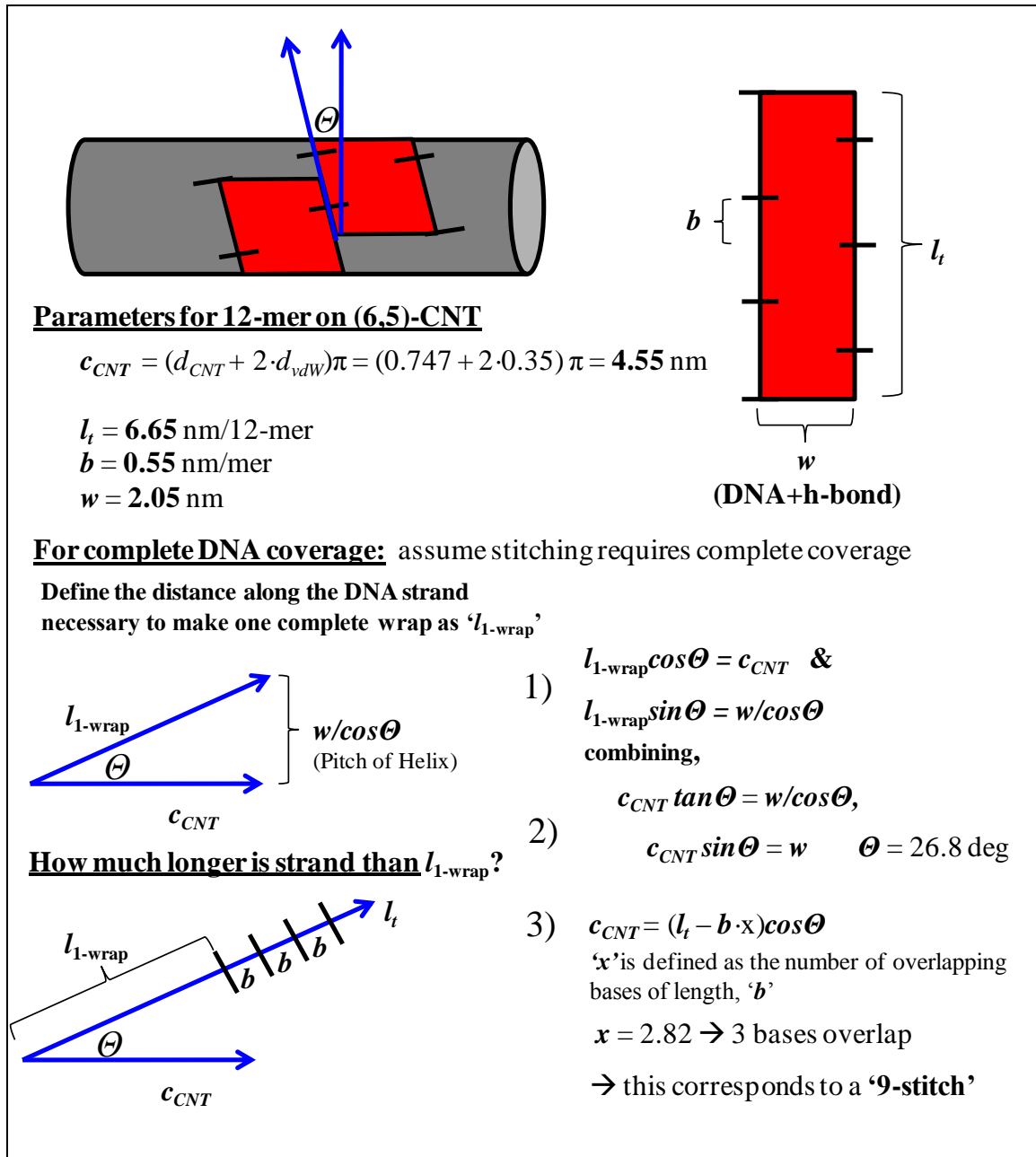
Although these three stitching forms are found in all DNA compositions ((TAT)<sub>4</sub>, A<sub>12</sub>, T<sub>12</sub>, and T<sub>4</sub>A<sub>4</sub>T<sub>4</sub>), their prevalence in each can vary dramatically. As shown in red on Figure 9g, the percentage of structures that stitch depends strongly on the DNA composition and sequence. With the abundance of adenine bases near DNA strand ends, sequences such as (TAT)<sub>4</sub> and A<sub>12</sub> can form the stronger AT and AA hydrogen bonds,<sup>33</sup> and have relatively high total stitching percentages (number of structures in trajectory that stitch / total number in trajectory) of 61 and 62%, respectively. Contrary to this, a sequence such as T<sub>12</sub> has a comparatively low stitching percentage of 21%, consistent with the weaker hydrogen bond strengths stated above. Also from Figure 4e, DNA sequences with adenine-rich ends show no preference for having either an 8-stitch or a 9-stitch. The sequence, T<sub>4</sub>A<sub>4</sub>T<sub>4</sub>, shows a strong preference for an 8-stitch, while T<sub>12</sub> prefers a 9-stitch, suggesting to sequence-specific changes in surface-bound backbone undulations (essentially shortening the P-P distance) allowing for a tighter wrap.



**Figure 4.9.** Analysis of REMD conformations shows the emergence of structures comprising a wrapped configuration stabilized by hydrogen bonding between bases at distal ends of the DNA chain. In all cases, three major modes of stitching DNA ends together around a SWCNT were found. The term “8-stitch” refers to a hydrogen bond between one base, and another which is 8 bases away ( $i$  and  $i+8$ ). Shown are illustrations for the 8-stitch, 8/9-stitch, and 9-stitch (a-c) and molecular models taken from actual trajectories (d-f), although these are only representations and not the only conformations possible for each stitch. Stitching populations are also plotted amongst DNA sequences with total structures stitched found in red (g).

We have previously proposed  $\beta$ -sheet and  $\beta$ -barrel structures formed by hydrogen bonding between (alternating) bases on different strands.<sup>19</sup> However, we neglected the possibility of an ordered structure resulting from the self-hydrogen-bonding, ‘stitching’ motif presented here. It appears reasonable that the geometric compatibility between

parameters such as SWCNT diameter, distance between bases along the backbone, and effective width of the DNA chain will determine which stitching conformations are permissible for a given DNA-SWCNT pair. To quantify this idea, we present a simple geometric model based on DNA-strand and SWCNT parameters. Consider Figure 4.10, where one strand of a 12-mer oligonucleotide (red) is placed on a (6,5)-SWCNT (gray) with circumference  $c_{CNT}$ . Using minimized flat DNA molecular representations, parameters  $w$  and  $l_t$ , width and length respectively, were extracted from multiple simulations. These two parameters tend to be fairly insensitive to DNA composition, as phosphorus-phosphorus distances do not vary much. For stitching to occur, it is assumed that DNA must exhibit complete coverage on the SWCNT. The helical angle is then found, first by defining a parameter,  $l_{1-wrap}$ , as the distance along the DNA backbone necessary to complete one wrap around the SWCNT, allowing strand ends to just meet with no overlap. A complete wrap of DNA, with no gaps in coverage, has pitch  $w/\cos\theta$ , where  $\theta$  is the helical angle, and is found through equations 4.10.1 and 4.10.2. We then ask the question, how much longer is the strand,  $l_t$ , than  $l_{1-wrap}$ ? The number of overlapped bases,  $x$ , is then found by Equation 4.10.3, where  $b$  is the length per nucleotide along the backbone. It was found that a 12-mer on a (6,5)-SWCNT with complete coverage corresponds to a ‘9-stitch’. Because of the intrinsic flexibility of DNA backbones and hydrogen bonds, a more comprehensive thermodynamic model is needed to accurately predict stitching modes and their associated probabilities.



**Figure 4.10.** Schematic of geometric model used to predict the most probable type of stitch found for a 12-mer DNA strand on a (6,5)-SWCNT. Parameters were extracted from multiple minimized simulations. Neglecting any DNA backbone or hydrogen bond flexibility, this model predicts a 9-stitch as the stitching mode of choice.

It is instructive to consider contributions to the free energy of different conformations to understand the main competing terms that determine whether a stitched structure can be stable. Because we are considering a strongly adsorbed regime, all

conformations can be taken to be equally well adsorbed and the large free energy of adsorption per base no longer plays a role in determining competition between different surface conformations. Instead, we examine the relative contributions of four terms. (a) Hydrogen bonding, the first, favors stitch formation, The remaining three all oppose it and are (b) loss of conformational entropy due to stitch formation, (c) increase in free energy due to enhanced electrostatic repulsion on stitch formation, and (d) increase in free energy due to bending as well as the penalty for bases switching sides with respect to the backbone to accommodate a certain stitch.

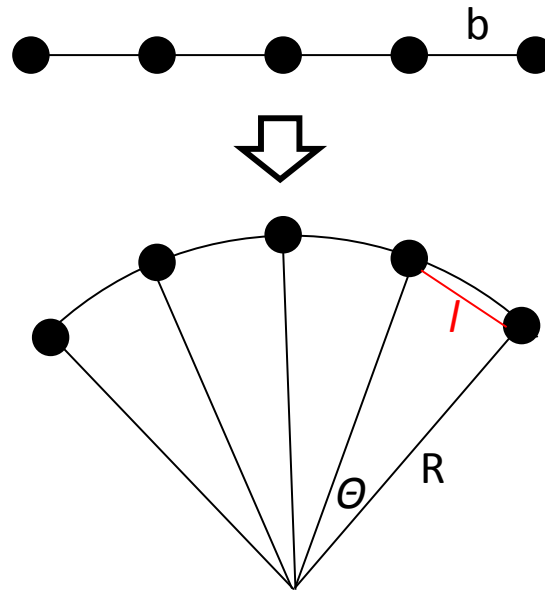
(a) Hydrogen bond energies have been reported as  $10.9 k_B T/bond$  and  $3.4 k_B T/bond$  in vacuum and fully solvated states<sup>1, 34</sup>. Because DNA bases are only half solvated on a SWCNT sidewall, the energy for one bond can be expected to lie between these two values. For simplicity, we can estimate a maximum of about  $5.0 k_B T/bond$ . Since stitched structures are stabilized usually by two hydrogen bonds, this term contributes about  $-10 k_B T$ .

(b) Loss of conformational entropy due to stitching is estimated approximately by the work required to pull a 2D Gaussian chain to extension equal to its contour length<sup>32</sup>, since in order to accommodate a stitch, the DNA must become fully stretched in the two-dimensions of the SWCNT surface. Kuhn length,  $l_k$  of short single-stranded DNA has been measured by AFM to be between 0.5 and 1.0 nm;<sup>31</sup> for the present estimations, we take it to be 1.0 nm. (Corresponding persistence length  $l_p = l_k/2 = 0.5$  nm). For a 12-mer, taking P-P distance to be 0.65 nm, the contour length is 7.15 nm and therefore the number of Kuhn lengths is about 7. The free energy due to stretching of the backbone can be approximated as

$$G_{conf} = Nk_B T = 7k_B T \quad (4.1)$$

which is clearly of the same order of magnitude as the hydrogen bonding term (but of opposite sign).

(c) We wish to determine the potential electrostatic contribution to *differences* in free energy between different adsorbed conformations. Consider a line of charges solvated in an aqueous salt solution. To estimate the electrostatic contribution to free energy differences, we compute the difference in energy between a straight line of charges and one in which the charges are placed on circle with a given radius of curvature.



**Figure 4.11.** To estimate the electrostatic contribution to the difference in free energy between surface-adsorbed conformations, we compute the difference in energy between a straight and curved line of charges. Note: figure not drawn to scale.

In Figure 4.11,  $b$  represents the distance between charges on the phosphate sugar backbone. From simulation, this is found to be  $6.5 \text{ \AA}$ . In the curved conformation,  $b$  becomes the arc length, while  $l$  is the Euclidean distance between charges. The radius of curvature,  $R$ , depends on the type of SWCNT; for (6,5)-SWCNT, phosphorus atoms are found  $\sim 10 \text{ \AA}$  from the center of the SWCNT, i.e.,  $R$  is taken to be  $10 \text{ \AA}$ .

The arc length between adjacent charges is related to angle and radius by

$$l = 2R \sin \frac{\theta}{2} \quad (4.2)$$

For small angles,

$$\sin \theta \approx \theta - \frac{\theta^3}{6} + \dots \quad (4.3)$$

so that

$$l \approx 2R \left( \frac{\theta}{2} - \frac{1}{6} \left( \frac{\theta}{2} \right)^3 + \dots \right) = R \left( \theta - \frac{\theta^3}{24} \right) \quad (4.4)$$

We use the Debye-Huckel potential<sup>2</sup> to compute the electrostatic energy of interaction between two identical charges in water:

$$U_{el} = \frac{q^2 e^{-\frac{l}{l_D}}}{4\pi\epsilon\epsilon_o l} \quad (4.5)$$

Substituting (3), we get

$$U_{el} = \frac{q^2 e^{-\frac{R\theta}{l_D} - \frac{R\theta^3}{24l_D}}}{4\pi\epsilon\epsilon_o R \left( \theta - \frac{\theta^3}{24} \right)} \quad (4.6)$$

In the straight case,  $l = b$  and  $\theta = 0$ ; in the curved case,  $R\theta = b$ . Written to  $O(\theta^2)$ .

$$U_{el}(\text{straight}) = \frac{q^2 e^{-\frac{b}{l_D}}}{4\pi\epsilon\epsilon_o b} \quad (4.7)$$

$$U_{el}(\text{curved}) = \frac{q^2 e^{-\frac{b}{l_D}}}{4\pi\epsilon\epsilon_o \left( b - \frac{b^3}{24R^2} \right)} \quad (4.8)$$

$$\Delta U_{el} = U_{el}(c) - U_{el}(s) = \frac{q^2 b e^{-\frac{b}{l_D}}}{4\pi\epsilon\epsilon_o (24R^2)} \quad (4.9)$$

The above derivation was made in the limit of high salt. From the simulation box size and number of counterions, the concentration of salt was **191.5** mM. This particular concentration gives a Debye screening length<sup>2</sup>,  $l_D$ , of **6.95** Å, which is on the order of the charge separation distance. Because of this, it can be assumed that charges are affected only by their nearest neighbors. For the simulation conditions, we find that:

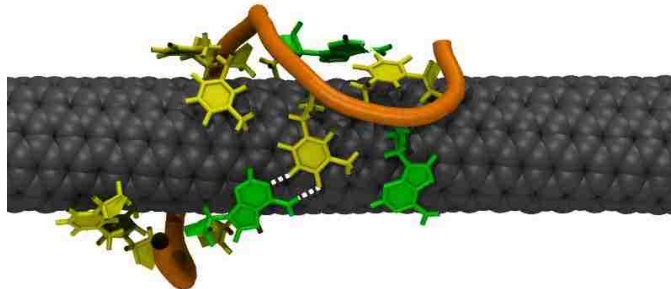
$$\Delta U_{el} \approx 0.1k_B T \quad (4.10)$$

(d) The energy required to bend ssDNA at a radius of 0.98 nm (radius at which phosphorus sits from center of SWCNT axis) is

$$G_{bend} = \frac{l_p l_t k_B T}{2R^2} \approx 0.85k_B T \quad (4.11)$$

where  $l_p$  and  $l_t$  refer to the DNA persistence<sup>35</sup> and total length, respectively.

When a base switches sides of the backbone, a penalty must be assessed to account for the imposed crowding. Although we do not have an estimate for this contribution, we can assume a small value since all DNA sequences have significant populations of the base-backbone flipping 8-stitch. A snapshot of this conformation is shown in Figure 4.12.



**Figure 4.12.** A (TAT)<sub>4</sub>-SWCNT hybrid in an A-T 8-stitch configuration exhibiting base crowding. The thymine (yellow) which is hydrogen bonding to the adenine (green) has to flip sides of the backbone in order to achieve the stitch. This results in an energetic penalty as adjacent bases to the thymine are now more confined.



This approximate analysis shows that very likely the equilibrium between stitched and random conformations is governed by competition between attractive hydrogen bonding interaction between bases and attendant reduction in conformational entropy.

#### **4.4 Conclusions**

A sequence-dependent equilibrium MD study has been presented for short (12-mer) single strands of ssDNA on a particular SWCNT (6,5). We find that some broad characteristics of adsorption onto the SWCNT surface are not sequence dependent. For instance, adsorption is sufficiently strong so that nearly all bases remain stacked on the surface and the backbone usually assumes a right handed helical conformation with characteristic distance from the SWCNT surface. This finding is consistent with the experimental finding that nearly all DNA sequences are effective dispersants of SWCNTs. However, we find that the actual structural motif of the adsorbed strand depends strongly on the sequence and composition. The basis of the sequence dependence is the highly variable nature of base-base hydrogen bonding, which competes with backbone conformational entropy to result in different, sequence-dependent self-stitched wrapped structures. That is, short strands of DNA, of differing sequence and/or composition, have the ability to form highly sequence-specific structures on SWCNTs. If strands are of adequate length, hydrogen bonding will enable DNA to wrap completely around a SWCNT and self-stitch.

## **4.5 Acknowledgement**

I would like to acknowledge Anand Jagota and Jeetain Mittal who have served as mentors for me during this work. Additionally, this work was supported by the National Science Foundation through grant CMMI-1014960. This research was supported in part by the National Science Foundation through TeraGrid resources provided by the Texas Advanced Computing Center (TACC) under grant number [TG-MCB100049]. We specifically acknowledge the assistance of Mr. Chris Hempel and Dr. Hang Liu.

## 4.6 References

- (1) Saenger, W., Springer-Verlag: New York, 1984.
- (2) Zheng, M.; Jagota, A.; Strano, M. S.; Santos, A. P.; Barone, P.; Chou, S. G.; Diner, B. A.; Dresselhaus, M. S.; Mclean, S. R. L.; Onoa, G. B.; Samsonidze, G. G.; Semke, E. D.; Usrey, M.; Walls, D. J., *Science* **2003**, *302* (5650), 1545-1548.
- (3) Campbell, J. F.; Tessmer, I.; Thorp, H. H.; Erie, D. A., *J. Am. Chem. Soc.* **2008**, *130* (32), 10648-10655.
- (4) Dukovic, G.; Balaz, M.; Doak, P.; Berova, N. D.; Zheng, M.; McLean, R. S.; Brus, L. E., *J. Am. Chem. Soc.* **2006**, *128* (28), 9004-9005.
- (5) Manohar, S.; Tang, T.; Jagota, A., *Journal of Physical Chemistry C* **2007**, *111* (48), 17835-17845.
- (6) Johnson, R. R.; Johnson, A. T. C.; Klein, M. L., *Nano Letters* **2008**, *8* (1), 69-75.
- (7) Johnson, R. R.; Johnson, A. T. C.; Klein, M. L., *small* **2010**, *6* (1), 31-34.
- (8) Zheng, M.; Jagota, A.; Semke, E. D.; Diner, B. A.; Mclean, S. R. L.; Richardson, R. E.; Tassi, N. G., *Nature Materials* **2003**, *2*, 338-343.
- (9) Barone, P. W.; Baik, S.; Heller, D. A.; Strano, M. S., *Nature Materials* **2005**, *4*, 86-92.
- (10) Heller, D. A.; Jin, H.; Martinez, B. M.; Patel, D.; Miller, B. M.; Yeung, T. K.; Jena, P. V.; Hobartner, C.; Ha, T.; Silverman, S. K.; Strano, M. S., *Nature Nanotechnology* **2008**, *4*, 114-120.
- (11) Huang, X.; Mclean, S. R. L.; Zheng, M., *Analytical Chemistry* **2005**, *77* (19), 6225-6228.
- (12) Albertorio, F.; Hughes, M. E.; Golovchenko, J. A.; Branton, D., *Nanotechnology* **2009**, *20*.
- (13) Tu, X. M.; Manohar, S.; Jagota, A.; Zheng, M., *Nature* **2009**, *460* (7252), 250-253.
- (14) Khripin, C. Y.; Manohar, S.; Zheng, M.; Jagota, A., *Journal of Physical Chemistry C* **2009**, *113* (31), 13616-13621.
- (15) Roxbury, D.; Tu, X.; Zheng, M.; Jagota, A., *Langmuir* **2011**, *27* (13), 8282-8293.
- (16) Sugita, Y.; Okamoto, Y., *Chem. Phys. Lett.* **1999**, *314* (1-2), 141-151.
- (17) Sugita, Y.; Kitao, A.; Okamoto, Y., *J. Chem. Phys.* **2000**, *113*, 6042-6051.
- (18) Johnson, R. R.; Kohlmeyer, A.; Johnson, A. T. C.; Klein, M. L., *Nano Letters* **2009**, *9* (2), 537-541.
- (19) Roxbury, D.; Manohar, S.; Jagota, A., *J. Phys. Chem. C* **2010**, *114* (31), 13267-13276.
- (20) Alexiadis, A.; Kassinos, S., *Chem. Rev.* **2008**, *108*, 5014-5034.
- (21) Reddy, S. Y.; Leclerc, F.; Karplus, M., *Biophysical Journal* **2003**, *84*, 1421-1449.
- (22) *Materials Studio (R)*, Accelrys Inc.: San Diego, CA.
- (23) Humphrey, W.; Dalke, A.; Schulten, K., *J. Molec. Graphics* **1996**, *14* (1), 33-38.
- (24) Berendsen, H. J. C.; van der Spoel, D.; van Drunen, R., *Computer Physics Communications* **1995**, *91* (1-3), 43-56.
- (25) Lindahl, E.; Hess, B.; van der Spoel, D., *J. Mol. Model* **2001**, *7* (8), 306-317.
- (26) van der Spoel, D.; Lindahl, E.; Hess, B.; Groenhof, G.; Mark, A. E.; Berendsen, H. J. C., *J. Comput. Chem.* **2005**, *26* (16), 1701-1718.
- (27) Foloppe, N.; MacKerell, A. D., *J. Comput. Chem.* **2000**, *21* (2), 86-104.

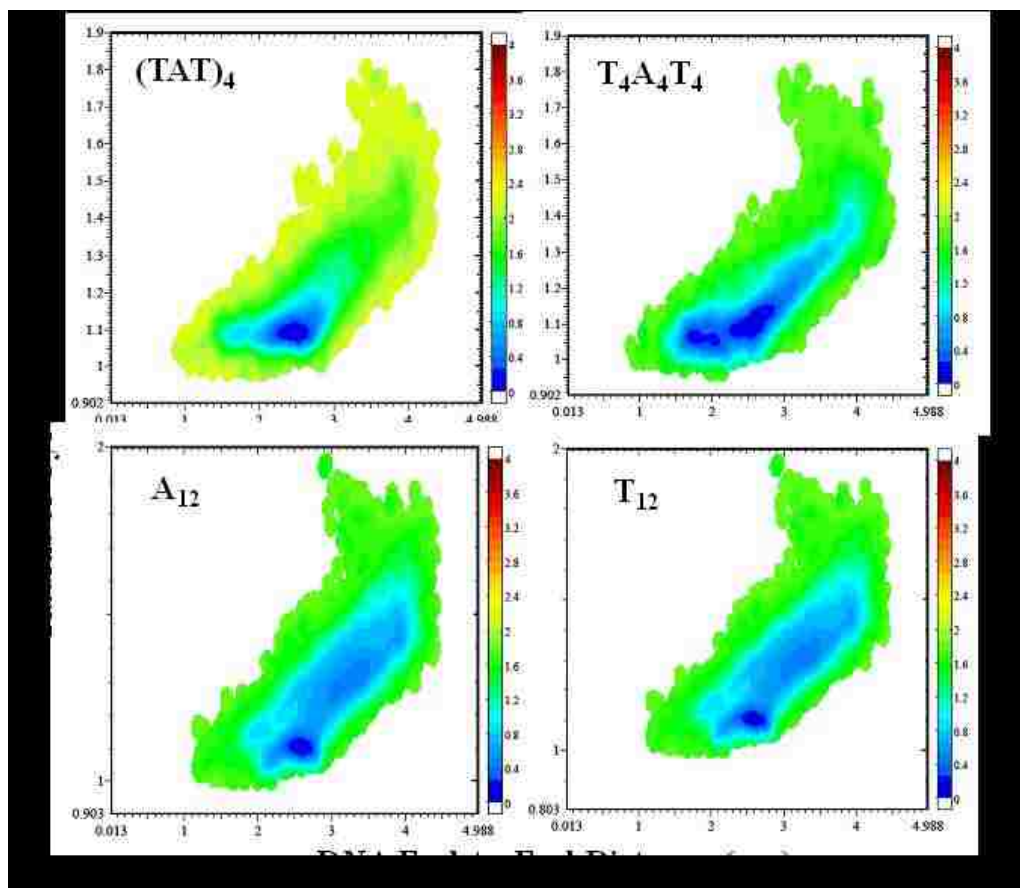
- (28) MacKerell Jr., A. D.; Banavali, N. K., *J. Comput. Chem.* **2000**, *21* (2), 105-120.
- (29) Jorgensen, W. L.; Chandrasekhar, J.; Madura, J. D.; Impey, R. W.; Klein, M. L., *J. Chem. Phys.* **1983**, *79*, 926.
- (30) York, D. M.; Darden, T. A.; Pedersen, L. G., *J. Chem. Phys.* **1993**, *99* (10).
- (31) Manohar, S.; Mantz, A. R.; Bancroft, K. E.; Hui, C. Y.; Jagota, A.; Vezenov, D. V., *Nano Letters* **2008**, *8* (12), 4365-4372.
- (32) Rubinstein, M.; Colby, R. H., Oxford University Press: 2003.
- (33) Mamdough, W.; Dong, M. D.; Xu, S. L.; Rauls, E.; Besenbacher, F., *Journal of the American Chemical Society* **2006**, *128* (40), 13305-13311.
- (34) Stofer, E.; Chipot, C.; Lavery, R., *J. Am. Chem. Soc.* **1999**, *121*, 9503-9508.
- (35) Tinland, B.; Pluen, A.; Sturm, J.; Weill, G., *Macromolecules* **1997**, *30* (19), 5763-5765.
- (36) van Gunsteren, W. F.; Daura, X.; Mark, A. E., **2002**.

## 4.7 Appendix

### 4.7.1 Additional Data Mining of Single Strands of DNA Simulated on (6,5)-SWCNTs

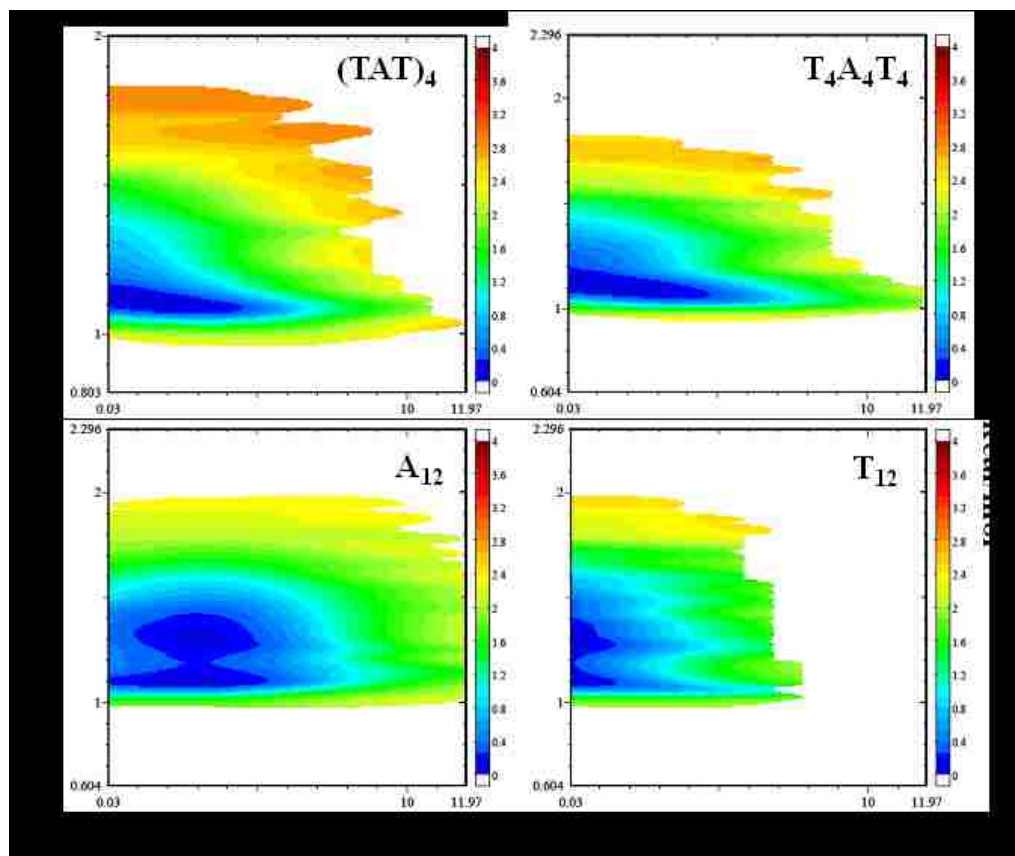
In the extended replica exchange simulations presented in this chapter, it is assumed that adequate sampling of accessible states is accomplished under equilibrium conditions. For this reason, calculating the probability distributions of certain physical characteristics can be useful tools for finding the most probable structures. By first finding the system partition function with respect to a certain variable/reaction coordinate, differences in Helmholtz free energy,  $A(n,v,t)$ , can be found along the same reaction coordinate.<sup>36</sup> Furthermore, two variables can be plotted against each other to extract two-dimensional potential of mean force (PMF) plots.

The first constructed PMF plots are those of DNA radius of gyration and DNA strand end-to-end distance. In Figure 4.13, it is seen that  $(TAT)_4$ -(6,5)-SWCNT has the most pronounced energy well (dark blue), suggesting a fairly stable structure with very small deviation from that minimum. Configurations such as  $A_{12}$  and  $T_{12}$  appear to have a more spread out energy plateau (light blue) and suggest a more flexible structure.



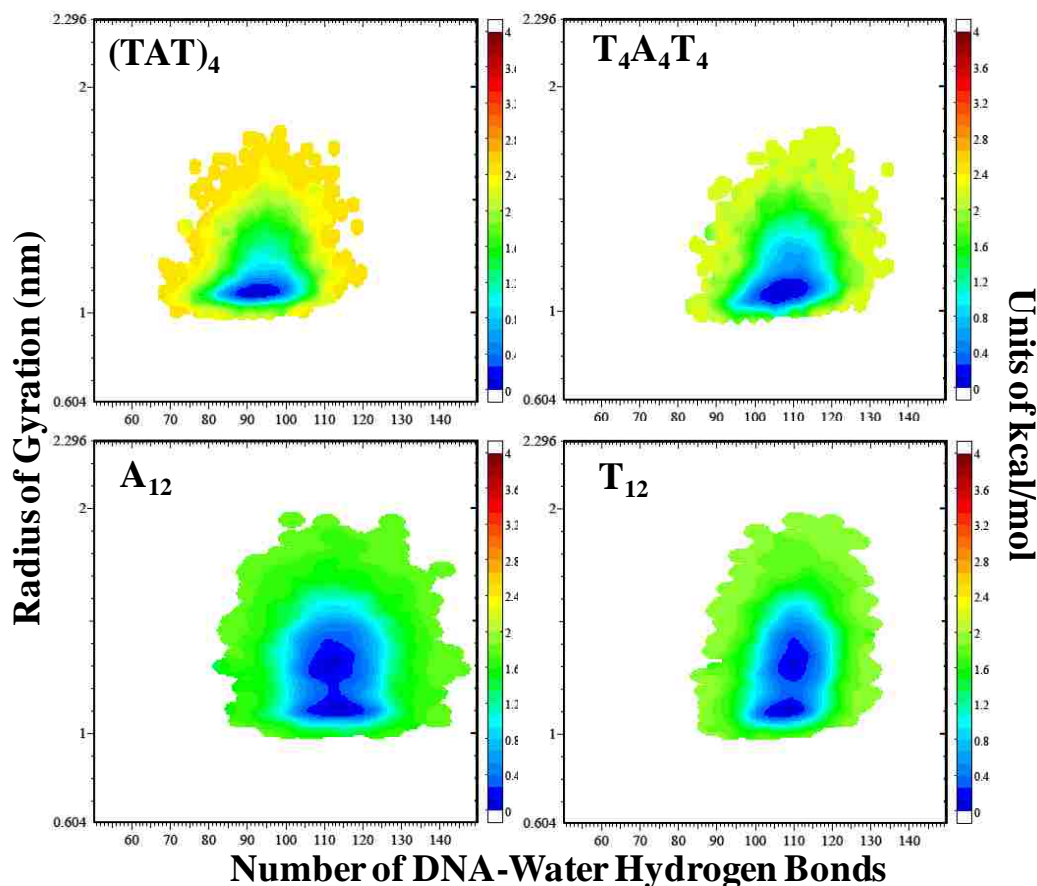
**Figure 4.13.** Two-dimension PMF plots for radius of gyration versus DNA end-to-end distance of all simulated configurations.

In the next constructed PMF plot, DNA radius of gyration is compared against the number of DNA-DNA hydrogen bonds (Figure 4.14). In general, it is seen that the number of DNA-DNA hydrogen bonds can vary quite substantially in the energy wells. For  $(TAT)_4$ , the deepest well encompasses 0-5 hydrogen bonds, while the entire observable range is 0-12. This may be accounted for by slight variations in DNA structure that temporarily cause breakage of a number of DNA-DNA hydrogen bonds, while the radius of gyration basically remains unchanged. Across configurations,  $A_{12}$  appears to have the highest number of DNA-DNA hydrogen bonding and is most likely a result of the higher than average percentage of the trajectory in a loop structure.



**Figure 4.14.** Two-dimension PMF plots for radius of gyration versus the number of DNA-DNA hydrogen bonds.

In the final constructed PMF plot, the relationship between DNA radius of gyration is compared against the number of DNA-water hydrogen bonds (Figure 4.15). It is seen that  $(TAT)_4$  has a significantly lower number of DNA-water hydrogen bonds than the other simulated configurations. This relative decrease in energy must be accounted for by an increase in energy elsewhere; generally in the form of DNA-DNA and DNA-counter-ion interactions.



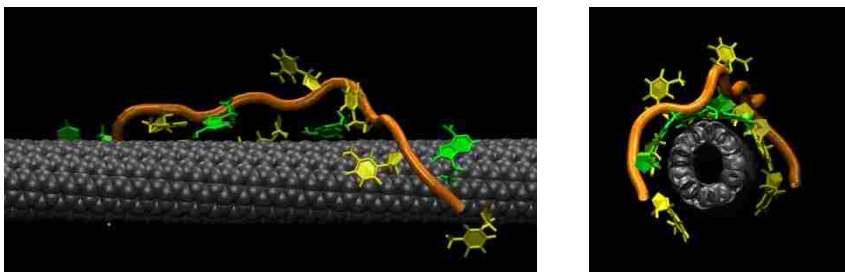
**Figure 4.15.** Two-dimension PMF plots for radius of gyration versus the number of DNA-water hydrogen bonds.

#### 4.7.2 Analysis of Highest Temperature Replica

When performing simulations of replica exchange molecular dynamics, it is important to know the behavior of the highest temperature replica in addition to that of the target temperature. The behavior at the highest temperature indicates whether or not the simulation is truly sampling all of the available states, else the simulation is not actually in equilibrium. In this chapter, the target temperature is 300 K, and that of the highest temperature was 587 K. When examining the trajectory of the 587 K replica, it was observed that the DNA strand was stretched out along the length of the SWCNT due to the dominating entropy term (Figure 4.16). In addition, it was found that at any given



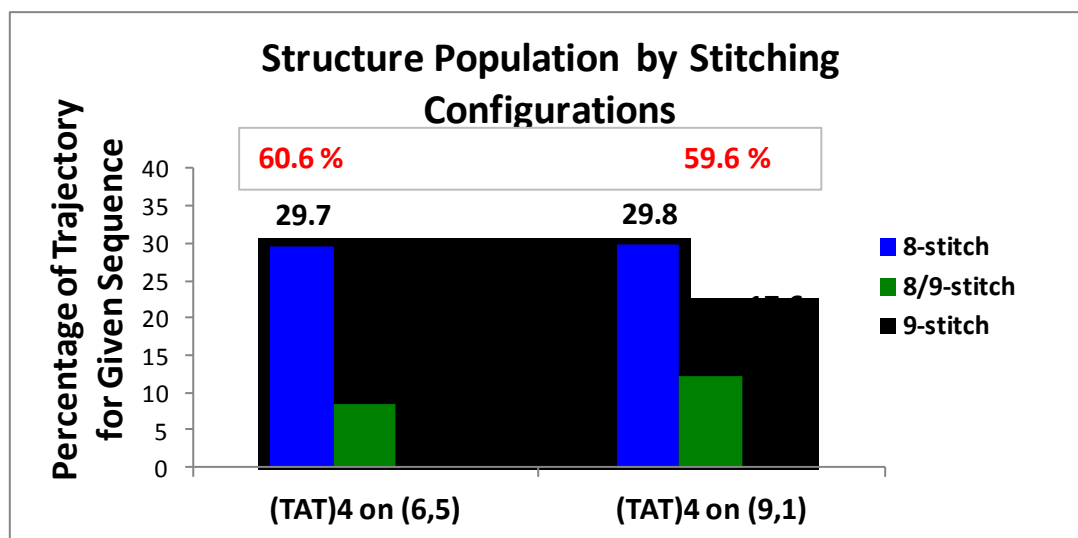
time the propensity for DNA bases to be desorbed from the SWCNT surface was significantly greater than that of the 300 K replica. The percentage of adsorbed DNA bases (SWCNT and DNA base normal vectors less than  $30^\circ$ ) dropped from 98% to 86% for the  $(TAT)_4$  configuration when comparing the 300 K replica to the 587 K one. This property is important for DNA bases to be able to flip sides of the backbone in order to form stable self-stitched equilibrium structures.



**Figure 4.16.** Snapshots of the sequence  $(TAT)_4$  on the (6,5)-SWCNT at 587 K. The DNA is in an outstretched conformation (along the length of the SWCNT), with several bases desorbed from the SWCNT surface at any time.

### 4.7.3 Additional Simulated Structures

In addition to the structures presented in the main text of this chapter, a simulation was performed in which  $(TAT)_4$  was adsorbed to a (9,1)-SWCNT. The (6,5) and (9,1)-SWCNTs have identical diameters, 0.747 nm, but vary in the intrinsic chiral angle of the carbon atoms. One strand of  $(TAT)_4$  was simulated on a (9,1)-SWCNT for 100 ns of REMD,. Results found in Figure 4.17 suggest that the variation in SWCNT chiralities of the same diameter have negligible effects on the equilibrium structures of the configuration.



**Figure 4.17.** Populations by stitching configuration are found for  $(TAT)_4$  simulated on (6,5) and (9,1)-SWCNTs. The total percentage of structures in a stitched configuration is found in red and does not vary substantially between SWCNT chirality.

## **Chapter 5**

### **Molecular-Basis of Single-Walled Carbon Nanotube Recognition by Single-Stranded DNA \***

*Hybrids of biological molecules and single-walled carbon nanotubes (SWCNT) have proven useful for SWCNT sorting and are enabling several biomedical applications in sensing, imaging, and drug delivery. In the DNA-SWCNT system, certain short (10-20mer) sequences of single-stranded DNA recognize specific SWCNT, allowing the latter to be sorted from a chirality-diverse mixture.<sup>1</sup> However, little is known about the DNA secondary structures that underlie their recognition of SWCNTs. Using replica exchange molecular dynamics (REMD) of multiple strands on a single SWCNT, here we report that DNA forms ordered structures on SWCNTs that is strongly DNA sequence and SWCNT dependent. DNA sequence (TAT)<sub>4</sub> on its recognition partner, the (6,5) SWCNT,<sup>1</sup> forms an ordered right-handed helically wrapped barrel, stabilized by intra-strand, self-stitching hydrogen bonds and inter-strand hydrogen-bonding. The same sequence on the larger-diameter (8,7)-SWCNT forms a different and less-stable structure, demonstrating SWCNT selectivity. In contrast, homopolymer (T)<sub>12</sub>, with weaker tendency for intra-strand hydrogen bonding, forms a distinctly left-handed wrap on the (6,5)-*

---

\* Portions of this chapter have been published in Nano Letters:

D Roxbury, J Mittal, A Jagota. "Molecular-Basis of Single-Walled Carbon Nanotube Recognition by Single-Stranded DNA" *Nano Lett.* **133**, 3, 1464 (2012).

*SWCNT, demonstrating DNA sequence-specificity. Experimental measurements show that (TAT)<sub>4</sub> selectively disperses smaller diameter SWCNTs more efficiently than (T)<sub>12</sub>, establishing a relationship between recognition motifs and binding strength. The developing understanding of DNA secondary structure on nanomaterials can shed light on a number of issues involving hybrids of nanomaterials and biological molecules, including nanomedicine, health-effects of nanomaterials, and nanomaterial processing.*

## **5.1 Introduction**

Hybrids of nanomaterials and biological molecules have recently been utilized for numerous applications such as chemical sensing,<sup>2</sup> targeted cellular drug and siRNA delivery,<sup>3-4</sup> and *in vivo* imaging.<sup>5-6</sup> Little is known about the structural organization of such hybrids, although it usually controls their function and properties. One characteristic example is the hybrid of amphiphilic single-stranded DNA (ssDNA) and hydrophobic single-walled carbon nanotubes (SWCNTs), which are rendered water-dispersible upon wrapping by DNA.<sup>7-8</sup> DNA-SWCNT hybrids permit sorting by SWCNT chirality (a physical property determining the electronic nature).<sup>1,9</sup> Through a systematic but empirical search, Tu et al. have identified a set of short DNA oligomers (10-20 nucleotides long) that can each recognize a particular chirality of SWCNT contained in mixture.<sup>1</sup> There is a generic underlying trend that thermal stability of DNA-SWCNT hybrids increases with increasing DNA sequence length,<sup>10-11</sup> e.g., hybrids composed of 10-mer and 60-mer DNA strands have room temperature thermal stabilities of hours and months, respectively.<sup>10</sup> There are a few notable exceptions, primarily the recognition sequences identified by Tu et al.,<sup>1</sup> in which case short strand SWCNT hybrids

can have a stability similar to those much longer.<sup>12</sup> Surfactant-exchange experiments confirm that these *recognition sequences* bind with significantly greater strengths (~ factor of 20 ) to their target SWCNTs compared to sequences that differ by only one base.<sup>12</sup> It has been proposed that recognition and corresponding increase in binding strength is due to the formation of ordered structures comprised of hydrogen-bonded DNA networks.<sup>1, 13</sup> However, whether any such structures will emerge spontaneously in equilibrium has not been established.

Molecular dynamics simulation, utilizing all-atom explicit solvent models, has been a useful tool for studying DNA-SWCNT hybrid interactions. Hybridization simulations, performed on specific chirality-SWCNTs with double stranded DNA (dsDNA)<sup>14</sup> as well as ssDNA,<sup>15-17</sup> have clearly illustrated the affinity that DNA possesses for the hydrophobic SWCNT. A single DNA molecule of sufficient length (>14 nucleotides) was found to wrap spontaneously around a SWCNT within 20 ns.<sup>17</sup> Advanced sampling techniques are needed to obtain equilibrium ensemble structures as the time scales involved are large. One such method is replica exchange molecular dynamics (REMD)<sup>18</sup>, and has been successfully used by Johnson et al.<sup>19</sup> Based on results from *one* strand of (GT)<sub>7</sub> on an (11,0)-SWCNT, they concluded that no preferred configuration exists, but rather that the equilibrium ensemble corresponds to a wide range of structures very similar in free energy. Previously, we have shown with extensive REMD simulation that DNA sequence *is* in fact critical for determining populations of equilibrium structures, even among strands of the same DNA base composition (e.g., (TAT)<sub>4</sub>, i.e. TATTATTATTAT, versus T<sub>4</sub>A<sub>4</sub>T<sub>4</sub>).<sup>20</sup> For a *single* 12-mer oligonucleotide on (6,5)-SWCNTs, we discovered a stable self-stitching motif in which DNA makes a

complete right-handed helical wrap around the SWCNT, allowing distant adsorbed bases to hydrogen bond to each other. However, for hydrogen-bonding networks to stabilize a structure with long range order requires consideration of interactions between multiple strands. While a  $\beta$ -barrel structure with multiple strands has been hypothesized, no previous investigation has sought to ask if and what types of ordered DNA structures form in equilibrium on an SWCNT.<sup>13</sup>

In this study, we pose and answer the following specific questions: **1)** Do multiple strands of DNA on a SWCNT form stable structures? **2)** Do these structures depend on the type of SWCNT for a given DNA sequence? and, conversely, **3)** Do these structures depend on the type of DNA for a given SWCNT? To address questions (1) and (2), we have performed multi-strand REMD simulations of the sequence (TAT)<sub>4</sub> on its recognition partner,<sup>1</sup> the (6,5)-SWCNT, as well as on a much larger diameter (8,7)-SWCNT. Additionally, the homopolymer, (T)<sub>12</sub>, is simulated on a (6,5)-SWCNT to address question (3). To support simulation results we have performed photoluminescence experiments. The resultant photoluminescence maps show differences in dispersion efficiencies correlated with sequence, confirming the importance of SWCNT-chirality as well as DNA sequence in hybrid strength, presumably linked to structure. We propose that mutual recognition in the (TAT)<sub>4</sub>-(6,5) hybrid is based on a special stable arrangement comprising an array of self-stitched right-handed DNA helices, adsorbed on the SWCNT, and further stabilized by inter-strand hydrogen bonding.

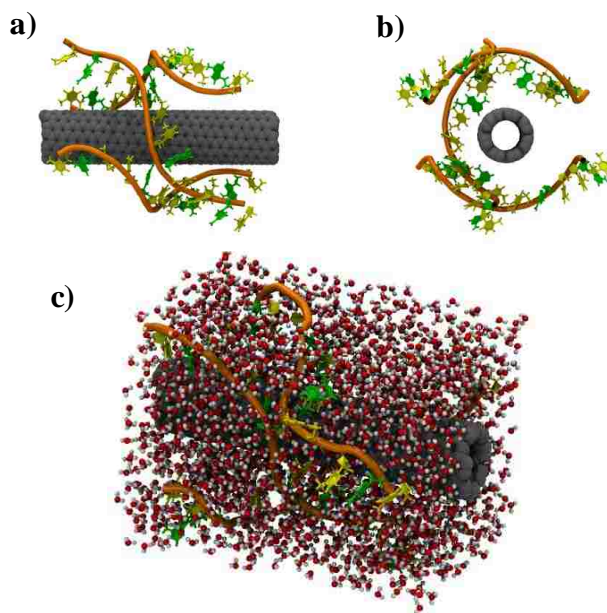
## 5.2 Methodologies

### Molecular Dynamics Simulations

The configurations and simulation parameters were identical to those used in a previous molecular dynamics study.<sup>20</sup> Three strands of (TAT)<sub>4</sub> were placed around (in desorbed states) both (6,5) and (8,7)-SWCNTs (the recognized SWCNT and one with significantly larger diameter, respectively) in independent simulations, see Figure 5.1a,b. In the same manner, three strands of (T)<sub>12</sub> were placed around a (6,5)-SWCNT to address the effect of DNA-composition on hybrid structure. The SWCNTs used were of length 79.7 Å and 55.3 Å, with diameters of 7.46 Å and 10.18 Å for (6,5) and (8,7) chiralities, respectively. End carbons were covalently bonded to adjacent image carbons, mimicking an infinitely long SWCNT. Structures were first created in *Materials Studio*,<sup>21</sup> and then visualized in *VMD*.<sup>22</sup>

The GROMACS 3.5.3 simulation package<sup>23-25</sup> was used in conjunction with the CHARMM27 force field<sup>26-27</sup> for extended REMD simulations. DNA-SWCNTs hybrids were solvated in 79.7 x 34.6 x 34.6 Å and 55.3 x 40.0 x 40.0 Å water-boxes for (6,5) and (8,7) configurations, respectively. This contained approximately 2,500 TIP3P model<sup>28</sup> water molecules with the appropriate amount of sodium counter-ions to balance the negative phosphate charges, (Figure 5.1c). Total system size remained at ~10,000 atoms. Periodic boundary conditions were applied in all directions with long-range electrostatics calculated using the particle mesh Ewald method (PME)<sup>29</sup>. All structures were subjected to 100 ps heating (NVT) to attain a 300 K starting temperature. Forty replicas of each configuration were created for REMD NVT simulation, having temperatures ranging from 296 K to 587 K. Replica temperatures were chosen such that exchange acceptance

ratios remained around 20% with an exchange time of 2 ps. Each configuration was run for a minimum of 400 ns, for a total computation time of  $40 \times 400 = 16 \mu\text{s}$ . The time step of the simulation was 2 fs. The trajectories were saved at every 10 ps, yielding a total of 40,000 snapshots for production analysis.



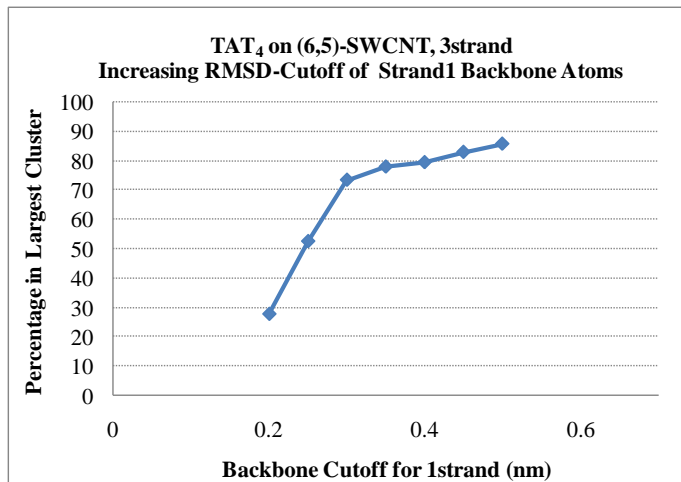
**Figure 5.1.** (a) Side view for three strands of  $(\text{TAT})_4$  placed around a periodic  $(8,7)$ -SWCNT. Note that DNA bases do not start adsorbed to the SWCNT surface, but rather in a desorbed base-base stacked state. (b) Cross-sectional view of the same representation. (c) Configurations are solvated in a water-box containing approximately 2,500 water molecules and the appropriate number of sodium counter-ions.

Data analysis was performed on the last 300 ns of available data using the 300 K replica trajectory, discarding a 100 ns initial equilibration period. When examining a trajectory, it is important to group structures into clusters based on universal predetermined criteria. For this, DNA backbone atoms were subjected to root mean squared deviation (RMSD) cutoffs of 0.45 nm and 1.3 nm for individual-strand and multi-strand clustering, respectively, while removing rigid body rotations and

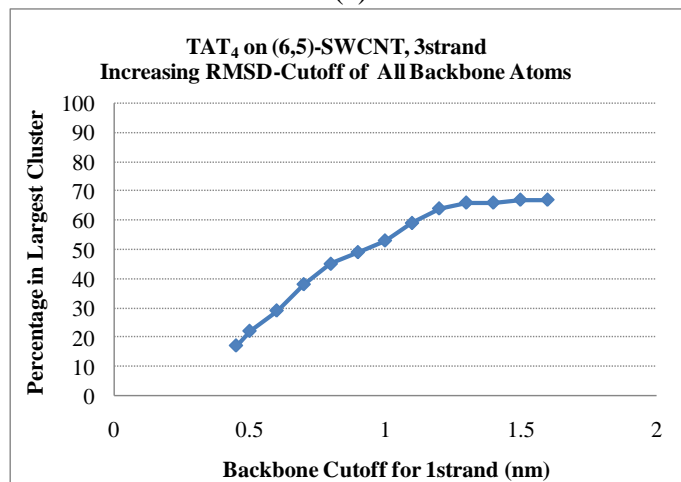


translations. Choosing an appropriate RMSD cutoff for clustering is also of significant importance. If the RMSD value is too low, percentages in the largest cluster drop off significantly, as well as the contrast between hybrids of different DNA composition. For individual-strand clustering of (TAT)<sub>4</sub> on (6,5)-SWCNT, systematically increasing the RMSD cutoff from 0.2 to 0.5 nm, we find that by ~0.4 nm, the percentage of structures in the largest cluster essentially remains at ~80%, (Figure 5.2a). To compare, the percentage of trajectory in the largest cluster was 83%, 39%, and 59% for (TAT)<sub>4</sub>-(6,5), (TAT)<sub>4</sub>-(8,7), and (T)<sub>12</sub>-(6,5) configurations, respectively. A greater population in the largest cluster should signify a more stable structure, as DNA is in a more-confined configuration. Likewise, in multi-strand clustering of (TAT)<sub>4</sub> on (6,5), for an RMSD cutoff of ~1.3 nm, the asymptotic limit of ~67% of the trajectory is reached, (Figure 5.2b). As such, this was the chosen cutoff. Comparing multi-strand configurations, (TAT)<sub>4</sub> on (6,5) still has the greatest population in the largest cluster (67%, 12%, and 17% of the trajectory for (TAT)<sub>4</sub>-(6,5), (TAT)<sub>4</sub>-(8,7), and (T)<sub>12</sub>-(6,5) hybrids, respectively). Cluster snapshots were then created which contained the overlaid selected group of atoms (generally backbone atoms of one or multiple strands). The mean smallest distances between DNA residues (consecutively numbered 1-36, since three 12-mer strands were simulated) were calculated and plotted in the form of a two-dimensional contact map. For comparison, we have computed the distance map for ideal single-stranded and double-stranded helices. The following averaged parameters were obtained from previous studies;<sup>13, 20</sup> 0.6 nm as the residue-residue distance along an outstretched DNA strand, 1.0 nm as the distance DNA residues sit from the center of a (6,5)-SWCNT,  $\pm 0.3$  nm as the distance residues are offset from the perfect helix in an alternating

fashion, and either  $\sim 9$  or  $\sim 12$  residues exist per helical turn for single-stranded and double-stranded helices, respectively. Moreover, the checkering pattern is a result of consecutive bases alternating sides of the backbone, modeled by the offset parameter in the ideal helix. For example, if a base  $i$  is close to base  $j$ , it will also be close to base  $j+2$  and  $j-2$ , but further from  $j+1$  and  $j-1$ , since bases are on alternating sides of the backbone.



(a)



(b)

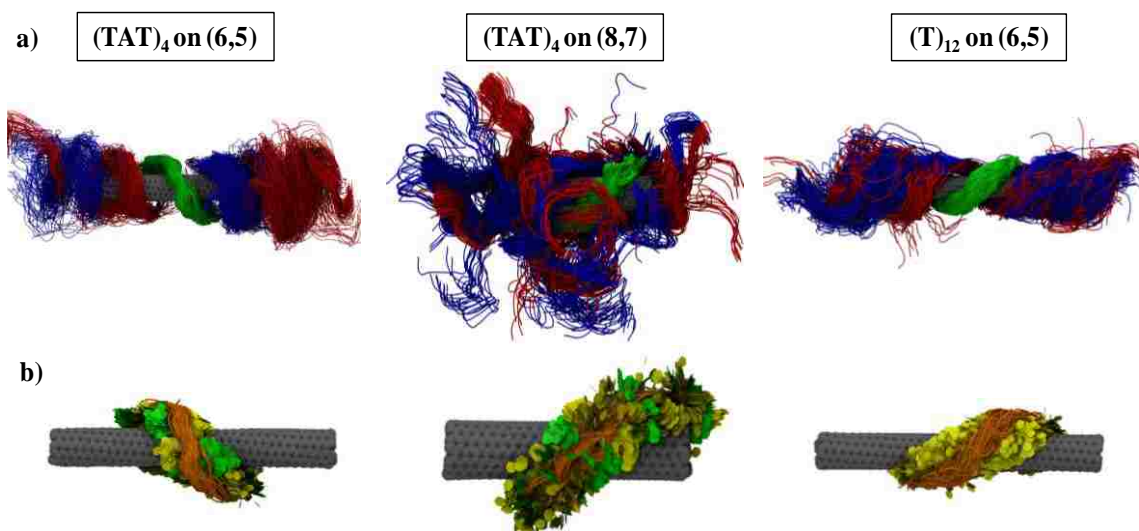
**Figure 5.2.** (a) Plot showing process for choosing individual-strand clustering criteria via backbone RMSD. The backbone RMSD cutoff values for strand1 were increased from 0.2 – 0.5 nm to find the optimum cutoff. (b) In a similar fashion, RMSD cutoff was increased for multi-strand clustering.

### **Photoluminescence of SWCNTs**

To explore the special affinity of (TAT)<sub>4</sub> for small diameter SWCNTs, two separate dispersions of *Hipco* SWCNTs (*NanoIntegris*) were produced. The *Hipco* nanotube sample was selected since SWCNT diameters ranged from 0.7-1.1 nm and contained significant amounts of 11 different types of SWCNT-chiralities.<sup>30</sup> In a weight ratio of 2:1 DNA:SWCNT, 0.5 mg of *Hipco* was dispersed with 1 mg of ssDNA (either (TAT)<sub>4</sub> or (T)<sub>12</sub>, purchased from *IDT DNA*) in a 10 mM phosphate buffer using 90 minutes of probe sonication (*Branson Ultrasonics*) at 8 Watts followed by 90 minutes of centrifugation (*Eppendorf*) at 16,000 xg. The resultant supernatant was extracted and diluted 20-fold. Two-dimensional fluorescence maps were made, using a Fluorolog-3 instrument (*Horiba-Jobin Yvon*) under the following conditions: 500nm-825nm excitation with increments of 3nm and slit width of 8nm; 900-1350 emission also with increments of 3nm and slit width of 8nm. Dark count correction factors were applied with a 1.0 s time of integration. Similar to a previous study,<sup>12</sup> we have exchanged the DNA coating of each sample with a surfactant, sodium dodecylbenzene sulfonate (SDBS) (*Sigma-Aldrich*), by heating the DNA-*Hipco* samples in the presence of 0.1 wt% SDBS at 60°C for 10 minutes. Since photoluminescence intensity is related to SWCNT concentration as well as the degree to which the SWCNT is shielded from the surrounding water environment, by substituting DNA for a control covering (SDBS), we have eliminated any variations in intensity due to DNA-coating among different SWCNT-chiralities.

### 5.3 Results and Discussion

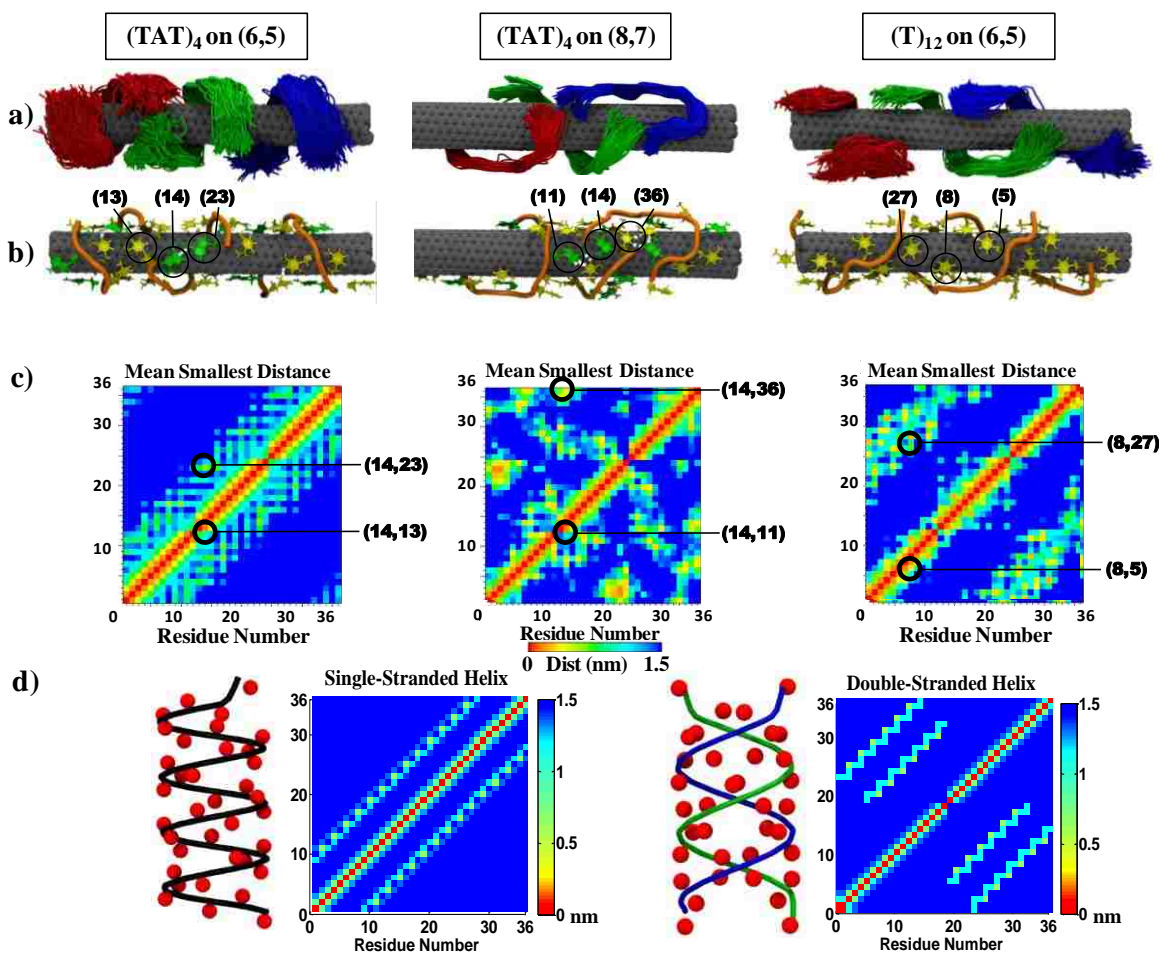
To identify the stable equilibrium structures, we use a structural clustering method. Initially, simulated multi-strand hybrids were examined in a strand-by-strand approach, allowing for the extraction of the underlying individual strand structure. In Figure 5.3a, clusters were constructed, subjected to the atom positions of only one strand (green). Upon collectively displaying all three strands, a qualitative degree of disorder can be inferred from the positions of the remaining two strands (red and blue). In Figure 5.3b, the DNA strand used for single-strand clustering, including backbones as well as bases, is shown for the three respective clusters. Clearly, the adenine (green) and thymine (yellow) bases of  $(TAT)_4$ -(8,7) sample the greatest volume as compared to the other two hybrids, signifying a disordered structure. From individual strand clustering the following conclusions become apparent: **a)** Each  $(TAT)_4$  strand adopts a right-handed helical self-stitched conformation on the (6,5) SWCNT, maintaining the structure discovered previously for a single strand;<sup>20</sup> the interactions between neighboring strands (red and blue) are well-correlated (low RMSD) with the strand used for clustering (green), **b)**  $(TAT)_4$  on (8,7) forms a much more disordered structure than that on (6,5), **c)**  $(T)_{12}$  on (6,5) forms a different, left-handed, helix with poorer inter-strand correlation compared to  $(TAT)_4$ , and **d)** DNA base positions help to distinguish ordered vs. disordered structures.



**Figure 5.3.** (a) Clustering of trajectory structures according to backbone atom positions of strand 1 (green strand) for  $(TAT)_4$  on (6,5),  $(TAT)_4$  on (8,7), and  $(T)_{12}$  on (6,5)-SWCNTs. After clustering strand 1, strands 2 and 3 (red and blue, respectively) are overlaid onto the same image to extract a relative degree of stability in the overall hybrid, as illustrated by the effective volume taken up by the red and blue strands. (b) Nucleic acid representations are shown for their respective hybrid clusters. The positions of the bases, adenine (green) and thymine (yellow), again signify a qualitative degree of disorder.

In contrast to examining the local order established from individual strands of adsorbed DNA, long-range order can be probed by monitoring all of the strands as a single entity. In essence, the previous clustering analysis was broadened to encompass backbone atom positions of all three strands. In Figure 5.4a, it is clear that the same DNA sequence can form two completely different structures depending on the type of SWCNT, demonstrating SWCNT-based selectivity. On the (6,5)-SWCNT,  $(TAT)_4$  strands appear to adjoin at their ends to mimic that of one long right-handed helical strand. As evident in Figure 5.4b, this particular hybrid is stabilized by intra- and inter-strand hydrogen bonded interactions (white-dashed lines). This structure is practically non-existent on the (8,7)-SWCNT, where DNA forms small loop configurations on the surface. To elucidate this difference in structure, two-dimensional distance maps (see

methods section) are constructed to show the presence of an emergent stable structure as compared to idealized structures, Figure 5.4c,d. In the distance maps, a primary band is always seen along the 45° line, as self-distances are reported as zero and distances among consecutive residues are generally small. More importantly, a secondary band is predicted 9-10 residues from the 45° line of a single-stranded helix, precisely as is seen in the distance map of (TAT)<sub>4</sub>-(6,5) based on simulation results. In contrast, the map of (TAT)<sub>4</sub>-(8,7) signifies a high degree of disorder with no corresponding idealized form. Because of this, the sequence (TAT)<sub>4</sub> can selectively form stable structures on smaller diameter SWCNTs that are not possible on those with larger diameters. This is one, relatively coarse, mode of recognition, i.e. recognition based on diameter-controlled self-stitching.



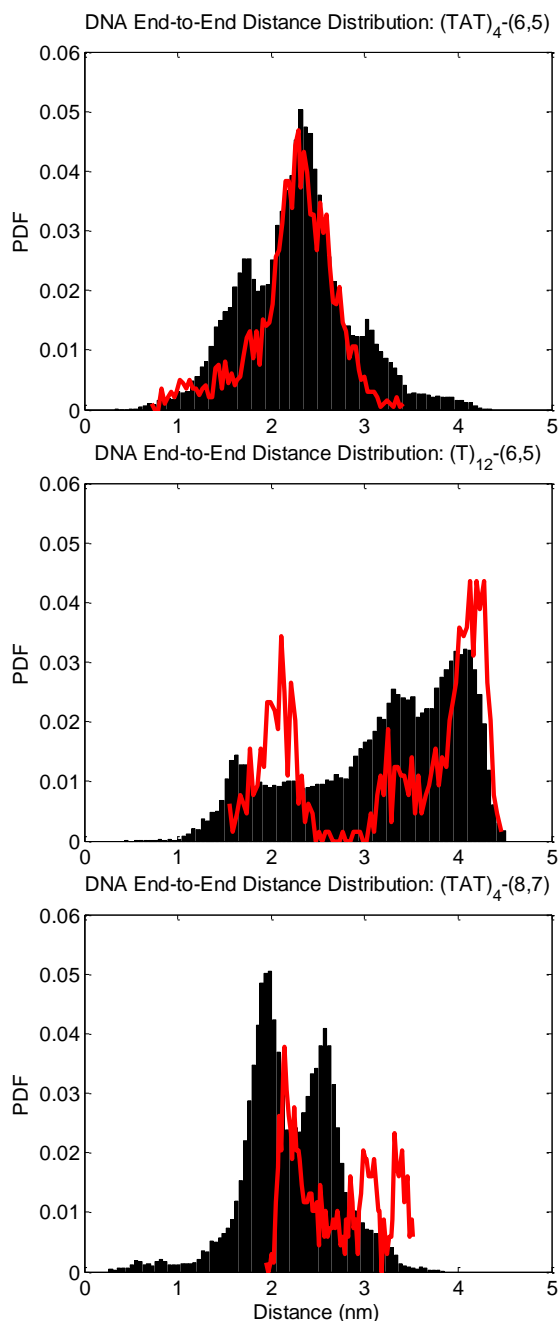
**Figure 5.4.** (a) Further clustering analysis of equilibrium structures was performed using backbone positions of all three DNA strands simultaneously. Overlaid snapshots of the largest cluster for (TAT)<sub>4</sub> on (6,5), (TAT)<sub>4</sub> on (8,7), and (T)<sub>12</sub> on (6,5) show immense variability in structure as SWCNT-chirality and/or DNA sequence is altered. **b**, Snapshots illustrating DNA bases adenine (green) and thymine (yellow) are shown for the largest clusters, respectively. **c**, Two-dimensional mean smallest distance maps based on nucleic acid residue distances in the largest respective cluster. To help interpretation of this map, selected residues have been labeled in (b); distances between pairs are labeled in the corresponding mean smallest distance maps in (c). For example, bases 14 and 23 in the structure of (TAT)<sub>4</sub> on (6,5) SWCNT come close due to intra-strand self-stitching as shown in (b). The corresponding point appears in (c) with a short distance. (d) As measures of comparison, distance maps of perfect helices, containing 36 nodes offset from the helix to emulate a base-backbone alternating motif, are plotted for single-stranded and double-stranded configurations. Comparing (TAT)<sub>4</sub> on (6,5) to the single-stranded control, a secondary band is seen ~10 residues from the 45° line. Likewise, (T)<sub>12</sub> on (6,5) can be compared to the double-stranded control as a partial secondary band is seen ~12-22 residues away.

The forgoing discussion considers how a given DNA strand can select a particular SWCNT. We now consider the structure of two different strands on the same SWCNT. We have previously reported that a single strand of (T)<sub>12</sub> exhibits far less hydrogen-bond mediated self-stitching than (TAT)<sub>4</sub> on a (6,5)-SWCNT, hypothesized to be from a lack of Watson-Crick base pairs (Adenine-Thymine or Guanine-Cytosine) near the strand ends.<sup>20</sup> For multiple-strand simulations, we find that the switching of the DNA helical-handedness between (TAT)<sub>4</sub> (right-handed) to (T)<sub>12</sub> (left-handed) is accompanied by the relaxation of the helical angle. A DNA wrap more loosely wound in the (T)<sub>12</sub>-(6,5) hybrid results in the formation of the previously proposed double-stranded  $\beta$ -barrel.<sup>13</sup> Most importantly, the double-stranded barrel structure does not allow individual strands of DNA to self-stitch via intra-strand hydrogen bonds. Instead, it relies exclusively on inter-strand hydrogen bonds for its stability. This can again be seen in the distance maps (Figure 5.4c,d), where two shorter secondary bands are predicted for a double-stranded helix at 12 and 22 residues from the 45° line, the beginnings of which are seen in the (T)<sub>12</sub> on (6,5) hybrid.

As another method to compare equilibrium structures amongst simulated configurations, the three-dimensional DNA end-to-end distances, i.e. H3T (3' terminal hydrogen) to H5T (5' terminal hydrogen), are calculated throughout the trajectory for each individual DNA strand. Histograms of end-to-end distances are constructed and used to predict and compare the most probable distances. Initially, the full equilibrium trajectory is used to construct the histogram for each configuration, e.g. 100-400 ns for (TAT)<sub>4</sub>-(6,5) configuration. These are shown as the solid black bar graphs below in Figure 5.5. The range of distances was found to be between 0 and 5 nm with a bin size of



0.0625. Additionally, the end-to-end distance histograms of the clusters found in Figure 5.4a were plotted as red lines on top. It is seen that the peaks in the cluster probability distribution functions (PDFs) do not always correlate with those in the full trajectory PDFs. This can be thought of as two entirely unique methods to cluster the data: end-to-end distance versus RMSD of backbone atom positions. It is not necessarily the case that dominant structures in each method must be identical.



**Figure 5.5.** End-to-end distribution plots for DNA strands on the various DNA-SWCNT simulated combinations. Solid black bar histograms encompass the full equilibrium trajectory while the overlaid red lines are the distributions of the clusters found in Figure 5.4a of the main text.

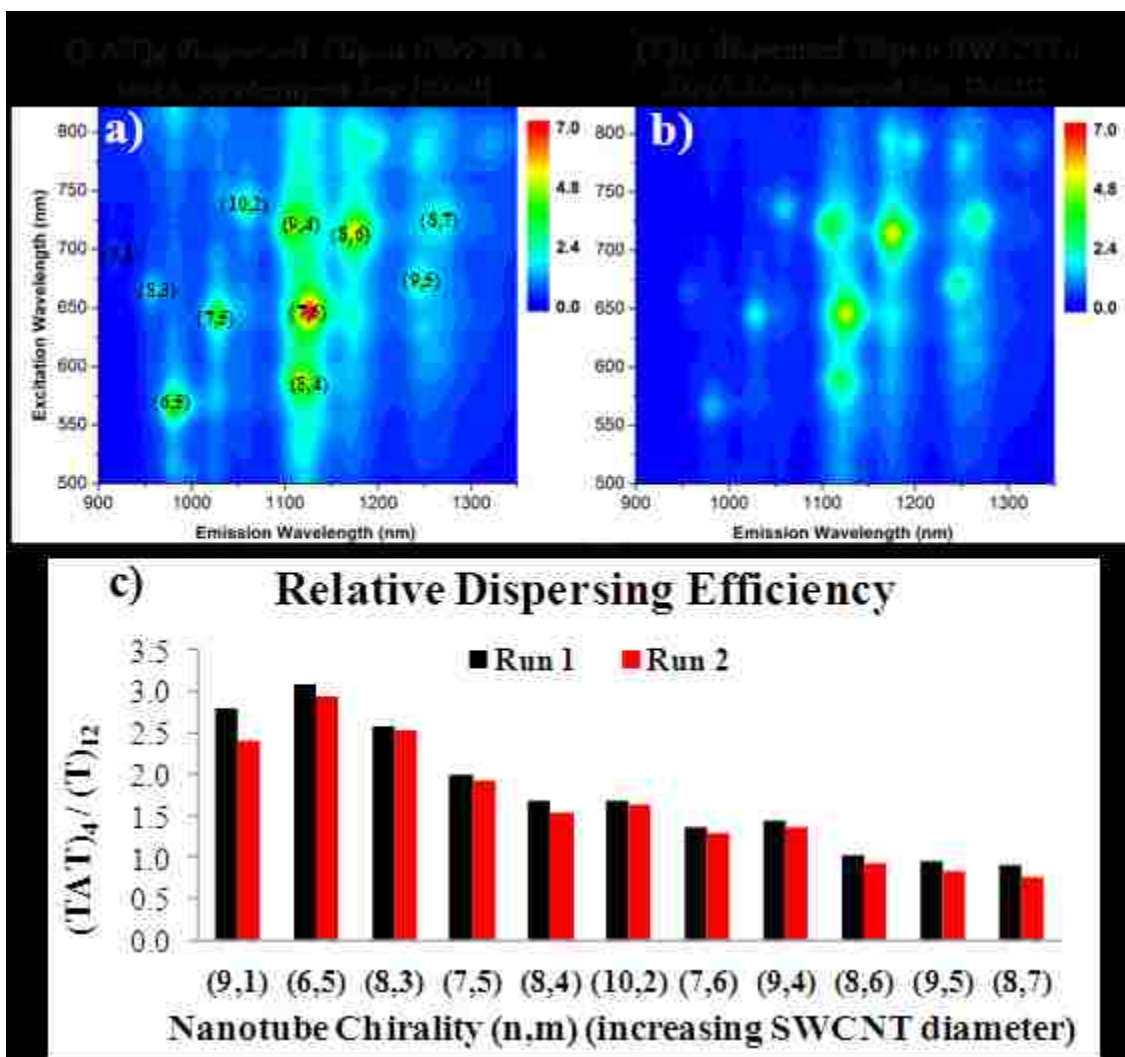
Regarding Figures 5.4a and 5.5, it is seen that  $(TAT)_4-(6,5)$  has one dominant peak at 2.3 nm. This is reminiscent of a single-stranded helical structure where short DNA strand ends line up to mimic that of one much longer. In the case of the cluster

PDF for  $(T)_{12}$ -(6,5), the green and blue strands have much more outstretched configurations, which become evident in their end-to-end distribution peaks at 4.2 nm. This is further proof that these two strands are exhibiting double-stranded DNA  $\beta$ -barrel behavior. In this same configuration, the third strand (red) is not able to participate in the  $\beta$ -barrel, and thus forms a more tightly bound wrap with end-to-end distance of 2.1 nm. In the final configuration,  $(TAT)_4$ -(8,7), because individual DNA strands are not able to fully wrap the SWCNT, the end-to-end distributions are populated by looped and disordered DNA structures.

In summary, a comparison of the structures adopted by  $(TAT)_4$  vs.  $(T)_{12}$  suggest the following; **a)** The  $(TAT)_4$  self-stitching structure will be disallowed for larger diameter SWCNTs. **b)** The  $(T)_{12}$   $\beta$ -barrel structure should not depend as much on SWCNT diameter. **c)** Sequences that rely on self-stitching should show better binding for small diameter SWCNTs than  $(T)_{12}$ , whereas the two should show similar binding for larger diameter SWCNTs.

To test these hypotheses, we have investigated DNA sequence-dependent SWCNT dispersion efficiencies (Figure 5.6). From simulation studies, we expect very different behavior between hybrids of  $(TAT)_4$  and  $(T)_{12}$ . We observe that both sequences disperse larger diameter SWCNTs with roughly equal efficacy, represented by a ratio of photoluminescence intensity near unity. However,  $(TAT)_4$  is far more efficient than  $(T)_{12}$  in dispersing small-diameter SWCNTs, with the largest ratio corresponding to its recognition partner, (6,5) (Figure 5.6c). Furthermore, the overall trend that  $(TAT)_4$  disperses smaller diameter SWCNTs better than  $(T)_{12}$  is easily seen. We hypothesize that

the systematic diameter selectivity seen in  $(TAT)_4$ -dispersed samples but not in  $(T)_{12}$  is consistent with the variation in DNA structure observed during simulation.



**Figure 5.6.** (a,b) Two-dimensional photoluminescence maps for as-produced Hipco-SWCNT hybrids with  $(TAT)_4$  and  $(T)_{12}$  DNA oligomers after exchanging with SDBS to remove DNA wrapping effects. (c) Peak intensities were compared to accurately find the differences in dispersion efficiencies among the two types of DNA sequences. Clearly,  $(TAT)_4$  selectively disperses more smaller diameter SWCNTs than  $(T)_{12}$ , with the peak intensity ratio located at the known recognition (6,5)-SWCNT.

## 5.4 Conclusions

Through the use of equilibrium molecular dynamics data, we have shown strong sequence & chirality-dependent structural variability among DNA-SWCNT hybrids. We

find certain characteristics that enable structure-based selectivity, consistent with experimental data on dispersion efficiency. In particular, DNA helical handedness and pitch are directly related to the sequence when simulated on the same SWCNT, a property most probably related to the emergence of long-range order. We also find that structure is directly related to the SWCNT diameter, since ordered structures on small-diameter SWCNTs are not sustained on a larger one. This study represents the first unbiased and detailed theoretical indication to support the notion that multiple strands of surface-adsorbed DNA can organize in an ordered manner on one particular SWCNT and not on another, a basic requirement for recognition.

## **5.5 Acknowledgements**

I would like to acknowledge Anand Jagota and Jeetain Mittal who have served as mentors for me during this work. Additionally, this work was supported by the National Science Foundation through grant CMMI-1014960, and a Faculty Innovation Grant (FIG) to Anand Jagota from Lehigh University. This research was also supported in part by the National Science Foundation through TeraGrid resources provided by the Texas Advanced Computing Center (TACC) under grant number [TG-MCB100049]. We specifically acknowledge the assistance of Mr. Chris Hempel and Dr. Hang Liu.

## 5.6 References

- (1) Tu, X. M.; Manohar, S.; Jagota, A.; Zheng, M., *Nature* **2009**, *460* (7252), 250-253.
- (2) Jin, H.; Heller, D. A.; Kalbacova, M.; Kim, J. H.; Zhang, J.; Boghossian, A. A.; Maheshri, N.; Strano, M. S., *Nature Nanotechnology* **2010**, *5*, 302-309.
- (3) Kam, N. W. S.; Liu, Z.; Dai, H., *J. Am. Chem. Soc.* **2005**, *127*, 12492-12493.
- (4) Liu, Z.; Chen, K.; Davis, C.; Sherlock, S.; Cao, Q.; Chen, X.; Dai, H., *Cancer Res.* **2008**, *68* (16), 6652-6660.
- (5) Welsher, K.; Liu, Z.; Daranciang, D.; Dai, H., *Nano Letters* **2008**, *8* (2), 586-590.
- (6) Zerda, A.; Zavaleta, C.; Keren, S.; Vaithilingam, S.; Bodapati, S.; Liu, Z.; Levi, J.; Smith, B. R.; Ma, T. J.; Oralkan, O.; Cheng, Z.; Chen, X.; Dai, H.; Khuri-Yakub, B. T.; Gambhir, S. S., *Nature Nanotechnology* **2008**, *3*, 557-562.
- (7) Saenger, W., Principles of Nucleic Acid Structure. Cantor, C. R., Ed. Springer-Verlag: New York, 1984; pp 134-135.
- (8) Zheng, M.; Jagota, A.; Semke, E. D.; Diner, B. A.; Mclean, S. R. L.; Richardson, R. E.; Tassi, N. G., *Nature Materials* **2003**, *2*, 338-343.
- (9) Khripin, C. Y.; Manohar, S.; Zheng, M.; Jagota, A., *Journal of Physical Chemistry C* **2009**, *113* (31), 13616-13621.
- (10) Albertorio, F.; Hughes, M. E.; Golovchenko, J. A.; Branton, D., *Nanotechnology* **2009**, *20*.
- (11) Vogel, S. R.; Kappes, M. M.; Hennrich, F.; Richert, C., *Chem. Eur. J.* **2007**, *13*, 1815-1820.
- (12) Roxbury, D.; Tu, X.; Zheng, M.; Jagota, A., *Langmuir* **2011**, *27* (13), 8282-8293.
- (13) Roxbury, D.; Manohar, S.; Jagota, A., *J. Phys. Chem. C* **2010**, *114* (31), 13267-13276.
- (14) Zhao, X.; Johnson, J. K., *J. Am. Chem. Soc.* **2007**, *129* (34), 10438-10445.
- (15) Karachevtsev, V. A.; Karachevtsev, M. V.; Leontiev, V. S.; Lytvyn, O. S.; Bogorosh, A. T., *Fullerenes, Nanotubes and Carbon Nanostructures* **2010**, *18* (4-6), 531-537.
- (16) Karachevtsev, M. V.; Karachevtsev, V. A., *J. Phys. Chem. B* **2011**, *115* (29), 9271-9279.
- (17) Johnson, R. R.; Johnson, A. T. C.; Klein, M. L., *Nano Letters* **2008**, *8* (1), 69-75.
- (18) Sugita, Y.; Kitao, A.; Okamoto, Y., *J. Chem. Phys.* **2000**, *113*, 6042-6051.
- (19) Johnson, R. R.; Kohlmeyer, A.; Johnson, A. T. C.; Klein, M. L., *Nano Letters* **2009**, *9* (2), 537-541.
- (20) Roxbury, D.; Jagota, A.; Mittal, J., *J. Am. Chem. Soc.* **2011**, *133* (34), 13545-13550.
- (21) *Materials Studio (R)*, Accelrys Inc.: San Diego, CA.
- (22) Humphrey, W.; Dalke, A.; Schulten, K., *J. Molec. Graphics* **1996**, *14* (1), 33-38.
- (23) Berendsen, H. J. C.; van der Spoel, D.; van Drunen, R., *Computer Physics Communications* **1995**, *91* (1-3), 43-56.
- (24) Lindahl, E.; Hess, B.; van der Spoel, D., *J. Mol. Model* **2001**, *7* (8), 306-317.
- (25) van der Spoel, D.; Lindahl, E.; Hess, B.; Groenhof, G.; Mark, A. E.; Berendsen, H. J. C., *J. Comput. Chem.* **2005**, *26* (16), 1701-1718.
- (26) Foloppe, N.; MacKerell, A. D., *J. Comput. Chem.* **2000**, *21* (2), 86-104.

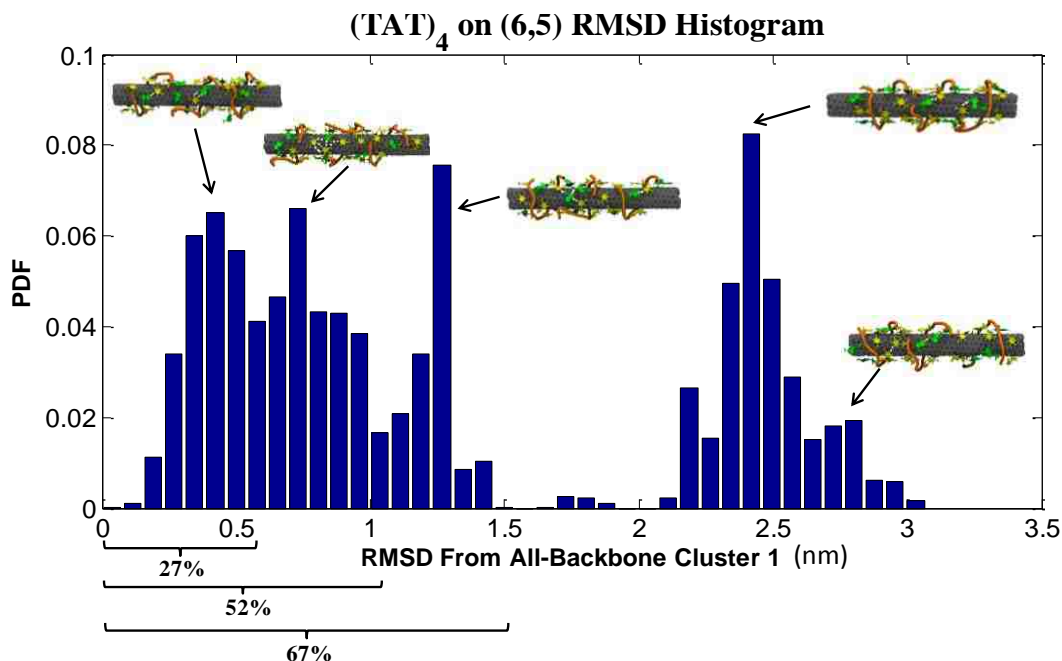
- (27) MacKerell Jr., A. D.; Banavali, N. K., *J. Comput. Chem.* **2000**, *21* (2), 105-120.
- (28) Jorgensen, W. L.; Chandrasekhar, J.; Madura, J. D.; Impey, R. W.; Klein, M. L., *J. Chem. Phys.* **1983**, *79*, 926.
- (29) York, D. M.; Darden, T. A.; Pedersen, L. G., *J. Chem. Phys.* **1993**, *99* (10).
- (30) Chiang, I. W.; Brinson, B. E.; Huang, A. Y.; Willis, P. A.; Bronikowski, M. J.; Margrave, J. L.; Smalley, R. E.; Hauge, R. H., *J. Phys. Chem. B* **2001**, *105*, 8297-9301.
- (31) Choi, J. H.; Strano, M. S., *Applied Physics Letters* **2007**, *90*, 223114.
- (32) Grigoryan, G., Kim, Y.H., Acharya, R., Axelrod, K., Jain, R.M., Willis, L., Drndic, M., Kikkawa, J.M., DeGrado, W.F., *Science* 2010, *332*, 6033, 1071.

## 5.7 Appendix

### 5.7.1 Additional Data Analysis of Published Results

As additional measures of analysis for *on-recognition* hybrids, the full trajectory of the three stranded (TAT)<sub>4</sub>-(6,5) configuration was examined in further detail. A number was assigned to each timeframe of the trajectory based on its RMSD from the most prevalent structure (i.e. the cluster found in Figure 5.4a). In Figure 5.7, a histogram is constructed displaying the probability distribution function reported as deviation from cluster 1. It is seen that 67% of the trajectory is within 1.5 nm RMSD from the most probable cluster. Selected snapshots are shown for various peaks in the PDF plot. The only observable difference between selected snapshots is the degree to which DNA strand ends ligate. In some instances, strand 1 perfectly aligns with strand 2 such that two strands mimic one twice as long. Else, the DNA strand ends tend to loop back, in a hook fashion. Structures like these visually appear more disordered than the first described scheme. Overall, the DNA remains in a right-handed single-stranded helical conformation, distinct from many of the other simulated configurations presented in this chapter.

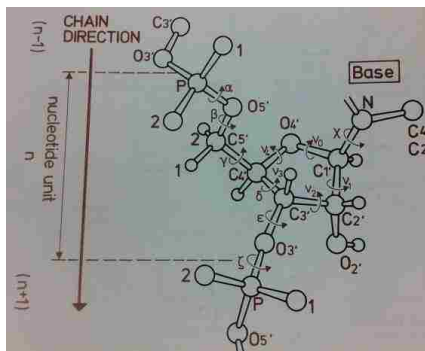




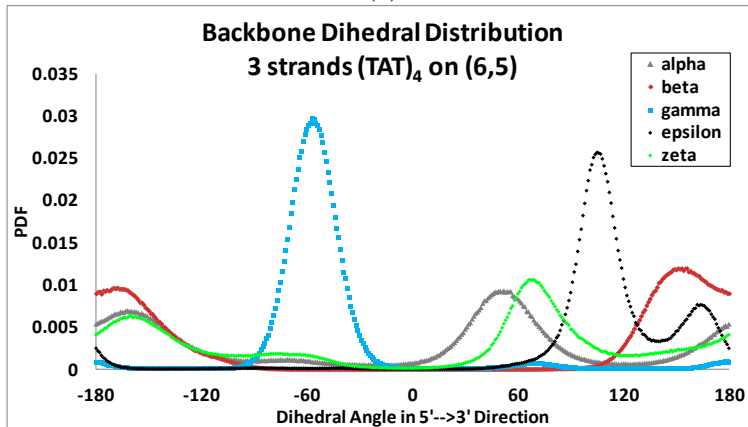
**Figure 5.7.** Histogram of the RMSD distance from the most prevalent structure for the full trajectory of the three stranded  $(TAT)_4-(6,5)$  configuration. Selected snapshots of various peaks in the PDF are shown, with the only observable differences arising from the degree of DNA strand end ligation.

From Figure 5.4, it was observed that under equilibrium conditions,  $(TAT)_4-(6,5)$  hybrids exhibited right-handed helical wrapping while  $(T)_{12}-(6,5)$  were left-handed. To further explore, distributions of the DNA backbone dihedral angles were examined. Figure 5.8a displays all of the dihedral angles found in a typical nucleotide.<sup>7</sup> In this schematic, the 5 backbone dihedrals that vary depending on overall DNA conformation are  $\alpha$ ,  $\beta$ ,  $\gamma$ ,  $\epsilon$ , and  $\zeta$ . These particular dihedral angles have been tracked over the course of the 100-400 ns trajectory for the  $(TAT)_4-(6,5)$  and  $(T)_{12}-(6,5)$  configurations. In Figure 5.8 b&c, distinctly different probabilities are observed between the two configurations when analyzing the data in a consistent 5'→3' manner. Across the 0° line, the two sets of distributions are nearly symmetrical with respect to each other. The switching of wrapped DNA overall helicity can explain this symmetrical behavior. As such, on a scale of -180° to 180°, it appears that each backbone dihedral angle is reflected across the 0°

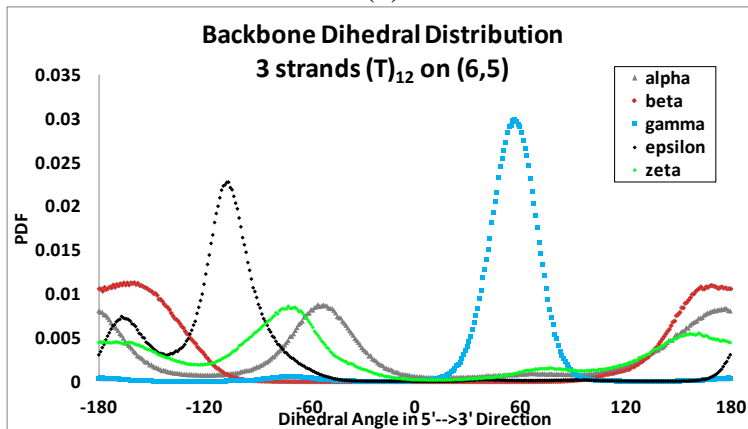
degree line when the overall helicity is switched (e.g. right-handed to left-handed). It is, however, interesting to note that every dihedral angle is reflected by the change in helicity, not just a select few.



(a)



(b)

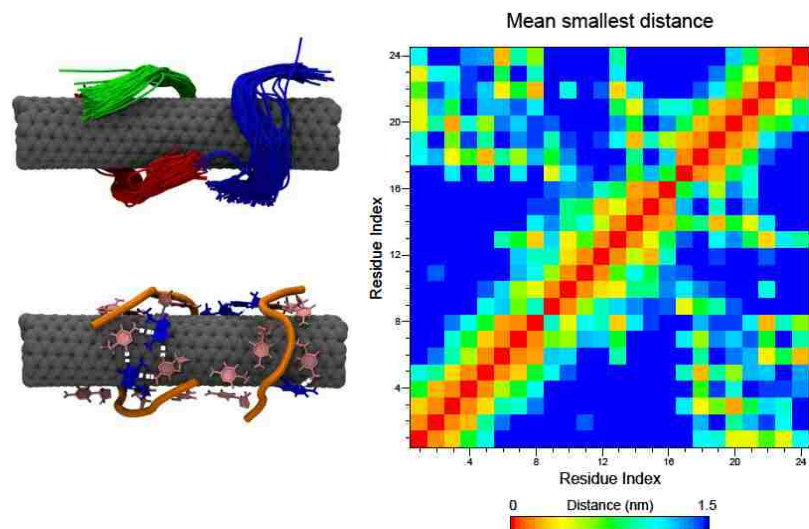


(c)

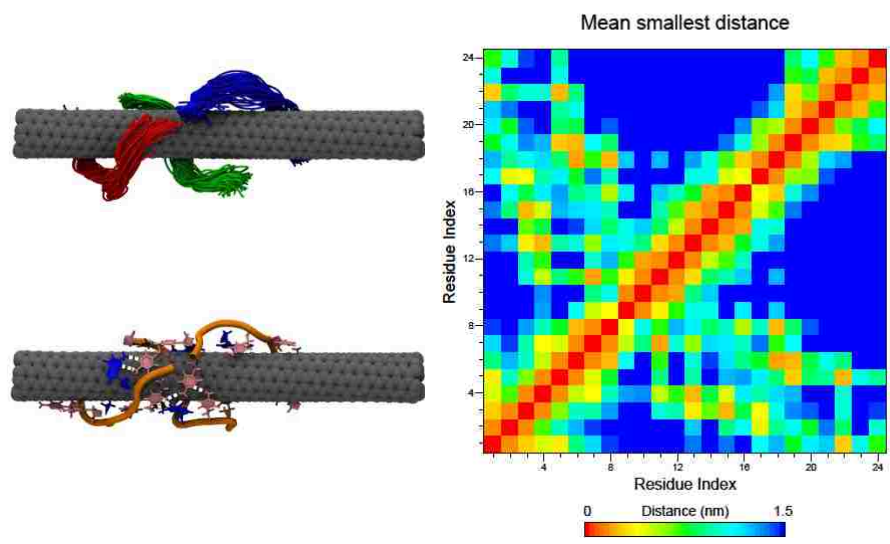
**Figure 5.8.** (a) Schematic of DNA nucleotide illustrating the backbone dihedral angles.<sup>7</sup> Distributions of the 5 major dihedral angles are shown for (a)  $(TAT)_4$ -(6,5) and (b)  $(T)_{12}$ -(6,5) configurations. The symmetric nature, with respect to each other, suggests right-handed versus left-handed overall DNA helicity.

## 5.7.2 Additional Simulated Configurations

In addition to the configurations found in the published portion of this chapter, several other DNA sequence-SWCNT chirality combinations were examined. Lending to its innate recognition ability, three strands of  $(CCG)_2CC$  were examined on the (8,7)-SWCNT. Additionally, an *off-recognition* configuration was examined, i.e.  $(CCG)_2CC$  on (6,5). In Figures 5.9 and 5.10, the top clusters are found for three strands of  $(CCG)_2CC$  on (8,7) and (6,5)-SWCNTs, respectively. It is observed that the degree of DNA-DNA hydrogen bonding (h-bonding) is much greater in the  $(CCG)_2CC$  sequence versus  $(TAT)_4$ . Qualitatively, in both configurations single-strands of DNA are not long enough to wrap entirely around the SWCNT into order to h-bond self-stitch. Yet, the DNA does not exhibit the loop-like structures seen in configurations like  $(TAT)_4$ -(8,7). With ligation between adjacent strands arising from interstrand h-bonding, multiple strands of  $(CCG)_2CC$  completely wrap the SWCNT surface. Additionally, the mean smallest distance maps are constructed for the clusters found in Figures 5.9 and 5.10. Both maps exhibit the appearance of secondary structure, as lines perpendicular to the 45° line.



**Figure 5.9.** Three strands of DNA sequence  $(CCG)_2CC$  simulated on an  $(8,7)$ -SWCNT for 400 ns of REMD. A typical DNA backbone cluster is shown (top left) with DNA cartoon model (bottom left). The two-dimensional mean smallest distance map is constructed, showing the prevalence secondary structure not seen in previous configurations.

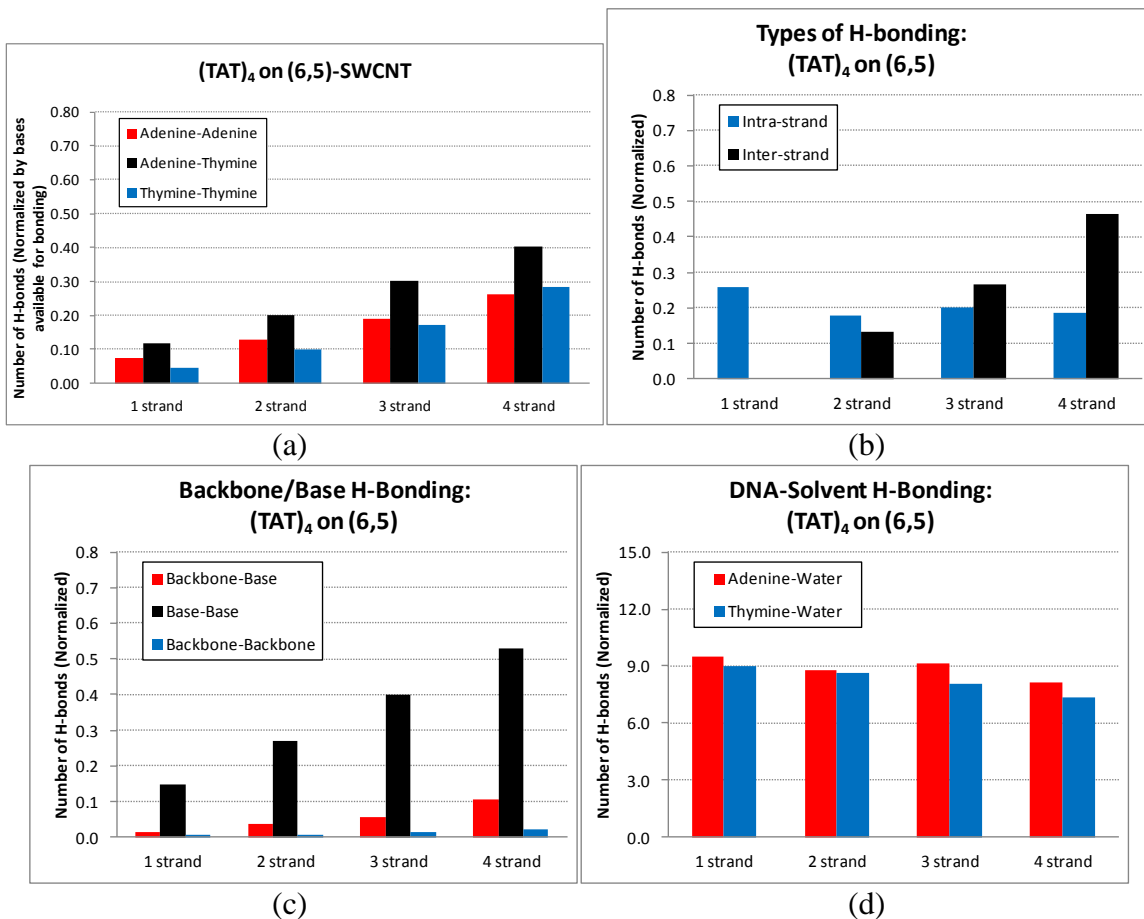


**Figure 5.10.** Three strands of DNA sequence  $(CCG)_2CC$  simulated on a  $(6,5)$ -SWCNT for 400 ns of REMD. A typical DNA backbone cluster is shown (top left) with DNA cartoon model (bottom left). The two-dimensional mean smallest distance map is constructed, showing the prevalence secondary structure not seen in previous configurations.

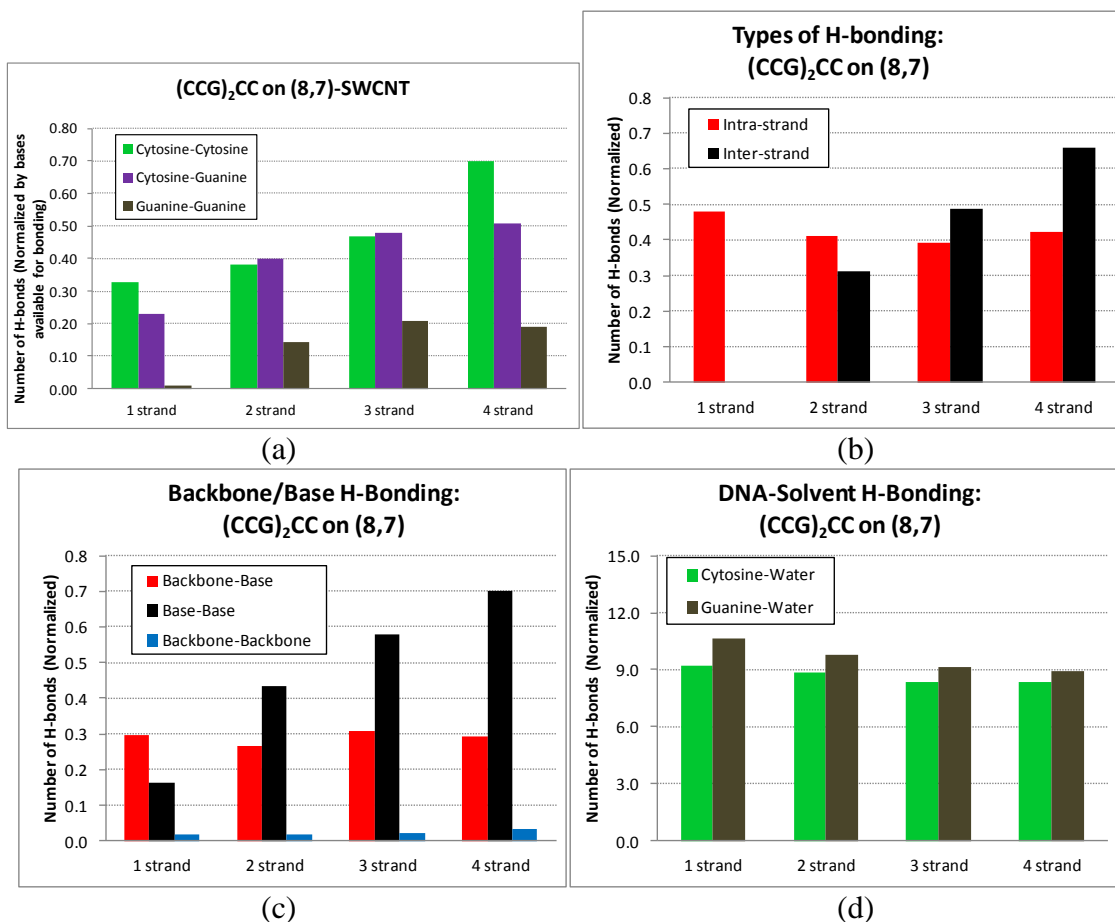
It is proposed that much of the DNA-SWCNT hybrid secondary structure arises from h-bonded interactions between SWCNT-adsorbed DNA strands. These can be intra-strand (between DNA bases on the same strand) or inter-strand (bases on different strands). H-bonding trends were examined for the recognition DNA-SWCNT pairs on additionally simulated configurations of one, two, three, and four strand conformations for both  $(TAT)_4-(6,5)$  and  $(CCG)_2CC-(8,7)$ . Results from the last 100-400 ns of simulation (discarding an initial 100 ns of equilibration) are shown in Figures 5.11 and 5.12, respectively. In order to compare among configurations with different quantities of DNA, h-bond numbers have been normalized in the plots by the number of DNA bases available for bonding, e.g. in the case of 1 strand of  $(TAT)_4$ , the number of Adenine-Adenine and Thymine-Thymine bonds are normalized by 4 and 8, respectively. In Figures 5.11a and 5.12a, an increasing trend is seen signifying that the number of DNA strands increases the degree to which hydrogen bonding occurs. The canonical Watson-Crick h-bonding pairs, Adenine-Thymine and Guanine-Cytosine, generally comprise the majority of observed configurations. Figures 5.11b and 5.12b show that the prevalence of inter-strand h-bonding leads to the overall increase in normalized h-bonding. Furthermore, normalized intra-strand h-bonding is generally a constant that depends on DNA sequence (e.g. 0.2 h-bonds/base for  $(TAT)_4$  and 0.4 h-bonds/base for  $(CCG)_2CC$ ).

Upon further analysis, it is seen that DNA backbone-base h-bonding interactions are negligible in the  $(TAT)_4-(6,5)$  configurations (Figure 5.11c). Conversely, in the  $(CCG)_2CC-(8,7)$  configurations, backbone-base h-bonding plays a rather significant role. This is due largely to the tendency of Guanine to form a stable h-bond with a sugar-oxygen located on the backbone. Finally, Figures 5.11d and 5.12d show that DNA-water

h-bonding is relatively constant and insensitive of DNA sequence. In constant NVT simulations, an increase in DNA-DNA h-bonding is generally compensated by a decrease in energy elsewhere, i.e. DNA-water h-bonding.



**Figure 5.11.** For simulations of (TAT)<sub>4</sub> on (6,5)-SWCNT, h-bonding trends based on (a) DNA base designation, (b) inter-strand vs. intra-strand, (c) backbone and base considerations, and (d) DNA-water interactions are compared. Reported h-bond numbers are normalized by the number of available DNA bases.

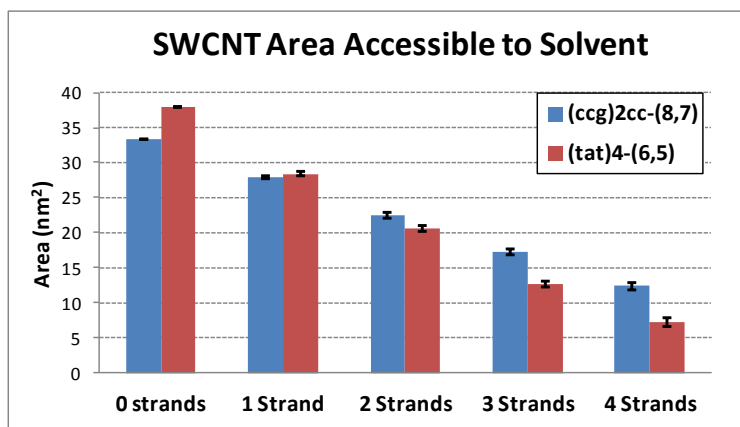


**Figure 5.12.** For simulations of  $(CCG)_2CC$  on (8,7)-SWCNT, h-bonding trends based on (a) DNA base designation, (b) inter-strand vs. intra-strand, (c) backbone and base considerations, and (d) DNA-water interactions are compared. Reported h-bond numbers are normalized by the number of available DNA bases.

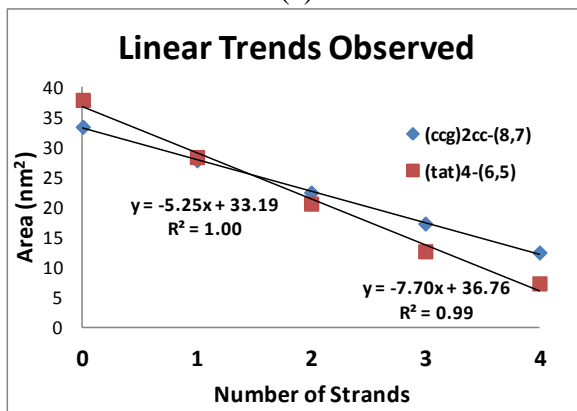
In the case of proteins and other biological molecules, the solvent accessible surface (SAS) area is a useful quantity to know for predicting enzymatic activity and free energies of solvation. In the simulated hybrids of DNA and SWCNTs, the area of nanotube surface available to solvent (water and counter-ions) is useful in the sense that it signifies the degree of shielding. This is important for sensing and detection applications as SWCNT photoluminescence is dependent on this degree of shielding from the solvent.<sup>31</sup>

For the 8 configurations examined previously for h-bonding trends, the SAS areas were calculated and averaged over the same region of analyzed trajectory. In Figure

5.13a, average quantities for SAS area are shown with standard deviation for the 8 configurations. It was observed that the SAS areas decreased in a linear fashion as the number of occupying strands increased. For  $(TAT)_4-(6,5)$  and  $(CCG)_2CC-(8,7)$ , SAS area (in  $\text{nm}^2$ ) could be calculated as  $-5.25x + 33.19$  and  $-7.70x + 36.76$ , respectively, where  $x$  indicated the number of DNA strands. Upon DNA saturation of the SWCNT surface, an asymptotic minimum value of SAS area will be reached. There is small evidence (as deviation from the linear trend) for saturation in the  $(TAT)_4-(6,5)$  configuration at the 4 strand data point.



(a)



(b)

**Figure 5.13.** Solvent accessible SWCNT surface area for various configurations of DNA-SWCNT hybrids. As the number of strands increases, SAS decreases linearly at a rate dependent upon the DNA sequence.

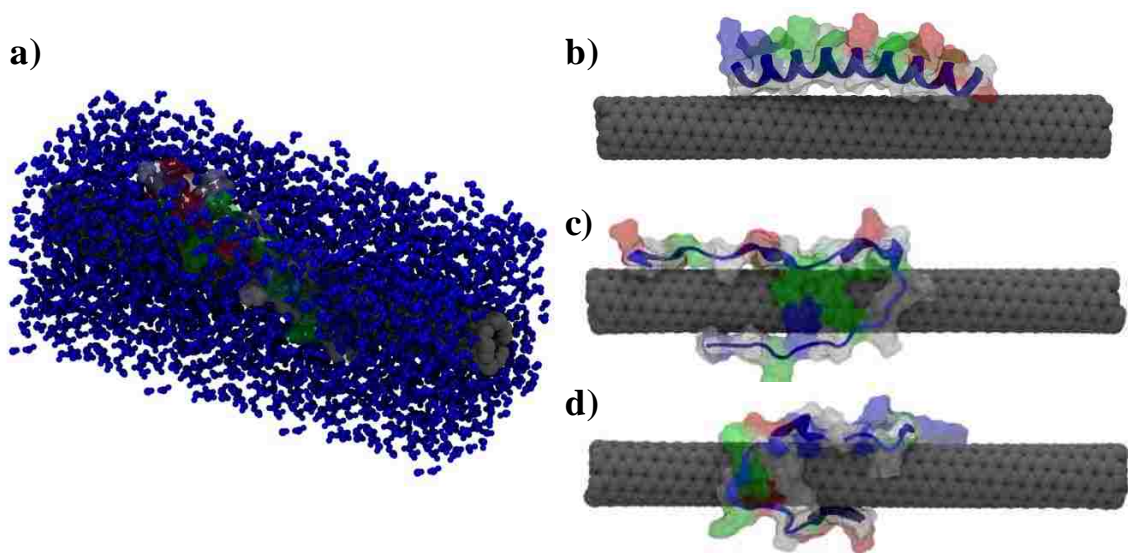


### 5.7.3 Peptide-SWCNT Simulations

From Chapter 2, Section 2.9.3, a specific peptide was introduced known as “HexCoil-Ala.” This is a peptide engineered and graciously donated to us by Dr. William Degrado of the University of California at San Francisco.<sup>32</sup> The peptide is known for its remarkably high dispersing efficiency of the (6,5)-SWCNT and other SWCNTs of similar diameter (e.g. (9,1) and (8,3)). The peptide is given the designation HexCoil for its tertiary appearance under certain physiological conditions. At salt concentrations near 100 mM and pH 7.4, six molecules of the HexCoil-Ala peptide will coalesce through several non-bonded interactions to form a supramolecular hollow barrel structure. Additionally, hydrophobic residues, such as Alanine and Tyrosine, were positioned in the sequence such that they faced the interior of the barrel. Moreover, polar and charged residues of the sequence faced the exterior. The barrel was then engineered to possess an interior void diameter roughly the size of the (6,5)-SWCNT. Upon normal sonication and centrifugation techniques (see Section 2.9.3), very stable dispersions of HexCoil-Ala-(6,5)-SWCNT hybrids have been synthesized.

Here, molecular dynamics simulations have been performed to probe the structures that the HexCoil-Ala peptide forms on a (6,5)-SWCNT. The simulation water box sizes were created in a similar way to those used for the DNA-SWCNT simulations presented in this chapter, Figure 5.14a. Therefore, REMD was performed using the same replica temperature distribution. A single molecule of HexCoil-Ala, in its native coiled state, was placed on the SWCNT (Figure 5.14b). It was oriented such that hydrophobic residues (designated as white residues in Figure 5.14b) were in close proximity to the SWCNT surface. It was then simulated for 200 ns of REMD. While examining the

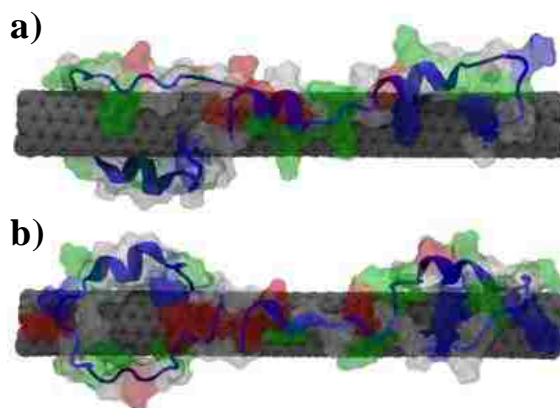
lowest temperature trajectory, 300 K, it was observed that the peptide had lost much of its secondary helical structure. Clustering performed on the data, using peptide backbone RMSD of 0.3 nm, resulted in a large distribution of structures. Representing only 5 and 4 % of the trajectory, respectively, the first two clusters are shown in Figure 5.14c,d. In general, the peptide unwound from its helical starting state and sampled the entirety of the SWCNT surface. The majority of these conformations were akin to a freely-jointed chain confined in the two-dimensions of the SWCNT surface.



**Figure 5.14.** (a,b) Replica exchange molecular dynamics simulation of HexCoil-Ala peptide in an initially coiled state on a (6,5)-SWCNT. (c,d) After 200 ns of simulation, much of the secondary structure is lost, yet the peptide remains adsorbed to the surface.

After simulation of the single-strand configuration, two strands of HexCoil-Ala peptide were placed on the same (6,5)-SWCNT. The starting configuration was created by selecting the peptides from the two largest clusters obtained from single-strand clustering, i.e. peptides from Figure 5.14c&d were combined to form the starting configuration for two-strand simulation. The newly constructed configuration was then run for 150 ns of REMD simulation. The dominant cluster, based on peptide backbone positions, still resembled a very disordered structure. Though both strands remained

adsorbed to the surface, there was little interaction between the two peptide molecules. Most importantly, the coiled structures reported by DeGrado et al. were not seen in the simulations. It is hypothesized that at least six molecules of the peptide are needed to form the idealized barrel structure. Moreover, in the simulation, an artificially high concentration of peptide as well as simulations on the order of milliseconds may be required in order to witness the emergence of the hexa-coiled barrel structure. At present, we can conclude that single and double strands of HexCoil-Ala peptide on the (6,5)-SWCNT do not form advanced secondary structures.

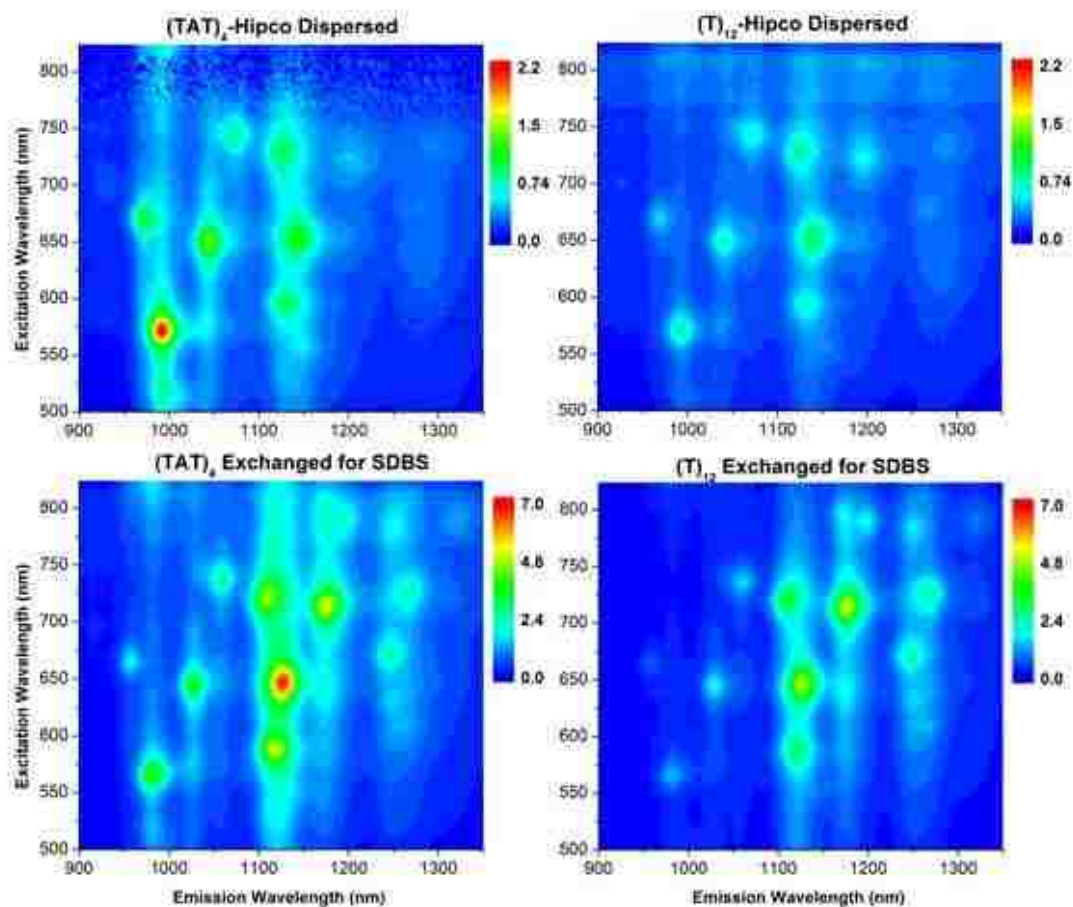


**Figure 5.15.** (a) Two strands of HexCoil-Ala were placed on a (6,5)-SWCNT. The starting structure was obtained from the two dominant clusters of the single-strand configuration. (b) After 150 ns simulation, the dominant cluster still shows much disorder among the two strands.

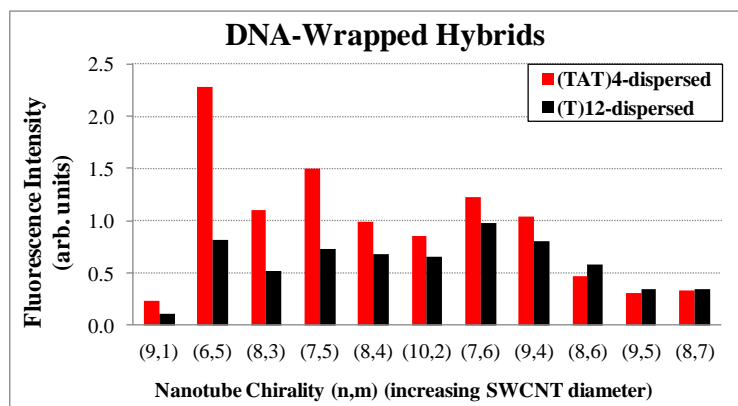
#### 5.7.4 Additional Photoluminescence Studies

It is known that DNA-wrapped SWCNTs exhibit extraordinarily different photoluminescence characteristics than those which are surfactant coated. It is hypothesized that differences in secondary structure of the adsorbed DNA molecules can account for this. Previously, surfactant had been used to displace the DNA from the surface of SWCNTs before taking a photoluminescence map in order to remove the effect

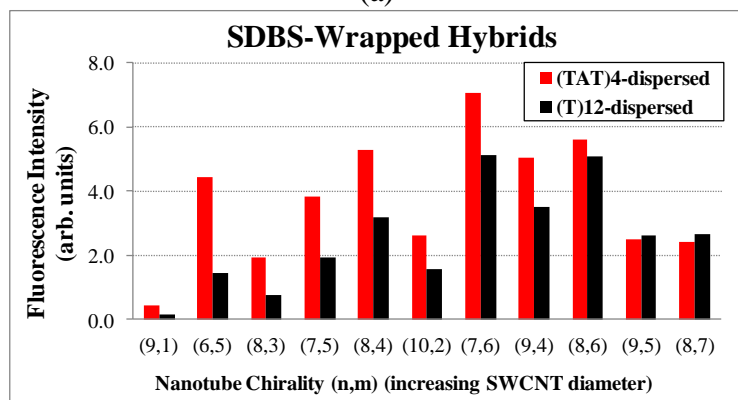
of DNA-wrapping. In Figure 5.16, the effect of DNA-wrapping is clearly displayed between samples of (TAT)<sub>4</sub> and (T)<sub>12</sub>-dispersed Hipco SWCNTs. The (TAT)<sub>4</sub>-wrapped sample shows the brightest peak at (ex. 575 nm, em. 990 nm), corresponding to (6,5)-SWCNTs. Likewise, the brightest peak in the (T)<sub>12</sub> sample is at (ex. 652, em. 1140), corresponding to (7,6)-SWCNT. This is seen more clearly in Figure 5.17a where under the same conditions (amount of DNA and SWCNT sample), the fluorescence intensity of (TAT)<sub>4</sub>-dispersed sample is much greater for (6,5), (8,3), and (7,5)-SWCNTs than that of (T)<sub>12</sub>. Upon exchange of the DNA-covering for SDBS surfactant, the absolute photoluminescence intensities change significantly and varies according to chirality designation, Figure 5.17b. In both the (TAT)<sub>4</sub> and (T)<sub>12</sub> samples, the (7,6)-SWCNT is the dominant chirality at (ex. 647, em. 1122).



**Figure 5.16.** (top) Two-dimensional photoluminescence maps for Hipco SWCNT sample dispersed in either (TAT)<sub>4</sub> or (T)<sub>12</sub> DNA oligomers. (bottom) Since DNA-wrapping can have significant effects on the photoluminescence of SWCNTs, surfactant induced exchange was performed on the dispersed samples in order to remove the DNA covering. Resultant maps show great variation in photoluminescence intensity between DNA-wrapped and SDBS-wrapped SWCNTs.



(a)

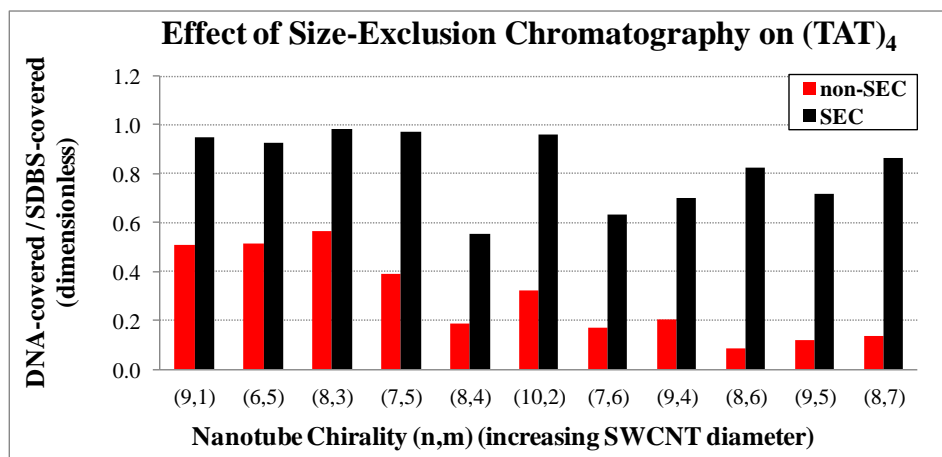


(b)

**Figure 5.17.** Peak intensities from the photoluminescence maps found in Figure 5.12 for (a) DNA-wrapped and (b) SDBS-wrapped samples. A measure of absolute dispersing efficiency can be inferred from comparing the intensities of the SDBS-wrapped sample.

It is known that the size-exclusion chromatography (SEC) can have a profound effect on DNA-dispersed SWCNT sample. Not only does SEC sort SWCNTs by length, it was also found to alter the structure of adsorbed DNA in such a way that the rate of DNA displacement from the surface changed significantly (see Chapter 3). This phenomenon was left unprobed by further surfactant exchange experiments. Here, the difference in photoluminescence intensity between SEC and non-SEC samples is dramatic. In Figure 5.18, the ratio of intensities between DNA-covered and SDBS-covered samples is near 1 for SEC samples with few exceptions. In the non-SEC samples, the ratio for smaller diameter SWCNTs is roughly 0.5, while falling to 0.2 or below for larger diameter SWCNTs. These results may be directly related to the

secondary structure of the adsorbed DNA strands. A higher degree of shielding of the SWCNT surface from water yields higher photoluminescence intensity. It is known that surfactant covering affords for a superbly shielded SWCNT. In this plot then, a ratio near 1 suggests an intricate DNA secondary structure with a high degree of shielding. There is a need to examine these effects from SEC sample in more detail in future studies.



**Figure 5.18.** Photoluminescence intensity ratios of DNA-covered to SDBS-covered (TAT)<sub>4</sub>-dispersed sample before and after size-exclusion chromatography

## **Chapter 6**

### **DNA Conjugated SWCNTs Enter Endothelial Cells via Rac1 Mediated Macropinocytosis\***

*Several applications of single walled carbon nanotubes (SWCNT) as nanovectors in biological systems have been reported, and several molecular pathways of cellular entry have been proposed. We employed transmission electron microscopy, confocal fluorescent microscopy, and NIR spectroscopic analysis to confirm the internalization of DNA-SWCNT in human umbilical vein endothelial cells (HUVEC). Additionally, by using pharmacological inhibitors as well as genetic approaches, we have found that SWCNT is endocytosed through Rac1- GTPase mediated macropinocytosis in normal endothelial cells.*

---

\* Portions of this chapter have been published in Nano Letters:

S Bhattacharya, D Roxbury, X Gong, D Mukhopadhyay, A Jagota. "DNA Conjugated SWCNTs Enter Endothelial Cells Via Rac1 Mediated Macropinocytosis" *Nano Lett.* **12**, 4, 1826, (2012).



## 6.1 Introduction

By virtue of their high surface area and tunable properties, biologically-compatible nanomaterials have recently opened up a number of potential biomedical applications in sensing, imaging, and targeted intracellular delivery. Functionalized single-walled carbon nanotubes (SWCNTs) are a prime example due to their unique optical and physical properties.<sup>1</sup> Molecules can be attached to an SWCNT covalently or non-covalently; the latter of the two methods generally retains the SWCNT's optical integrity (NIR photoluminescence signals).<sup>2</sup> Cargo bound to SWCNTs have included antibodies,<sup>3</sup> chemotherapy drugs,<sup>4</sup> single-stranded DNA (ssDNA),<sup>5</sup> siRNA,<sup>6-7</sup> and short peptides.<sup>8</sup> Much effort has also been expended in developing conjugated SWCNTs as imaging and sensing entities in living organisms such as using fluorescence,<sup>9-11</sup> Raman,<sup>3, 12-13</sup> and photoacoustic<sup>14</sup> techniques after substrate binding. In addition, there is considerable interest in understanding the potential health risks associated with carbon nanomaterials. Thus, it is vital to study their interactions at the cellular and molecular level. The biocompatibility of functionalized SWCNTs is strongly correlated with the nature of the surface conjugation. For example, a well-coated biopolymer-conjugated SWCNT yields relatively low levels of toxicity.<sup>6, 15-16</sup> Long multi-walled SWCNTs (>10 $\mu$ m in length) have been found to promote carcinogenesis when administered through intraperitoneal injection.<sup>17-19</sup> However, far reduced toxicity is seen in SWCNTs less than 1 $\mu$ m in length.<sup>18</sup>

Nanomaterial uptake by cells may take place through numerous different mechanisms; these can broadly be classified as phagocytosis, receptor mediated endocytosis, and pinocytosis. Phagocytosis facilitates the uptake of large particles by

utilizing cell surface receptors.<sup>20</sup> Receptor mediated endocytosis is a distinct mechanism where internalization of receptor and its ligand is carried within clathrin-coated or uncoated vesicles.<sup>21,22</sup> Endocytosis of various membrane receptors may also occur via lipid rafts<sup>23</sup> which enable the internalization of receptors, adaptors, regulators, and other downstream proteins as a signaling complex. Moreover, sometimes it may be accompanied by caveolae-mediated entry. Caveolae are involved in plasma membrane invaginations 50- to 80-nm in size including cholesterol and sphingolipids, receptors and caveolins.<sup>23, 24</sup> On the other hand, clathrin-coated pits of 100–200 nm have been shown to be associated with the key protein clathrin and other scaffold proteins such as AP-2 and eps15.<sup>25</sup> Pinocytosis can take place through two different pathways, namely micropinocytosis and macropinocytosis. The micropinocytosis variety involves the uptake of particles no larger than 0.1  $\mu\text{m}$  in diameter whereas macropinocytosis is carried out with relatively large vesicles (0.2–5  $\mu\text{m}$  in diameter). It is the result of cell surface membrane ruffles folding back on the plasma membrane. Macropinosomes are not coated with clathrin or caveolin but encircled by actin in its early stages. Macropinocytosis provides an efficient process for non-selective uptake of nutrients and solute macromolecules.<sup>26</sup>

Several mechanisms have been proposed and studied for SWCNT internalization into cells. It has been shown that protein- or DNA-coated SWCNTs can pierce cells *via* energy-dependent endocytosis<sup>27,28,29-30</sup> and also via an energy-independent non-endocytotic pathway,<sup>31,32</sup> involving the insertion and diffusion of SWCNTs through the lipid bilayer of the cell membranes. Moreover, there are reports that SWCNTs can enter cells such as macrophages.<sup>33,34</sup> An active endocytotic pathway was hypothesized and

further investigated using a single-particle fluorescence tracking method<sup>29</sup> to explore rates of endo- and exocytosis. Another study hypothesizes a clathrin-dependent endocytosis mechanism for the uptake of 15-base randomer DNA-SWCNTs.<sup>28</sup> SWCNTs have also been reported to directly enter living cells through spearing of the cell membrane.<sup>35</sup> Single stranded DNA-SWCNT hybrid cellular uptake experiments have shown SWCNT accumulation in perinuclear endosomes of murine myoblast stem cells,<sup>36</sup> but these hybrids did not enter the nuclear envelope. Possibly, the diversity of proposed mechanisms is due to different surface modifications of SWCNTs as well as the differences in experimental cell types. Much remains to be understood in SWCNT uptake and its relationship with known endocytic pathways.

In this study, we have systematically explored several modes of proposed DNA-coated SWCNT cellular uptake in the human umbilical vein endothelial cell line (HUVEC), a primary normal cell extensively used for exploring endothelial cell functions. Cellular entry of DNA-SWCNT hybrids is confirmed by transmission electron microscopy. We have thoroughly explored the possibility of SWCNT internalization by clathrin, caveolae, macropinocytosis and microtubules associated pathways with the aid of five known classical pharmacological inhibitors. The effects of these inhibitors on the DNA-SWCNT uptake have been monitored quantitatively by laser scanning confocal fluorescence microscopy and near infra-red spectroscopy. Actin polymerizations emerge as the key mechanism for this DNA-SWCNT hybrid endocytosis in endothelial cells. The gene *Rac1* plays an important role in actin polymerization near the plasma membrane, regulating macropinocytosis. We use a dominant negative *Rac1* (*Rac1-T17DN*) to down regulate DNA-SWCNT uptake, confirming the uptake mechanism.

These findings provide information on the specific endocytic pathway that DNA-coated SWCNT employ to enter endothelial cells. Given the importance of endothelial cells in the transfer of agents between blood and tissue, this understanding can serve to improve the efficacy of SWCNT associated sensors and drug delivery vectors for the diagnosis and treatment of cancer.

## 6.2 Experimental Methods\*

### 6.2.1 SWCNT preparation

Raw (6,5)-rich (>80%) *CoMoCAT* carbon nanotubes, obtained from *South West NanoTechnologies (SWeNT)*, and oligo-DNA sequence (TAT)<sub>4</sub> (selected for its ability to recognize the (6,5)-SWCNT),<sup>49</sup> obtained from *Integrated DNA Technologies (IDT)*, were used throughout the study. They were sonicated in a 1 mg: 1 mg weight ratio using a *Branson* probe ultrasonicator for 90 minutes at 8 W output power in 4 mL of 1xPBS buffer. For fluorescence studies, DNA was modified with a 5'-FAM fluorescent tag. All chemicals other than SWCNTs and DNA were purchased from *Sigma-Aldrich*. The resultant dispersion was centrifuged (*Eppendorf* micro-centrifuge) for 90 minutes at 16000g to precipitate any undispersed SWCNTs and heavy-metal catalyst particles. Concentrations of (6,5) SWCNTs in solution were found by optical absorbance (*Varian Cary 50* Spectrophotometer) at the E<sub>11</sub> transition, A<sub>990</sub> nm, using the ratio of 13 µg/mL SWCNT for 1.0 absorbance at 990 nm.<sup>50</sup> The resulting dispersion contained SWCNT with diameters in the range 0.7 – 0.9 nm and lengths in the range 100-500 nm.

---

\* All of the cell culture, TEM, and fluorescence microscopy work was performed at the Mayo Clinic in Rochester, Minnesota by Santanu Bhattacharya, Xun Gong, and Debabrata Mukhopadhyay

### **6.2.2 Cell culture**

Human Umbilical Vein Endothelial Cells (HUVEC) were used throughout the study. HUVECs were cultured in a similar method to which Dr. Mukhopadhyay had devised previously.<sup>47</sup> Briefly, HUVECs were grown on 30 µg/ml collagen-coated dishes in EGM-MV bullet kit (5% fetal bovine serum in EBM with 12 µg/ml bovine brain extract, 1 µg/ml hydrocortisone, and 1 µg/ml GA-1000) purchased from Cambrex Bio Science Walkersville, Inc, MD, USA, in a humidified atmosphere with 5% CO<sub>2</sub> at 37°C. HUVECs (passage 4) that were ~80% confluent, were used for most experiments.

### **6.2.3 Transmission electron microscopy study**

Transmission Electron Microscopy (TEM) was used to examine SWCNTs inside the cell. On 60 mm collagen coated dishes,  $1.7 \times 10^5$  cells were plated and allowed to grow overnight in the incubator. Cells were then collected after treatment with 2 µg-SWCNT/mL SWCNTs for 6 hours and being resuspended in Trump's fixative solution, composed of 4 vol% formaldehyde and 1 vol% glutaraldehyde in 0.1 M phosphate buffer at pH 7.2. Then the cells were subjected to several washes with 0.1 M phosphate buffer, 1% osmium tetroxide in 0.1 M phosphate buffer, distilled water, 2 vol% uranyl acetate, distilled water, ethanol and absolute acetone in sequence. Finally cells were put into resin and a resin block was prepared. The resin block was sliced to prepare the TEM grid, which was examined using a *Philips Technai T12*.

#### **6.2.4 Following uptake by confocal fluorescence microscopy and NIR optical spectroscopy**

Four common endocytotic pathways were investigated using pharmacological inhibitors. The associated mechanism and treatment conditions for these inhibitors are described in Table 6.1. HUVEC cells were pre-treated with these inhibitors for a specified duration. Then, the inhibitors were removed and the cells were exposed to DNA-SWCNT suspension. Cells were plated in 60 mm collagen coated dish for absorption measurement and were separately cultured under otherwise identical conditions on collagen coated cover glass slides for study by confocal microscopy. Uptake was quantified by NIR spectroscopy, for which HUVEC cells were incubated with (TAT)<sub>4</sub>-conjugated SWCNT hybrids. Approximately  $1.7 \times 10^5$  cells were plated and allowed to grow overnight in the incubator. It was assumed that for a given number of cells, an approximate cellular volume could be established. This, however, will introduce great uncertainty in determining the intracellular concentrations via NIR absorbance since cellular volumes are known to fluctuate. We acknowledge this fact and ask the reader to keep this in mind when viewing data in Figures 6.4 and 6.6.

A concentration of 2  $\mu\text{g/mL}$  of SWCNTs was used for various periods of time in the range, 0-6 hour. After incubation, the cells were lysed with RIPA buffer mixed with PIC and HALT (*Boston BioProducts*). Cellular lysates from the longer incubation times appear to have pellets of aggregate SWCNTs. In order to re-disperse the SWCNTs individually, 1 mL of a 0.2 wt% surfactant solution, sodium dodecylbenzene sulfonate (SDBS), was added to each sample, which was sonicated for 10 minutes using the same apparatus as before. The resultant lysates were again scanned using the

spectrophotometer to measure absorbance at 990 nm, and accounting for dilutions, concentrations were obtained. For the confocal microscopy study, 5'-FAM was fused to (TAT)<sub>4</sub> to visualize its location inside the cells. After 6 hours of exposure of 5'-FAM-(TAT)<sub>4</sub>-SWCNT, cells were processed for confocal study. Briefly, HUVEC cells were thoroughly washed with 1xPBS to exclude any presence of SWCNTs outside the cells as well as from the culture plates. They were then fixed with paraformaldehyde followed by three 1xPBS washes. The cells were then mounted with mounting medium containing DAPI (a blue dye used to stain the nuclei) on a glass slides and examined with a Zeiss LSM 780 microscope using 100X lens.

<b>Table 6.1.</b> Pharmacological Inhibitors and Methods				
Cellular Component/Mechanism	Inhibitor	Inhibition Mechanism	Dosage	Incubation Time
Clathrin	Chlorpromazine	Inhibits pit formation by clathrin relocation at the endosomes	20 $\mu$ M	30 min.
Caveolae	Nystatin	Inhibits caveolin pit formation; sequesters cholesterol	54 $\mu$ M	30 min.
Macropinocytosis	Amiloride	Inhibits Na/H -ATPase exchangers, prevents membrane extension	100 $\mu$ M	15 min.
	Cystochalasin D	Inhibits actin polymerization for membrane extension	10 $\mu$ M	60 min.
Microtubules	Nocodazole	Inhibits tubulin subunit polymerization; inhibits endosome trafficking	10 $\mu$ M	60 min.

### 6.3 Cytotoxicity of DNA-SWCNT on HUVEC Cells

The potential cytotoxicity of functionalized SWCNTs is one concern that has prevented the wide acceptance in practical applications such as cancer therapy and

drug/gene/vaccine delivery. Properties such as solubility, size, the amount of impurity, and functional groups available on the surface of SWCNTs all play a role in determining cellular viability. Synthesis of SWCNTs commonly involves precursors containing carbonaceous impurities and transition-metal catalysts which in general present high toxicity to living cells. The well-controlled DNA-SWCNT production method used in this study, involving centrifugation and size-exclusion chromatography, is able to remove most impurities.

For viability studies, DNA-SWCNT dispersions were produced as described in the methods section. In addition, following the centrifugation, the extracted supernatant was fed through size exclusion columns (2000 Å, 1000 Å and 300 Å pore size, *Sepax Technologies*) via HPLC (*AKTA UPC-10 GE*) and fractionated to further remove excess DNA and to sort SWCNTs according to length. The length of SWCNTs used for the experiments was verified by atomic force microscopy (AFM) imaging (*Veeco Nanoscope*) of DNA-SWCNT hybrids deposited on hydrophobic silane coated silicon wafers (*SPI*).

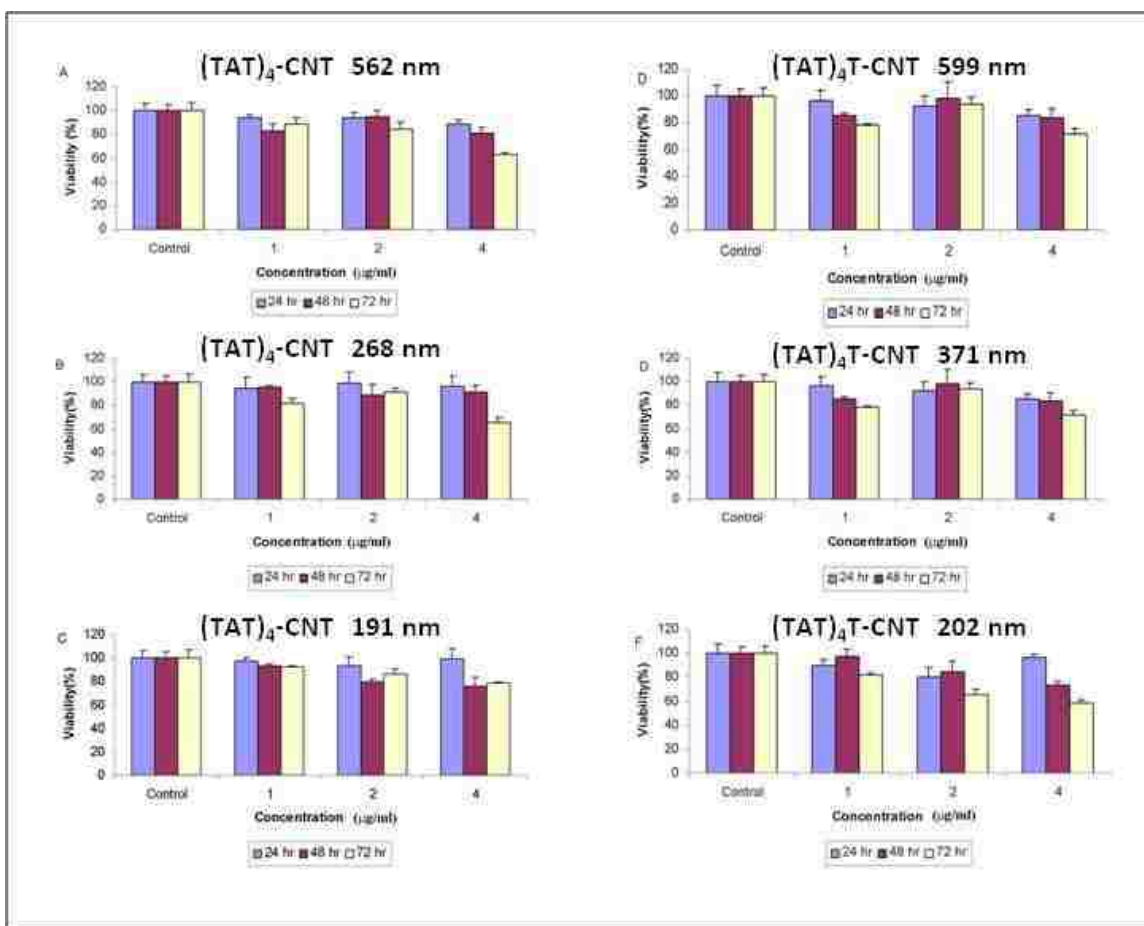
Cells were cultured onto collagen coated 96 well plates in EBM complete medium. Viability was studied using MTT assay (CellTiter 96 Aqueous non-radioactive cell proliferation assay from *Promega*). This assay was composed of solutions of a novel tetrazolium compound [3-(4,5-dimethylthiazol-2-yl)-5-(3-carboxymethoxyphenyl)-2-(4-sulfophenyl)-2H-tetrazolium, inner salt; MTS] and an electron coupling reagent (phenazine methosulfate; PMS). Dehydrogenase enzymes found in metabolically active cells convert MTS into aqueous, soluble formazan. Using a 550nm filter, the absorbance of the formazan was collected at 550nm ( $A_{550}$ ) which is directly proportional to the



number of living cells in culture. For each experiment, 2500 cells were plated in 96 well and incubated for 12 hours in a humidified atmosphere with 5% CO<sub>2</sub> at 37°C. The HUVEC cells were then incubated in DNA-SWCNT dispersions with sequences (TAT)<sub>4</sub> and (TAT)<sub>4</sub>T for various durations, e.g., 24h , 48h, 72h. Following the termination of each treatment, cells were washed and promptly assayed for viability using the MTT assay kit. Results were expressed as percent viability = [(A<sub>550</sub> treated cells)-background]/[(A<sub>550</sub> untreated cells)-background] x 100. By appropriate choice of the type of SWCNT used, the type of DNA used to disperse it, and by processing the dispersions using size exclusion chromatography (SEC), we were able to control several parameters. For example, by choosing CoMoCAT SWCNTs, we obtained a dispersion rich in (6,5) SWCNTs. We have previously shown that a sequence with just one more Thymine base, (TAT)<sub>4</sub>T, binds ~20 times weaker than (TAT)<sub>4</sub>. The choice of these two sequences allowed us to study the effect of strength of binding using very similar molecules. Further, by using SEC to control SWCNT length, we investigated the effect of SWCNT length on toxicity in a systematic manner.

To test cellular viability, HUVEC were incubated with DNA-SWCNTs of various length, concentration, time, and DNA sequence. Three different concentrations, 1, 2, and 4 µg-SWCNT/mL, were used for the treatment. Additionally, (TAT)<sub>4</sub>-conjugated SWCNTs of length 562 ± 108 nm, 258 ± 45 nm, and 191 ± 62 nm (Figure S1a-c), and (TAT)<sub>4</sub>T-conjugated SWCNTs of length 599 ± 198 nm, 371 ± 90 nm, and 202 ± 68 nm (Figure S1d-f) were used for incubation. The time of incubation varied from 24 – 72 hours.

General trends observed included the decrease in viability as a function of incubation time as well as DNA-SWCNT concentration. At the concentration used throughout the fluorescence study, (2  $\mu\text{g-SWCNT/mL}$ ), viability was greater than 80% in all samples up to and including 72 hours of incubation. Hybrids of (TAT)<sub>4</sub>T with short SWCNTs (~202 nm), on a *per mass* basis, gave the highest levels of toxicity (less than 60% viable cells after 72 hours of incubation). Subsequent incubation studies have been performed at this particular concentration.

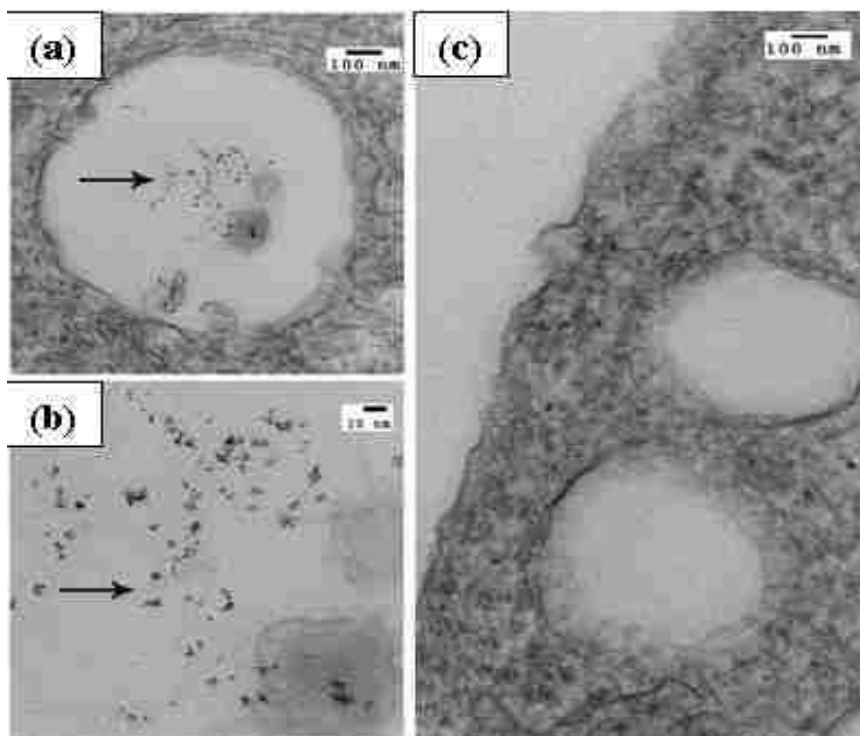


**Figure 6.1.** MTT assay for cytotoxicity of purified, length-sorted DNA-SWCNT hybrids. HUVEC cells were incubated with (TAT)<sub>4</sub>-SWCNT hybrids under three different lengths  $562 \pm 108$  nm,  $258 \pm 45$  nm, and  $191 \pm 62$  nm (a-c) for 24, 48, and 72 hours. Viability results for the treatment with (TAT)<sub>4</sub>T of SWCNT length  $599 \pm 198$  nm,  $371 \pm 90$  nm, and  $202 \pm 68$  nm were reported in a similar fashion (d-f).

## 6.4 Cellular Internalization Confirmed by Electron Microscopy

To visually confirm the uptake of DNA-SWCNT, cells were first examined by transmission electron microscopy (TEM). Figure 6.2 demonstrates that SWCNTs are indeed taken up by the cells after 6 hours of incubation. In cellular vacuoles, clear accumulations of SWCNTs are found (localized black regions), which are absent in the control sample (Figure 6.2). The aggregation of SWCNTs suggests that they have been stripped of their amphiphilic DNA coating. Once stripped, SWCNTs tend to clump together due to hydrophobic attraction and their high aspect ratios.<sup>37-38</sup>

In light of recent concerns over the validity of this presented image, we would like to note that the black regions in the TEM micrographs have not been confirmed as SWCNTs. The sample thickness is known to be on the order of 100 nm. It is thought that longer SWCNTs should have been observed in the TEM images. The short objects actually observed in the images suggest that the SWCNTs were cut in some way. To create the cross-sectional TEM image of the cell, samples are cut with a diamond knife which we assume can also cut the SWCNTs. We therefore make the hypothesis that what is seen in the TEM images are the cross-sections of many SWCNTs in bundled form. For future studies, additional methods such as X-Ray TEM may be used to identify the SWCNTs in the cells as such.



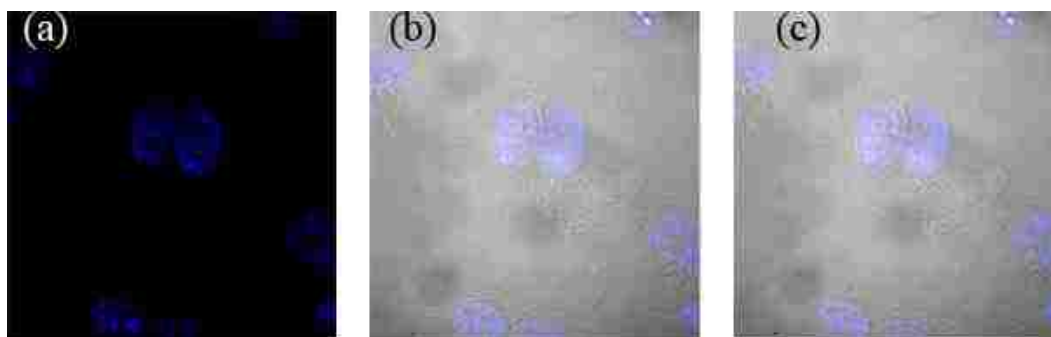
**Figure 6.2.** (a,b) Transmission electron microscopy (TEM) images of HUVEC cells incubated with DNA-SWCNTs. Intracellular congregation, particularly inside the vacuoles, is evident in SWCNT-incubated samples, not seen in the control sample (c).

## 6.5 Uptake Inhibition Studies

To identify the pathway for DNA-SWCNT uptake into the HUVEC cells, a pharmacological inhibition study is performed using different inhibitors which include chlorpromazine,<sup>39,40</sup> nystatin,<sup>39, 41</sup> amiloride,<sup>39,42</sup> cytochalasin D,<sup>39, 43</sup> and nocodazole.<sup>39,44</sup> Chlorpromazine is used to inhibit pit formation by clathrin relocation at the endosomes. Nystatin acts as inhibitor for caveolin pit formation. Amiloride and cytochalasin D are both used to inactivate macropinocytosis. Amiloride inhibits  $\text{Na}^+/\text{H}^+$  - ATPase exchangers whereas cytochalasin D helps in actin depolymerization for membrane extension. Nocodazole, on the other hand, is used to hinder tubulin subunit

polymerization and also to obstruct endosome trafficking. (See Table 6.1 in the methods section for more information).

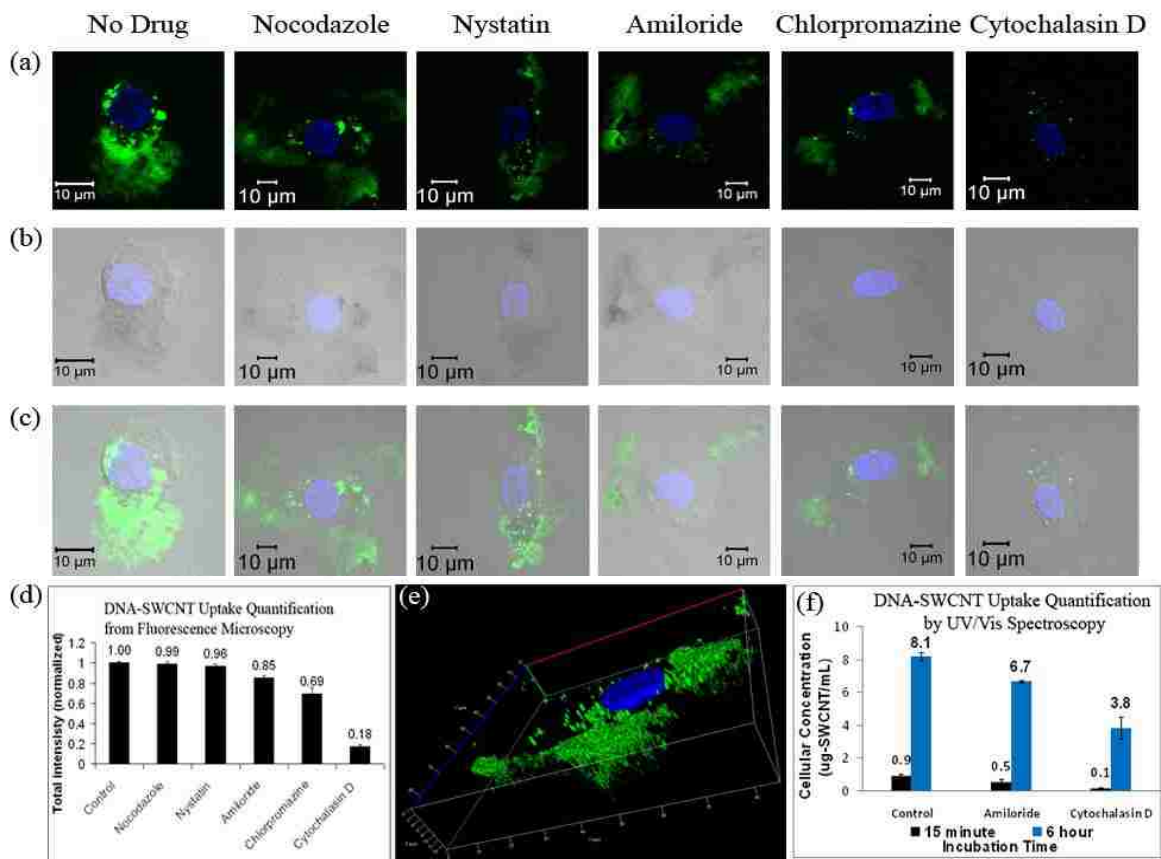
Uptake was monitored by laser scanning confocal microscopy using 5'-FAM-fluorophore labeled DNA to create its hybrid with SWCNT. To confirm that DNA alone is not able to be freely internalized into HUVEC cells, a control experiment was performed. Cells were incubated with fluorescently labeled 5'-FAM-DNA, at a concentration equal to that used for DNA-SWCNT incubation experiments (2  $\mu\text{g}/\text{mL}$ ), for 6 hours. From the resultant fluorescence micrographs, it was established that negligible green fluorescently labeled DNA entered the cells. This is important since we use fluorescence intensity as a proxy for SWCNT quantity inside the cell. Once the hybrid molecules were inside, it is not clear from our studies whether or not the DNA remained on the SWCNT. The fact that in cell lysates SWCNT are often clumped suggests that at least some of the DNA is stripped off the SWCNT. See Figure 6.3, below.



**Figure 6.3.** HUVEC cells are incubated with 5'-FAM dye conjugated to the DNA for 6hrs. DAPI (blue) is used for nucleus staining. . Panel (a) is for blue and green corresponding to DAPI and 5'-FAM, respectively, inside of the HUVEC cells. (b) Phase contrast image showing cell morphology along with stained nucleus. (c) Merged composition of (a) and (b). The green color from 5'-FAM-DNA is not observed inside the cells.

Note, however, that its spatial distribution is not necessarily indicative of where SWCNT reside inside the cell since the 5'-FAM-DNA might well be stripped off the SWCNT inside the cell. Figure 6.4 shows micrographs with the nucleus, stained in blue, and 5'-FAM-DNA-SWCNT, indicated by green, under the influence of different drugs corresponding to various endocytotic pathways for DNA-SWCNT uptake. A confocal z-stack image for HUVEC incubation with DNA-SWCNT in the absence of drug inhibitors is shown in Figure 6.4e. It is known that SWCNTs can adsorb onto the plasma membrane prior to internalization.<sup>29</sup> However, the quantity of cell-internalized SWCNTs is so much greater than what could be accommodated on the plasma membrane that fluorescence of the former overwhelms any signal from the latter. Comparing images from different drug treatment with the control, as shown in Figure 6.4a-c, and also from the mean fluorescence intensity variation of pixel data, Figure 6.4d, we note that nocodazole and nystatin do not influence the DNA-SWCNT uptake significantly, whereas amiloride and chlorpromazine have a comparable effect (85% and 69% of the control, respectively). Moreover, cytochalasin D treatment significantly inhibits DNA-SWCNT cellular uptake (18% of the control, Figure 6.4d). In an independent experiment, intracellular SWCNT concentrations were monitored by NIR absorbance spectroscopy of cell lysate (Figure 6.4f). These confirm a distinct difference (albeit smaller in magnitude) between amiloride, cytochalasin D, and control samples (Figure 6.4f). There is some uncertainty about the relationship between fluorescence intensity and SWCNT concentration. The former depends on the extent to which 5'-FAM-DNA remains conjugated to SWCNT, for separation of the fluorophore from the SWCNT vicinity will presumably increase its yield. However, if one assumes that DNA removal from

SWCNT is about the same under all conditions (recall that the drugs are removed prior to exposure of cells to DNA-SWCNT), we expect relative fluorescence intensity to approximately represent relative amounts of SWCNT internalized. Furthermore, agreement of trends with the independent NIR absorbance measurements gives additional confidence that the relative ranking is correct. Interestingly, intracellular concentrations, measured by absorbance intensities, exceed that of the incubation media, demonstrating that an active process of SWNCT accumulation is operative.

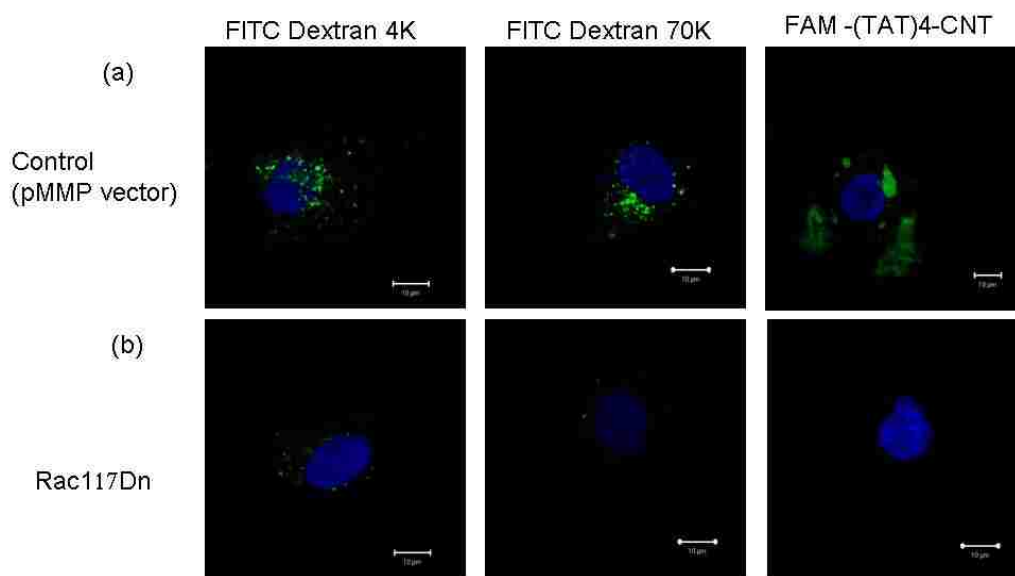


**Figure 6.4.** Phase contrast confocal imaging after application of different pharmacological inhibitors. DAPI (blue) is used for nucleus staining. The green color represents 5'-FAM dye conjugated to the DNA used in DNA-SWCNT hybrid production. (a) Images illustrating the presence of 5'-FAM-DNA-SWCNT inside the HUVEC cells. (b) Phase contrast image showing cell morphology in each case along with stained nucleus. (c) Merged composition of (a) and (b). (d) Quantitative estimation from different drug treatments using the mean fluorescence intensity variation of pixel data. (e) Typical z-stack image that is used for quantitative analysis. (f) Intracellular SWCNT concentrations from cell lysates obtained after various drug treatments. In agreement with fluorescence data, cytochalasin D induces the highest level of SWCNT uptake inhibition.

To interrogate independently whether DNA-SWCNT internalization operates by an actin polymerization-mediated pathway, a gene-knockout technique was employed. Macropinocytosis is known to be associated with the activation of Rho GTPases, such as Rac1 and Cdc42, which are responsible for triggering membrane ruffles by actin polymerization.<sup>45</sup> Therefore we have tested the role of Rac1 by use of a dominant



negative Rac1 (Rac1-T17DN)<sup>46</sup> retrovirus. Retrovirus preparation and HUVEC infection with retrovirus are carried out as described previously.<sup>47,48</sup> The fragments encoding the genes are subcloned to a retroviral vector pMMP.<sup>47</sup> Upon infection, it turns off the actin mediated endocytotic mechanism. Rac1-T17DN expression is confirmed with the uptake of FITC conjugated dextran, MW 4,000 (Dex 4k), and dextran, MW 70,000 (Dex-70k), indicating that the expression of Rac1-T17DN inhibited macropinocytosis. In Figure 6.5, we show that this method inhibited the internalization of DNA-SWCNT into cells by 90% compared with that of pMMP control vector.



**Figure 6.5.** (a) Fluorescence micrographs illustrating the uptake of dex 4k, dex 70k and DNA-SWCNT (from left to right) in HUVEC cells which are treated with retrovirus containing pMMP control vector. (b) After treatment with Rac1-T17DN, uptake of the same respective molecules is inhibited.

## 6.6 Conclusions

Hence, using well-controlled DNA-SWCNT hybrids and by studying the effect of a number of mechanism-specific inhibitors, we demonstrated clearly that internalization

of these hybrids into HUVEC cells is by macropinocytosis-mediated endocytosis, more specifically by actin polymerization based endocytosis. This observation is confirmed by retrovirus infection that independently blocks the same mechanism. Understanding the mechanism of SWCNT uptake in this manner is of importance both for the development of SWCNT-based biomedical technologies such as imaging, sensors, and drug delivery. Finally, this evidence serves to address fundamental issues related to their toxicity.

## **6.7 Acknowledgements**

This work was performed in direct collaboration with Santanu Bhattacharya, Xun Gong, and Debabrata Mukhopadhyay of the Mayo Clinic in Rochester, MN. There, they performed the cell cultures, TEM imaging, and confocal fluorescence microscopy. I would like to thank Anand Jagota and Debabrata Mukhopadhyay who have mentored me during this work. Additionally, this work was supported by National Institutes of Health (NIH) grant HL70567 and CA150190, National Science Foundation (NSF) grant CMMI-1014960, a Faculty Innovation Grant (FIG) to Anand Jagota from Lehigh University, and a generous gift from Bruce and Martha Atwater to Debabrata Mukopadhyay.

## 6.8 References

- (1) Prato, M.; Kostarelos, K.; Bianco, A., *Acc. Chem. Res.* **2008**, *41*, 60-68.
- (2) Liu, Z.; Tabakman, S. M.; Welsher, K.; Dai, H., *Nano Research* **2009**, *2*, 85-120.
- (3) Chen, Z.; Tabakman, S. M.; Goodwin, A. P.; Kattah, M. G.; Daranciang, D.; Wang, X.; Zhang, G.; Li, G.; Liu, Z.; Utz, P. J.; Jiang, K.; Fan, S.; Dai, H., *Nature Biotechnology* **2008**, *26* (11), 1285-1292.
- (4) Liu, Z.; Chen, K.; Davis, C.; Sherlock, S.; Cao, Q.; Chen, X.; Dai, H., *Cancer Res.* **2008**, *68* (16), 6652-6660.
- (5) Zheng, M.; Jagota, A.; Semke, E. D.; Diner, B. A.; Mclean, S. R. L.; Richardson, R. E.; Tassi, N. G., *Nature Materials* **2003**, *2*, 338-343.
- (6) Liu, Z.; Winters, M.; Holodniy, M.; Dai, H., *Angew. Chem.* **2007**, *119*, 2069-2073.
- (7) Kam, N. W. S.; Liu, Z.; Dai, H., *J. Am. Chem. Soc.* **2005**, *127*, 12492-12493.
- (8) Kam, N. W. S.; Liu, Z.; Dai, H., *J. Am. Chem. Soc.* **2004**, *126*, 6850-6851.
- (9) Welsher, K.; Liu, Z.; Daranciang, D.; Dai, H., *Nano Letters* **2008**, *8* (2), 586-590.
- (10) Heller, D. A.; Jin, H.; Martinez, B. M.; Patel, D.; Miller, B. M.; Yeung, T. K.; Jena, P. V.; Hobartner, C.; Ha, T.; Silverman, S. K.; Strano, M. S., *Nature Nanotechnology* **2008**, *4*, 114-120.
- (11) Strano, M. S.; Jin, H., *ACS Nano* **2008**, *2* (9), 1749-1752.
- (12) Liu, Z.; Li, X.; Tabakman, S. M.; Jiang, K.; Fan, S.; Dai, H., *J. Am. Chem. Soc.* **2008**, *130* (41), 13540-13541.
- (13) Zavaleta, C.; Zerda, A.; Keren, S.; Cheng, Z.; Schipper, M.; Chen, X.; Dai, H.; Gambhir, S. S., *Nano Letters* **2008**, *8* (9), 2800-2805.
- (14) Zerda, A.; Zavaleta, C.; Keren, S.; Vaithilingam, S.; Bodapati, S.; Liu, Z.; Levi, J.; Smith, B. R.; Ma, T. J.; Oralkan, O.; Cheng, Z.; Chen, X.; Dai, H.; Khuri-Yakub, B. T.; Gambhir, S. S., *Nature Nanotechnology* **2008**, *3*, 557-562.
- (15) Liu, Z.; Davis, C.; Cai, W.; He, L.; Chen, X.; Dai, H., *PNAS* **2008**, *105* (5), 1410-1415.
- (16) Liu, Z.; Cai, W.; He, L.; Nakayama, N.; Chem, K.; Sun, X.; Chen, X.; Dai, H., *Nature Nanotechnology* **2007**, *2*, 47-52.
- (17) Poland, C. A.; Duffin, R.; Kinloch, I.; Maynard, A.; Wallace, W. A. H.; Seaton, A.; Stone, V.; Brown, S.; MacNee, W.; Donaldson, K., *Nature Nanotechnology* **2008**, *3*, 423-428.
- (18) Kostarelos, K., *Nature Biotechnology* **2008**, *26*, 774-776.
- (19) Warheit, D. B.; Laurence, B. R.; Reed, K. L.; Roach, D. H.; Reynolds, G. A. M.; Webb, T. R., *Toxicology Sciences* **2003**, *77* (1), 117-125.
- (20) Stuart, L. M.; Ezekowitz, R. A., *Immunity* **2005**, *22* (5), 539-50.
- (21) Mellman, I., *Annu Rev Cell Dev Biol* **1996**, *12*, 575-625.
- (22) Conner, S. D.; Schmid, S. L., *Nature* **2003**, *422* (6927), 37-44.
- (23) Nichols, B., *J Cell Sci* **2003**, *116* (Pt 23), 4707-14.
- (24) Pelkmans, L.; Puntener, D.; Helenius, A., *Science* **2002**, *296* (5567), 535-9.
- (25) Ehrlich, M.; Boll, W.; Van Oijen, A.; Hariharan, R.; Chandran, K.; Nibert, M. L.; Kirchhausen, T., *Cell* **2004**, *118* (5), 591-605.
- (26) Swanson, J. A.; Watts, C., *Trends Cell Biol* **1995**, *5* (11), 424-8.

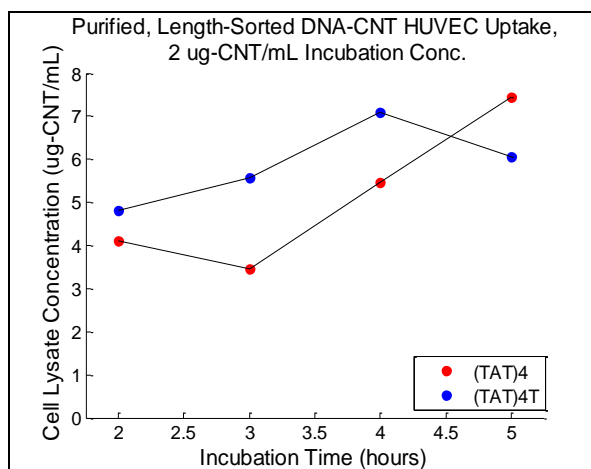
- (27) Shi, X.; von dem Bussche, A.; Hurt, R. H.; Kane, A. B.; Gao, H., *Nat Nano* **2011**, *advance online publication*.
- (28) Kam, N. W. S.; Liu, Z. A.; Dai, H. J., *Angewandte Chemie-International Edition* **2006**, *45* (4), 577-581.
- (29) Jin, H.; Heller, D. A.; Strano, M. S., *Nano Letters* **2008**, *8* (6), 1577-1585.
- (30) Jin, H.; Heller, D. A.; Sharma, R.; Strano, M. S., *ACS Nano* **2009**, *3* (1), 149-58.
- (31) Pantarotto, D.; Briand, J. P.; Prato, M.; Bianco, A., *Chem Commun (Camb)* **2004**, (1), 16-7.
- (32) Kostarelos, K.; Lacerda, L.; Pastorin, G.; Wu, W.; Wieckowski, S.; Luangsivilay, J.; Godefroy, S.; Pantarotto, D.; Briand, J. P.; Muller, S.; Prato, M.; Bianco, A., *Nat Nanotechnol* **2007**, *2* (2), 108-13.
- (33) Porter, A. E.; Gass, M.; Muller, K.; Skepper, J. N.; Midgley, P. A.; Welland, M., *Nat Nanotechnol* **2007**, *2* (11), 713-7.
- (34) Cherukuri, P.; Bachilo, S. M.; Litovsky, S. H.; Weisman, R. B., *J Am Chem Soc* **2004**, *126* (48), 15638-9.
- (35) Cai, D.; Mataraza, J. M.; Qin, Z. H.; Huang, Z.; Huang, J.; Chiles, T. C.; Carnahan, D.; Kempa, K.; Ren, Z., *Nature Methods* **2005**, *2*, 449-454.
- (36) Heller, D. A.; Baik, S.; Eurell, T. E.; Strano, M. S., *Advanced Materials* **2005**, *17* (23), 2793-2799.
- (37) Bahr, J. L.; Mikkelsen, E. T.; Bronikowski, M. J.; Smalley, R. E.; Tour, J. M., *Chem. Commun.* **2001**, 193-194.
- (38) Furtado, C. A.; Kim, U. J.; Gutierrez, H. R.; Pan, L.; Dickey, E. C.; Eklund, P. C., *J. Am. Chem. Soc.* **2004**, *126*, 6095-6105.
- (39) Boisvert, M.; Fernandes, S.; Tijssen, P., *J Virol* **2010**, *84* (15), 7782-92.
- (40) Hasebe, R.; Suzuki, T.; Makino, Y.; Igarashi, M.; Yamanouchi, S.; Maeda, A.; Horiuchi, M.; Sawa, H.; Kimura, T., *BMC Microbiol* **2010**, *10*, 165.
- (41) Chen, Y.; Wang, S.; Lu, X.; Zhang, H.; Fu, Y.; Luo, Y., *Blood* **2011**, *117* (23), 6392-403.
- (42) West, M. A.; Bretscher, M. S.; Watts, C., *J Cell Biol* **1989**, *109* (6 Pt 1), 2731-9.
- (43) Tremblay, P. L.; Auger, F. A.; Huot, J., *Oncogene* **2006**, *25* (50), 6563-73.
- (44) Sawyer, S. J.; Norvell, S. M.; Ponik, S. M.; Pavalko, F. M., *Am J Physiol Cell Physiol* **2001**, *281* (3), C1038-45.
- (45) Ridley, A. J.; Paterson, H. F.; Johnston, C. L.; Diekmann, D.; Hall, A., *Cell* **1992**, *70* (3), 401-10.
- (46) Zeng, H.; Zhao, D.; Mukhopadhyay, D., *J Biol Chem* **2002**, *277* (48), 46791-8.
- (47) Zeng, H.; Dvorak, H. F.; Mukhopadhyay, D., *J Biol Chem* **2001**, *276* (29), 26969-79.
- (48) Zeng, H.; Sanyal, S.; Mukhopadhyay, D., *J Biol Chem* **2001**, *276* (35), 32714-9.
- (49) Tu, X. M.; Manohar, S.; Jagota, A.; Zheng, M., *Nature* **2009**, *460* (7252), 250-253.
- (50) Zheng, M.; Diner, B. A., *J. Am. Chem. Soc.* **2004**, *126*, 15490-15494.

## 6.9 Appendix

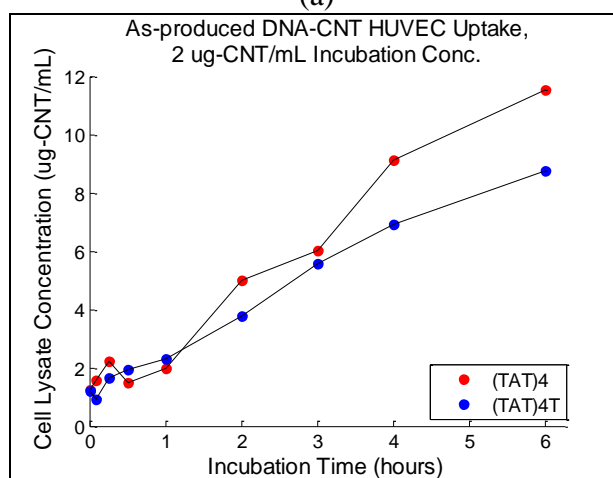
### 6.9.1 Kinetics of Length-Sorted SWCNT Cellular Uptake

Upon finding the relative levels of toxicity for purified, length-sorted DNA-SWCNTs, the kinetics of cellular uptake were examined. HUVEC cells were incubated with (TAT)<sub>4</sub> and (TAT)<sub>4</sub>T-conjugated SWCNTs for different durations up to five hours. The SWCNTs that were used for this experiment had an average length of ~300 nm at a concentration of 2 µg-SWCNT/mL. Figure 6.6a shows kinetics of uptake for the given incubation times. As a comparison, we have reported cellular uptake results for ‘as-produced’ (not size-sorted) DNA-SWCNTs, Figure 6.6b. Uptake was observed to increase linearly with time for both (TAT)<sub>4</sub> and (TAT)<sub>4</sub>T hybrids. In the length-sorted samples, there was little difference between the two sequences. However, in the as-produced sample, (TAT)<sub>4</sub> cellular lysate concentrations clearly remain higher than (TAT)<sub>4</sub>T.

Interestingly, by one hour of incubation time, intracellular SWCNT concentration matches that of the surrounding medium, which can be thought of as an infinite source (at fixed concentration). After this time, intracellular concentrations exceed that of their surroundings, thus proving the existence of an active process of DNA-SWCNT uptake. After 5 hours of incubation with purified, length-sorted DNA-SWCNT hybrids, intracellular concentrations were three to four times as much as the incubation medium, and there was no indication that concentrations have saturated.



(a)

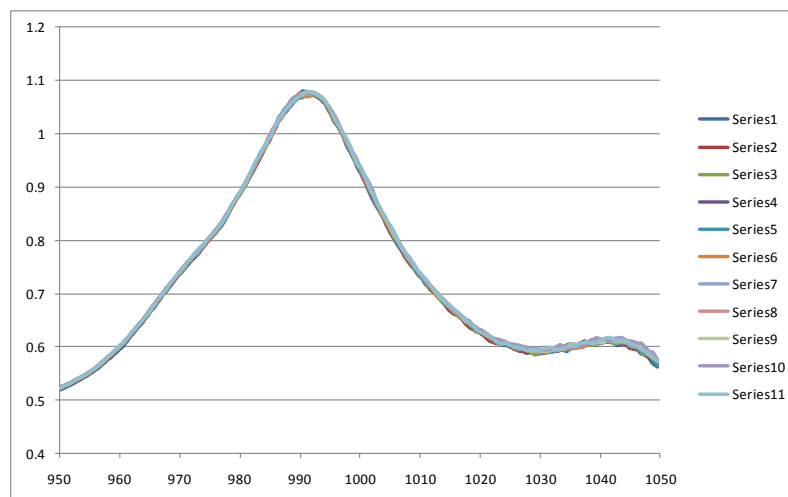


(b)

**Figure 6.6.** Monitoring the amount of DNA-SWCNT internalized by HUVEC cells as a function of incubation time. DNA-conjugated SWCNT hybrids were made from (TAT)<sub>4</sub> or (TAT)<sub>4</sub>T in a purified, length-sorted (a) or as-produced (b) fashion. The incubation concentration, 2  $\mu\text{g-SWCNT/mL}$ , was exceeded in both cases and reached levels 3-4 times for length-sorted and 4-6 times as high for as-produced DNA-SWCNTs.

### 6.9.2 Cell Culture Media Effect on DNA-SWCNT Hybrids

Since cell culture media generally contains numerous salts, amino acids, and other macromolecules, it is beneficial to check any possible interactions between it and DNA-SWCNTs hybrids. Figure 6.7 shows time-dependent NIR absorbance scans. Each scan represents one hour that the mixture stands at 37°C. It was seen that over the course of 10 hours, there was no interaction evident in the NIR signature of the SWCNT.



**Figure 6.7.** Time-dependent NIR absorbance scans of DNA-SWCNT hybrids are overlaid in the wavelength range of 950-1050 nm. The dominant (6,5)-SWCNT peak was seen at 990 nm, and did not change over the course of 10 hours at elevated temperature with cell culture media.

## **Chapter 7**

### **Conclusions**

*The research presented in this thesis features a multi-faceted approach to investigating the sequence dependent nature of DNA-SWCNT interactions. In Chapter 2, experimental methods were put forth to extract quantitative information about the strengths of DNA-SWCNT binding. Chapters 3, 4, and 5 feature several computational simulation techniques to probe the DNA-SWCNT hybrid structure at the molecular level. Finally, in Chapter 6 the DNA-SWCNT hybrids and a well-studied human cell-line were incubated to investigate methods of internalization for future biomedical work in drug delivery and gene therapy. It is through both theoretical and experimental studies that novel nanomaterials, such as DNA-SWCNTs, can be utilized to their full therapeutic potential.*



## 7.1 Experimental Determination of DNA-SWCNT Binding Strengths

Hybrids of DNA and SWCNTs are known for their relative stability in a singly-dispersed aqueous manner. In order to spectroscopically measure the DNA-SWCNT binding strengths, a surfactant was used to competitively adsorb to the surface of the SWCNT, effectively displacing the DNA. In Chapter 2, the rates of this process were extracted over a range of temperatures for hybrids of different DNA composition. Analyzing the extracted data, using Eyring kinetics, free energies of activation could be compared against one another.

From the experimental data, the (6,5)-SWCNT recognition sequence, (TAT)<sub>4</sub>, was found to have a binding strength ~20 times larger than any of its compositional family, e.g. (TAT)<sub>4</sub>T. It is striking that one small change in DNA sequence can have such a dramatic effect on the macroscopically observable rate of displacement. We hypothesize that minute differences at the molecular level, due in part to hydrogen bonding, explain this discrepancy.

## 7.2 Molecular Simulation of Various DNA-SWCNT Structures

For many decades, scientists have utilized the tool of computational simulation on ever more impressive supercomputers to probe what they are experiencing on their laboratory bench tops. As such, DNA-SWCNT hybrids are an ideal system to molecularly model due to their relatively small size and basic intra-molecular interactions. Chapters 3, 4, and 5 all pertain to the molecular simulation of DNA-SWCNT hybrids using deterministic molecular dynamics methods. In Chapter 3, idealized novel DNA structures, termed  $\beta$ -barrels, were proposed to explain the stabilized wrapped structure found in hybrids of SWCNTs and (GT)-rich DNA sequences. In Chapter 4, simulations were run for 50 times longer than previous studies. Additionally, the simulations had access to artificially high temperatures, those which are needed to cross high barriers of activation in order to find wells in the free energy landscape. Chapter 5 extended upon this study by placing multiple strands of DNA on a single SWCNT. In experimental conditions

there may be several hundred strands of DNA on one SWCNT. The interactions between the adsorbed DNA strands are then crucial to understanding the stability and function of such hybrids.

The main conclusion from the molecular simulation studies is that the DNA-SWCNT hybrid structures depend on *both* the sequence of DNA as well as the chirality of SWCNT. This is most apparent by the fact that (TAT)<sub>4</sub> simulated on a (6,5)-SWCNT possessed a single right-handed helical conformation. If the sequence was switched to (T)<sub>12</sub>, the overall DNA structure was then a  $\beta$ -barrel left-handed helix. Furthermore, switching chiralities from (6,5) to (8,7) disrupted the initially observed ordered structure that (TAT)<sub>4</sub> prefers.

### **7.3 Cellular Interactions with DNA-SWCNT Hybrids**

Important for their adoption into clinical biomedical applications, the mode of functionalized SWCNT internalization into human endothelial cells is one that needs a clear irrefutable answer. Unfortunately, there have been numerous proposed methods of cellular entry in the literature. In Chapter 6, the objective was to instill a level of confidence in the scientific community by showing that certain proposed methods of uptake could indeed be ruled out. By a pharmacological induced knockout study, the energy-intensive pathway of Rac1-macropinocytosis was identified as the means for internalization of DNA-SWCNT hybrids into healthy human endothelial cells.

### **7.4 Future Work**

In Chapter 2, a novel method was introduced where a surfactant-induced displacement reaction was able to find the binding strengths of DNA on SWCNTs. Because of the simplenature of the experiment, this method of surface displacement can be used to find the relative binding strengths of many other organic and inorganic molecules adsorbed onto

SWCNTs. Initial studies at the end of Chapter 2 have shown that certain peptide sequences, such as HexCoil-Ala, form strongly bound complexes with SWCNTs of specific chirality. In this case, the surfactant SDBS was not able to displace the peptide under the normal conditions used for DNA displacement. In future work, a different surfactant with a higher binding affinity for the SWCNT (e.g. sodium cholate or Triton-X-100) can be used in an attempt to displace the peptide.

For biomedical applications, understanding the interactions between SWCNTs and other classes of biological polymers (e.g. lipids of varying structure and composition) will be of much use in cellular targeting purposes and govern the controlled release of cargo. Outside of SWCNTs, this surfactant-displacement method can be applied to any material which exhibits a modulating absorbance, fluorescence, or Raman peaks as its surface is modified.

To continue the computational work, additional nanomaterial hybrids (e.g. lipid-SWCNT) can be simulated until equilibrium is reached in order to explore the innate intricacies at the molecular level. As the available computing power increases, larger simulations can be run in shorter periods of time. It will be of great interest to simulate an excess of DNA in solution around a SWCNT. In this way, free energies of interaction can be extracted from  $\mu$ VT simulation (constant chemical potential, volume, and temperature) since DNA will freely adsorb and desorb from the surface to reach an equilibrium. In addition, simulating interactions between the DNA-SWCNT hybrids and other molecules, such as surfactant, lipids, and/or peptides, will provide an abundance of information to their stability and reactivity. Attempting to model hybrids in physiological media conditions will be of great use biomedically as the prospect of SWCNT-based nanomedicines eventually come to fruition.

The biomedical collaboration with the Mayo Clinic should eventually focus on the controlled delivery of drugs, peptides, and nucleic acids to specific sites in living cells as well as organisms. As a proof of the principle experiment, DNA should be replaced with micro RNA (miRNA) which is known to silence target genes in an organism. The delivering efficacy of miRNA in relation to the miRNA-SWCNT hybrids should be examined in control cells

susceptible to gene silencing. As another very useful experiment, SWCNTs should be bi-functionalized with targeting ligands (i.e. short peptides that direct substances into specific cells) as well as miRNA. In this way, bi-functionalized hybrids can be intravenously injected with expectations that miRNA be delivered only to specific cells in the organism.

## DANIEL E. ROXBURY

54 West Ettwein Street

Bethlehem, PA 18018

908-295-9279

daniel.roxbury@gmail.com

**SUMMARY:** Chemical engineering PhD candidate seeking a research-oriented postdoctoral position. Possesses strong leadership skills and research experience investigating DNA-carbon nanotube interactions for use in electronic devices as well as targeted cellular delivery for therapy applications.

### TECHNICAL SKILLS:

#### Experimental

- HPLC (Size-exclusion & Ion-exchange), UV/Vis & Fluorescence Spectroscopy
- Protein Synthesis & Mass Spectrometry
- Biofermentation Process Control & Cell Culturing Techniques
- Electrophoresis (Iso-electric focusing gel & Capillary)
- Atomic Force Microscopy, Dynamic Light Scattering

#### Computational

- Molecular Dynamics simulation packages (*CHarMM*, *NAMD*, & *Gromacs*), Visualization software (*VMD*, *Materials Studio*)
- MATLAB, Mathematica, Maple, Aspen, Excel, Powerpoint, Word

### EDUCATION:

#### Lehigh University

Bethlehem, PA

*Ph.D. Chemical Engineering, GPA: 3.6/4.0*

Aug 2007 – May 2012

Thesis Project: *Sequence Specific DNA-Carbon Nanotube Interactions*

Advisor: Professor Anand Jagota

#### Lehigh University

Bethlehem, PA

*B.S Chemical Engineering, GPA: 3.2/4.0*

Aug 2003 – May 2007

Deans List: 2003-2005

### RESEARCH EXPERIENCE:

#### DNA-Carbon Nanotube Chirality-Dependent Recognition Bethlehem, PA

*Thesis Project, Department of Chemical Engineering* Jan 2008 – May 2012

- Probing the recognition ability of certain oligo-DNA sequences for specific chirality carbon nanotubes
- Cell culture studies investigating DNA-carbon nanotube biocompatibility
- Modeling of DNA-carbon nanotube hybrid structures with molecular dynamics (MD) simulation

#### Capillary Electrophoresis at NIST National Laboratory Gaithersburg, MD

Supervisor: Dr. Ming Zheng

Sept 2010

Use of CE to measure charge densities of DNA-CNT hybrids to compare differing DNA sequences for future electronic applications

**Two-Phase Convective Heat-Transfer Enhancement  
Opportunity for Student Innovation (OSI)**

**Bethlehem, PA**  
Aug 2006 – May 2007

Advisor: Professor Kemal Tuzla

- Investigated methods to enhance convective heat transfer by increasing turbulence in a narrow pipe
- Top 10% of senior class selected to participate in research project

**PUBLICATIONS:**

**Roxbury, D.;** Manohar, S.; Jagota, A. “Molecular Simulation of DNA  $\beta$ -Sheet and  $\beta$ -Barrel Structures on Graphite and Carbon Nanotubes” *J. Phys. Chem. C* **2010**, *114*, 31, 13267.

**Roxbury, D.;** Tu, X.; Zheng, M.; Jagota, A. “DNA-Carbon Nanotube Recognition Ability Directly Relates to its Binding Strength” *Langmuir* **2011**, *27*, 13, 8282.

**Roxbury, D.;** Jagota, A.; Mittal, J. “Sequence Specific Self-Stitching Motif of Short Single-Stranded DNA on a Single-Walled Carbon Nanotube” *J. Am. Chem. Soc.* **2011**, *133*, 13545.

**Roxbury, D. ;** Mittal, J.; Jagota, A. “Molecular-Basis of Single-Walled Carbon Nanotube Recognition by Single-Stranded DNA” *Nano Lett.* **2012**, *12*, 3, 1464.

Bhattacharya, S.; **Roxbury, D.;** Gong, X.; Mukhopadhyay, D.; Jagota, A. “DNA Conjugated SWCNTs Enter Cells via Rac1 Mediated Macropinocytosis” *Nano Lett.* **2012**, *12*, 4, 1826.

**SELECTED WORKSHOPS & POSTER SESSIONS:**

**The Gordon Science of Adhesion Research Conference, Lewiston, ME**  
July 2011

- Poster presented titled “Sequence-Specific DNA-Carbon Nanotube Interactions”

**TCBG Computational Biophysics Hands-On Workshop, UI Urbana Champaign, IL** Dec 2010

Advanced topics in molecular dynamics simulations using *NAMD* & *VMD*

**The 4<sup>th</sup> Carbon Nanotube Workshop at NIST, Gaithersburg, MD**  
Sept 2010

- Topics on measurement and control of chirality
- Poster presented titled “DNA-Carbon Nanotube Interactions”

**Nano-Energy Workshop, Lehigh University, Bethlehem, PA**  
Sept 2010

- Topics on nanotechnology for energy applications
- Poster presented titled “Molecular Dynamics Simulations of DNA  $\beta$ -Sheet and  $\beta$ -Barrel Structures on Graphite and Carbon Nanotubes”

**AWARDS & SEMINARS**

**Excellence in Polymer Science and Engineering Award**

Dec 2011

Lehigh Valley Chapter

**Seventh Annual SPE Polymer Nanocomposites Conference, *Bethlehem, PA***

March 2012

Invited Seminar Speaker

**TEACHING EXPERIENCE:**

**Teaching Assistant, *Lehigh University, Bethlehem, PA***

**Five Semesters:** Fall 2007, Fall 2008, Spring 2009, Spring 2010, Spring 2011

- Assisted with undergraduate bio-engineering physiology and biotechnology courses
- Conducted weekly physiology and biotechnology laboratories

**Undergraduate Teaching Apprentice, *Lehigh University, Bethlehem, PA***

- Chemical Engineering Thermodynamics, Fall 2006
- As a junior, led weekly homework review sessions for sophomore class

**PROFESSIONAL AFFILIATIONS:**

- AIChE
- ACS